THE UNIVERSITY *of* EDINBURGH

Using Novel Methods to Investigate the Phloem of Higher Plants

Karen Bell

THE UNIVERSITY *of* EDINBURGH

Thesis submitted for the degree of

Doctor of Philosophy

University of Edinburgh

School of Biological Sciences

Year of Submission

2018

Declaration

I declare that this thesis was written by myself and that the research presented is my own work, except where stated otherwise. This work has not been submitted for any other degree or professional qualification.

Karen Bell

Abstract

This thesis presents the results of an investigation into the phloem of higher plants. The functional unit of the phloem is the sieve element companion cell (SE:CC) complex. Following a period of surgical proteolysis the mature SE joins with others in a file to create a syncytial distribution network called the sieve tube (ST). This living conducting unit has a much-reduced protoplasm with the adjoining, ontogenically related, CC underwriting much of its basic functions. The SE is principally responsible for the long-distance transport of photosynthate from areas of production to areas of growth and storage. Additionally, this transport stream carries a myriad of dissolved growth factors, RNA and proteins that can act at discrete sites along the way. The mechanisms by which the phloem achieves this specificity amidst bulk flow remain to be resolved, but by accomplishing both the phloem coordinates concerted plant growth and development. Much of these details remain obscure as the phloem is recalcitrant to conventional study.

The aim of this project was to tailor emerging technologies and develop new methodology specific to the study of the phloem.

This thesis contains descriptions of the first ever super-resolution images taken of plants. This required a specific tissue processing schedule to be developed. The new insight afforded a greater understanding into the arrangement of viral movement proteins throughout the sieve plate and the parietal layer of the SE. Next a new technique for preserving fluorescence, antigenicity and fine structures is presented. This correlated imaging method allows vascular tissues to be examined by conventional light microscopy, super-resolution microscopy and the electron microscope. Through using this unifying method of sample preparation, it is possible to conduct an investigation from the tissue level to the nanometer scale. Finally, there is a survey of the SE parietal layer where a variety of the techniques discussed above are brought to bear upon the structures that survive the autolytic purge.

It is hoped that these tools will find a wider use in the plant science community.

Acknowledgement and thanks

I would like to sincerely thank Professor Karl Oparka for giving me this opportunity to develop myself. I have benefitted enormously from his generous support, insight, enthusiasm and occasional kick up the backside.

I am very grateful to the School of Biological Sciences at the University of Edinburgh for the staff scholarship that allowed me to undertake this PhD project on a part-time basis letting me to maintain my role as laboratory manager alongside.

I have been very fortunate to have worked in a supportive environment surrounded by engaged, intelligent lab-mates and IMPS staff. Steve Mitchell in particular spent a lot of time discussing all aspects of electron microscopy, resin embedding and the SPFL. The contributions of the media kitchen, glasshouse and workshop staff are also gratefully acknowledged.

To my wonderful family who have supported me endlessly I thank you. Special mention to David and Cathy for giving me generous access to their city centre pied-à-terre. This allowed me to get the very most out of my limited working hours. To Kenny, my best friend, I am proud to have earned this doctorate but the only title I ever wanted was mum and you gave me that. I love you.

Lay summary

The principal constituents of the plant vascular system are xylem and phloem. Both are conducting tissues and facilitate bulk flow as well as lateral exchange. Although broadly accommodating the same function they differ markedly anatomically. At functional maturity, xylem is a network of dead lignified vessels that transports water and minerals from the root to the leaves using negative pressure. In contrast, the phloem is alive at maturity and uses positive pressure to transport sugars, proteins, and other molecules from areas of production (e.g. photosynthesising leaves) to areas of demand (e.g. growing roots and fruits).

Although the phloem is widely acknowledged to play a fundamental role in plant growth, development, and regulation, comparatively little is understood about its structure and function. This is because the phloem is a tissue recalcitrant to conventional study. Direct microscopic observations are difficult as the phloem is embedded amongst supporting tissues and this depth exceeds the working distances of objective lenses. Whereas cutting sections releases the high internal pressures which generates cellular artefacts. Regardless, microscopic investigations have proved vital in understanding phloem.

Presented in this thesis are methods that allow the phloem to be imaged with light and the electron microscope, as well as a correlative imaging method that lets the same phloem samples be imaged by both consecutively. It is anticipated that the methods in this thesis will be useful to researchers studying this vital and challenging tissue.

Abbreviations

3D-SIM	three dimensional structured illumination microscopy
BSA	bovine serum albumin
CC	companion cell
CCD	charge coupled device
CF	carboxyfluorescein
CLEM	correlative light electron microscopy
CMV	cucumber mosaic virus
CSLM	confocal laser scanning microscopy
DAB	3,3′-diaminobenzidine
DAPI	4′,6-Diamidine-2′-phenylindole dihydrochloride
ddH_2O	double distilled water
$DiOC_6$	3,3'-dihexyloxacarbocyanine iodide
DTT	dithiothreitol
EGTA	ethylene glycol-bis(β-aminoethyl ether)-N,N,N',N'-tetraacetic acid
EM	electron microscopy/ microscope
ER	endoplasmic reticulum
Fab	fragment antigen-binding
FRAP	fluorescence recovery after photobleaching
GFP	green fluorescent protein
GUS	β-glucuronidase
HPTS	8-hydroxypyrene-l,3,6- trisulphonic acid
isoSTED	isotropic stimulated emission depletion microscopy
LLSM	lattice light sheet microscopy
LR	London resin
mCherry	monomeric cherry
mCitrine	monomeric citrine
MP:GFP	movement protein green fluorescent protein
MT	microtubules
NA	numerical aperture
OMX	optical microscope eXperimental

P-plastids	protein plastids
P-protein	phloem protein
PAGFP	photactivated green fluorescent protein
PALM	photoactivated localisation microscopy
PD	plasmodesma
PDCB1	plasmodesmata callose binding protein 1
pH	potential of hydrogen
PI	propidium iodide
PIPES	piperazinediethanesulfonic acid
PM	plasma membrane
PPU	pore plasmodesma unit
PSF	point spread function
RTN	reticulon
S-plastids	starch plastids
SE	sieve element
SER	sieve element reticulum
SIM	structured illumination microscopy
SP	sieve plate
ST	sieve tube
STED	stimulated emission depletion microscopy
STORM	stochastic optical reconstruction microscopy
TEM	transmission electron microscopy
TIRF	total internal reflection microscopy
TMV	tobacco mosaic virus
TMV.MP:GFP	tobacco mosaic virus movement protein green fluorescent protein
UV	ultra violet
YFP	yellow fluorescent protein
ZIO	zinc iodide osmium

Figures and tables

Table of Contents

1. Introduction

The purpose of this study was to develop novel methods to investigate the sieve element. The aim of this chapter is to introduce the sieve element as a conducting element of the phloem, discuss its development and organisation and to survey the methods that have been used previously in its investigation

The principal constituents of the plant vascular system are the xylem and the phloem. Both are conducting tissues and function to facilitate bulk axial flow and lateral exchange of water and solutes. At functional maturity, the xylem is a network of dead lignified vessels that transports water and minerals from the root to the leaves using negative pressure. In contrast, the phloem is living tissue consisting of an ensemble of cell types that facilitate long-distance movement of diverse cargos. This main cargo is photosynthate, but several growth factors and diverse RNAs also move from carbon-exporting sources, e.g. photosynthesing leaves, to carbon-importing sinks, e.g. developing fruits and meristematic tissues (Knoblauch and Peters, 2017). The conducting cells of the phloem are termed sieve elements (SEs) and they are supported by parenchyma cells, principally the ontogenically related companion cells (CCs). A file of SEs, joined end to end, is referred to as a sieve tube (ST). The structure of the phloem is intimately related to its function, and the SE has a refined structure that maximises its effectiveness as a living conducting element.

During maturation the SE undergoes a period of incomplete autolysis that denudes the cell of ribosomes, Golgi bodies, microtubules, actin, nucleus and vacuole. At maturity, only the plasma membrane, endoplasmic reticulum (ER), plastids, mitochondria and phloem proteins (P-proteins) remain (Van Bel, 2003; Heo et al., 2017). Without a capacity for protein synthesis or genetic control, it is believed that the limited protoplasm of the SE relies upon the CC to support its basic functions, although the exact nature of the

support remains to be established (Otero and Helariutta, 2017). Although the phloem is widely acknowledged to play a fundamental role in plant growth, development and regulation, only now are the factors that underpin and influence its development and conductance emerging (Furuta et al., 2014; Ross-Elliott et al., 2017). This is because the phloem is a tissue recalcitrant to conventional study. Microscopic analysis is complicated by the high internal positive pressures within the SE. This makes the SE very sensitive to damage, which hinders processing for electron microscopy (EM), whereas direct observations are complicated by its position deep amongst supporting tissues (Knoblauch and Van Bel, 1998). Regardless, microscopic investigations have proved vital in understanding the phloem. Whereas EM investigations have provided a structural context (Everts, 1990), light microscope imaging has revealed much about movement into, through and out from the phloem (Oparka et al., 1994; Froelich et al., 2011; Ross-Elliott et al., 2017). With the emergence of super-resolution microscopy (Betzig et al., 2006; Schermelleh et al., 2008) and correlative imaging methodologies (Keene et al., 2008), microscopy continues to offer a fruitful avenue for discovery in the phloem.

Historical context and early investigations

An anatomical description of the phloem was first made by Theodor Hartig in 1837 when examining woody trees. Elementary 'sap skin' was observed to contain 'Siebröhren' (sieve tubes) that contained 'Siebporen' (sieve pores) (Behnke and Sjolund, 1990). The elementary 'sap skin' was also seen to contain other cells, and this assembly was called the phloem by Nägeli (1858; as discussed in Behnke and Sjolund, 1990). Prior to this, the results of tree bark ringing had concluded that this zone was crucial for movement. Progress in understanding phloem anatomy was slower than for xylem due to their 'soft conducting cells' which complicated sample processing and that also compromised historical surveys of the fossil record or herbarium materials (Cheadle, 1956). Refinements to sample processing, e.g., use of

cytological dyes (Harrar, 1928) offered avenues for further study but the advent of the EM was necessary to allow phloem ultrastructure to be investigated. This increase in resolution did not, however, result in a consensus of phloem structure. The first paper to examine SE with the EM was published by Huber and Kolbe (1948; reviewed in Weatherley and Johnson, 1968) but it, and other initial investigations, offered little insight due to crude sample preparation methods. Studies continued, and the use of osmic acid as a fixative and methacrylate as an embedding medium greatly improved sample quality (Hepton et al., 1955 as discussed in Weatherly and Johnson, 1968), but an appreciation was yet to be made of the effect that processing had upon SE integrity. In 1965 the renowned plant anatomist, Katherine Esau (Esau,1965), served to highlight these difficulties and provided a critical appraisal of the prevailing methodologies. Esau (1965) demonstrated the effects that different fixatives had upon the fidelity of membrane preservation and this led to a wide adoption of gluteraldehyde and osmic acid (aqueous solution of osmium tetroxide, OsO_4) as fixatives of choice. Esau also addressed the issue of 'surge artefacts' that occur when the STs are severed. The high internal pressure is released causing a physical shifting of cellular constituents from their *bona fide* positions towards the cut end of the tissue, complicating structural studies. An appreciation of this phenomenon, however, allowed microscopists to critically assess the fidelity of their micrographs and the quality of their material. In spite of these difficulties, the changes that occur in the SE protoplast during maturation were chronicled and a conserved timeline of SE maturation emerged.

SE development studies using the EM

Initially the SE contains all the cellular components characteristic of a young plant cell, and so is virtually indistinct from the surrounding meristematic cells. The first discernible change that occurs is that the lateral walls thicken. This is mediated by cortical microtubules (MT) and the Golgi apparatus (Thorsch and Esau, 1982). The MT align perpendicularly to the cell axis, and cell wall material is delivered via smooth Golgi vesicles that liberate their cargo following fusion at the plasma membrane. At this time both Golgi and MT are abundant in the protoplasm but following cessation of cell-wall synthesis the relative numbers declines sharply (Thorsch and Esau, 1982). Concomitant with this cessation, changes are apparent in the ER and the nucleus (Esau, 1972). There is an increase in scattered ER cisternae, which then begin to stack, becoming more abundant towards the cell periphery. As the stacking becomes tighter, an electron dense material becomes apparent between the contiguous cisternae (Esau, 1972). Those membranes that face the cytoplasm are now the only ones associated with ribosomes. In the nucleus, chromatin begins to condense. This process, known as chromatolysis, continues with a gradual loss of all stainable content and the rupturing of the nuclear envelope (Esau, 1972). At this point the ribosomes invade the nucleus and the autolytic process is at its peak. The change to a completely differentiated state is sudden; the tonoplast begins to breakdown, Golgi are removed and MT and actin disappear. Mitochondria undergo only minor structural changes, as do the plastids, designated as p-plastids or s-plastids depending on the ergastic material they contain (**p**rotein or **s**tarch, respectively; Behnke and Schulz,1983). Both survive the autolytic purge and assume a parietal (peripheral) position. A proportion of the ER remains stacked and parietal, often in an intimate association with mitochondria and plastids, whereas some ER remains as an anatomising network next to the plasma membrane (Evert, 1990). Whereas the changes to the lateral cell wall precedes the major autolytic events, remodelling of the end walls occurs

later, and perforation of the end walls does not begin until the nucleus degenerates. When the ER stacks and the nuclear material condenses, the site of the future sieve plate (SP) is still apparent as a thin transverse wall with plasmodesmata (PD) at future pore sites (Esau and Gill, 1973). Callose begins to form on either side of the wall and these paired deposits (platelets) enlarge, almost encapsulating the PD. Even at this stage, and whilst extensive stacking is underway elsewhere in the cytosol, the ER remains associated with the PD. The perforation of the future pore begins as the nuclear body degenerates and wall material is removed from the middle lamella. Whilst some ER may remain, traversing the pore, most is removed as the pores reach their full diameter. The pores are set amongst the remnants of the end wall, a structure termed the SP. The perforated SP provides cytoplasmic and plasma membrane continuity throughout the ST. The SP is not a benign conduit and is of central importance following ST injury. It is at the SP that P-protein and dislodged organelles collect, occluding the plate and thereby limiting photosynthate loss and isolating the damaged phloem tissue. This crude occlusion is thought to precede the synthesis of callose that eventually seals the pores (Levy, 2007).

CCs also share connections with SEs. The PD that exist between CC and SE have a distinct form. Adjacent PD in the CC form a branched structure in the CC half of the shared wall. These then fuse, emerging as a single orifice in the SE (see figure 1.1). This form of symplastic connection is unique and is termed a pore-plasmodesma unit (PPU; van Bel and Kempers, 1996). The connection is vital to supporting the enucleate SE and has a role in loading assimilates into the SE. The desmotubule of the PPU provides ER continuity between the CC and SE. Evidence of dynamic cell-to- cell lumenal transport via the ER, has been demonstrated in epidermal cells (Barton et al., 2011) but it has yet to be established if the ER conduits in the PPU are competent for this type of exchange.

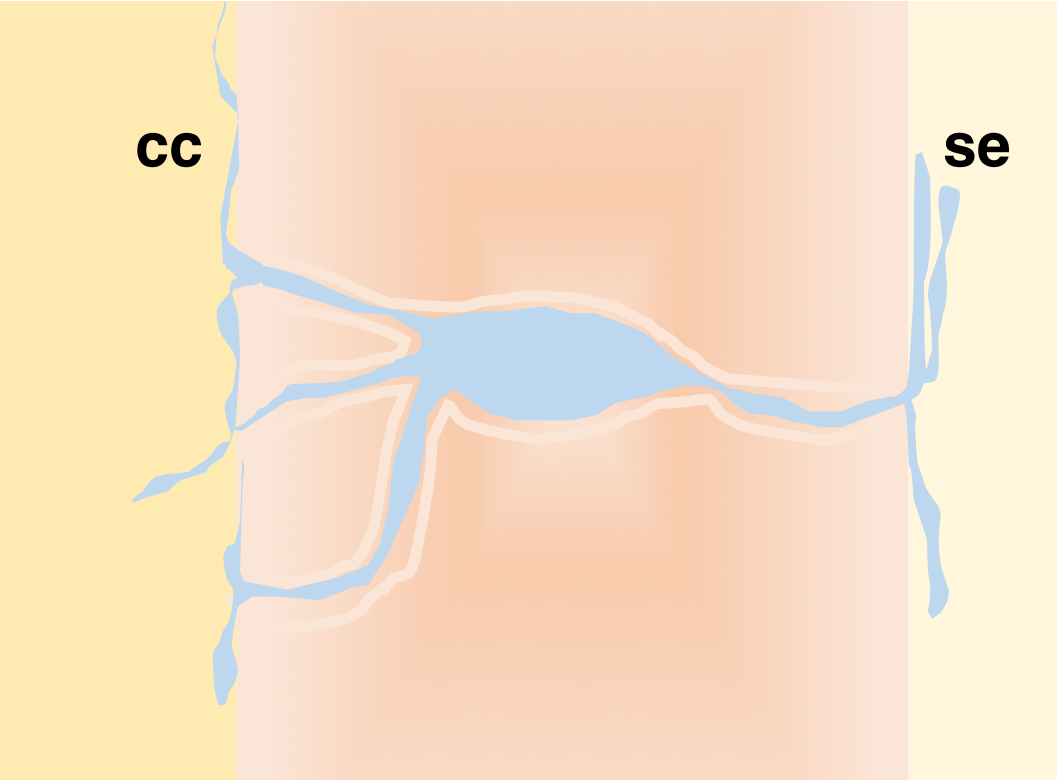

Figure 1.1 Diagram of a PPU

Sketch showing three orifices from the CC linking to a central lacuna. On the SE (se) side a single pore overlays this. The ER (blue) runs through the branched PPU structure connecting the ER in the CC and SE.

Concomitant with the dramatic changes occurring in the cell interior, the SE is subject to lateral pressure and longitudinal stretching from the surrounding tissues (Esau and Gill, 1973). This results in an elongated and narrower final cell profile. The initial lateral wall thickenings are reduced in the mature SE, suggesting that this period of thickening accommodates the external stretching forces.

Whereas SE maturation is manifestly a depletion process, it is during this time that one of the most characteristic, and intriguing, constituents of the SE increases in prominence. Often present in young undifferentiated cells as a small inclusion, P-protein exists in a variety of forms; filamentous, fibrillar, tubular, crystalline or amorphous (Knoblauch et al., 2012). During early stages of differentiation, small filaments associate with helical polysomes

(functional aggregates of ribosomes) that synthesise the protein which is then distributed throughout the SE lumen. As the nucleus degenerates and the ribosomes are cleared, the protein forms aggregates, and these increase in size. By the time the ER becomes parietal, so does the P-protein, forming a fine network of strands. The 'normal' position of P-protein has remained contentious as it often physically reflects damage more than any other of the remaining SE constituents (Evert, 1977). P-protein is now widely agreed to be parietal, with the extent of dispersal varying in a species-specific fashion. Although once thought to be involved in movement (Thaine et al., 1967), most researchers agree that P-protein functions in occlusion (hence its renaming as Sieve Element Occlusion (SEO) protein), acting in consort with callose to plug sieve pores in damaged SEs (Peliessier et al., 2008).

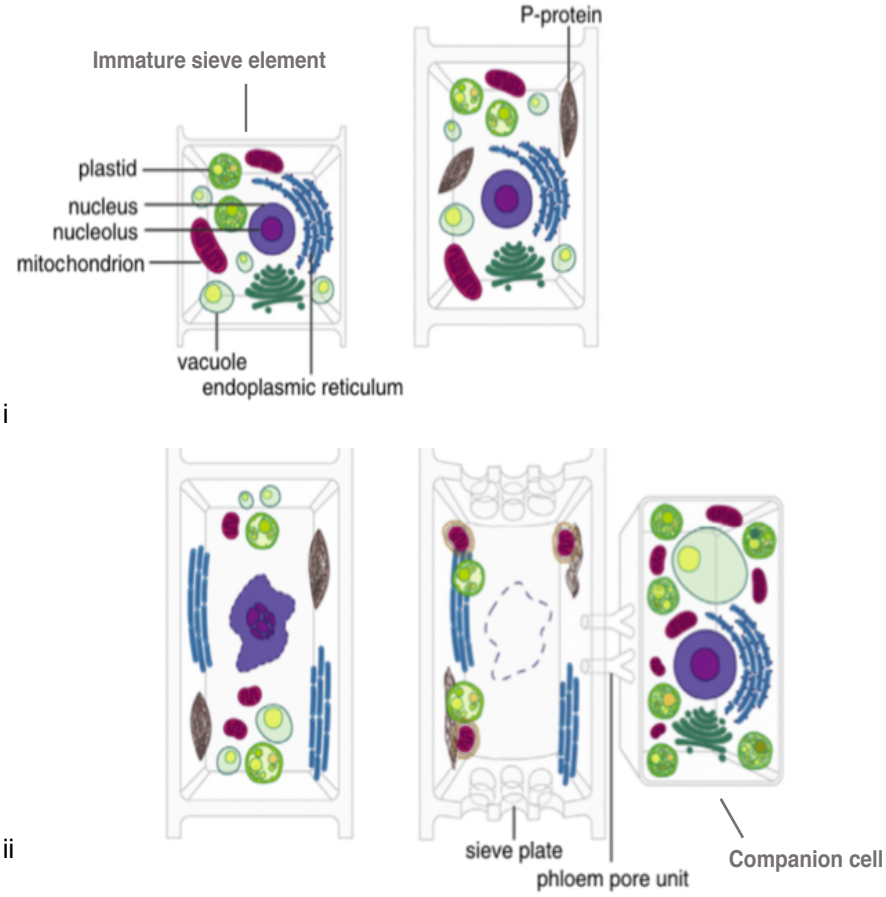

Figure 1.2 Summary of SE maturation

Diagrammatic representation of the changes to the SE protoplasm during maturation (i -ii). Showing organelle removal and their final parietal positions. Adapted from Heo et al., 2017.

The timeline of SE maturation (summarised in figure 1.2) was established using EM and by cataloguing the morphological changes apparent in differentiating SEs across many species (Evert, 1990). The genes underwriting this process were recently described in an elegant study that analysed gene expression whilst following the fate of fluorescent nuclear markers (Furuta et al., 2014). The markers allowed nuclear disintegration to be imaged, providing a visual context to the genetic analysis, and found that it was completed in around 10 minutes.

Epifluorescence microscopy and immunofluorescence

EM investigations between 1950 and 1980 provided an ultrastructural context for SE development. In addition, dynamic information was added through developments in light microscopy and allied methodologies. Epifluorescence microscopy and immunofluorescence led a renaissance in light microscopy (White et al., 1987). Through harnessing the specificity of antibodies it became possible to visualise the position of biomolecular targets in a cell, or throughout a tissue, by tagging antibodies with fluorescent dyes. The epifluorescence microscope uses a mercury arc lamp to illuminate the sample through the objective lens. Fluorescence occurs when a substance absorbs light of a low wavelength, gets excited to a higher energy state and on decay emits a light of longer wavelength. This spectral separation represents the energy required to make that transition and ensures that the light generated by the substance is distinct from the light that illuminates it. The fluorescence emitted then passes through an emission filter, allowing only prescribed wavelengths to pass, before reaching the eye or camera. A limitation of epifluorescence is that the mercury lamp illuminates the whole sample and this generates signal from above and below the plane of focus. Sample preparation techniques were devised to ameliorate this inherent problem, leading to the use of flattened cells and cutting tissue into sections (White et al., 1987). Both introduce technical challenges as well as problems

interpreting 3D structure. SEs are embedded in ground tissue, necessitating sample sectioning to limit the effect that out of focus light from surrounding bulk tissues would generate. This limits its usefulness as a tool for SE cell-biology research. However, epifluorescence microscopy and immunofluorescence were used successfully to identify phloem cells and phloem p-proteins (Toth et al., 1994). Due to the background flare, and a lack of resolution, images identified P-protein at the gross tissue level but EM images confirmed the ability of the antibodies to detect P-protein.

Confocal laser scanning microscopy

Confocal laser scanning microscopy (CSLM) uses a focussed laser beam to illuminate the sample. It images within a limited volume, 'optically sectioning' the sample using a pinhole in front of the detector that stops any out of focus light from reaching it. By illuminating only one focal plane at a time image quality is enhanced. Through scanning the laser across the sample in a raster, an image of the sample is reconstructed, and by combining successive scans from multiple focal planes a volume projection can be made to generate a 3D view of the sample. This method does not excite the bulk tissue in the same way as a mercury-arc lamp does in epifluorescence microscopy, thereby reducing out of focus flare, phototoxicity and fluorochrome bleaching concomitant with intense illumination.

The first use of CSLM in phloem biology was in 1992 (Schulz, 1992) to study gymnosperm phloem. In gymnosperms the phloem operates under the same principles as in angiosperms, but some of the terminology differs when describing largely analogous structures. For example, SP and SE in angiosperms are referred to as sieve areas and sieve cells in gymnosperms (Schulz, 1992). Schulz (1992) examined differentiating sieve cells, observing the disappearance of nuclear fluorescence and central vacuoles. *In vivo* staining of the ER, using the fluorescent dye, $DiOC_6$, confirmed that it

covered the sieve areas that link mature sieve cells. This arrangement had also been seen in the EM but had been disregarded as artefactual as the presence of the ER over sieve-area pores patently has consequences for mass-flow. The 3D optical sectioning abilities of the CSLM allowed the ER form to be appreciated in relation to the sieve area.

The CSLM was also used to provide the first direct non-invasive observations of phloem transport and unloading in an intact plant (Oparka et al., 1994). 5(6) carboxyfluorescein (CF) was ester loaded into a cotyledon where upon it then translocated rapidly to the root tip. The utility of the CSLM was extended further by concentrating the laser in a clearly defined region of the root and bleaching the dye at the unloading zone, (rendered non-fluorescent by inducing a non-reversible entry into the triplet-state), allowing the unloading phenomenon to be scrutinised further. This study represented a considerable advance over the methods used previously to investigate phloem transport. Radioactive isotopes (^{14}C and ^{3}H) were used widely for this purpose but required the tissues to be dead prior to autoradiography, preventing dynamic information from being gathered. However, *in vivo* detection was achieved using strongly emitting isotopes but these studies lacked spatial resolution. (both discussed in Oparka et al., 1994). CSLM imaging of fluorescent dyes provided the first platform for high temporal and spatial dissection of phloem loading and unloading, recently providing a detailed analysis of the phloem unloading process in Arabidopsis roots (Ross-Elliot et al., 2017).

Endogenous protein and genetic labelling strategies

β-glucuronidase gene (GUS) was first used in higher plants 30 years ago to monitor expression of chimeric genes (Jefferson et al., 1987). This is a histochemical technique that monitors GUS expression as a proxy for target gene expression. The GUS gene is fused to the promoter of interest and is expressed wherever the promoter is active. GUS is visualised following a reaction between it and an exogenously applied substrate (5-bromo-4-chloro-

3-indolyl glucuronide; X-gluc). The reaction product is blue and the gene expression profile within cells or throughout tissues are apparent with the light microscope. GUS was used to show that the CC-specific promoter (*pAtSUC2*) is expressed in nematode induced syncytia but that the promoter of another transporter (*AtSTP*) was not (Juergensen et al., 2003). GUS staining is very sensitive, with less than 100 molecules detectable in a cell (Köhler, 1998). Jellyfish green fluorescent protein (GFP) was first used as a reporter for virus infections in plants. (Baulcombe et al., 1995). GFP is 238 amino acids and is arranged as a beta barrel structure with the chromophore at its centre. It allowed virus spread through the plant to be observed at the whole-plant level, using a hand-held ultra violet light, or at the tissue / cellular level with the epi-fluorescence microscope. Although reportedly less sensitive than GUS (< 100 molecule detection threshold GUS vs >10,000 molecule detection threshold for GFP; Köhler, 1998) the main advantage of GFP over GUS staining is that it does not require any exogenous substrates to be applied to visualise the signal. It is therefore possible to observe expression on an intact plant and watch to see how it develops over time. Improvements were made to tailor GFP expression and stability in plants which served to increase its utility (Haseloff et al., 1997). GFP has been used in the phloem to visualise symplastic unloading into sinks (Imlau et al., 1999), as a reporter to demonstrate that viral infection can overcome the symplastic barrier between the CC-SE complex and surrounding cells (Peleg et al., 2007), and to study vein maturation in developing tobacco leaves (Wright et al., 2003).

Limits of optical microscopy

Whereas the above studies described general phloem structures, greater detail was required to inform models of movement. For example, transitory responses to Ca^{2+} flux or pathogen challenge may not be observed. This is due to the limited spatial and temporal resolution of the imaging systems

discussed so far. Spatial resolution is a product of the resolving power of the microscope and the properties of the sample. The resolving power is the ability to separate features and show them as distinct entities. The power of the system dictates how close these objects can be and for an optical system this is dependent on the numerical aperture (NA) of the objective lens. The greater the NA, the greater the angle of the cone of light the lens can collect in which sample information is contained (see figure 1.3).

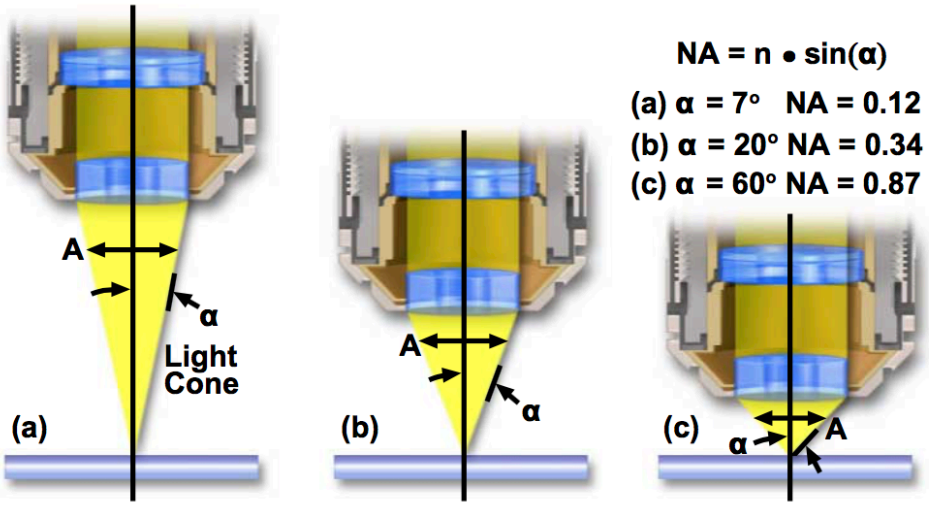

Figure 1.3 Relationship between lens numerical aperture and relative working distance
Illustration of the relationship between the numerical aperture (NA) of a lens, its working distance and light gathering abilities. The NA increase from a – c but note the concomitant decrease in objective lens distance from the sample. Adapted from www.microscopyu.com

It is not possible, however, to arbitrarily increase the NA as the working distance of the lens decreases inversely with increasing NA, and a point is reached at which this becomes impracticable. The theoretical limits of an optical imaging system were first established in 1873 by Ernst Abbe (as discussed in Sahl et al., 2017). The mathematical expression for this is $\mathbf{d = \lambda/2n \sin \alpha}$ where (**d**) is the minimum distance between objects required to resolve them as single entities and is a product of the wavelength (**λ**) of light divided by the numerical aperture of the lens (**n sin α**) multiplied by 2. A minimum value for **d** is reached as it is not possible to arbitrarily increase the numerical aperture because light will no longer be able to enter the lens.

Nor is it feasible to use wavelengths of light shorter than 400 nm as these can damage biological samples. Abbe's theorem predicted that objects closer than approximately 200 nm laterally (x–y) and 500 nm axially (z) cannot be resolved. Whilst the lateral resolution limit is a direct consequence of light diffraction, the much higher axial limit is due to microscope design. Anisotropy results as light is collected from only one side of the specimen, causing an elongation of the point spread function (PSF) in the axial plane (point spread function is the 3D intensity distribution of a point object; see figure 1.4). Optical sectioning using a confocal microscope allows greater sample penetration and increased resolution by creating an effectively smaller PSF, but the axial resolution remains comparatively poor.

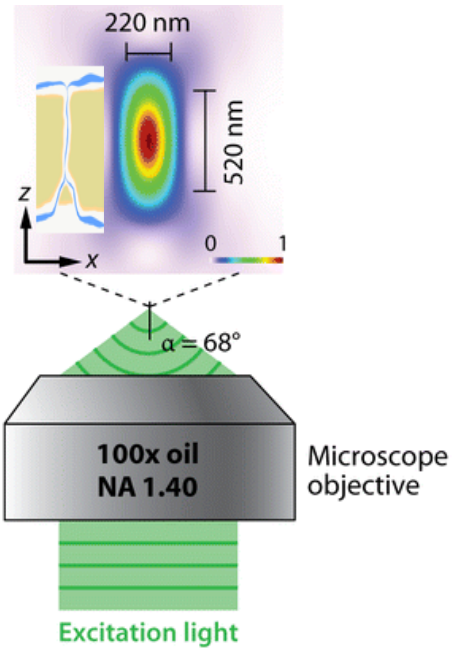

Figure 1.4 Point spread function

The point spread function visualised when using an oil immersion objective and illuminating light of 550 nm. The dimensions of a PPU are shown to scale. Note that the majority of the PPU pore falls within the PSF. Adapted from Huang et al., 2009.

I^{5}M and 4Pi microscopy boost axial resolution by using opposing objective lenses with high NAs. In this scheme, a much greater portion of the full spherical angle is covered and a common focal area is imaged coherently. I^{5}M is a widefield system in which an arc lamp illuminates the sample (Gustafsson et al. 1999). In 4Pi microscopy, a laser is used and the samples are optically sectioned (Hell and Stelzer, 1992). This was used by Vasilchenko et al. (2016) to determine the biological activities of a new anti-

microbial peptide by revealing its association with the surface of a pathogenic fungi conidia and its subsequent entry into the cytoplasm.

Super-resolution microscopy

The basic principles of a new technology that surpassed the theoretical limits set by Abbe were first published in the 1990s (Hell and Wichman, 1994; Gustafsson et al., 1999). These represented a paradigm shift as the solutions were not optical but instead exploited the photochemistry of the fluorophore and a novel way to illuminate samples. Practical applications of these techniques appeared soon after (Klar et al., 2000; Gustafsson, 2000). Structured illumination microscopy (SIM) (Gustafsson et al., 2008; Schermelleh, 2008) resolves objects beyond the diffraction limit using patterned excitation. When the incident light, with a defined patterned structure, interacts with the sample structure, as represented by the distribution of the dye/fluorescent protein, it produces emitted light that contains interference fringes (see figure 1.5)

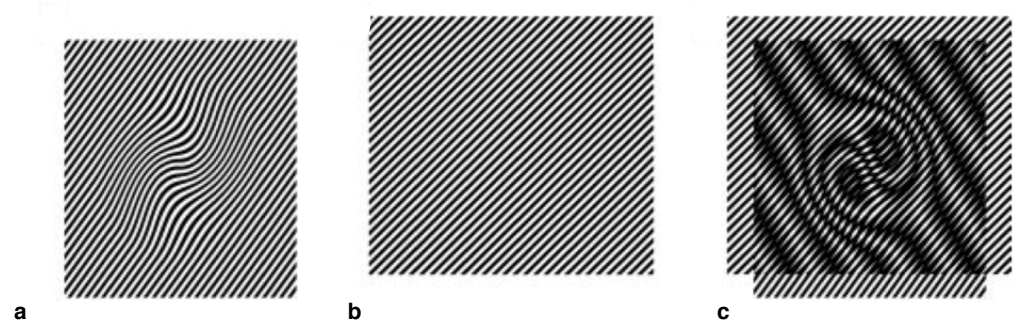

Figure 1.5 Moiré effect

a) Unknown sample structure b) Known regular illumination pattern. c) Moiré fringes occur when the different structures overlap. This interaction can generate patterns course enough to be seen through the microscope. Adapted from Gustafsson, (2005).

As the illumination pattern is known, this can be readily accounted for and the fringe may be coarser than either of the original patterns and so may be more readily observable in the microscope. As the patterning of the incident light is directional, it is necessary to shift and rotate the phase over 360° (Dobbie et al., 2011). The images are then processed to produce the final super-resolution image. Currently the routine resolution achievable with 3D-SIM is 100 nm in xy direction and 200 nm in z direction (reviewed in Komis et al., 2015). In addition to the enhanced resolution, the increased optical sectioning capacity offered is of significant benefit to plant cell biologists with images being collected every 125 nm. The typical plant cell wall is 700 nm thick and 3D-SIM allow up to five images to be taken in this volume (c.f., approximately only once every 500 nm with CSLM). This allows different components to be spatially resolved (figure 1.6).

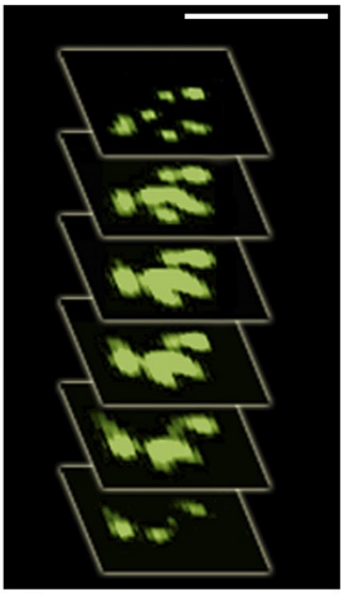

A further advantage is that 3D-SIM is also compatible with standard fluorochromes (e.g. GFP, mCherry, DAPI) and with the sample preparation methods commonly used for light microscopy.

Figure 1.6 3D-SIM resolves features of branched PD

The PD are labelled with a viral movement protein fused to GFP known to accumulate within central cavities. 3D-SIM detects GFP, and takes images every 125 nm allowing the distinct structures within a branched PD be determined non-destructively. Six distinct orifices overlie a convoluted central cavity from which only three pores emerge. Adapted from Fitzgibbon et al., 2010. Scale 1 μm.

In this thesis I present the first use of 3D-SIM to study phloem tissues in plants

Stimulated emission depletion (STED) was the first far-field super-resolution imaging technique to be applied to cell biology (Klar et al., 2000). Like SIM it uses patterned excitement to image samples and generate images that surpass the resolution limit described by Abbe. A red-shifted doughnut-shaped STED laser has an intensity zero at the focal centre and strong intensities at the periphery (figure 1.7).

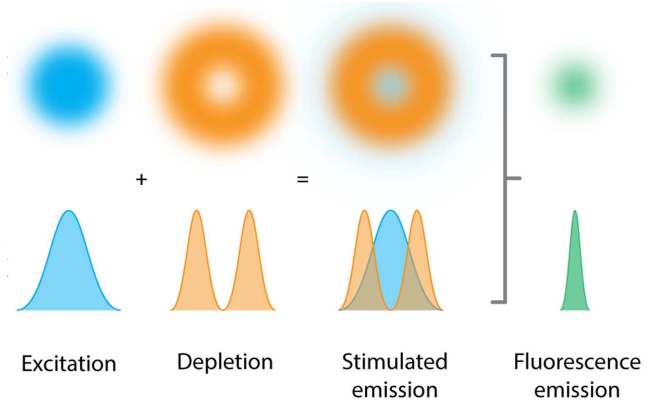

The excitation laser is then precisely co- aligned to occupy the STED zero point. The STED beam serves to de-excite potentially excited molecules through stimulated emission.

Figure 1.7 STED principle

The Gaussian shaped excitation beam is superimposed upon the minima at the centre of the doughnut-shaped depletion beam, these combine to minimise the area illuminated at the focal point reducing the fluorochrome PSF and increasing resolution. Adapted from Vangindertael et al., 2018

Stimulated emission occurs when an excited state fluorophore encounters a photon that contains the energy difference between the excited and ground state. Consequently, the fluorophore is brought back to the ground state before emission occurs. The fluorophores are therefore activated and imaged in a small region reducing the effective width of the PSF. Although reliant on the pattern generated by two diffraction-limited laser light sources, STED is truly super resolution as the size of the STED pattern is limited only by the power of the STED laser. STED offers a higher lateral resolution than 3D-SIM (20 nm; Komis et al., 2015) but a comparatively poorer axial resolution (500nm; Komis et al., 2015) but this aniosotropy has been corrected in a recent form of the technique called iso STED (Schmidt et al., 2009). STED has only been used in one research paper on plant cells (Klein-Vehn et al., 2011). This is most likely due to the wavelength of the STED laser. Leica

Microsystems produce commercial STED platforms with 592, 660, and 775 nm STED laser outputs. The first two wavelengths are known to be in the range that induce autofluorescence in plant tissues (discussed in Kodama, 2016). The 775 nm STED laser is not anticipated to excite chlorophyll but its utility in a super-resolution study of plant tissues has yet to be established.

Offering an even greater lateral resolution is single-molecule imaging. The principle underlying single molecule detection is that the position of a single emitter can be localised with a high degree of accuracy if enough photons are collected. This allows the centre of the fluorescent emission to be determined by fitting the photon output to the ideal PSF (figure 1.8).

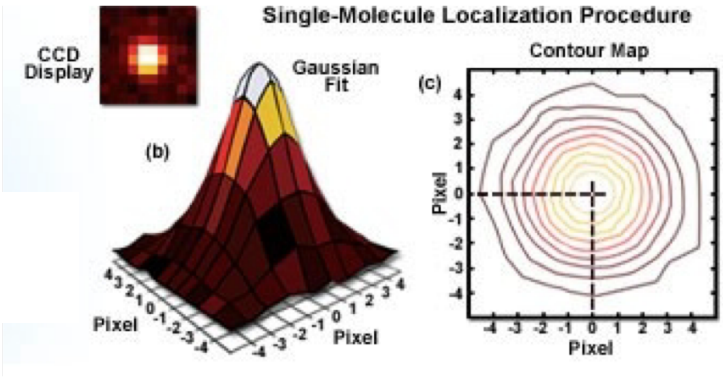

Figure 1.8 PALM principle
A contour map shows the intensity distribution of photons emitted from a single fluorochrome. If enough photons are collected the centroid of emission can be calculated and this data can be used to record their position. Adapted from Zeiss application notes.

Photoactivation localisation microscopy (PALM), is an example of a technique that uses this methodology (Betzig et al., 2006). To detect a single emitter from a sample containing many fluorescent molecules requires a probe with requisite photophysical properties (Lippincott-Schwartz and Patterson, 2009) and a sensitive detection system. Dronpa is a monomeric fluorescent protein used in single molecule detection experiments (Andro et al., 2004; Habuchi et al., 2005). It photoconverts from a green fluorescence to a dark state in response to prolonged 488 nm laser irradiation, with a sharp burst of 405 nm laser light restoring the initial green fluorescence. In single molecule studies, activation is stochastic, and the light–dark cycling

allows imaging and localisation without overlap. Through iteration of activation and imaging, a super-resolution image is constructed from the coordinates of many molecules. Resolution is directly dependent upon the total number of photons collected, and to that end it is essential to maximise the signal-to-noise ratio. In addition to using probes with a high dynamic range and contrast ratio, the imaging platform is frequently integrated with a total internal reflection (TIRF) microscope. In TIRF (Axelrod et al., 1984), the angle of incident light is such that it cannot cross the sample refractive index and so is deflected back into the objective. When the incident light hits the coverslip an evanescent wave is generated that decays exponentially, and so TIRF penetrates to only around 100 nm. Imaging in a limited focal volume limits background fluorescence from the bulk tissue increasing the signal to noise ratio by reducing noise. TIRF has been used in plant cell biology to study clathrin mediated endocytosis (Johnson and Vert, 2017). A lateral (x-y) resolution of 10 nm has been reported for PALM (Huang et al., 2016). The developers of STORM, an independently conceived single molecule detection methodology analogous to PALM, were the first to generate a 3D image using single molecule detection (Huang et al., 2009). They did so by using a cylindrical lens to generate an elliptical image of a single fluorophore. From this it was possible to measure the axial (z) position from the ellipticity and the lateral (x-y) position from the centroid. A resolution of 25 nm laterally (x-y) and 50 nm axially (z) was achieved (Huang et al., 2009).

Whilst the high lateral resolution offered by single molecule imaging has the potential to reveal much about the fine structure of the SE, even in very young *Arabidopsis thaliana* seedlings the phloem is not within 50 μm of the surface (Froelich et al., 2011). This makes direct observations of intact plants impossible, necessitating sensitive sample preparation methods.

In this thesis I describe methods to prepare samples for PALM imaging of the SE

Correlative light and electron microscopy (CLEM)

Because the resolution gap between that routinely achievable with light and EM is narrowing, there is a growing need to confirm that structures seen in the light microscope are indeed identical to those observed by transmission electron microscopy (TEM). Accordingly, a new area of biological imaging, correlative light and electron microscopy (CLEM), is emerging. Correlative microscopy is the application of two or more microscopy techniques to the same region of a sample, generating complementary structural and chemical information that would not be possible using a single technique (Jahn et al., 2012; Koster and Klumperman, 2003; reviewed in Tilsner and Oparka, 2010). This approach was used to image mitochondria expressing a fluorescent reporter using both PALM and TEM (Betzig et al., 2006). To retain fluorescence, the cells were frozen and cryosectioned before imaging. The PALM images were found to superimpose exactly on the TEM images, confirming the resolution of the PALM technique and accurately ascribing the correct protein localisation. Photo-oxidation is a method that translates a fluorescent signal to an electron-dense one. Upon illumination, virtually all fluorochromes produce singlet oxygen. Photo-oxidation harnesses singlet oxygen to convert the chromogen DAB (3,3′-diaminobenzidine tetrachloride) to a highly localised osmiophilic granular precipitate (Maranto, 1982). The conversion takes place in fixed tissues that have been incubated in an oxygenated DAB solution (Meisslitzer- Ruppitsch et al., 2009). Upon illumination with high intensity excitation light, reaction products develop, visualised as a gradual browning under bright field. Following treatment with osmium tetroxide, the samples can then be processed for EM as normal (Maranto, 1982). The success of the photo-oxidation reaction depends largely upon the capacity of the fluorochrome to generate sufficient singlet oxygen. Lucifer Yellow was the first fluorochrome used (Maranto, 1982), but subsequent studies have used other fluorochromes due principally to their greater singlet oxygen yield (Geipmans et al., 2006; Meisslitzer- Ruppitsch et al., 2009). The omnipresent GFP has been used successfully to catalyse the

photo-oxidation reaction but only in a few studies (Grabenbauer et al., 2005; Meisslitzer-Ruppitsch et al., 2009). Aside from conventional TEM imaging, photoconverted samples have also been used in electron tomography studies (Cortese et al., 2009). Electron tomography offers a three-dimensional insight into tissues by collecting a series of two-dimensional micrographs around a tilt axis. By back projecting these, a three-dimensional final image is reconstructed. Electron tomography can achieve an axial resolution between 4 and 7 nm (McIntosh et al., 2005). A branch of traditional TEM, electron tomography promises to offer significant insight into ultrastructure.

Many findings based on fluorescent protein imaging benefit from a structural context provided by the EM (Lippincott-Schwartz and Patterson, 2009). By using a super-resolution method in a correlative approach, a direct comparative analysis of imaging capabilities is possible. Perinetti et al. (2009) correlated 4Pi images of Golgi stacks with TEM serial sections and 3D reconstruction. They first mapped the positions of separated Golgi stacks with a wide field microscope before imaging them in 3D using confocal and then 4Pi microscopy. The correlation was achieved by detecting a fluorescent Golgi protein using a nanogold conjugated antibody, followed by careful TEM serial sectioning and recording. Whilst this approach required a second step to make the fluorescent signal visible in the EM, a bifunctional probe allows the sample to be directly detectable at both the light and EM level. FluoroNanogold is an example of a dual labelling reagent that contains fluorescent and electron-dense particles. It is an immunoglobulin fragment (the fragment of antigen binding, Fab) that is covalently bound to a fluorochrome and gold particle. Fab fragments are smaller than whole antibodies and as such can yield enhanced labelling efficiency. Greater penetration is also afforded by the comparatively small gold conjugate (between 0.8 and 1.4 nm; Robinson and Takizawa, 2009). A consequence of

this is that silver enhancements may be needed to increase the size of the gold particles to allow ready light microscope visualisation.

As immunocytochemistry is already a routine lab technique, with an ever-expanding toolbox of antibodies, using bifunctional probes in place of standard secondary antibodies is a potentially high-return imaging investment. However, a simpler processing schedule would be to conduct correlative imaging in which constitutively expressed fluorescent protein fusions are imaged first with light microscopes then examined by TEM. Pfeiffer et al. (2003) were able to image SEs and CCs using high-pressure freezing, followed by freeze substitution in acetone and resin embedding. They then used thick optical sections of the tissue to locate cells of interest, and these were subsequently imaged using TEM. Lee et al. (2011) examined cryo-sectioned *Arabidopsis thaliana* seedlings with the confocal microscope. After confocal mapping the sections were then processed for TEM. These authors were able to locate the same PD pit fields using confocal and TEM, providing important information on the localization of a novel PD protein. As a general rule, cryo-sectioning is a time-consuming process, and subcellular details may be obscured in cryo-sections because of poor tissue contrast (Watanabe et al., 2011).

Thompson and Wolniak (2008) described retention of the fluorescent protein mCitrine fused to an SE-plasma membrane protein in glycol methacrylate resin sections. The fluorescent signal was stable when viewed with wide-field microscopy but bleached rapidly under the confocal microscope. A major problem with imaging fluorescent proteins in resin sections has been that GFP and its derivatives are quenched by the acidic, oxidizing conditions required for fixation, dehydration, and embedding of delicate specimens (Tsien, 1998; Keene et al., 2008). Recently, however, Watanabe et al. (2011) explored the retention of fluorescent proteins in *Caenorhabditis elegans* cells

after fixation by different aldehydes and embedding media. This provided an excellent basis from which a plant-specific method could be devised.

Details of a new sample preparation method suitable for correlative 3D-SIM, confocal microscopy and TEM of the phloem are presented in this thesis.

2. Materials and Methods

2.1 Plant growth conditions

Nicotiana tabaccum plants were grown from seed in soil in a heated glasshouse and used for experiments between 30 and 55 days old. *Arabidopsis thaliana* seeds were surface sterilised by washing in 70% ethanol for two minutes and then 100% ethanol for two minutes. They were then allowed to air-dry on a piece of sterile filter paper. Seeds were germinated and grown on petri dishes on solid Murashige and Skoog medium (4.9 g/l MS salts, 3g/l sucrose, 10 g/l Difco Agar. pH 5.8) and sealed with Parafilm (Bemis). Plates were stratified for two days at 4 °C in the dark and then placed upright in racks to encourage the seedlings to grow along the surface of the media. Seedlings were used between three and five days post germination.

2.2 Fixative solution for light microscopy

The aldehydes used were from stocks in single-use glass ampules. The glutaraldehyde was electron microscopy grade and the formaldehyde a methanol-free preparation (both TAAB). The fixative solution consisted of 4% (v/v) formaldehyde and 0.25% glutaraldehyde diluted with 50mM 1,4-piperazinediethanesulfonic acid (PIPES) pH 6.9, 2mM EGTA, 1% (w/v) bovine serum albumin (BSA) in ddH_2O.

2.3 Xylem delivery of fixative

This was achieved by immediately submerging the cut petiole or stem in the fixative solution and then trimming the bottom 5 mm from the submerged tissue to eliminate any potential airlocks. These were then left to transpire in an illuminated fume hood for 60 minutes.

2.4 Producing sections using a vibrating microtome

Sections of fixed petiole were prepared using a Vibroslice Tissue Slicer HA752 (Camden Instruments). It is necessary to support the tissue during sectioning. Phytoagar is a plant tissue culture agar with a high gel strength and can be used at a minimal concentration of 5.0 g/l to obtain a solid gel. This concentration matches the mechanical properties of a young petiole well and so adequately supports sectioning. Trimmed petioles were added to cooled (approximately 40°C), molten 5% Phytoagar (Duchefa Biochemie) in a 5 cm diameter Petri dish. These were pushed down gently with a blunt implement to submerge them, taking care to remove any surrounding air bubbles and to orientate the samples to reflect the direction of sectioning e.g., lying flat at 180° to the surface to produce longitudinal sections or at 90° to the surface to cut transversely. Once set, excess agar was trimmed from the surface and the block was put on the microtome stub and the surrounding bath filled with Phosphate buffered saline (PBS; 1 mM KH_2PO_4, 155 mM NaCl and $Na_2HPO_4.7H_2O$ in ddH_2O, pH 7.4; illustrated in figure 2.1). A medium-fast setting was used to produce sections of around 100 µm thick.

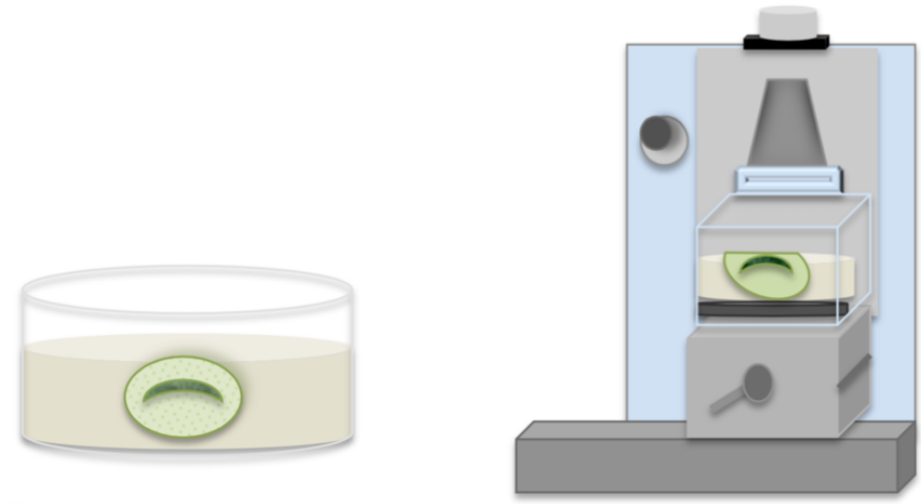

Figure 2.1 Cutting phloem sections using the vibrating microtome

Fixed, trimmed, petiole sections are immersed in phytoagar within a 5 cm diameter Petri dish. This disc is then trimmed and mounted upon the stub and the surrounding reservoir filled with phosphate buffered saline. Adapted from Bell and Oparka, 2015

These were then transferred to the fixative solution and held until there were sufficient numbers for downstream processing. For immediate imaging the tissues were washed for 10 minutes, with gentle agitation, using wash buffer, consisting of 2 mM EGTA (ethylene glycol-bis (β-aminoethyl ether)-N,N,N',N'-tetraacetic acid (EGTA; Fisher Scientific), 1% (w/v) BSA (Sigma), 50 mM PIPES (Sigma), pH 6.9 in ddH_2O. The wash buffer was changed a further two times, every ten minutes as before. The sections were then ready to be imaged or processed further.

2.5 Immunofluorescence

All processing occurred at room temperature with gentle agitation unless stated otherwise.

Driselase is useful when processing vasculature as it allows the sectioned material to separate slightly, affording a better view of phloem strands. If this was desired, the sections were incubated in driselase solution; 2% (w/v) driselase (Sigma) in PBS (w/v) with 1% (w/v) BSA and 5 mM ethylenediaminetetraacetic acid (EDTA) for 15 minutes at 37 °c without agitation. Sections were rinsed with wash buffer three times, replacing the buffer every ten minutes. They were then washed with PBS three times, changing every five minutes. A blocking solution; 3% (w/v) BSA and 50 mM Glycine (Fisher Scientific) in 1% (w/v) PBS was then added and left for 20 minutes. The sections were then incubated with primary antibody diluted in the antibody solution which consisted of 1% (w/v) BSA and 0.02% (v/v) Tween-20 (Thermo-Fisher) in PBS for 16 hours (overnight) at 37°C without agitation. For callose labelling the anti-callose primary antibody (Biosupplies) was used at a 1:400 dilution. For actin labelling the C4 anti-actin primary antibody (Merck) was used at 1:500. The primary antibody solution was replaced by the blocking solution and the sections washed three times for 10 minutes each. The sections were then washed a further three times (10 minutes each) with a rinse solution of 50 mM PIPES, 2 mM EGTA, 1% (w/v)

BSA in ddH_2O with 10% (v/v) glycerol and 0.2% (v/v) Triton X-100 (Fisher Scientific). The secondary antibody was then applied, diluted in the antibody solution, and incubated at 37°C for 90 minutes without agitation. The anti-mouse Alexa 594 antibody (Invitrogen) was used at a 1:500 dilution. This final solution was then removed and the sections washed with 1% (w/v) PBS for two minutes, with the solution being replaced three times. The sections were then ready to be mounted.

2.6 Mounting slides

Sections were mounted directly on a number 1.5 coverslip. A drop of citifluor AF1 antifade medium (Citifluor Ltd) was added to the slide and the section upon the coverslip placed directly on top. This was pressed gently to spread the mountant. For 3D-SIM, in particular, the best results were achieved when the sections were within 16 μm of the coverslip. The coverslips were then sealed using nail varnish to prevent leaking and to allow long-term storage at 4°C

2.7 Confocal microscopy

Images were taken with a Leica SP2 microscope using the lenses and filters below:

Lens	Objective Name	Part Number
5x dry	HCX PL FLUORTAR 5x/0.15	506224
10x dry	HC PL FLUORTAR 10x/0.30	506505
20x dry	N PLAN L 20x/0.35	506247
40x water dipping	HCX APO L 40x/0.80 W U-V-I	506155
63x water dipping	HCX PL APO 63x/1.20 W CORR	506213
63x water dipping	HCX APO L 63x/0.90 W U-V-I	506148

Table 2.1 Lenses available for Oparka Laboratory Leica SP2

Filter Block	excitation range	Excitation and Suppression Filter	part number
D	UV/ violet	Ex BP 355/25 Su LP 470	11513875
analyser		*for confocal imaging*	11513909
I3	blue	Ex BP 450/90 Su LP 515	11513878
Red GFP	green	Ex BP 546/12 Su BP 605/75	11513894
TX2	green	Ex BP 560/40 Su BP 645/75	11513885
A	UV	Ex BP 340/80 Su LP 425	15513873
N2.1	green	Ex BP 515/60 Su LP 590	11513882
FI/RH	blue	Ex BP 490/15; 560/25 Su BP 525/20; 605/30	11513891
L5	blue	Ex BP 480/40 Su BP 527/30	11513880
N3	green	Ex BP 546/12 Su BP 600/40	11513883

Table 2.2 Filter blocks available for use with Oparka Laboratory Leica SP2

The following laser lines were available: 405 nm, 488 nm, 561 nm and 663 nm. Images were taken using the Leica confocal suite software.

2.8 FRAP

FRAP of TMV.MP:GFP and $DiOC_6$ (as per Fitzgibbon et al., 2010).

Large petiole pieces were immersed in PBS and cut into fine longitudinal sections free-hand using a scalpel. Sections from TMV.MP:GFP plants were incubated in an aniline blue solution (Sigma; 0.25 mM in ddH_2O) while sections from wild-type tobacco (cv Samsun nn) plants were incubated in the aniline blue solution with $DiOC_6$ (Invitrogen; 2 μg/ ml in ddH_2O) for 10 minutes. Sections were then immersed PBS 1% (w/v) and washed for 5 minutes with agitation before being mounted with PBS on slides with size 1.5 coverslips. FRAP was performed using the SP2 Leica Confocal Suite FRAP Wizard. Five pre-bleach images were collected with a 488 nm laser at 20% intensity (63 x water dipping objective, unidirectional scan, zoom x3, resolution 512 x 512), and then a 10 μm^2 region was specifically bleached using 10 scans with the 488 nm laser at 100% intensity. Post-bleach images

were then collected using the same settings as the pre-bleach images for approximately 15 minutes in total. Scans were taken every 1 second for the first 30 seconds, then every 10 seconds for the next 150 seconds, and then every 1 minute for the subsequent 12 minutes. The background fluorescence was subtracted from all values, and each series was corrected for bleaching during the post-bleach acquisition phase using an area of fluorescence outside of the cell containing the region of interest for reference. Fluorescence readings were then normalized to percentage values of the pre-bleach fluorescence, and the normalised measurements were averaged.

FRAP of pSEO2.HDEL:GFP

FRAP was performed using the Leica Confocal Suite FRAP wizard as above. However, post-bleach images were taken for 1 minute due to sample movement. Plant material was prepared as for the live-cell imaging, described below (2.16), with FRAP being conducted through the imaging window cut into the main vein of large (20 cm long) leaves.

2.9 Imaging with 3D-SIM

As described in Fitzgibbon et al., 2010; Bell et al., 2013; Bell and Oparka 2015; Knox et al., 2016 and Bell et al., 2018. The protocol is based upon that described by Schermelleh et al., 2008.

The OMX microscope (Applied Precision) is equipped with 405 nm, 488 nm, and 593 nm solid-state lasers and a UPlanSApochromat 100x 1.4 numerical aperture, oil immersion objective lens (Olympus). The auxiliary microscope, (PersonalDV Deltavision) was used to locate the best areas of the sample and these were marked using the point visiting tool. The slide was then transferred to the OMX 3D-SIM microscope (Applied Precision). Using the 'saved list' the marked areas were located using the spiral mosaic function of the OMX microscope. Samples were illuminated by a coherent scrambled laser light source that had passed through a diffraction grating to generate

the structured illumination by interference of light orders in the image plane to create a three-dimensional sinusoidal pattern, with lateral stripes approximately 0.2 mm apart. The pattern was shifted laterally through five phases and through three angular rotations of 60° for each Z-section, separated by 0.125 mm. Exposure times were typically between 100 and 200 milliseconds, and the power of each laser was adjusted to achieve optimal intensities of between 2,000 and 4,000 counts in a raw image of 16-bit dynamic range, at the lowest possible laser power to minimize photo bleaching. Raw images were processed and reconstructed to reveal structures with greater resolution (Gustafsson et al., 2008) implemented on SoftWorx, version 6.0 (Applied Precision). The channels were then aligned in x, y, and rotationally using predetermined shifts as measured using 100-nm TetraSpeck (Invitrogen) beads with the SoftWorx alignment tool (Applied Precision).

2.10 PALM

Imaging DRONPA

Arabidopsis thaliana *p35s*.PDCB1:Dronpa was a kind gift from Dr. Christine Faulker (John Innes Centre). Dronpa was visualised using the Leica SP2 confocal microscope 488 nm laser line at 17% power. It was then shifted to the dark state using the 488 nm laser at 100% with averaging for 20 frames. The fluorescence was restored by the 405 nm laser at 100% power, averaging for four frames.

Etiolation

p35s.PDCB1:Dronpa seedlings were etiolated by covering stratified plates with aluminium foil prior to imaging. This took approximately three days. Seedlings were then either mounted in 1% (w/v) PBS under a 1.5 coverslip and imaged, or subjected to driselase treatment and fixation exactly *as per 2.5.* They were then squashed slightly under the coverslip when mounting, to

separate the tissues, and then imaged with the Leica SP2 confocal microscope.

2.11 LR White

Pertinent to London Resin embedding (see chapter 4.3.1)

All steps were performed on ice unless stated otherwise.

Petioles were fixed via the xylem at room temperature as described above (2.3) but fixed in 4% paraformaldehyde and 1% glutaraldehyde in 1% (w/v) PBS for 2 hours. The petiole was then cut into small sections (approximately 10mm x10mm) before rinsing twice for 5 minutes in 1% (w/v) PBS. Dehydration was via a graded ethanol series: 50% then 70% for 15 minutes followed by 2 x 15 minutes in 90%. Samples were then infiltrated for 45 minutes each in 90% (v/v) ethanol and London Resin Medium Grade (LR; Agar Scientific) at the following ratios 1:1, 1:2, 1:3. Two 60 minute incubations in 100% LR White preceded a final 60 minute incubation of LR White at room temperature. Samples were then polymerized over night at 55°C in gelatin capsules.

As a variation (see chapter 3.3.3), petioles were fixed via the xylem exactly as described above (2.3). The petiole was then cut into small sections (approximately 2 mm x 2 mm) before fixing further by incubating on a rolling-bed platform in the dark for 16 hours (overnight) at 8°C. *Subsequent processing was done at 8°C in the dark with constant gentle agitation using a rolling-bed platform unless otherwise stated.* The samples were then removed from the fixative and rinsed three times in wash buffer (50 mM PIPES (pH6.9) and 1mM $CaCl_2$ in ddH_2O), changing every 10 minutes. Dehydration was via a graded ethanol series: 50, 70 and 90% (v/v) ethanol diluted with ddH_2O and supplemented with 1 mM dithiothreitol (DTT). 50, 70% (v/v) ethanol dehydrations were for 15 minutes each followed by 2 x 15 minutes in 90% (v/v). Samples were then infiltrated with the infiltration solution (90% (v/v) ethanol with 1mM DTT and LR, Agar Scientific)) for 45

minutes each in the following ratios 1:1, 1:2, 1:3. The final infiltration was with 100% LR and this was done twice for 60 minutes each time prior to a final 60 minute infiltration in 100% LR White at room temperature. Samples were then polymerized overnight at 50°C in gelatine capsules (TAAB).

2.12 Imaging LR White

Cutting sections

The gelatine capsule was removed with a razor blade and the block trimmed carefully to a trapezoid with the section area being as small as possible to include the part(s) of the specimen of interest. Semi-thin sections (1-2 µm) were cut using a glass knife. These were then mounted and imaged or stained first to highlight cellular components.

En bloc imaging and staining

The base of the polymerised block was stuck to a slide with adhesive tack and the objective lens lowered into place. The optical sectioning properties of a confocal microscope should allow imaging up to 40 µm into the block where, if present, the fluorescent protein should still be visible, which is useful for identifying structures of interest and to allow targeted sectioning. The cell-wall staining solutions, propidium iodide (Invitrogen; 1mg/mL in ddH_2O) or calcofluor white (Sigma; 10µg/mL in ddH_2O) penetrated the resin block well and provided a useful reference point for imaging cell walls. A drop of either staining solution to the trimmed block face allowed the stain to penetrate into the tissue for 20 minutes at room temperature. The remaining dye was then rinsed from the block face by immersing it in distilled water for two minutes and gently agitating the block using a rolling-bed platform. Stained or unstained, the blocks may be stored for up to one year in the dark at 4°C

Staining sections for fluorescence microscopy

Semi-thin sections were stained readily. The slides were coated by immersing them in Poly-L-Lys (Sigma) diluted 1:10 with ddH_2O and agitated for five minutes. The slides were then drained and dried at 60°C for 60 minutes or at room temperature overnight. Sections were affixed to a slide by heating them briefly (1 to 2 minutes) on a slide warmer. These were rinsed with 1% (w/v) PBS, twice for five minutes, and replaced with a staining solution. Sections were mounted in Citifluor (Citifluor Ltd) antifade agent under a number 1.5 coverslip, sealed to the slide with nail varnish.

Immunolabelling LR sections

Sections were affixed to coated slides as above and then incubated for 10 minutes in blocking solution (as per 2.5 above) before being rinsed with 1% (w/v) PBS three times for 1 minute each. They were then incubated for 90 minutes in mouse anti-callose (Biosupplies) antibody solution (as per 2.5 above) at a 1:400 dilution at 37°C. Sections were rinsed three times for 1 min in the blocking solution (as per 2.5 above) before incubation with secondary antibody, anti-mouse Alexa 594 (Invitrogen) diluted 1:500 in antibody solution (as per 2.5 above), for 1 h at 37°C. The sections were rinsed in 1% (w/v) PBS three times for 1 minute each before staining with 10 mM in ddH_2O calcofluor (Invitrogen). After 2 minutes, excess stain was rinsed off using 1% (w/v) PBS. The sections were then allowed to air dry before mounting with Citifluor AF1 antifade agent (Agar Scientific) under a number 1.5 coverslip and then sealed with nail varnish.

TEM imaging of LR White sections

Ultrathin (60 nm) sections were cut from blocks using a Leica Ultracut T ultramicrotome (Leica Microsystems, Milton Keynes UK) with a glass or diamond knife and mounted on an EM grid (TAAB). Grid mounting was achieved by floating sections on water and touching the dull side of the grid to the centre of the section briefly, taking care not to break the surface

tension of the water. If the grids were clean, the sections were readily transferred from the water to the grid. Sections were then stained by quickly wetting the grids in ddH_2O and floating them, section side down, on a drop of 1% aqueous (w/v) uranyl acetate for 45 minutes. Section were washed by using forceps to grasp the grid by its edge and dipping it rapidly in ddH_2O for one minute, repeating for a further one minute in a fresh pool of ddH_2O. The sections were counterstained with Reynolds lead citrate (Hayat, 1973) by inverting the grid section side down onto a drop and leaving for ten minutes. The sections were viewed in a Philips CM120 transmission electron microscope (FEI) with images captured on a Gatan Orius CCD camera (Gatan).

2.13 Preserving fluorescence in methacrylate embedded tissues

Petioles were fixed via the xylem (as per 2.3 above) with a fixative solution containing 4% (v/v) formaldehyde (TAAB), 2% (v/v) glutaraldehyde (TAAB), 50mM PIPES (pH 7) and 1mM $CaCl_2$. They were then trimmed into approximately 2 mm slices and washed three times in 50mM PIPES pH 7, 1mM $CaCl_2$ in ddH_2O for ten minutes. *Unless stated otherwise the following steps occurred at -20°C.* Tissues were dehydrated in a graded ethanol series for 15 minutes each time with: 50, 70, 90%, 90% (v/v) ethanol diluted with ddH_2O supplemented with 1 mM dithiothreitol (DTT). The tissues were then infiltrated with a methacrylate resin solution. The proportions of methacrylate monomers varied depending on the hardness of block desired. 80/20 methacrylate resin consisted of 8ml n-butyl methacrylate, 2ml methyl methacrylate, 0.5% benzoin ethyl ether (all 2Spi) with 10 mM DTT.
60/40 methacrylate resin consisted of 6ml n-butyl methacrylate, 4ml methyl methacrylate, 0.5% benzoin ethyl ether (all 2Spi) with 10 mM DTT.
Whatever the proportion of constituents the tissues were infiltrated at a ratio of resin to 90% (v/v) ethanol plus 1mM DTT of 1:4; 1:1; 3:1 and then 100%. The infiltrations were 30 minutes long until 100% resin was achieved and then this was left for two hours, then two overnight incubations. Tissue

sections were transferred to flatbed moulds (Agar) and submerged in 100% methacrylate resin and covered by ACLAR film (Agar). Benzoin ethyl ether is a photo-initiator and catalyses the UV polymerisation of the methacrylate resin. ACLAR film has a high UV transparency and was used to exclude oxygen and prevent evaporation whilst letting polymerising light through. The sealed flatbeds were then placed 8 cm from the 15 watt UV light source in the Lecia EMPACT AFS processing unit for 48 hours.

Pre-polymerising methacrylate resin

The methacrylate resin was exposed to UV light from the Lecia EMPACT AFS processing unit for 60 or 120 minutes during which time it become viscous in a dose-dependent way. The tissue infiltration time was doubled when using methacrylate resin that had been pre-polymerised to compensate for the anticipated slower tissue penetration rate.

2.14 Measuring loss of tissue fluorescence

To measure losses in fluorescent protein fluorescence during resin embedding, tissue slices were removed at each stage of the fixation and embedding process and their fluorescence compared with fresh hand sections of the petiole. For each section of the line expressing *pSEO2*.HDEL:GFP (Knoblauch and Peters, 2010), a region of the phloem was photographed at 5x (HCX PL FLUORTAR 5x/0.15) under identical settings on the confocal microscope. For each stage of fixation and embedding the fluorescence was measured in 11 phloem bundles, using ImageJ (Schneider et al., 2012), and the mean fluorescence value calculated as a percentage of the initial fluorescence.

2.15 Processing tissues for transmission electron microscopy using zinc iodide osmium (ZIO) *As published in Bell et al., 2018.*

Petioles were fixed via the xylem as described in 2.3 but using a fixative solution with 3 % (v/v) glutaraldehyde (TAAB) in 0.1 M sodium cacodylate (Sigma) buffer pH 7.3. After 60 minutes in fixative the leaf was removed and the petiole chopped into 5 mm by 5 mm sections. These were then washed twice for 10 minutes in 0.1M sodium cacodylate pH 7.3 (Sigma) buffer, then a further twice for 10 min in ddH_20 before incubating in Zinc iodide Osmium (ZIO). In the fume hood a fresh ZIO mixture was prepared as follows: 3% zinc powder (Fluka) and 5% resublimed iodine (Fluka) were combined with ddH_20, stirred for 5 minutes and then filtered using paper (Whatman). The tissue was then incubated in the ZIO solution at room temperature in the fume hood for four hours to allow the stain to develop. Immediately prior to use, an equal volume of zinc iodide and 2% osmium tetroxide (Agar) was combined. The material was incubated at room temperature for four hours whilst agitating on a rotating wheel. The material was washed in ddH_20 a further twice for 10 minutes prior to dehydration in a graded ethanol series (50, 70, 95% (v/v) ethanol for 15minutes and then 100% ethanol for 2 x 15 minutes). The infiltration procedure was initiated with a room temperature incubation in Epon 812 (Agar) and propylene oxide (Agar) at a 1:1 ratio for 2 hours ahead of an overnight incubation in a 2:1 Epon 812 propylene oxide at 58°C. Two one hour changes in 100% Epon 812, at room temperature, preceded embedding in flat bed moulds for 48 hours at 58°C. Semi-thin sections (0.5-1 μm) were cut using a glass knife on a Leica Ultracut T ultramicrotome (Leica Microsystems, Milton Keynes UK) and stained with a 2% solution of toludine blue (Fisher) before they were checked for orientation and quality using a bright field microscope. Once an appropriate area was identified, ultra-thin sections (<100 nm) were cut using a diamond knife and stained with uranyl acetate and lead citrate, exactly as in 2.12 These were

imaged using a Phillips CM120 Transmission electron microscope (FEI UK Ltd, Cambridge, UK).

2.16 Measurements

Images were loaded into ImageJ (Schneider et al., 2012). In the Analyse tab, 'set scale' was selected and a line drawn along a known area (e.g. scale bar) to set the scale. Measurements were made by drawing a line and then selecting 'Measure' from the Analyse tab. When sufficient areas had been analysed, results were generated by selecting Analyse > Summarise. The data were then exported as an Excel file.

2.17 Live-cell imaging

In situ observations of functional SE were made via an 'imaging window' described by Knoblauch and van Bel (Knoblauch and van Bel, 1998). The leaf was first removed from the plant with the adaxial surface stuck to a glass slide using double-sided tape. The cut petiole was threaded through the pierced cap of a 2ml Eppendorf tube filled with ddH_2O. A few cortical cell layers were removed using a new double-sided razor blade. The imaging window was then filled with ddH_2O and a x20 water dipping lens (HCX APO; Leica Microsystems) used to survey the tissue for obvious signs of damage, e.g. uncoiled xylem fibres. A x63 water dipping lens (HCX PLAPO CS; Leica Microsystems) was used to check for disturbance of the SER. ST conductance was assessed using the symplastic dye HPTS acetate (Invitrogen) which is subject to cleavage by intracellular esterases, yielding 8-hydroxypyrene-l,3,6- trisulphonic acid (HPTS) (Wright and Oparka, 1996). A second window was cut into the main vein tissue as above, which was then filled with 8.8mM HPTS (prepared as per Wright and Oparka, 1996). This reservoir was maintained throughout the experiment to ensure that a constant stream of dye filled the ST.

3. Imaging the Phloem at Super-Resolution

3.1 Introduction

The transport of assimilates through the phloem occurs in a network of interconnected cells called STs. Despite an estimated 90% of the food on Earth having passing through STs (Knoblauch 2014) there is much to learn about their structure and function (Knoblauch and Oparka, 2012). Direct observations are difficult as STs lie deep amongst supporting tissues, exceeding the working distance of objective lenses. Cutting sections of the vasculature can generate preparation artefacts unless extreme care is taken (Esau,1965; Knoblauch and van Bel, 1998). This is because STs are held under high turgor pressure, making them very sensitive to damage. When the pressure is released the cellular constituents are displaced, often occluding the perforated end walls, called SPs. These artefacts were so ubiquitous in the phloem literature that they led to the proposal of alternative translocation mechanisms to the pressure-flow model as it was felt that the

end walls could not provide a route for unimpeded flow (Thaine et al., 1967). Regardless, investigations using microscopy have proved vital in understanding the phloem. Whereas TEM provides a structural survey of the cell at unparalleled resolution, it is not readily compatible with facile protein localisation and requires that material is highly processed (fixed, dehydrated, resin infiltrated) so that it can withstand the rigours of imaging in a vacuum using high accelerating voltages (see also chapter 4). Light microscopy, however, allows the cell to be studied in a near native state and is readily compatible with the localisation of proteins either using genetic tags or endogenous epitopes. The resolving power of a light microscope determines the minimum distance that there can be between two points that still allows them to be recognised as distinct entities. A physical limit is reached due to light diffraction and this, in an ideal system is 200 nm laterally (x – y) and 500 nm axially (z; Sahl et al., 2017; Introduction). Recent developments in optical imaging have broken the diffraction barrier and these “super-resolution” imaging systems look set to bridge the gap between traditional light and EM (Sahl et at., 2017; Introduction). A plethora of new imaging approaches has been described which includes: structured illumination microscopy (SIM; Gustafsson, 2000) and photo-activation localisation microscopy (PALM; Betzig et al., 2006). Obtaining sub-diffraction images in different ways, the new technologies can be broadly classed as either ‘ensemble’ or ‘single molecule’ imaging approaches.

Three dimensional SIM (3D-SIM) takes images of an ensemble of molecules, achieving a resolution of 100 nm laterally (x-y) and 200 nm axially (z). In addition to providing extended resolution, 3D-SIM is also compatible with standard fluorochromes (e.g. GFP, mCherry, DAPI) and with the sample preparation methods commonly used for light microscopy.

Offering a much higher lateral resolution (10 nm; Huang et al., 2016) is PALM. This is an example of a single molecule imaging technique. The

principle underlying single molecule detection is that the position of a single fluorescent emitter can be localised with a high degree of accuracy if enough photons are collected. Resolution is directly dependent upon the total number of photons collected, and to that end it is essential to maximise the signal to noise ratio.

In this chapter, both 3D-SIM and PALM were used to image the phloem of plants and the results generated are discussed.

3.2 Aims

i) To process vascular tissues so that they are compatible with imaging at super-resolution using 3D-SIM and PALM.
ii) To preserve antigenicity in processed tissues.
iii) To use super-resolution imaging techniques specifically to study the phloem.

3.3 Results

3.3.1 Tissue preparation for 3D-SIM imaging.

Xylem irrigation of fixative

Neither 3D-SIM or PALM are readily compatible with imaging whole tissues. This is apparent for PALM, due to the limited focal volume imposed by TIRF (see Introduction), but is also the case for the 3D-SIM platform used in this project, as the high numerical aperture lens has a very short working distance (0.13mm; Fitzgibbon et al., 2010). As the vascular cylinder is in the centre of the petiole it was necessary to obtain sections, and so the tissues were first fixed. The goal of fixation is to preserve the cellular structure with minimum disruption to the living state. Additionally, tissues that have been well fixed are also more resilient to the tensile strains induced during sectioning (Hayat, 1973). Formaldehyde is the simplest of the aldehyde

family. It is a low molecular weight monoaldehyde that penetrates dense tissues rapidly (figure 3.3.1.; Hayat, 1973).

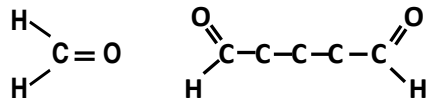

Formaldehyde CH_2O Gluteraldehyde $C_5H_8O_2$

Figure 3.3.1 Chemical formula of formaldehyde and glutaraldehyde

However, even given its ability to enter tissues, the time taken for formaldehyde to penetrate tissues is in the order of a few minutes, by which time the vasculature tissues are likely to be distressed. Robards and Humpherson (1967) irrigated young shoots of *Salix fragilis* with fixative prior to sectioning. The resulting electron micrographs showed cambial cells with good membrane continuity, without distortion or break, and a trilaminar conformation. The proximity of xylem to ST within the vascular bundle would seem to make it an ideal conduit through which to deliver fixative rapidly. Whilst Robards and Humpherson (1967) used glutaraldehyde as their principal fixative agent, formaldehyde was used in this thesis in an attempt to minimize the time taken to penetrate and fix the ST constituents. A small percentage of glutaraldehyde was used to supplement the fixation solution as it preserves fine structure better than any other aldehyde (Hayat, 1973). To that end, petioles were severed and then immersed immediately in 4% formaldehyde with 0.25% glutaraldehyde (*see* Methods for more details) before being trimmed further under the surface of the fixative to eliminate any airlocks. The petioles, with leaf still attached to maintain a strong transpiration pull, were then left in the fixative solution for 60 minutes in an illuminated chemical fume hood.

Sectioning with a vibrating microtome

Whilst the short working distance of the 3D-SIM microscope requires that tissues be sectioned to expose the vasculature, a coverslip can comfortably

accommodate 100 μm of tissue so ultramicrotomy (as for EM) is not required. The tissues need therefore only to be stabilized and not reinforced with resin prior to cutting, obviating the need for extensive tissue processing e.g. dehydration, infiltration of resin and polymerization. Phytoagar is a plant tissue culture agar with a high gel strength and can be used at a minimal concentration of 5.0 g/l to obtain a solid gel. This concentration matches the mechanical properties of a young petiole well and offers adequate support during cutting. Sectioning is done using a vibrating microtome. A vibrating blade exerts less pressure than a static blade, and with practice can produce 50 μm sections. To further expose the phloem strands, the sections were briefly immersed in a driselase (Sigma) solution and then washed prior to mounting. Driselase is a natural mix of fungal carbohydrolases known to digest the plant cell wall matrix (van Bel and Koops, 1985; Fitzgibbon et al., 2010).

3.3.2 Immunolabelling of callose

Callose is a cell wall constituent found at all PD where it is understood to have a role in regulating conductivity (Levy et al., 2007). The SEs and CCs of the phloem share specialized symplasmic connections called PPUs (van Bel and Kempers, 1996), which are surrounded by callose collars (Kempers et al., 1998). Callose is also abundant at the SPs in ST. The SP is a perforated structure that forms at the end walls of SEs during development, allowing lumenal and plasma membrane continuity within the ST

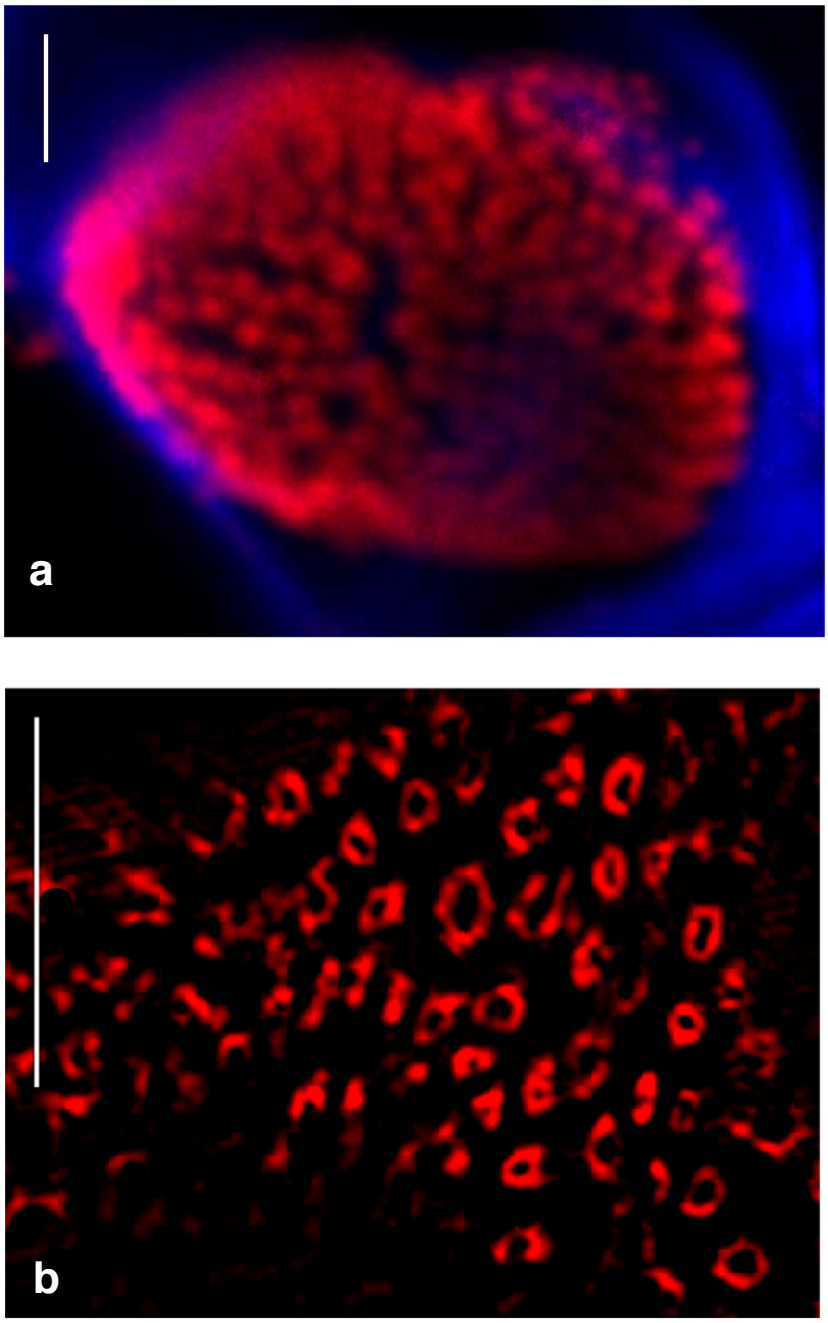

Figure 3.3.2 Callose immunolabelled at SP

a) Confocal microscope image of a *Nicotiana tabacum* SP. Callose is labelled with a monoclonal antibody and visualised using an Alexa 594 secondary antibody, false coloured red. Cellulose is highlighted with a calcofluor stain, false coloured blue. SP pores are apparent but not resolved. b) 3D-SIM resolves SP pores and callose collars lining them. Scale 5 μm in both images. Adapted from Fitzgibbon et al., 2010.

and facilitates mass flow (Esau and Gill, 1973). The progenitors of the SP pores are PD and whereas these are significantly modified during SP development, the callose remains. Aniline blue (Sigma) is used widely as a fluorescent stain to highlight callose (Radford et al., 1997). However aniline blue is not photostable and under intense or prolonged illumination the signal is progressively bleached (data not shown). 3D-SIM resolves sub-resolution structures by taking 15 images per z section, and the phase of the structured light is shifted over five steps and rotated to three positions at 60˚intervals (Dobbie et al., 2011). This requires the use of probes that are photostable. To that end callose was labelled immunologically. Callose is a plant polysaccharide that contains β-1,3- linkages between glucose residues. These β-1,3- linkages are the target of an callose monoclonal antibody (Biosupplies) and this was used in combination with an anti-murine Alexa 594 (Invitrogen) secondary antibody to visualise callose. Figure 3.3.2 a) shows a confocal image of callose labelled at a SP. Small red spots are apparent, consistent with the location of callose around the SP pores, but these cannot be resolved. 3D-SIM resolved the individual SP pores clearly (Figure 3.3.2 b). The average diameter of the pores was 276 ± 16 nm (n = 21), and the callose collars extended this diameter to 568 ± 22 nm (n = 21). The increased optical sectioning capacity of 3D-SIM (images captured every 125 nm in z; c.f. every 500 nm in confocal microscopy) in addition to the increased axial (z) resolution makes it ideal for resolving large complex structures.

Figure 3.3.3 - legend on next page

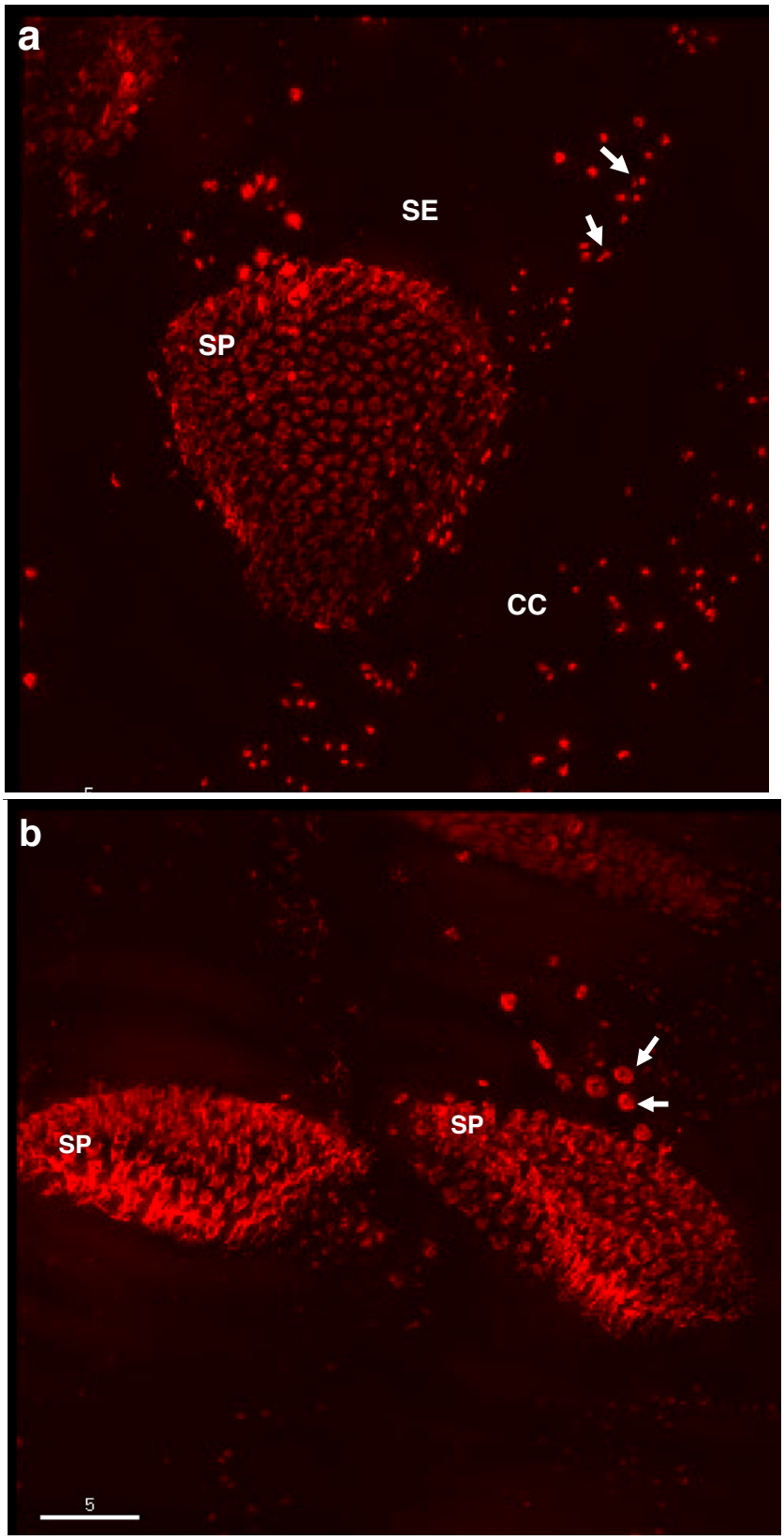

Figure 3.3.3 Projected 3D-SIM image of callose labelling in the SE CC complex

a) SP in face view and callose associated with PPUs (arrowed) that connect SE and CC. b) Lateral sieve area pores (arrowed) lie close to SP. Both images were reconstructed from 67 images. Scale in both images is 5 μm. Adapted from Fitzgibbon et al., 2010.

Figure 3.3.3 a) shows a projection of 67 images taken through a SE-CC complex. The projected image shows a whole SP in face-view and PPUs that connect SE and CC at their shared interface. Figure 3.3.3 b) shows another SP and the pores found at an individual lateral sieve area that connect adjacent SEs.

3.3.3 Using a transgenic plant expressing tobacco mosaic virus (TMV) movement protein

When developing a method, it is very useful to have a ready supply of plant material that constitutively expresses a fluorescent marker, allowing facile orientation within the tissues. The transgenic line selected for use here was a *Nicotiana tabacum* that had been engineered to express the tobacco mosaic virus movement protein fused to green fluorescent protein (TMV.MP:GFP) expressed from the 35s cauliflower mosaic virus promoter (Roberts et al., 2001). This promoter expresses constitutively throughout plant tissues. The TMV movement protein is a multi-functional protein and is known to bind microtubules and single-stranded RNA, as well as target PD and increase their SEL (Oparka and Roberts, 2001). The transgenic plants used here exploit the proteins ability to target and accumulate in the cavities of PD, a feature of those formed post-cytokinetically, and was used by Roberts et al., (2001) to highlight PD in developing leaves. PD facilitate local cell to cell movement but are integral in movement to and from the phloem. At 50 nm in diameter they challenge the resolving power of the 3D-SIM microscope. In the leaf epidermis, the GFP signal from the PD cavity was apparent as characteristic punctae in the cell wall, as described previously using confocal imaging (Figure 3.3.4 a; Roberts et al., 2001; Faulkner et al., 2008). When

immunolabelling the callose, the false-coloured green signal from the cavity overlapped with the false-coloured red signal from the callose collar to produce yellow.

Figure 3.3.4 – legend on next page

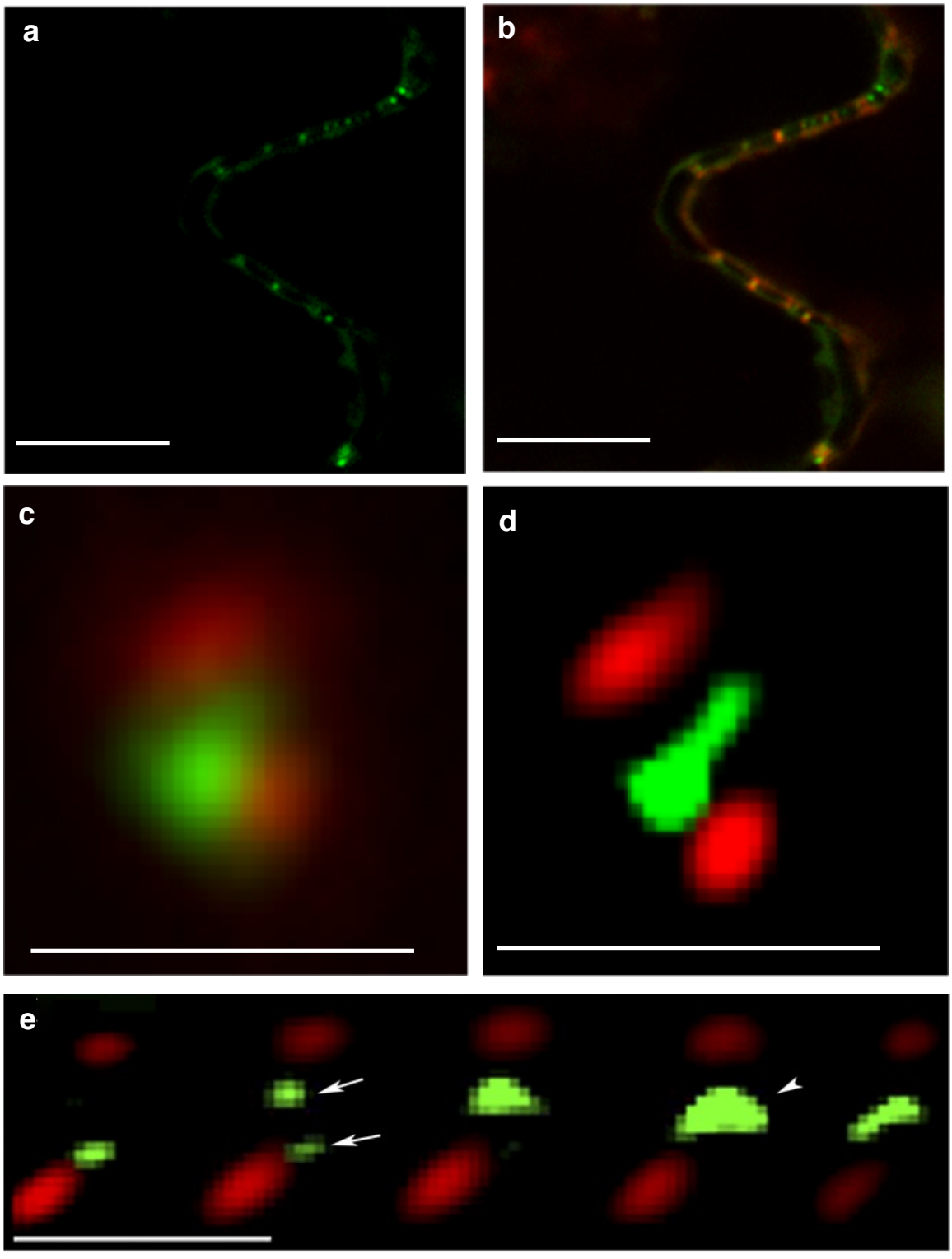

Figure 3.3.4.Fluorescence from PD cavities labelled with TMV.MP:GFP imaged with confocal, widefield and 3D-SIM

a) Confocal image shows MP-GFP fluorescence (green) emitted from cavities of PD in mesophyll cell walls. Scale 5 μm. b) Confocal image of the same region of mesophyll where callose also labelled (red). Confocal microscope cannot always resolve PD wall collar callose and MP signal from cavities. Yellow is from where signals overlap. Scale 5 μm. c) Widefield image of a PD where different signals can be detected but not resolved. Scale 1 μm. d) 3D-SIM image of the same PD that spatially resolves the callose collar from the central cavity. Scale 1 μm. e) A z series through a single PD pore where images have been taken 125 nm apart. Two pores are resolved (arrowed) which join to form a shared central cavity (arrowhead). Scale 1 μm. Adapted from Fitzgibbon et al., 2010.

points at the cell wall (figure 3.3.4 b). It was not possible to resolve the signals clearly using the confocal microscope. 3D-SIM has a dedicated auxiliary widefield microscope, which is used for sample location and mapping. The high precision motorised stage is cross-linked with that of 3D-SIM to allow co-ordinate sharing and comparative images of the same field of view. Images of the same PD captured by widefield and 3D-SIM are shown in figure 3.3.4 c and d. The widefield microscope is diffraction limited, as is the confocal microscope, so the images generated have significant signal overlap (figure 3.3.4 c). However, 3D-SIM separates the two signals clearly (figure 3.3.4 d). Measurements of individual PD estimated the Alexa 594 callose signal extended laterally in the cell wall for about 187 ± 6 nm (n = 32), slightly larger than the dimension of the raised wall collar that surrounds the PD pore, as estimated by field emission scanning electron microscopy (100 nm; Faulkner et al., 2008). Figure 3.3.4 e further demonstrates the optical sectioning capacity of 3D-SIM. It shows a series of successive images, taken 125 nm apart, through a PD longitudinally showing the two distinct pores that connect to the same central cavity.

3.3.4 Fine Strands of MP Interconnect PPUs at the SE-CC Interface

A survey of vibroslice-sectioned vascular tissues using the confocal microscope revealed that the TMV.MP:GFP was not exclusively present in the central cavities of the PPUs but was arranged along the periphery of the SE at its interface with the CC (figure 3.3.5 a). 3D-SIM images of the same region resolved MP-GFP strands of 144 ± 6 nm (n = 30) diameter. 3D-SIM confirmed that these strands were concentrated at the SE-CC junction but then extended up to 40 μm along cell margin, appearing to connect individual PPUs (figure 3.3.5 b). Optical sections, taken every 125 nm through PPUs, confirmed the intricate nature of the association with MP:GFP (figure 3.3.5 c i-iii). Conventional widefield imaging hints at these elaborate associations but failed to resolve the fine strands or the features of the PPUs (figure 3.3.5 d). Figure 3.3.6 shows even more clearly that the strands run around and then enter a pore. The average diameter of these strands was 89 ± 6 nm (n = 6), at the limit of resolution of 3D-SIM. However, we were unable to detect equivalent strands of MP in the adjoining CC. Measurements showed that the pores had a diameter of 188 ± 8 nm (n = 26) and that the callose collars extended the PPU diameter to 510 ± 19 nm (n = 26).

Figure 3.3.5 – legend on next page

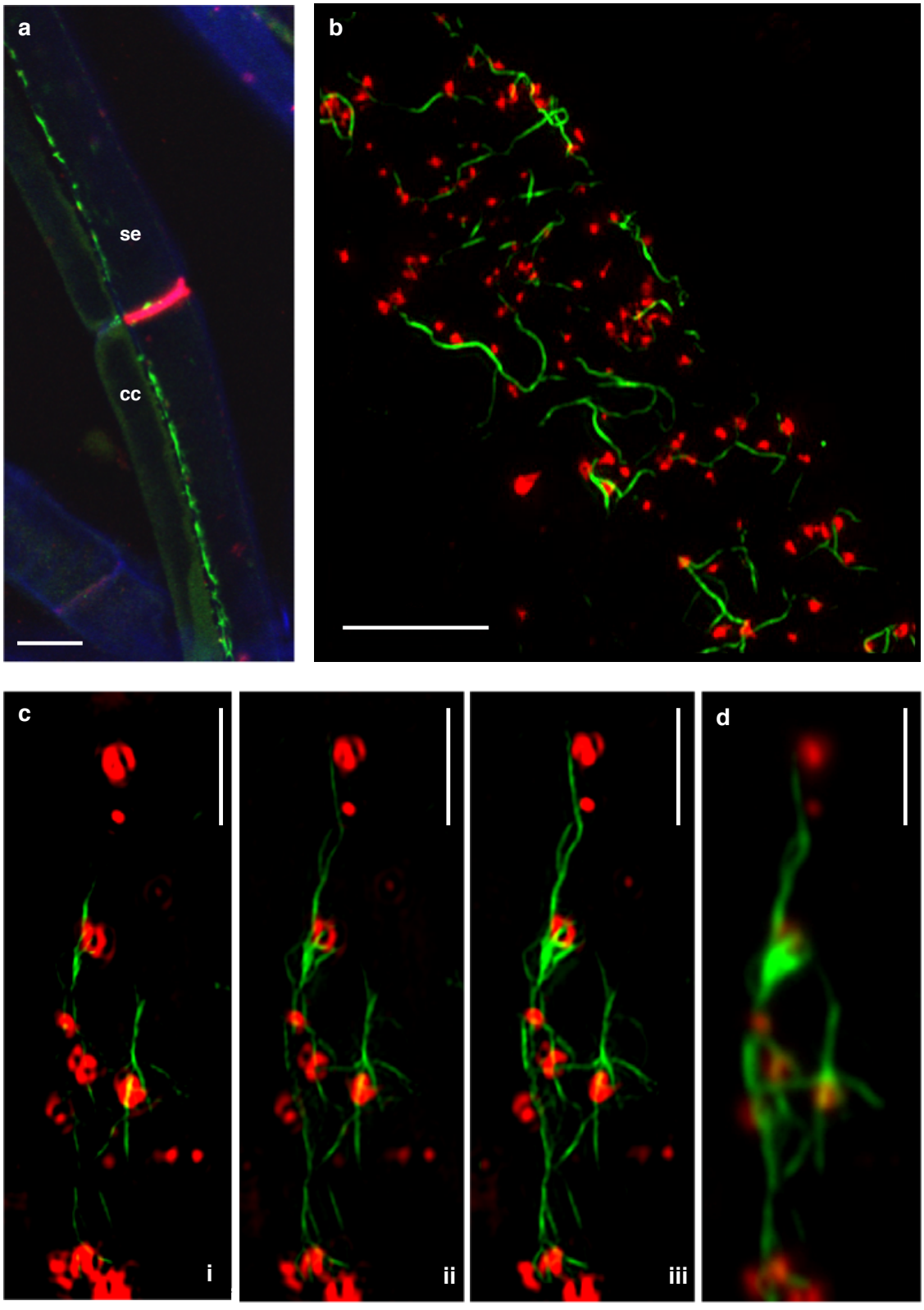

Figure 3.3.5 Fine strands of TMV.MP:GFP extend from PPU cavities along SE parietal layer

a) Confocal microscope image of SE (se) and CC showing TMV.MP:GFP (green) tubules in SE. Similar structures are absent from the cc and the association was limited to se-cc interface. Callose on SP was labelled immunologically (red). PPU callose was not apparent at this magnification. Cellulose was highlighted by calcofluor staining (blue). Scale 5 μm. b) 3D-SIM image of the se parietal layer. Strands of TMV.MP:GFP appear to extend from, and connect, many PPUs. PPU callose collars (red). Scale 5 μm c) i-iii images taken from a 3D-SIM z series (125 nm apart) reveal intricate association between MP:GFP tubules and PPU callose collars. Scale 2 μm d) Corresponding widefield image fails to resolve the PPU collars or many of fine tubules that run through or between them. Scale 2 μm. Adapted from Fitzgibbon et al., 2010.

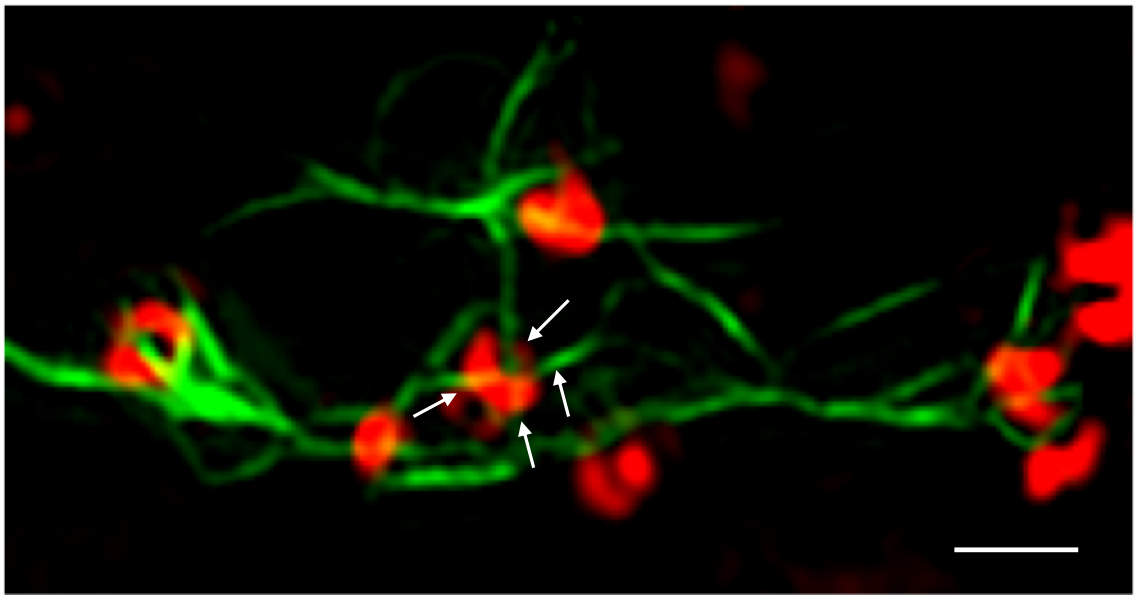

Figure 3.3.6 TMV.MP:GFP tubules imaged at the limit of 3D-SIM resolution

Four TMV.MP:GFP strands can be seen entering the PPU (arrowed). These taper to 89 nm before passing through. This exceeds the limit previously achieved for the 3D-SIM microscope used in this study. Scale 1 μm. Adapted from Fitzgibbon et al., 2010.

3.3.5 TMV.MP:GFP tubules decorate the SER

The tubular form of MP-GFP had not been reported before. Blackman et al. (1998) imaged a fibrillar form of *cucumber mosaic virus* (CMV) MP in SE during an infection but this could not be resolved clearly. Whilst the 3D-SIM images provide information about the form the tubules, and their associations with callose labelled structures, it is not clear if the tubules are a result of MP:GFP self-aggregation or if they had decorated an endogenous structure.

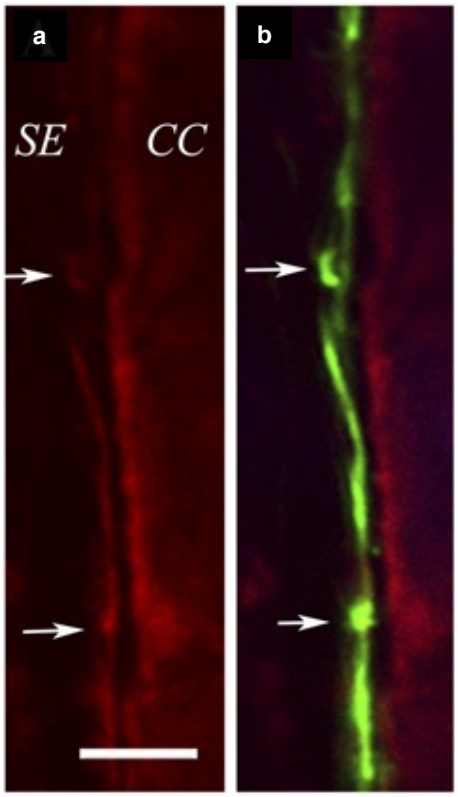

The mature SE are denuded of most cellular contents, and those that remain are held at its periphery in a region called the parietal layer (Evert, 1990; vanBel et al., 2002). The TMV.MP:GFP formed a network along the margin of the cell, making the SER a likely candidate for MP targeting. Hexyl rhodamine B is a vital ER stain and was used to highlight the SER and colocalisation between it and TMV.MP:GFP tubules. This dye has an excitation wavelength of 574 nm, which is not compatible with 3D-SIM imaging, so observations were made with the laboratory Leica SP2 confocal microscope.

Figure 3.3.7. Hexyl rhodamine B reveals TMV.MP:GFP association with tubular SER.
a) The vital ER stain hexyl rhodamine b accumulated in the SER (arrowed). The interface of the SE and CC is shown here. b) Confocal image with the imaging channel that collected TMV.MP:GFP included. This two-colour image shows that the MP:GFP tubules occupy the same area in the cell as the SER and that these structures are not in the adjoining CC. Scale 5 μm. From Fitzgibbon et al., 2010.

Images gathered suggest that TMV.MP:GFP colocalised with the tubular component of the SER (figure 3.3.7) but not with the stacked parietal cisternae. Also, while MP-GFP labelled the SER at the SE-CC interface only (figure 3.3.7 b), hexyl rhodamine b stained the entire SER. This differentiation may be due to the physical arrangement of the SER; the tubular component may be 'more available' for decoration whereas the stacked component may exclude extraneous elements when packing. The different structures may resemble different functional domains of the SER, with the stacked SER providing potential plasma membrane (PM) adhesion sites. The strength of ER-PM interactions has been established in centrifugation experiments, which demonstrated that conditions that dislodge the bulk of the ER and organelles failed to dislodge the cortical ER network (Staehelin, 1997). These sites have also been shown to resist plasmolysis and to remain coupled to the cell wall during the formation of Hechtian strands (Staehelin, 1997). The functional importance of ER-PM contact sites in parenchyma cells has been recognised and these are understood to be important for signalling and supporting ER architecture (Bayer et al., 2017). In the SE this association may also be required to hold the organelles in a parietal position, essential for efficient SE flow. The tubular SER may provide a selective transport pathway for molecules such as mRNAs that are often produced as part of a specific response with a discrete target site of action (Crawford and Zambryski, 2001). As stated earlier, virus MP fibrillar structures have been observed in the SE before. Blackman and colleagues (Blackman et al., 1998) noted the appearance of MP filaments during a cauliflower mosaic virus (CMV) infection but these were below the limit of resolution, and so no sub-cellular localisations were commented upon. That this observation was made during the natural infection context increases the significance of the observations made here; the SE MP:GFP tubular striations may represent a genuine feature of viral movement or a virus dissemination strategy, not simply the consequence of 35s promoter driven over-expression. The strands are only apparent in the SE and not the CC (or

any other cell type examined). During the early stages of TMV infection, TMV.MP:GFP decorates the ER but is subsequently removed, later appearing associated with microtubules (Gillespie et al., 2002). A logical conclusion to draw is that the removal of TMV.MP:GFP from the ER may involve a cytoskeleton-based degradation pathway (Gillespie et al., 2002; Reichel and Beachy, 2000) that is absent from the enucleate SEs that lose their cytoskeleton during maturation.

3.3.6 FRAP of TMV.MP:GFP

To establish if the TMV.MP:GFP strands were mobile, intact cells of the phloem were subject to fluorescence recovery after photobleaching (FRAP). Fluorescence recovery after photobleaching is an optical technique that establishes the ability of a population of molecules to diffuse. In FRAP a population of fluorescent molecules are bleached and recovery is measured by the percentage of the original fluorescence that is regained, recovery of fluorescence being a proxy for movement. The method can be used to dissect movement locally (within an organelle) or at greater distances (movement between cellular compartments or cells). Using high intensity 488 nm laser light the GFP signal was bleached and the recovery of this signal was monitored for several minutes. Very little recovery was noted (see figure 3.3.8) which shows that the GFP was not mobile. $DiOC_6$ labels the ER membrane, in contrast to Hexyl Rhodamine which accumulates in the lumen, allowing this domain to be subjected to FRAP analysis. The SER of entire SEs was bleached but showed rapid recovery, suggesting that the SER is continuous between the bleached and unbleached regions of the ST and also, crucially, that the SE has not been damaged by the preparatory steps. This result would suggest that the membrane of the SER offers a route for molecular movement that warrants further investigation.

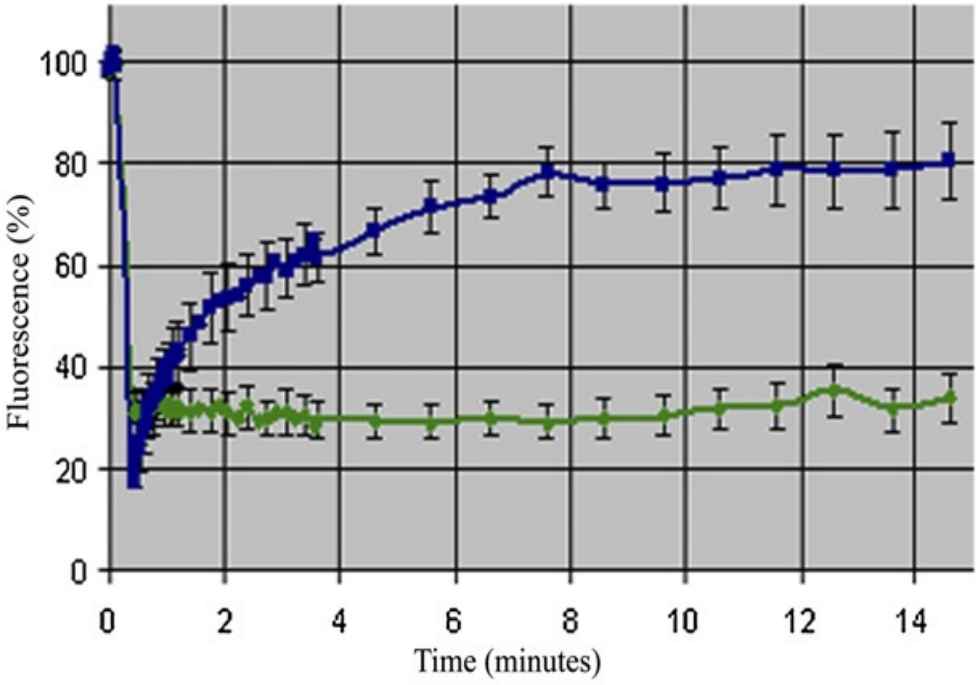

Figure 3.3.8 FRAP shows that TMV.MP:GFP tubules are immobile

A region of SE containing TMV.MP:GFP tubules were photobleached and their recovery profile over 15 minutes (green) shows that there is little movement into the monitored area. $DiOC_6$ (blue) is a vital ER membrane stain. It was photobleached as for the TMV.MP:GFP but the recovery profile is very different and shows recovery to around 80% of initial fluorescence, indicating movement of the stain into the bleached area. From Fitzgibbon et al., 2010.

3.3.7 100 nm Strands of MP-GFP Traverse SP Pores

The tubular TMV.MP:GFP was observed to be limited to the parietal layer and appeared to decorate the SER. The surface of SPs were examined to see if the TMV.MP:GFP was associated and if it ran through to the next SE in the file. TMV.MP:GFP tubules could be seen in association with the SPs and these passed through the pores. By collecting optical stacks of SPs and rotating them the structures of the pores became apparent. The callose formed hollow cylinders giving the appearance of 'cotton reels' (figure 3.3.9 a) and in many of these pores the tubular TMV.MP:GFP became thinned down into fine strands of 103 ± 3 nm (n = 30) in diameter that appeared to traverse the SPs (figure 3.3.9 b). By further rotating the stack it could be

seen that the fine strands were running longitudinally across individual pores from one SE to the next (figure 3.3.9 c i-iv). Using 3D-SIM, we have been able to resolve several structures seen previously only with the EM. Significantly, we were able to use standard cytological methods and fluorophores compatible with confocal imaging. The fields of cell biology and molecular plant pathology are likely to benefit enormously from the application of 3D-SIM.

Figure 3.3.9 legend on next page

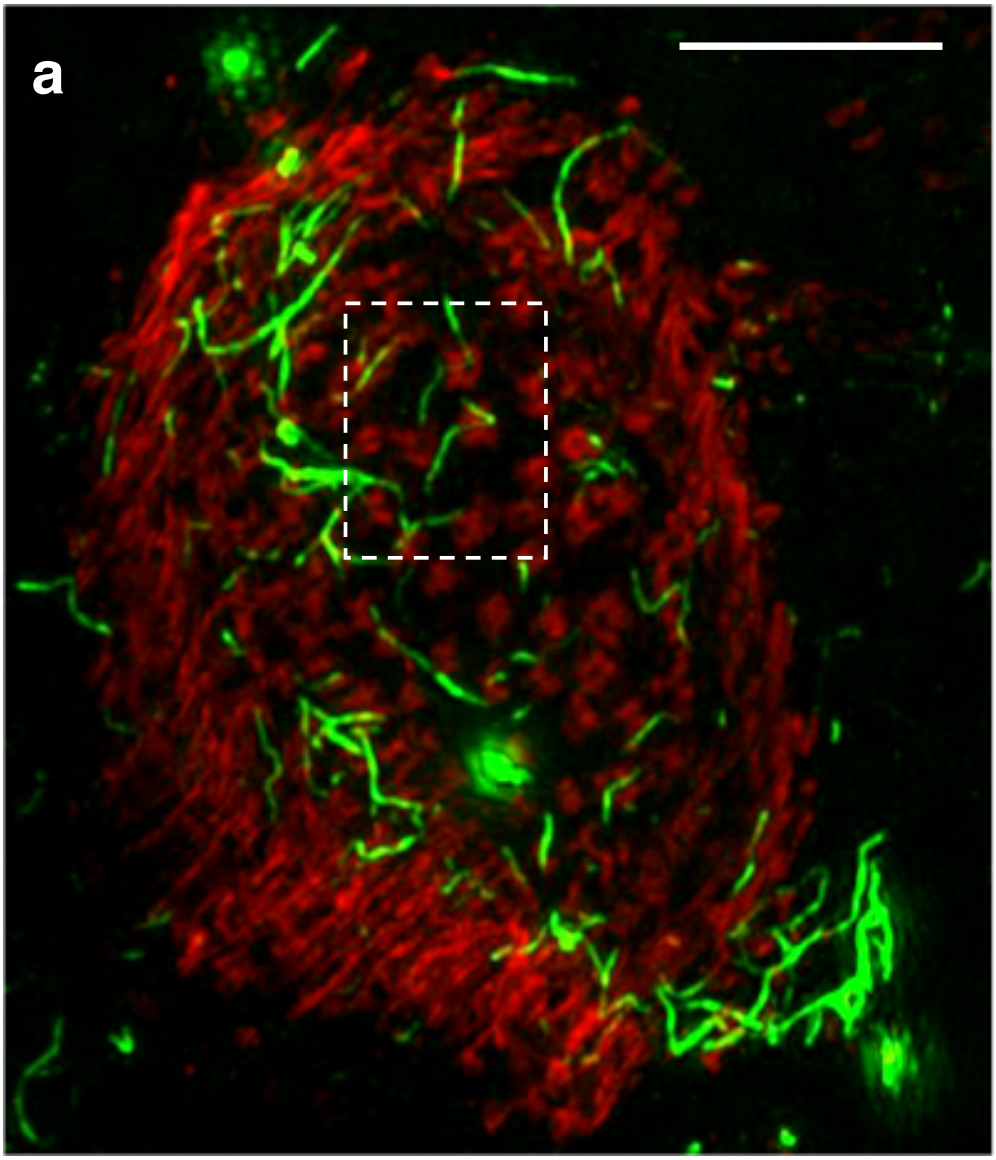

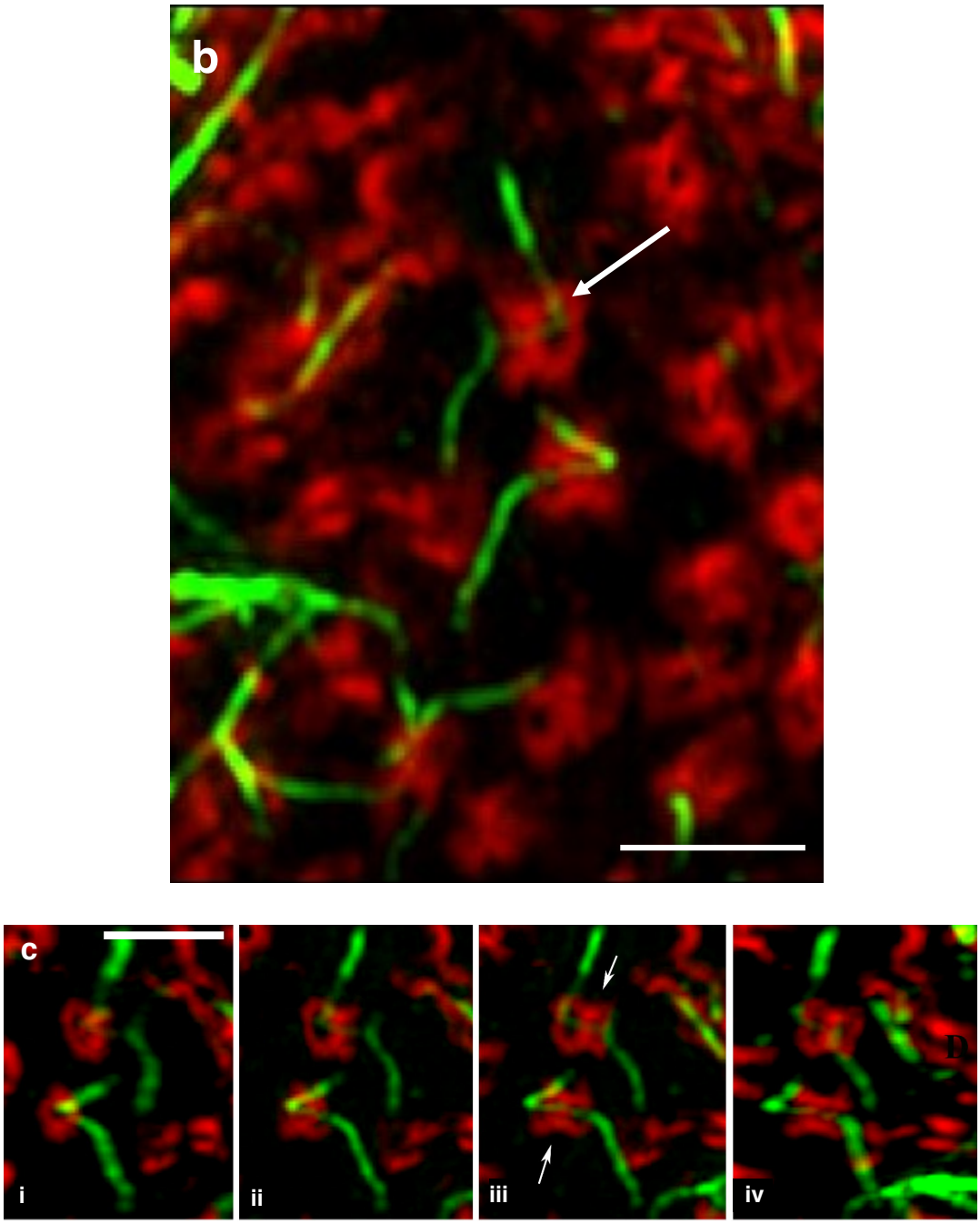

Figure 3.3.9 3D-SIM images resolve 100 nm TMV.MP:GFP strands that traverse SP pores

a) Projected z stack of a SP where SP pore callose is immunolabelled (red) and TMV.MP:GFP (green) tubules can be seen in intricate association. Scale 5 μm. b) Area highlighted in a) zoomed in electronically to show that the TMV.MP:GFP tubule thins down and enters the SP pore and then emerges from the other side (arrowed). Scale 1 μm c) i-iv Further details from the SP area highlighted in a). The images are taken from a rotated z series allowing single TMV.MP:GFP strands (arrowed in iii) to be traced as they pass through the callose-lined pores. Scale 1 μm. Modified from Fitzgibbon et al., 2010.

PALM

PALM imaging system

At the time these experiments were carried out (early 2010), no commercial PALM platforms were available. The system we used was assembled by Dr. Cristina Flors who at the time was a Royal Society and EPSRC (Engineering and Physical Sciences Research Council) fellow at the University of Edinburgh.

3.3.8 Tissue preparation for PALM

The resolution achievable with PALM is directly dependent upon the number of photons measured (Fernandez-Suarez and Ting, 2008). This requires samples with low/no background and the use of labels that have a high contrast ratio i.e. that are very bright once activated and emit minimally when in the dark state (Lipponcott-Schwartz and Manley, 2009). These twin requirements are difficult to satisfy for many researchers in plant-cell biology. Autofluoresence is inherent in plant tissues due to the presence of biomolecules such as chlorophyll, carotene and xanthophyll, and the biopolymer lignin (Kodama 2016). Frustratingly, this autofluorescence is often enhanced by tissue processing e.g. chemical fixation (Hayat, 1973). When the cryptic splice sites of GFP were removed to facilitate efficient expression *in planta* (Haseloff and Amos, 1995), GFP, and its spectral variants, were then used extensively to probe plant development, cell structure and virus movement (Chapman et al., 2005). Although GFP has long been known to alternate between light and dark states (‘blink’; Dickson et al., 1997), fluorescent proteins used most widely in single-molecule imaging experiments can change their spectral properties (from one wavelength to another or from an ‘off’ state to an ‘on’ state) in a defined manner in response to a permissive wavelength of light (Fernandez-Suarze and Ting, 2008). So, although it is technically possible to use GFP in single molecule studies, the sporadic nature of its blinking and its low photon output makes it unsuitable for single- molecule studies (Dr Cristina Flors, personal

communication). *CoralHue* Dronpa (Dronpa; Amalgaam Ltd. Japan) is a monomeric photoswitchable fluorescent protein that is imaged with low-power 488 nm light but is then converted to a dark state in response to prolonged high-power 488 nm laser light. A sharp burst of high-power 405 nm laser light restores the initial green fluorescence (Ando et al., 2004). This protein was fused to the PD callose-binding protein (PDCB1; Simpson et al., 2009) by Dr. Christine Faulkner and then expressed from the cauliflower mosaic virus 35s promoter in *Arabidopsis thaliana*. It labelled callose, just as the anti-callose antibody used in section 3.3.2 did, but this labeling was less specific at later times (> five days) post germination. Figure 3.3.10 (below, legend on next page) shows representative images of PDCB1-Dronpa expression in the leaf epidermis at three-day post germination, imaged with the CSLM.

Figure 3.3.10 – legend on next page

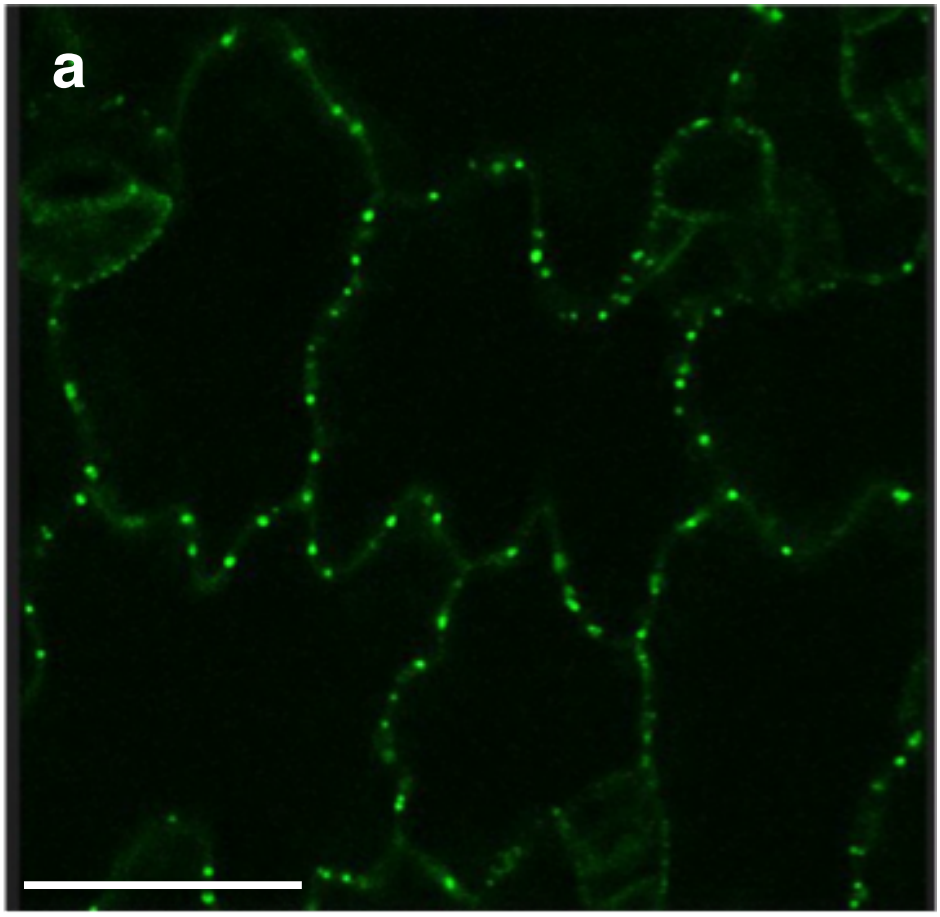

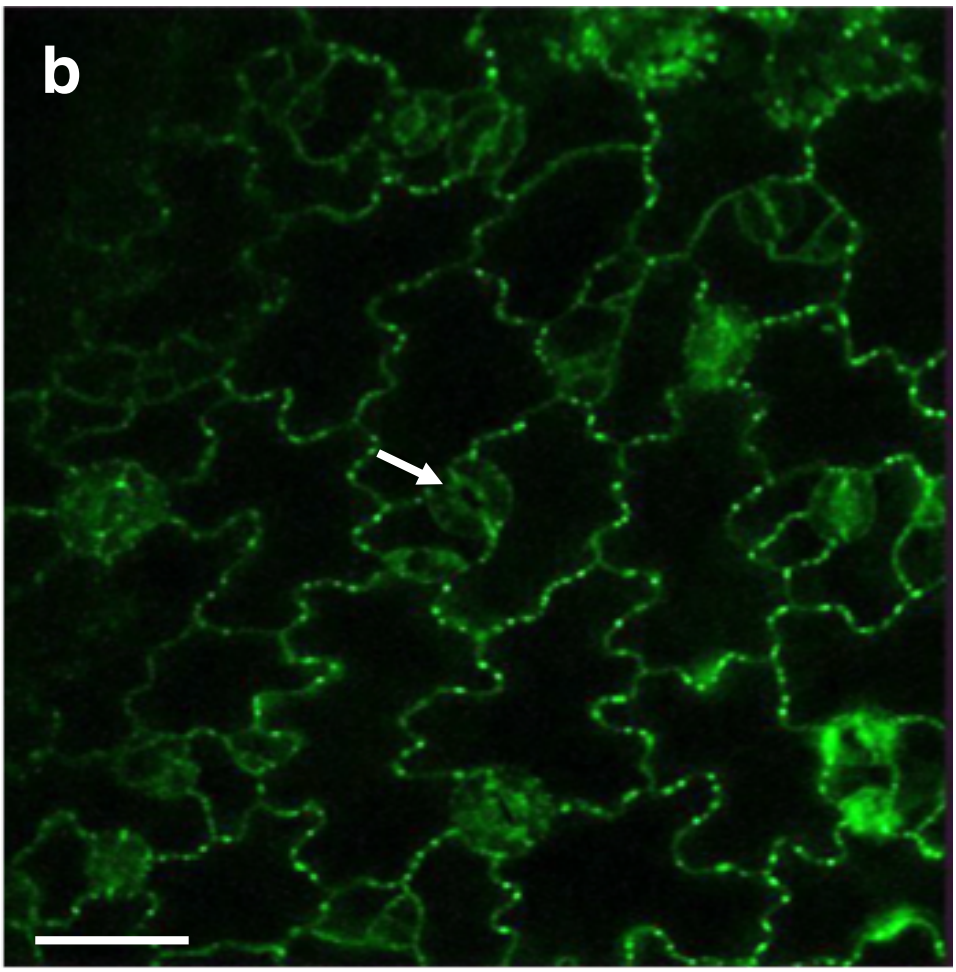

Figure 3.3.10 PDCB1-Dronpa Expression in *Arabidopsis thaliana* leaf upper epidermis
a) Punctate labelling at the cell periphery. Scale 5 μm b) A larger field view reveals that PDCB1:Dronpa is also expressed at cell walls generally with non-specific guard-cell labelling (arrow). Scale 5 μm

Dronpa is apparent as punctae at the cell periphery amidst some general cell wall labelling. PALM imaging of this sample was not successful as the chloroplast autofluorescence (filtered out of these images using a short-pass filter) was too high, and so the threshold count of Dronpa photons was too low to reconstruct an image (data not available). The hypocotyl was imaged next with representative images of a typical imaging, bleaching and reactivation cycle (figure 3.3.11). Similarly, PALM imaging was not successful as the chloroplast autofluorescence was too high (data not available).

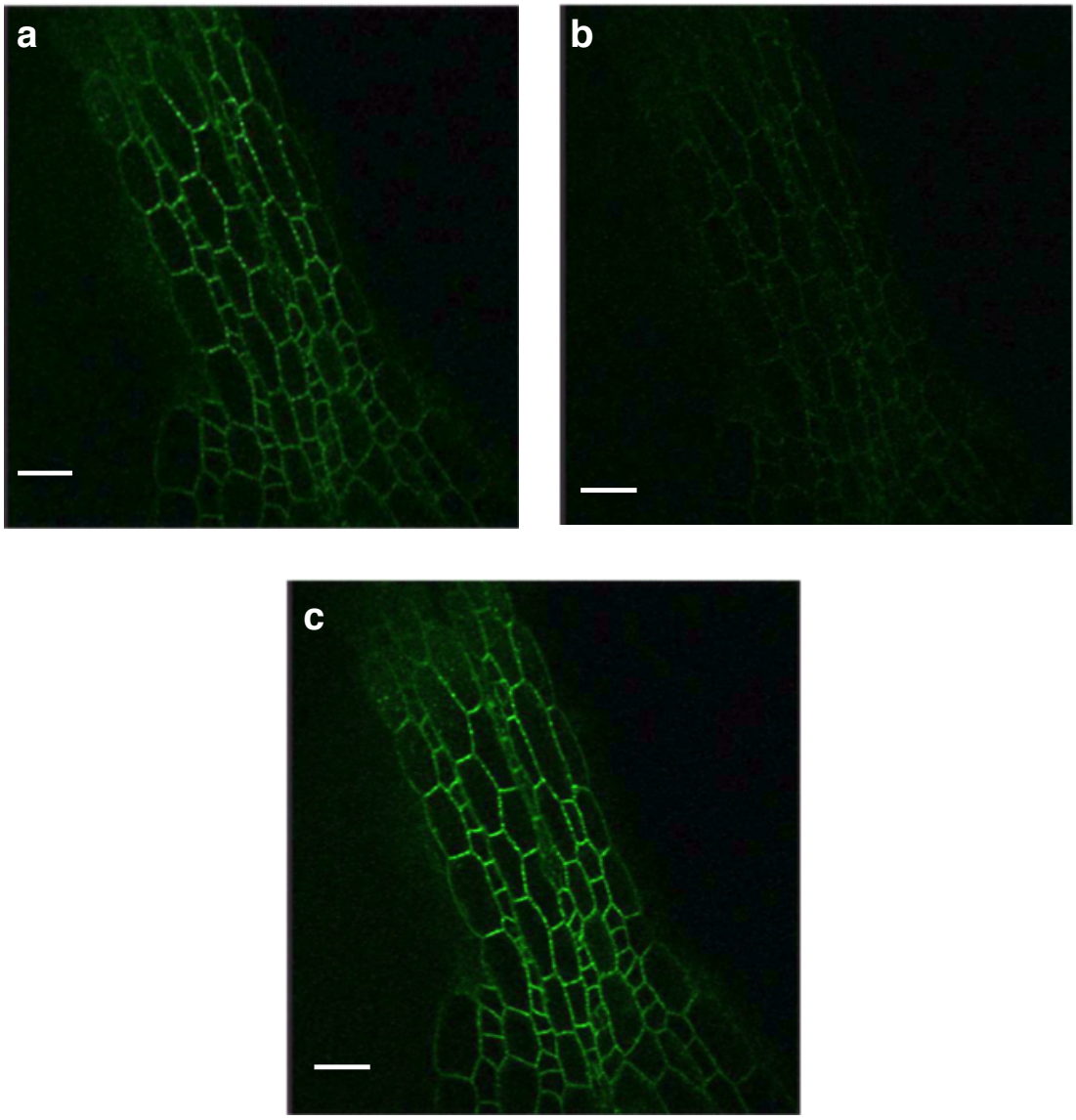

Figure 3.3.11. PDCB1:Dronpa Imaging cycle in *Arabidopsis thaliana* hypocotyl
a) Dronpa fluorescence in the hypocotyl following imaging with low (17%) laser power. b) Same region of tissue bleached with 100% laser power for 20 frames. Some residual fluorescence remains. c) Dronpa fluorescence is much brighter following reactivation with the 405 nm laser at 100% over four frames. Scale 5 μm in each image.

PDCB1 was also found in the vasculature (figure 3.3.12 a) but even at three days post germination the hypocotyl was not sufficiently transparent to allow direct imaging of the underlying vasculature using PALM. Also, although chloroplasts are much less prominent in the vasculature they are present in the surrounding parenchmya cells. Thus, it was decided to etiolate the

seedlings prior to fixation and driselase treatments (*see* Methods).

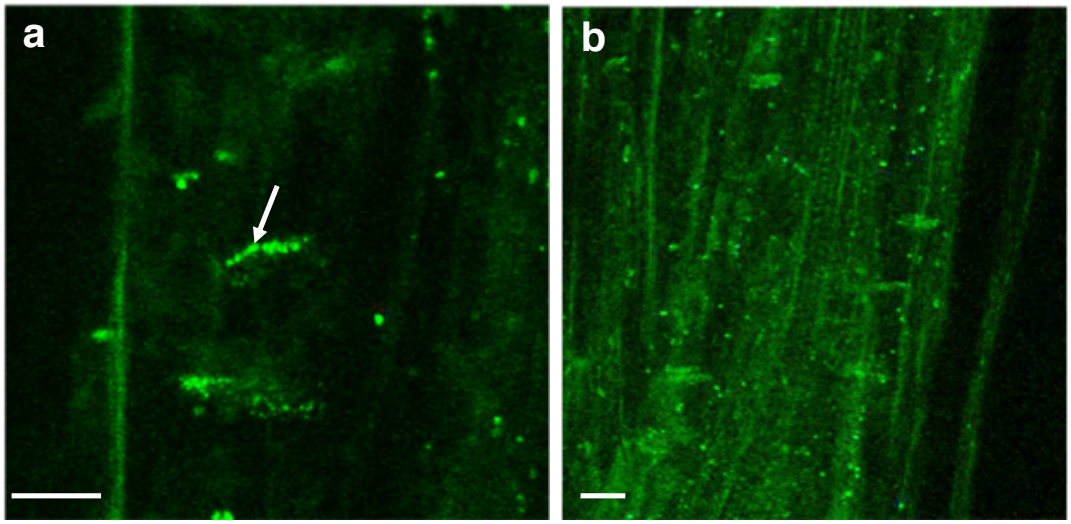

Figure 3.3.12 PDCB1 in vasculature of fixed and etiolated roots.

a) PDCB1:Dronpa labels SP (arrow) b) Same region as in (a), following an image, bleach and recovery cycle. Note high general background and disordered thick cell files. Scale 5 μm in both.

Even following driselase treatment it was apparent that the tissue was still too thick for PALM imaging (figure 3.3.12 b). A general background is apparent throughout the images also, which ensured subsequent PALM imaging was unsuccessful (data not available). Aware that fixation can markedly reduce probe brightness and lifetime (Lippincott-Schwartz, 2009), as well as generally raising background fluorescence, further attempts to capture PALM images were done with driselase treatment alone, but without any success. Dr. Flors left the University in 2011, before the samples were of sufficient quality to image with PALM. For this reason, this area of research was not progressed further.

3.2.4 Summary and future directions

This chapter contains the first super-resolution images of plant cells. These were published in a joint first authorship with Dr. Jessica Fitzgibbon in Plant Physiology (Fitzgibbon et al., 2010). Using 3D-SIM, structures previously seen only with the EM were resolved (e.g. *N.tabacum* sieve plate pores). This increased lateral resolution, combined with a unique optical sectioning capacity, allowed an entire SP and the CC-SE boundary to be reconstructed. This allowed measurements to be made of the respective pore diameters, which might usefully inform mathematical models of phloem flow. It is essential to obtain accurate anatomical measurements as frictional interactions at the SP could reduce ST conductivity by up to 85% (Thompson and Holbrook, 2003). An equation for calculating ST conductivity was proposed by Thompson and Holbrook (2003), and is currently regarded as being the most accurate (Mullendore et al., 2010). However, the resolution of their light microscope images was not sufficient to resolve the SP, so they could not empirically determine pore radius or number. For that reason a number of simplifying assumptions were used: that all pores are of an even size and that the largest visible pore provides a typical measure of pore radius. These assumptions were made in full cognizance of the acute requirement for accurate data sets to derive conductivity, and so the model provided only 'rough estimates' of flow.

Mulendore et al. (2010) obtained exceptionally clear scanning electron microscope (SEM) images of SP following flash freezing and enzyme clearing. These views allowed them to calculate ST conductivity based on empirical measurements, and when compared with those made by Thompson and Wolniak (2008) they found flow rates to be much higher. The method employed by Mullendore and colleagues requires freeze-substitution prior to a 15 day enzyme treatment to remove occluding membranes, before freeze drying and imaging with the SEM. Whilst magnetic resonance imaging experiments indicated that flow rates in hydrated conducting tissues were comparable to those calculated on the basis of stripped and frozen tissues,

the most complete understanding of movement would surely occur with reference to the volume occupied by the plasma membrane, the SER, plastids, mitochondria and phloem protein (p-protein) where applicable. A multi-scale integration of frictions at local and long distances will be required to gain a full understanding of phloem function (Thompson and Wolniak, 2008). 3D-SIM data could contribute meaningfully to these studies. The data presented here is, however, insufficient to allow meaningful testing of the existing models because the experiments reported here were designed to establish 3D-SIM as a 'proof of concept' platform for plant tissues, not to test existing mathematical models. The compatibility of 3D-SIM with standard cytological methods and fluorophores should allow interested groups to generate statistically significant amounts of data quickly. Since my studies, the 3D-SIM microscope has been refined significantly by AppliedPrecision and is now more widely available throughout the world. This is likely to benefit the advancement of plant-cell biology significantly. However, very few super-resolution images of plant cells have appeared since the Fitzgibbon et al. (2010) publication, suggesting that researchers have failed to apply techiques such as PALM and 3D-SIM to many plant systems.

Unfortunately, despite the time spent trying to devise a PALM-compatible methodology, efforts were not successful. This was largely due to the problematic nature of plant material, high inherent fluorescence background of chloroplasts and xylem, and sporadic access to the PALM platform at Edinburgh University. Below are a few suggested improvements that could be made to existing PALM protocols in the hope of obtaining good images with plant material.

Whilst Dronpa has a large dynamic fluorescence range, it displays negative photoswitching meaning that it is switched off by the same wavelength of light with which it is imaged, resulting in a lower number of collected photons per imaging cycle (Andresen et al., 2008). A reengineered Dronpa variant

called Padron, however, displays positive photoswitching, with 488 nm light used to switch it on and the distinct 405 nm line to switch it off (Andresen et al., 2008). The increased efficiency of photon output from this probe might just make the difference in these marginal plant samples and allow reconstruction of an image. Producing a transgenic tobacco line expressing the Padron fusion would also be of benefit. Even in young *Arabidopsis thaliana* seedlings the phloem is never closer than 50 μm to the surface (Froelich et al., 2011). A transgenic tobacco line could be sectioned with the vibrating microtome, as for 3D-SIM imaging, and mounted with the vasculature in direct contact with the coverslip. This would hopefully increase the yield of photons collected further.

4. Developing a Correlative Imaging Strategy for the Phloem

4.1 Introduction

So much of our knowledge of biological structures has come from our ability to visualize them. Investigations with the EM set a structural context (Cronshaw and Esau, 1968). Its ability to resolve cellular ultrastructure to a few nanometers is unrivalled. TEM generates images by transmitting a beam of electrons through a sample. The image is formed through an interaction between the electrons and the sample. The image is a two-dimensional projection. For the sample to be thin enough to allow electrons to pass through the cellular ultrastructure must be fixed well and the tissue reinforced (embedded in resin) to allow cutting with an ultramicrotome. Imaging thin sections makes it difficult to observe structures throughout large volumes of cytoplasm and thus it is extremely challenging to view whole cells within tissue unless time consuming serial sectioning is undertaken. This is a significant drawback as contextual information is crucial as a cell's position and is vital for its development (Barlow 1984).

In addition, trying to recognise specific proteins immunologically in thin sections, e.g. using immuno-gold, is complicated by the paucity of antigenic sites available for detection. This is a consequence of the methods used in

processing the samples. Chemical fixation crosslinks proteins while subsequent dehydration, resin-infiltration, and resin-curing leaves very few antigenic sites viable. So, whilst being able to localise proteins to positions within the cell to a few nanometers is desirable, to impart truly biological relevance it is necessary to observe proteins in the context of others (Gibson, 2009). While it is possible to detect more than one protein in a sample, e.g. by using secondary antibodies linked to gold particles of different sizes (Loussert-Fonta and Humbel, 2015), in practice this is technically challenging and has not seen wide-spread application in the plant sciences.

Genetic engineering can add fluorescent tags to proteins, and the pallet of colours now available allows researchers to label many different proteins in a sample, the number of which is limited only by the ability of the microscope to detect and separate them (Shaner et al., 2005). Due to the limits of diffraction (see Bell and Oparka, 2010) conventional light microscopes cannot resolve objects closer than approximately half the wavelength of light passing through them, which is maximally 200 nm laterally (x-y) and 500 nm axially (z). This leaves many subcellular structures unresolved and the spatial relationship of different proteins and cellular structures uncertain. Recent innovations in biological imaging have seen the diffraction limit broken (Bell and Oparka, 2010), allowing structures in amenable samples to be resolved to 10 nm (Huang et al., 2016). The field of biological super-resolution microscopy is still in its infancy but its application is yet to find wide-spread use, despite its universal appeal.

For the first time, researchers can access microscopes that image across biologically relevant scales, allowing the relationship between genetically labelled proteins and organelles to be established. Divergent specimen preparation methods have been optimized for each imaging platform, reflecting the different rigours they exert. As outlined above, specimens imaged with the TEM need to be in thin sections so that electrons can pass

through them. In the previous chapter, the sample requirements for super-resolution using 3D-SIM were discussed. Briefly, this also required sectioning, or the use of thin tissues that could be mounted under a coverslip. The optical sectioning capacity of confocal laser scanning microscopy (CSLM) is such that the tissue need not be sectioned at all, assuming the specimen fits onto the stage and the region of interest lies within the working distance of the lens: 4000 µm for a x10 dry lens to 210 µm for a x63 water dipping lens. This allows imaging of cells and tissues in a 3D context.

Attempts have been made to devise a unifying method that would allow the same samples to be imaged by light and EM, allowing a direct correlation of their output (Watanabe et al., 2011). Presented in this chapter is a correlative light and electron microscopy (CLEM) method that retains fluorescence and antigenicity in resin-embedded vascular tissues and that is compatible with CSLM, 3D-SIM and TEM (Bell et al., 2013).

4.2 Aims

i) To retain fluorescence in resin-embedded vasculature samples.
ii) To preserve antigenicity in resin-embedded vasculature samples.
iii) To image the same sample with the confocal and transmission electron microscope.

4.3 Results

4.3.1 Use of London Resin as an embedding medium

London Resin (LR) is an acrylic embedding agent that is hydrophilic and stable in the electron beam. It is cross-linked by free radical chain polymerization which shows no affinity for proteins or nucleic acids, meaning that these macromolecules are available for immunodetection (Keene et al., 2008). These properties make LR an attractive embedding medium for those researchers trying to devise a CLEM imaging strategy, and its use as such has already been published (Luby-Phelps et al., 2003; Keene et al., 2008).

Initial attempts to devise a correlative light and EM imaging strategy were made using LR very early in the course of this project, broadly following the method described by Keene and co-workers (2008). In that publication they preserved GFP and YFP in semi-thin sections of rat chondrosarcoma cells and correlated their fluorescence images with those taken in the TEM in which the fluorescent protein position was highlighted after immuno-gold detection (Keene et al., 2008).

A transgenic *Nicotiana tabacum* expressing the viral movement protein (MP) of tobacco mosaic virus (TMV) from the 35s cauliflower mosaic virus promoter (TMV.MP:GFP *p35s*; Roberts et al., 2001) was used in these experiments. This was selected as in an earlier publication we had shown that the form of the movement protein was different in the ST than in other cell types studied (Fitzgibbon et al., 2010; see also Chapter 3). In the SE, MP is not retained within the central cavities of PD but extends longitudinally within the SE, and so its further examination was of relevance here. In hindsight this material was not well suited for method optimization as the fluorescence is not readily apparent in transverse petiole sections, so checks on fluorescence levels during processing were difficult. To protect the water-dipping lenses it was necessary to mount samples under a coverslip as direct contact with the resin was likely to be deleterious. Checks were made with a

x20 lens to be certain if fluorescence was present in PD throughout the section. GFP fluorescence diminished during processing, and the tissue became increasingly autofluorescent. LR itself autofluoresces strongly so samples removed during embedding had to be first rinsed before an accurate fluorescence check could be made. This added both time and a potential complicating step to the assay as washing the partially embedded samples may have caused leaching of cell compounds, giving a false impression of the GFP fluorescence loss. Whereas these intermediate checks do not affect the end result of a given methodological approach, if not accurately recorded they complicate any attempts to identify and troubleshoot the stages of the protocol at which problems develop.

Figure 4.3.1 – legend on page 71.

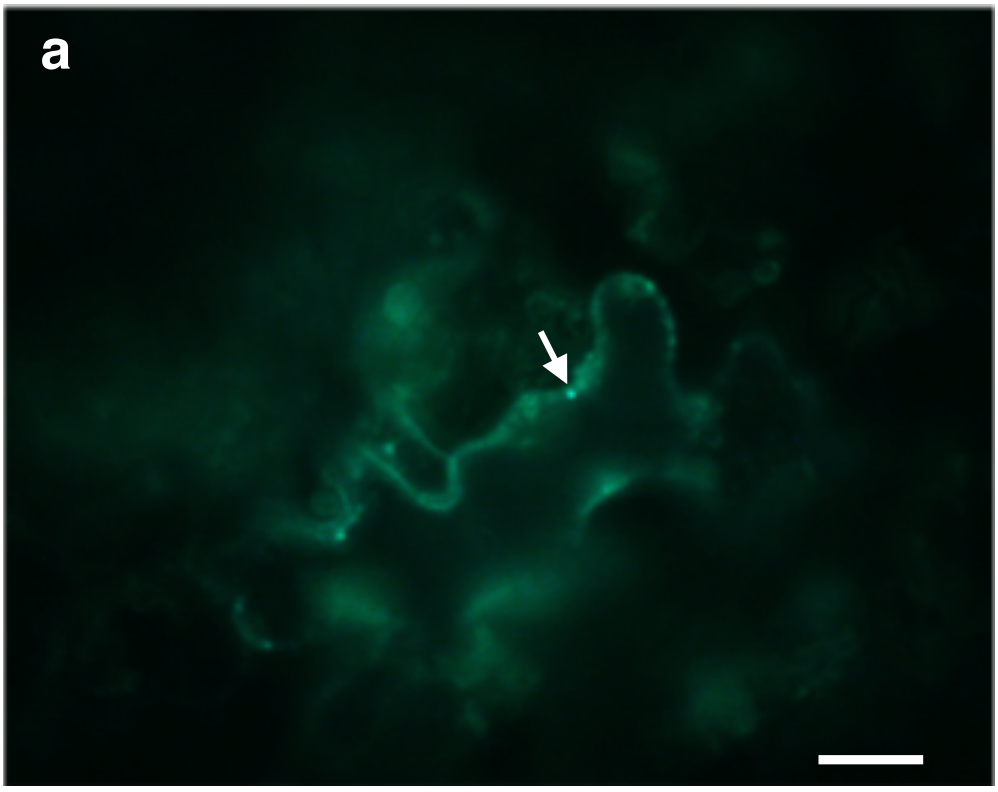

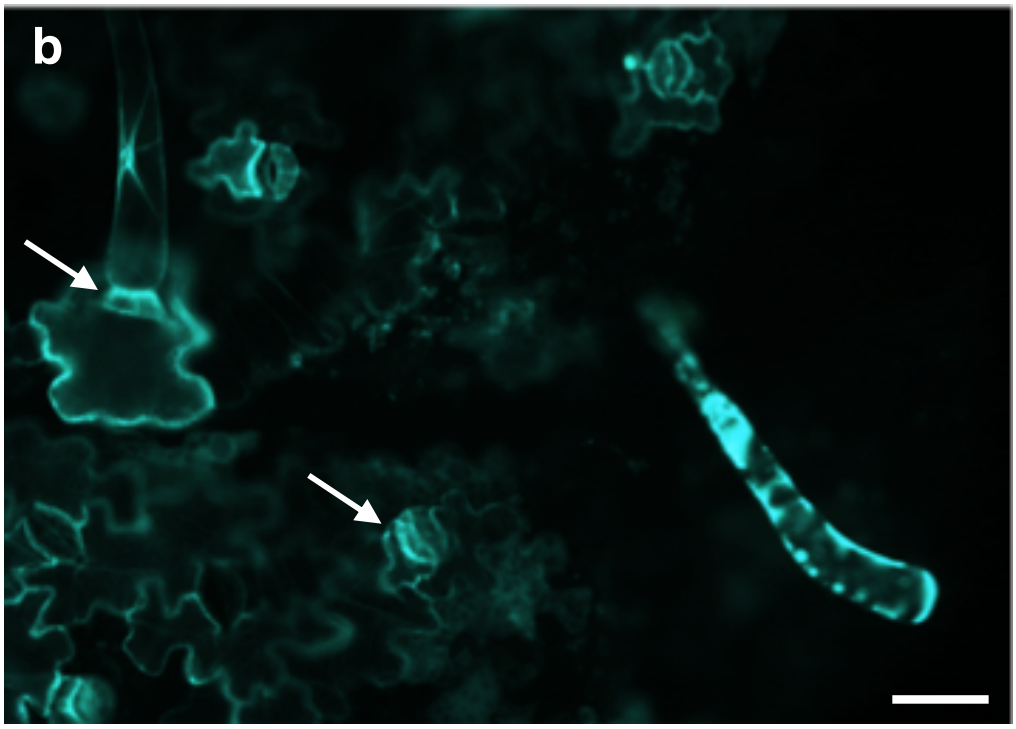
b

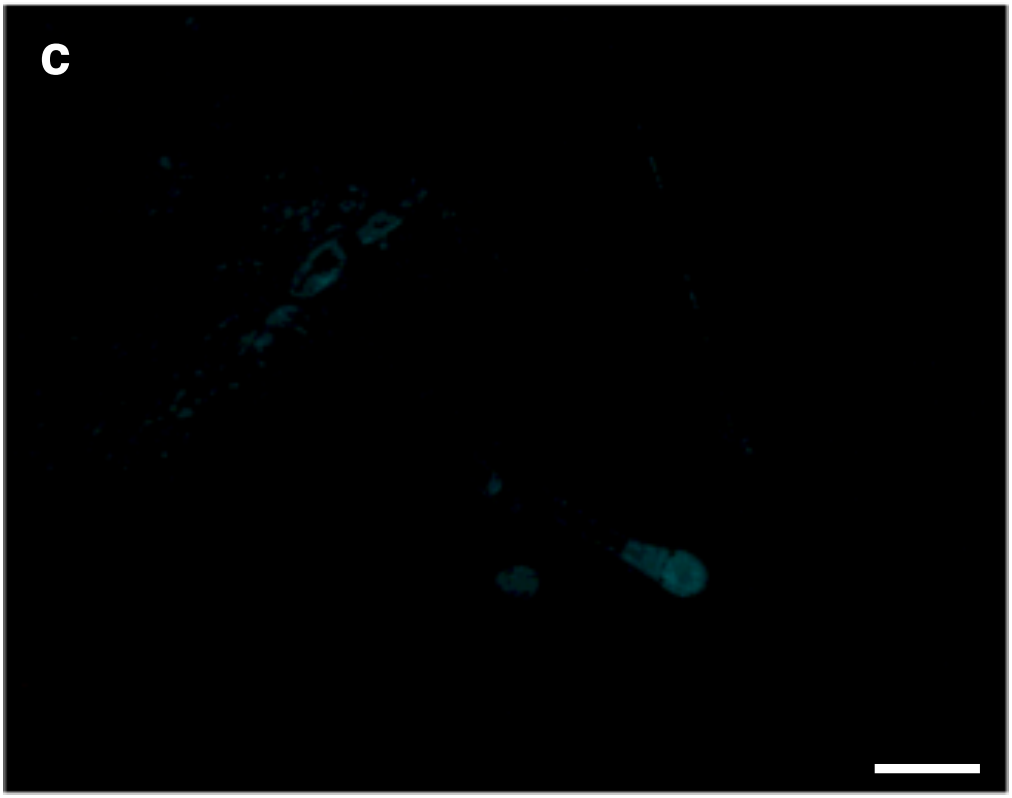
c

Figure 4.3.1. GFP fluorescence in LR White

Free-hand sections taken of TMV.MP:GFP (Roberts et al., 2001) expressing tobacco petioles removed during processing to check fluorescence signal. a) Section taken from material that had been fixed and dehydrated with 90% ethanol. GFP signal is retained at the periphery (arrow) of mesophyll amid background autofluorescence. b) Section cut following embedding in 100% LR White on ice. Fluorescence is still apparent in the pitfields that join the basal trichome cell to the epidermis (arrow). Guard cells (arrow) and stomata show autofluorescence. c) Section cut following overnight resin-cure at 60°C. GFP fluorescence had largely disappeared with only non-specific autofluorescence apparent. Scale 50 µm in all.

Figure 4.3.1 shows a typical series of images taken of tobacco petioles expressing TMV.MP:GFP during processing. 4.3.1 (a) is an image of material that was fixed and dehydrated to 90% ethanol. GFP fluorescence is apparent in punctae (arrow). This is significant as 1% of glutaraldehyde is much higher than that used previously (0.25%; chapter 3, Fitzgibbon et al., 2010), and it is widely thought that glutaraldehyde quenches fluorescence. Its inclusion in a correlative light and electron microscopy method was vital due to its unrivalled ability to preserve ultrastructure (Hayat, 1973). There are only a few punctae in this field of view, and this may be indicative of the success of this procedure in preserving fluorescence or simply reflect the plane of free-hand sectioning. Another disadvantage to using this material as a baseline for trouble shooting is that because fluorescence is only in the central cavities of PD, then insufficient reference material is available to accurately gauge the fluorescence present. However, it was clear that GFP fluorescence was tolerant to fixation with 1% glutaraldehyde and subsequent ethanol dehydration to 90%. The next image (b) was taken of material that was infiltrated on ice with 100% LR and shows that GFP fluorescence remains after LR embedding. Again, the image does not show a field of cells with fluorescent punctae at their periphery. However, in areas where GFP fluorescence is apparent, e.g., at the junction of a basal trichome cell with the epidermis (arrow), it does appear to be strong. Consistently, GFP fluorescence was detected when the material was in 100% LR on ice, but on

each occasion following polymerization the blocks showed no fluorescence (c). Whilst Keene et al., (2008) emphasized the requirement for low temperatures prior to polymerization, it was apparent that it was necessary to keep the temperature as low as possible at all times during processing. LR can be polymerised in three ways: chemical curing, heat curing and low temperature ultraviolet (UV) light curing. Chemical curing requires the addition of a catalyst (benzoyl peroxide) and can be achieved in only ten minutes. It is, however, vigorously exothermic with a transient increase in temperature of 20°C (Steve Mitchell, unpublished results). Heat curing simply involves heating the resin to the permissive cure temperature of 60°C. Here, the slower, self-catalysed reaction proceeds over the course of a few hours, usually overnight. Low temperature curing (-15°C to 4°C) using UV requires the addition of a proprietary LR accelerator and up to 24 hours of irradiation at 365 nm. The low temperature option seemed to be the most appropriate, so attempts were made to retain fluorescence following UV polymerisation at 4°C over 24 hours. Supplied in a liquid form, a drop of accelerator is added to the gelatin capsule containing the fully infiltrated sample filled with LR. The capsule is then sealed and the contents mixed prior to UV exposure.

Using UV the blocks polymerised unevenly. Many attempts were made to promote mixing of the accelerator and LR (vigorous shaking of the gelatin capsule following its addition; using a stir bar and magnetic stirrer to mix the resin and accelerator prior to filling the capsules), as well as ensuring the UV light source evenly bathed the sample (by rotating and re-orientating every few hours). However, the blocks could never be sectioned. At this point, it was decided to no longer pursue UV embedding.

4.3.2 Use of Methacrylate as an Embedding Media

In the intervening period, Watanabe and co-workers published a correlative light and scanning electron microscopy protocol in Nature Methods (Watanabe et al., 2011). In this study, they preserved the fluorescent protein citrine and the tandem dimer Eos in *Caenorhabditis elegans*. These authors also had difficulties using LR and dismissed it as due to batch-to-batch variability in its pH and water content. Instead they decided to optimize methacrylate for embedding their samples. Thompson and Wolniak (2008) used methacrylate to preserve the fluorescence and antigenicity of a plasma membrane anchored citrine fusion in Arabidopsis and tobacco SE that they examined under CSLM. They used a different formulation from that used by Watanabe et al., (2011), containing a mixture of the methacrylate monomers n-butyl methacrylate and methyl methacrylate. Using a mixture of pre-polymers gives an advantage in that, through altering their relative proportions, it is possible to adjust the hardness of the block, a harder block being more likely to support ultramicrotomy. In addition to the capacity to preserve fluorescence and antigenicity (Thompson and Wolniak, 2008), earlier reports showed that fine labile structures such as microtubules could be preserved in diverse taxa (*Pinus radiata, Zamia furfuracea, Azolla pinnata and Funaria hygrometrica;* Baskin et al., 1992) following embedding in methacrylate. In the above studies, processing and polymerization were done at low temperature (-20°C). Temperature seemed to be the critical factor for preserving fluorescence during LR processing (4.3.1) and the failure to establish a low-temperature polymerization method was the reason it was abandoned here.

4.3.2.1 Transgenic material

I next used a transgenic tobacco line that expressed the ER retention signal HDEL fused to GFP, expressed from the phloem-specific *SEO2* promoter (*pSEO2*.HDEL:GFP; Knoblauch and Peters, 2010). The strong and consistent fluorescence in the SER, visible as general fluorescence in the

phloem bundles at low magnification, made it suitable for identifying GFP in SE. The adjacent xylem vessels served as excellent markers for baseline and aldehyde-induced autofluorescence. (see figure 4.3.2 a)

Figure 4.3.2 – legend on next page

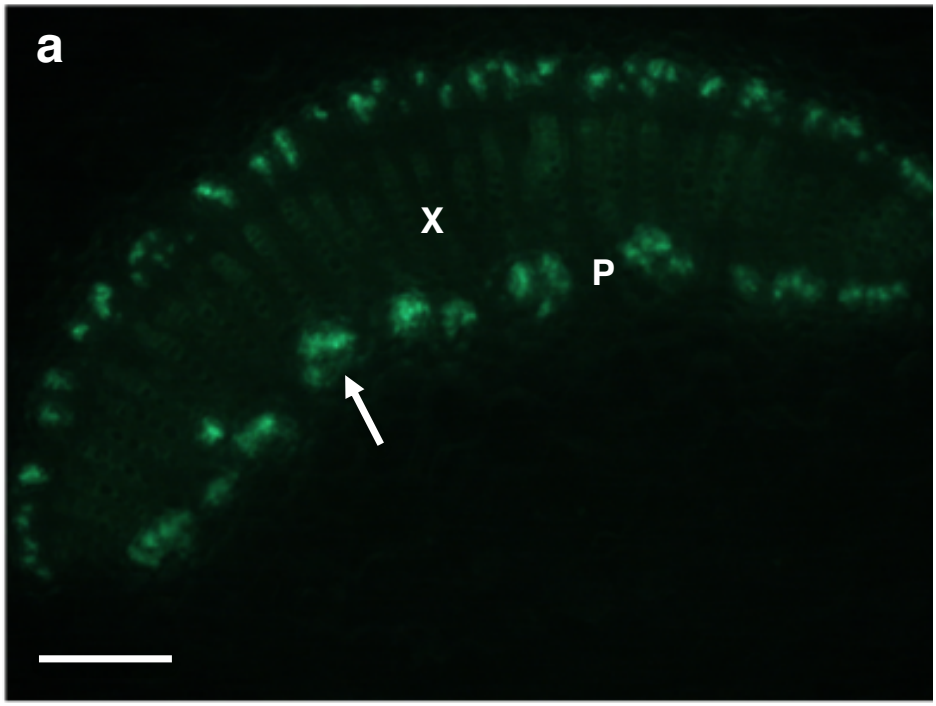

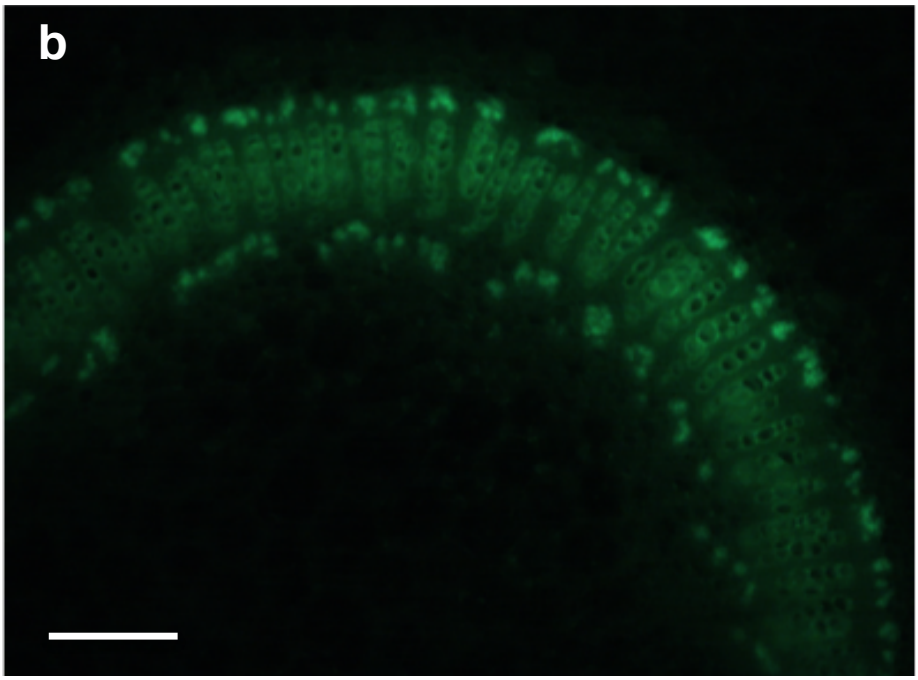

Figure 4.3.2 GFP fluorescence survives tissue fixation with 2% glutaraldehyde

a) A free-hand section cut from a tobacco petiole expressing *pSEO2*.HDEL:GFP (Knoblauch and Peters, 2010). This construct highlights the SER in ST, apparent here as bundles (arrow). X – xylem; P phloem. b) Following a one-hour fixation with fixative containing 2% glutaraldehyde phloem bundles are still fluorescent. There is an increase in xylem autofluorescence. Scale 600 μm.

4.3.2.2 Fixation

One positive result that emerged from the LR trials was that GFP fluorescence remained robust after fixation when the concentration of glutaraldehyde was increased to 1%. It was decided to increase the concentration even further to 2% in order to ensure good ultrastructural preservation (Mitchell, personal communication). A likely consequence of increasing glutaraldehyde concentration is an increase in aldehyde-induced autofluorescence (Billinton and Knight, 2001). After crosslinking proteins, free aldehyde groups (-CHO) remain. These can combine with antibodies and other histochemical reagents causing undesired cross-reactions and a general background autofluorescence (Billinton and Knight, 2001). Reducing the aldehydes to a hydroxyl group (-OH) ameliorates tissue autofluorescence and makes cross-reactions less likely. To reduce autofluorescence with 2% glutaraldehyde, the reducing agent dithiothreitol (DTT) was incorporated during processing. DTT has been shown to reduce background autofluorescence and preserve antigenicity (Baskin et al., 1992; 1996; Thompson and Wolniak, 2008).

Initial trials showed that GFP fluorescence survived fixation with 2% gluataraldehyde with an acceptable level of background fluorescence (figure 4.3.2 b). Thus, these fixation conditions were used in subsequent methacrylate embedding optimization steps.

Figure 4.3.3 – legend on page 78

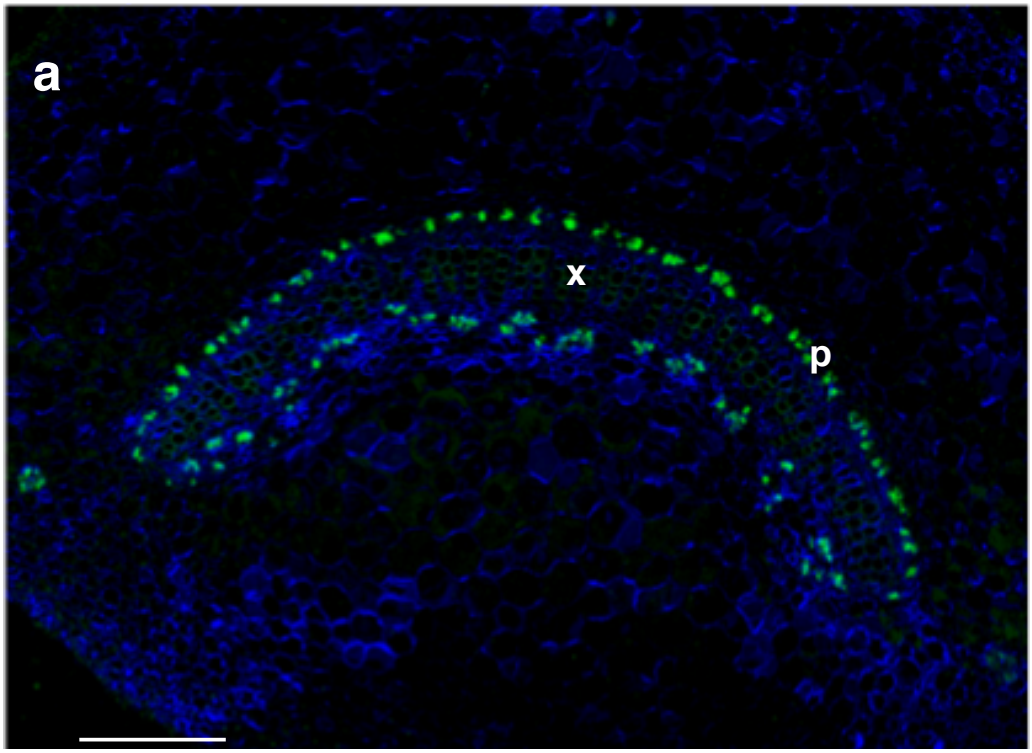

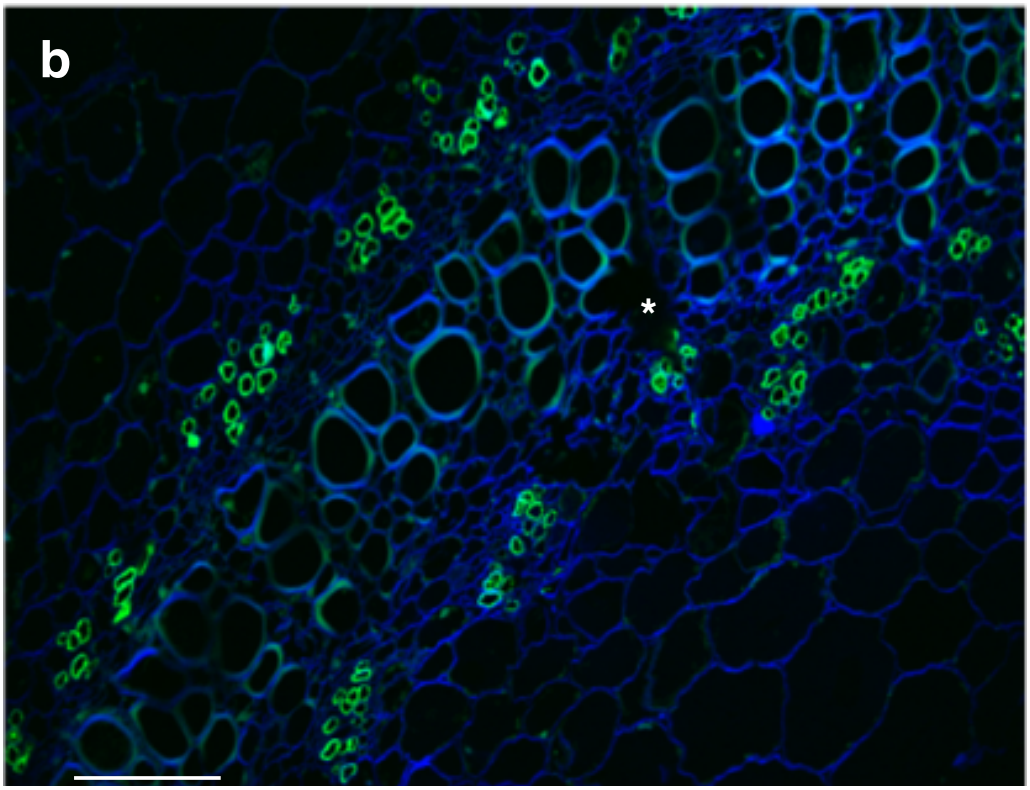

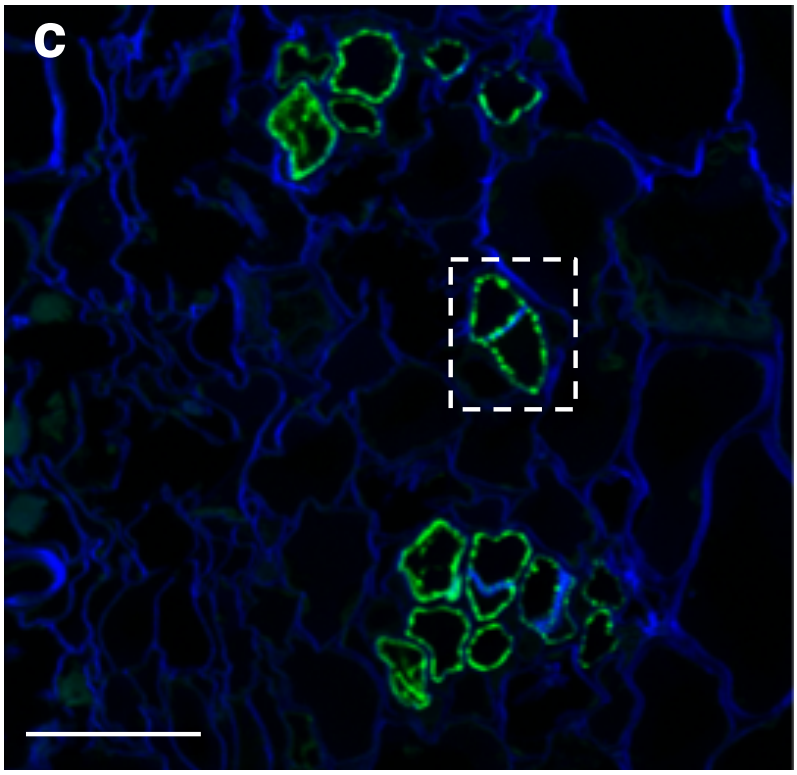
c

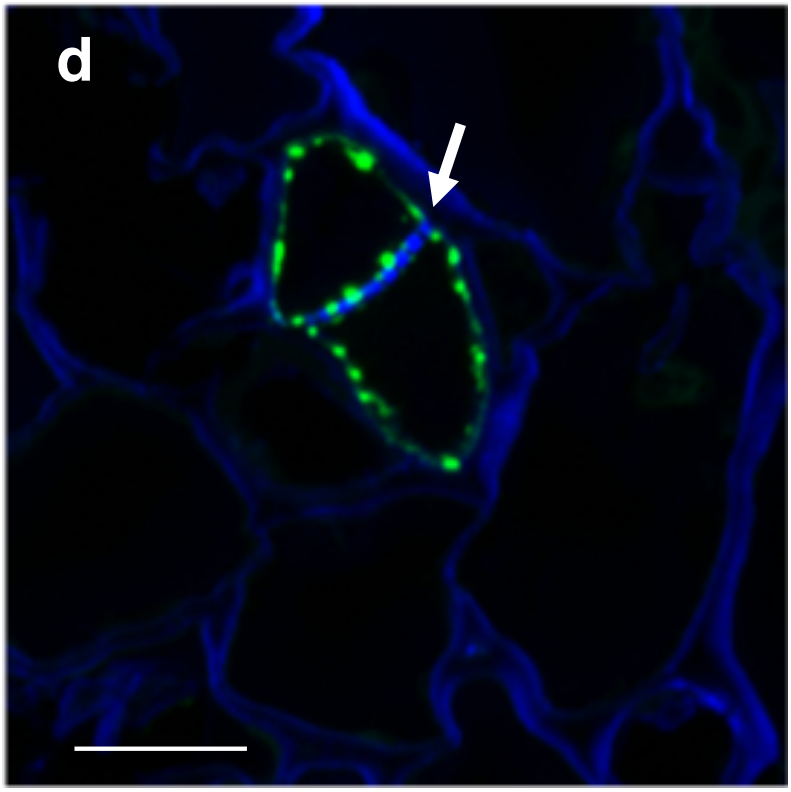
d

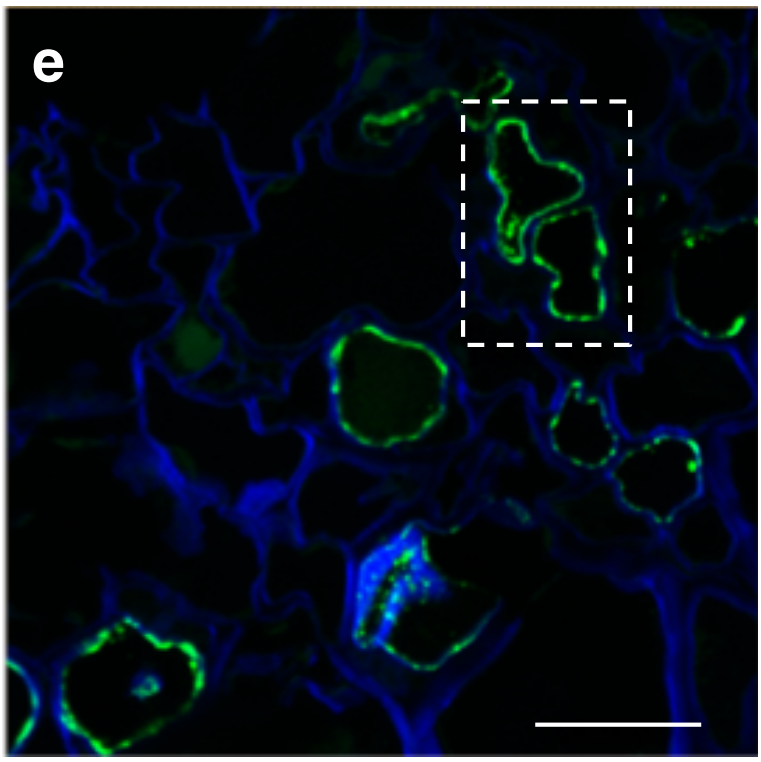

Figure 4.3.3 GFP fluorescence is preserved in polymerised methacrylate resin -previous pages

a) Polymerised block face with *pSEO2*.HDEL:GFP (Knoblauch and Peters, 2010) expressing *Nicotiana tabacum* petiole in transverse cross-section. General fluorescence in phloem bundles is apparent at low (x5) magnification. Cellulose stained with calcofluor white and shown in blue. Scale 600 μm. b) Semi-thin section from block shown in (a). Tissue appeared stretched in places and ripped slightly during cutting (*). Scale 75 μm c) Image of an individual phloem bundle showing a longitudinal view of a SE with a SP transecting it (dashed rectangle). Scale 40 μm d) Enlarged view of area highlighted in (c). SP arrowed. Fluorescence remained stable during imaging. Scale 20 μm. e) Another field of view shows tissue disruption. Area within dashed rectangle shows cells that appear partially collapsed. Scale 20 μm.

4.3.2.3 Processing

Figure 4.3.3 (a and b) shows that the general fluorescence from the phloem bundles, as highlighted by *pSEO2*.HDEL:GFP, was preserved well. The cellulose in the polymerized block face was readily counterstained with calcofluor white and this further aided tissue orientation. The fluorescence was stable and no fading was apparent when imaging the intact block face or

in semi-thin sections imaged for extended periods using the CSLM at high magnification (x40, x63 respectively; figure 4.3.3 c; c.f., Thompson and Wolniak, 2008). Unfortunately, even at the lower magnification (x5; figure 4.3.3 a and b) it is apparent that there was considerable deformation of the tissue. Methacrylate resins are known to deform during the strains exerted during sectioning (Hayat 1973), so the proportion of methyl methacrylate was doubled from 20% to 40% to create a harder block.

Figure 4.3.4 – legend on following page.

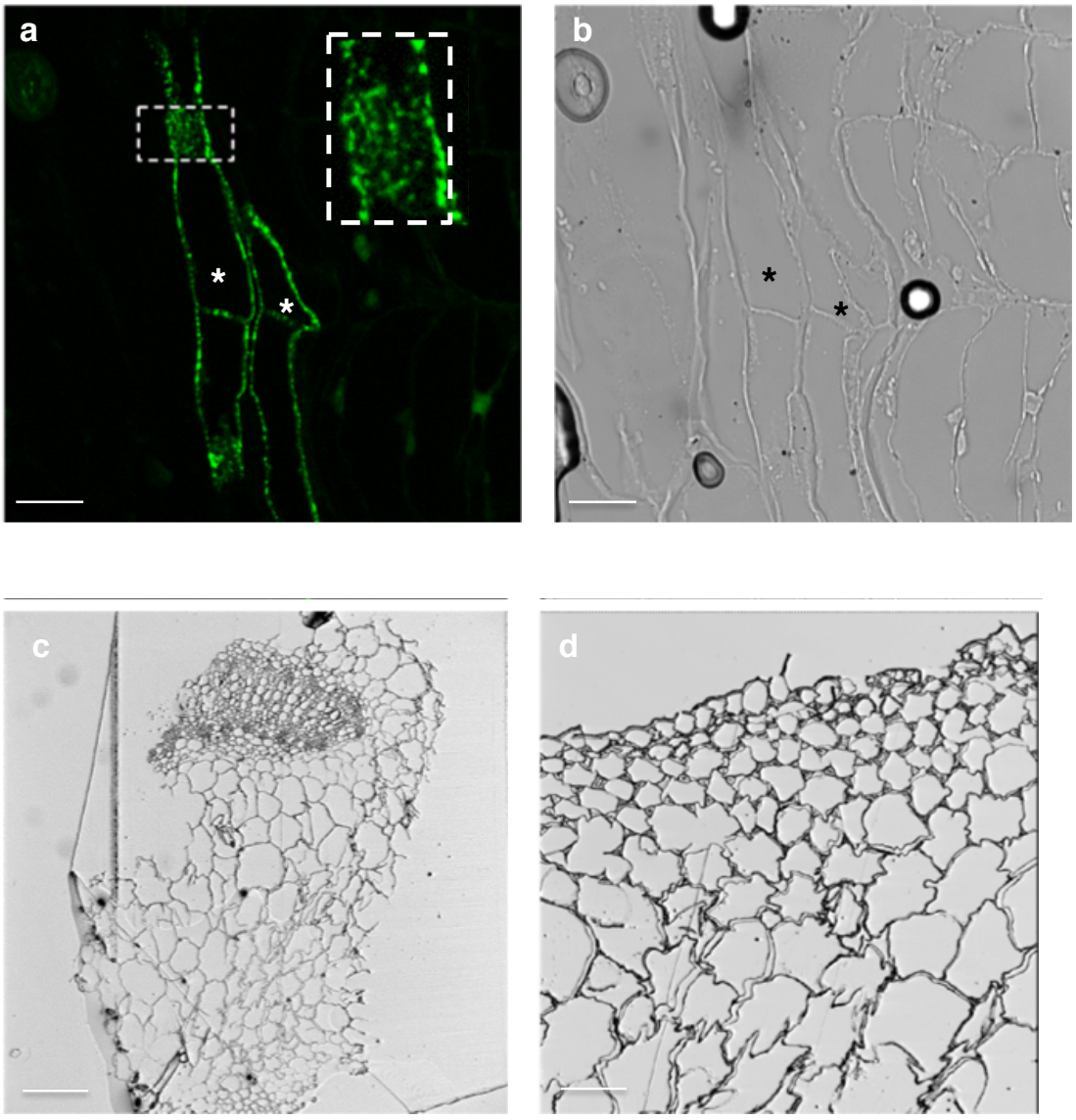

Figure 4.3.4 An increased proportion of methyl methacrylate supports fluorescence but not tissue structure – see previous page

a) Longitudinal orientation of ST. Reticulate arrangement of the SER appears well preserved. See inset. GFP fluorescence is stable during imaging. Scale 40 μm. b) Same section imaged with bright-field. The tissue appears compressed. Scale 40 μm. c) Section tears during cutting. Vasculature appears compact but surrounding cells are deformed. Scale 1 mm d) Cellular disruption is greatest in the cortex. Scale 500 μm

Figure 4.3.4 a shows that the increased proportion of methyl methacrylate still supported GFP fluorescence. Unfortunately, as shown in figure 4.3.4 (c and d) sections tore readily and the tissue generally showed disruption, especially in the cortex (d). However, the reticulate arrangement of the GFP-labelled SER, arrowed in 4.3.4 a, was similar to fresh sections, so it appeared that the methacrylate embedded material showed reasonable subcellular detail despite distortion at the tissue level.

Hayat (1973) described characteristic uneven polymerization and large shrinkage of tissues (about 20%), using methacrylate and suggested that partially pre-polymerised resin might ameliorate this problem. This involves inducing some structural changes to the resin before embedding the tissue. As increasing the block's hardness had not solved the problem, it seemed very likely that the structural damage was caused by shrinkage or uneven polymerization. Pre-polymerising the resin involves adding the catalyst to the resin mix (see materials and methods) and exposing it to UV light. Increased viscosity was apparent after 60 minutes of illumination. The maximum exposure time was 120 minutes by which time the resin was very viscous. A consequence of an increased viscosity is a slower tissue penetration rate, so care was taken to extend the infiltration time to compensate for this altered chemistry. Using pre-polymerised resin did not make any difference to the final tissue, which still stretched and ripped when cut (data not shown). It was decided not to pursue methacrylate embedding further.

4.3.3 London Resin revisited

I decided to try LR again with fixation in 2% glutaraldehyde and a washing regimen that included DTT. Figure 4.3.5 shows a panel of images captured following different stages of processing. Tissue slices were removed and the fluorescence compared with unprocessed transverse sections of petiole. For each section a region of the phloem was imaged with a x5 lens using identical settings on the CSLM.

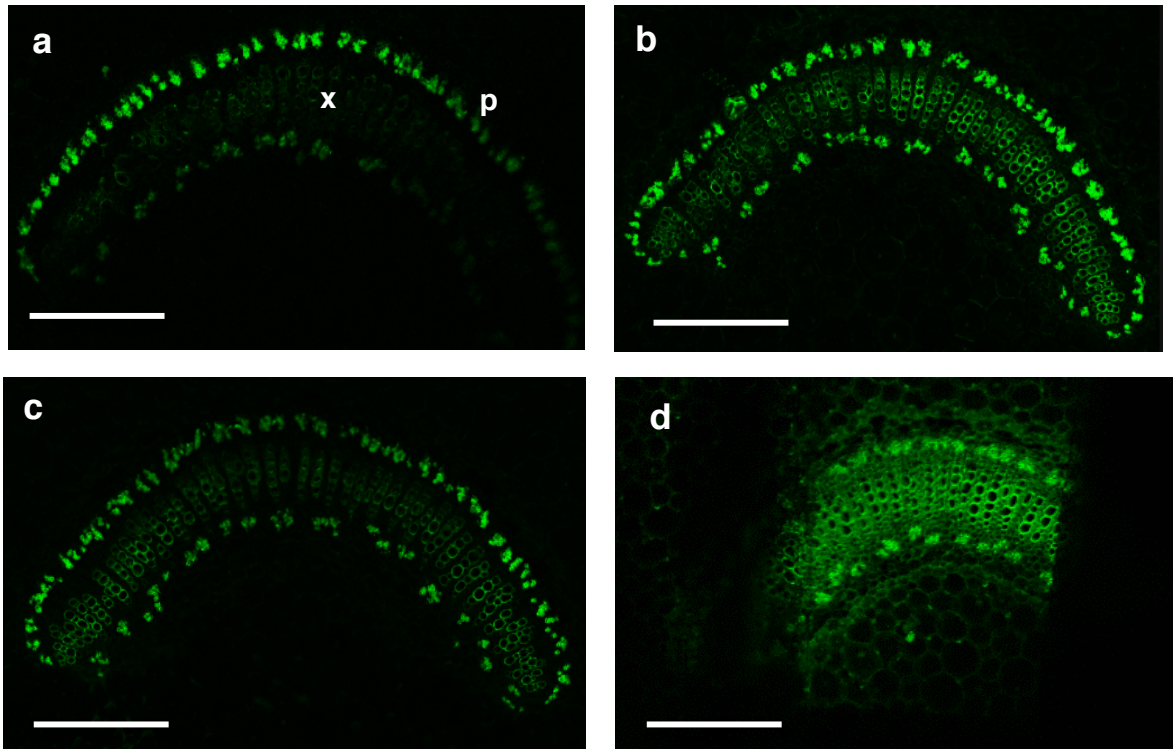

Figure 4.3.5 Images for fluorescence loss calculation during London Resin processing

a) Unprocessed, free-hand section of a *Nicotiana tabacum* petiole expressing *pSEO2*.HDEL:GFP (shown in green; Knoblauch and Peters, 2010) xylem (x), phloem (p). This is the baseline from which fluorescence loss is calculated. b) Tissue removed after overnight fixation. c) Tissue removed post dehydration with ethanol d) Tissue imaged *en bloc* . Scale 600µm

The fluorescence was measured in 11 phloem bundles using ImageJ software (Schneider et al., 2012) and the mean fluorescence value calculated as a percentage of the initial fluorescence.

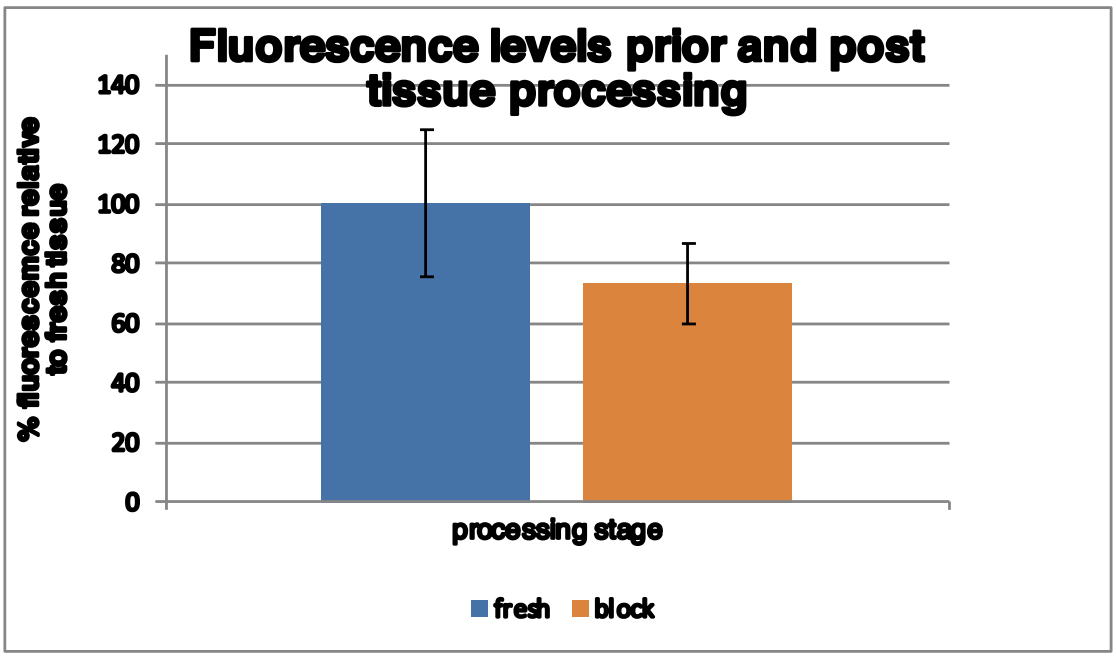

Graph 4.1 Fluorescence levels prior and post tissue processing

Average fluorescence was measured from 11 phloem bundles from one petiole section in fresh tissue and then one *en* bloc. Error bars show standard deviation of the mean.

Fluorescence loss from fresh to polymerized tissue was calculated as 27.5% (± 13.5%, $n = 11$; see graph 4.1). This was deemed to be an acceptable loss and the fixation and embedding regimens were not optimised further.

In this trial, a number of changes were made from the initial protocol that used LR to preserve fluorescence in embedded material (4.3.1). This included the requirement of the fluorescence to support a room-temperature infiltration step and polymerization in a heated oven. The embedding oven was set to 50°C, the lowest temperature that could reliably support polymerisation. The blocks polymerised completely at this temperature in a 24-hour period. Whilst it seems likely that the reduction in temperature of 10°C is critical to the ultimate success in preserving fluorescence in LR embedded material, there were other changes from the initial trial (4.3.1). These included the use of the *pSEO2*.HDEL:GFP transgenic line, fixation with 2% glutaraldehyde and subsequent washes and infiltration incorporating

DTT. Without testing each one of these parameters in turn it was not possible to say which was the most critical to the success of the method. However, it is likely that the reduction in polymerization temperature of 10°C was significant. DTT, incorporated in every step post-fixation, is a reducing agent that when used in combination with low temperature processing is understood to reduce background fluorescence, preserve antigenicity and prevent quenching of fluorescent proteins (Baskin et al., 1992; 1996 and Thompson and Wolniak, 2008). The protective effect of DTT may make the fluorescence more robust prior to polymerization.

4.3.3.1 *En bloc* imaging

Prior and co-workers (Prior et al.,1999) showed that it was possible to image plant cell walls *en bloc* following polymerization of tissues in the epoxy resin Araldite. Using the optical sectioning capacity of the CSLM it was possible to map the position of features of interest and image at that depth, facilitating more detailed studies with the light or EM. LR-embedded tissue was similarly compatible with this type of imaging.

Figure 4.3.6 – legend on page 85.

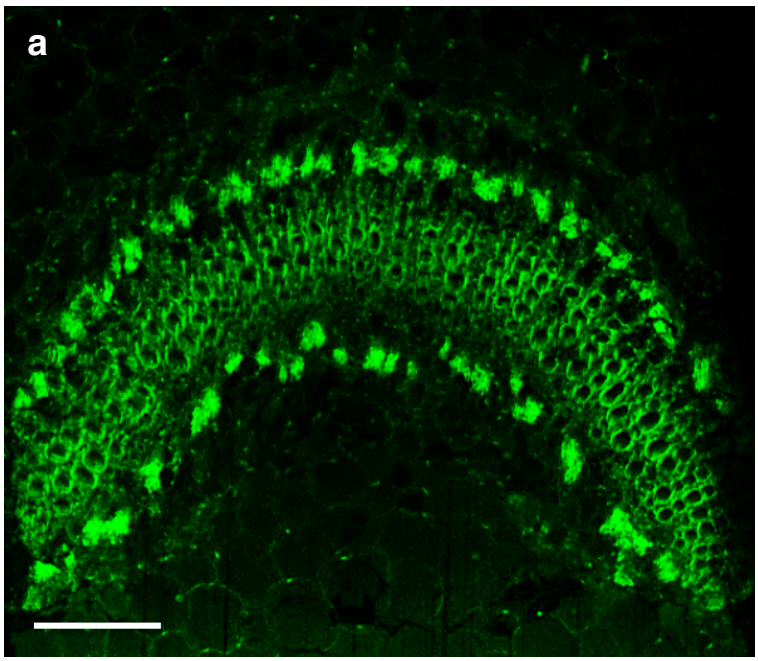

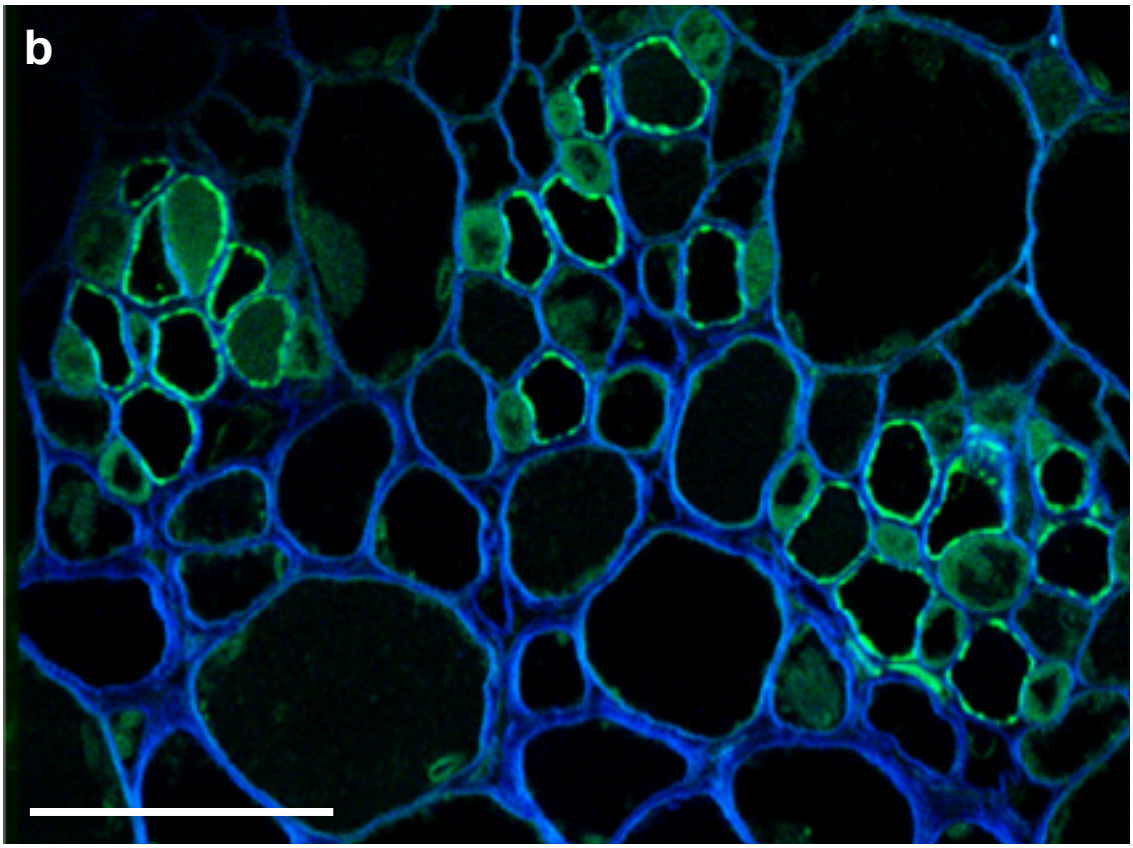
b

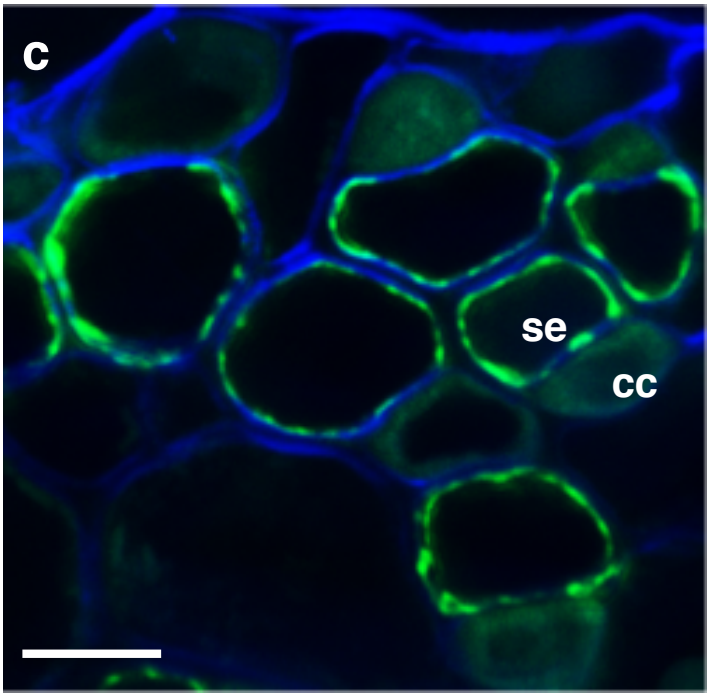
c
se
cc

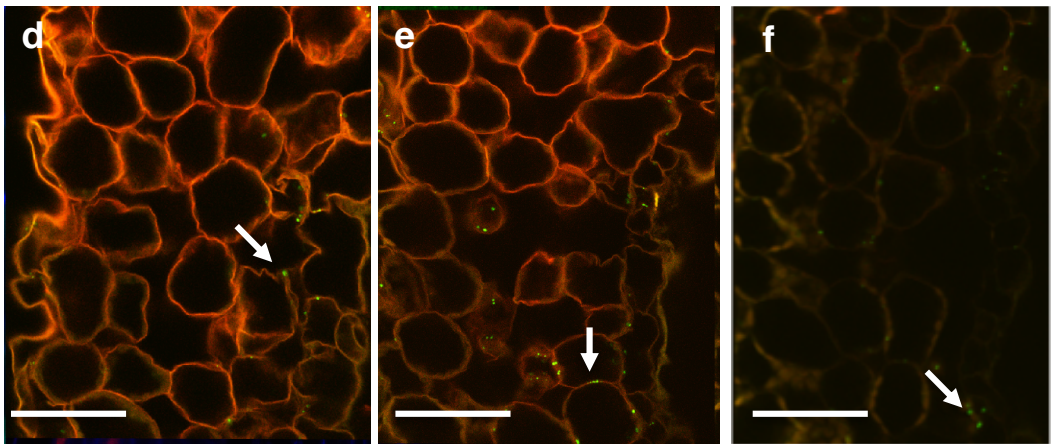

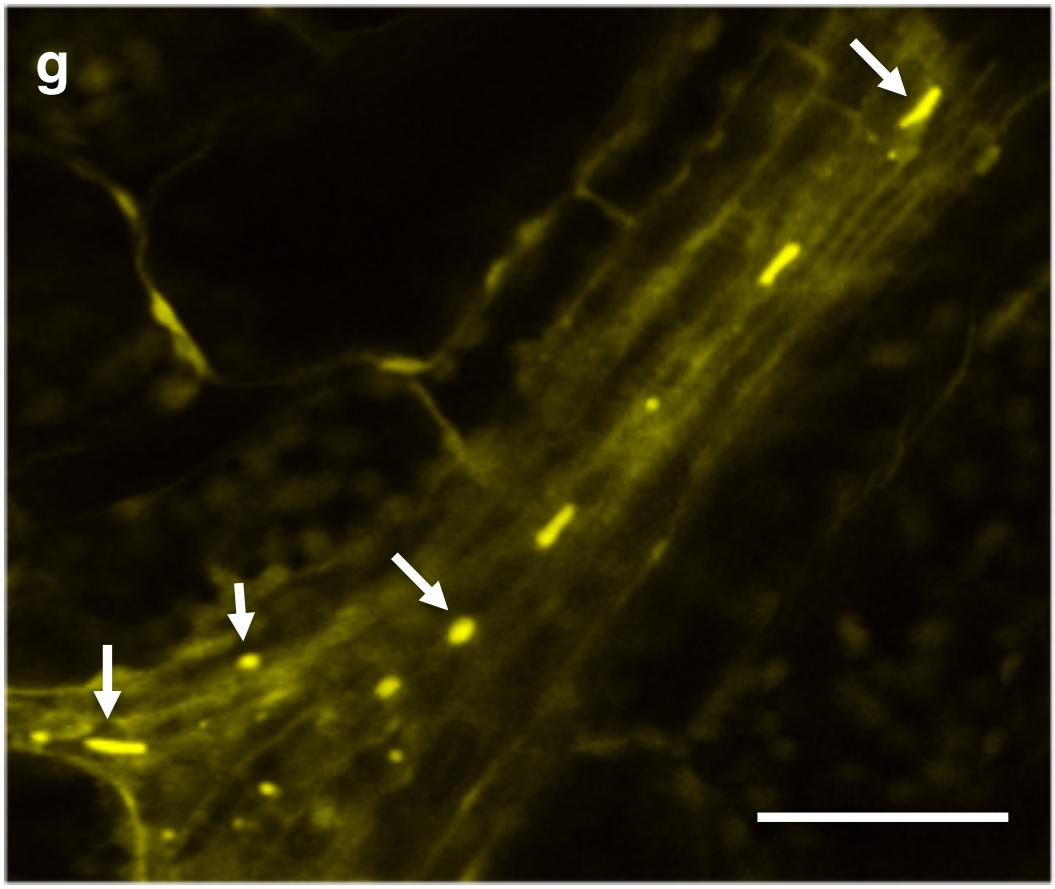

Figure 4.3.6 *en bloc* images of fluorescent proteins using confocal microscopy – preceding pages

a) *Nicotiana tabacum* petiole expressing *pSEO2*.HDEL:GFP imaged in a polymerized block of LR. Scale 600 μm. b) An embedded petiole expressing *pSEO2*.HDEL:GFP imaged with a 63× water-dipping lens. The SER is clearly visible at this magnification. Cell walls (blue) were highlighted with calcofluor white, which was added directly to the block face. Scale 40

μm. c) A region of the phloem at higher magnification. SEs (se) show conspicuous labelling of the SER, while CCs (cc) show background autofluorescence. Scale10 μm. (d–f) Imaging of an Arabidopsis line expressing a viral movement protein fused to GFP. GFP signal is evident from PD (arrow) in mesophyll cells of the leaf. Cell walls were counterstained *en bloc* with propidium iodide (red). The block was optically sectioned and images captured at the block surface (0 μm; E), at –32 μm (F), and at –42 μm (f) below the block surface. Note that GFP fluorescence from PD is apparent to a depth greater than the penetration of the propidium iodide stain. Scale 50 μm. g), *En bloc* imaging of SEOR1 protein (arrows; Froelich et al., 2011) tagged with YFP in the phloem of the midvein of an Arabidopsis leaf. Scale 25 μm. From Bell et al., 2013.

Figure 4.3.6 shows images from a range of different materials embedded in LR. In (b) a petiole in cross-section displaying the ER-GFP expressed from the ST-specific promoter *pSEO2* (Knoblauch and Peters, 2010) is depicted. With a x5 lens, general phloem fluorescence is apparent. The block was then counterstained with 10ug/mL calcofluor white (Bell et al., 2013), highlighting the cellulose in the cell walls (c). The dye penetrated readily from the trimmed surface following an incubation period of only 20 minutes. The ease with which dyes penetrate the block is most likely explained by the hydrophilic properties of the resin (Hawes, 1994), as well the nature of polymerization. As discussed earlier, LR polymerises following free-radical chain polymerization. This is a specific reaction that occurs between the free radical and the acrylic monomer, and one that shows no affinity for biological material. Without this incorporation the cutting tends to follow the natural interfaces between resin and proteins thereby exposing the cellular material (Keene et al., 2008). A higher magnification image of the counterstained *pSEO2*.HDEL:GFP block (c) shows conspicuous labelling of the SER whilst the CC show faint autofluorescence.

Propidium iodide (PI) was also used as a counterstain to highlight the walls *en bloc* (d-f). In this instance, the material was an *Arabidopsis thaliana*

transgenic line that had been modified to express the movement protein of *potato leaf roll virus* fused to GFP (MP17-GFP, Vogel et al., 2007). This transgene highlights the central cavity of PD and so produces a punctate fluorescence at cell peripheries, as seen in material also expressing TMV.MP:GFP (figure 4.3.1). Using optical sectioning it was established that PI labelled the cell walls to a depth of more than 30 µm (d) into the tissue. Further imaging revealed that even though the PI had failed to penetrate significantly it was possible to image PD in leaf mesophyll cells to a depth of more than 40 µm (f).

SEs in Arabidopsis are extremely small (Mullendore et al., 2010) making SE substructures difficult to detect in semi-thin sections. Using an Arabidopsis line expressing YFP fused to the sieve element occlusion related (SEOR1) protein (Froelich et al., 2011) it was possible to image P-protein bodies within individual SE *en bloc* from the midvein of an Arabidopsis leaf (g).

4.3.3.2 TEM imaging

Silver-grey (60 nm) ultrathin sections of GFP-expressing blocks were cut using a diamond knife and mounted on copper grids prior to staining with the standard contrast reagents (uranyl acetate and Reynolds lead citrate, see materials and methods).

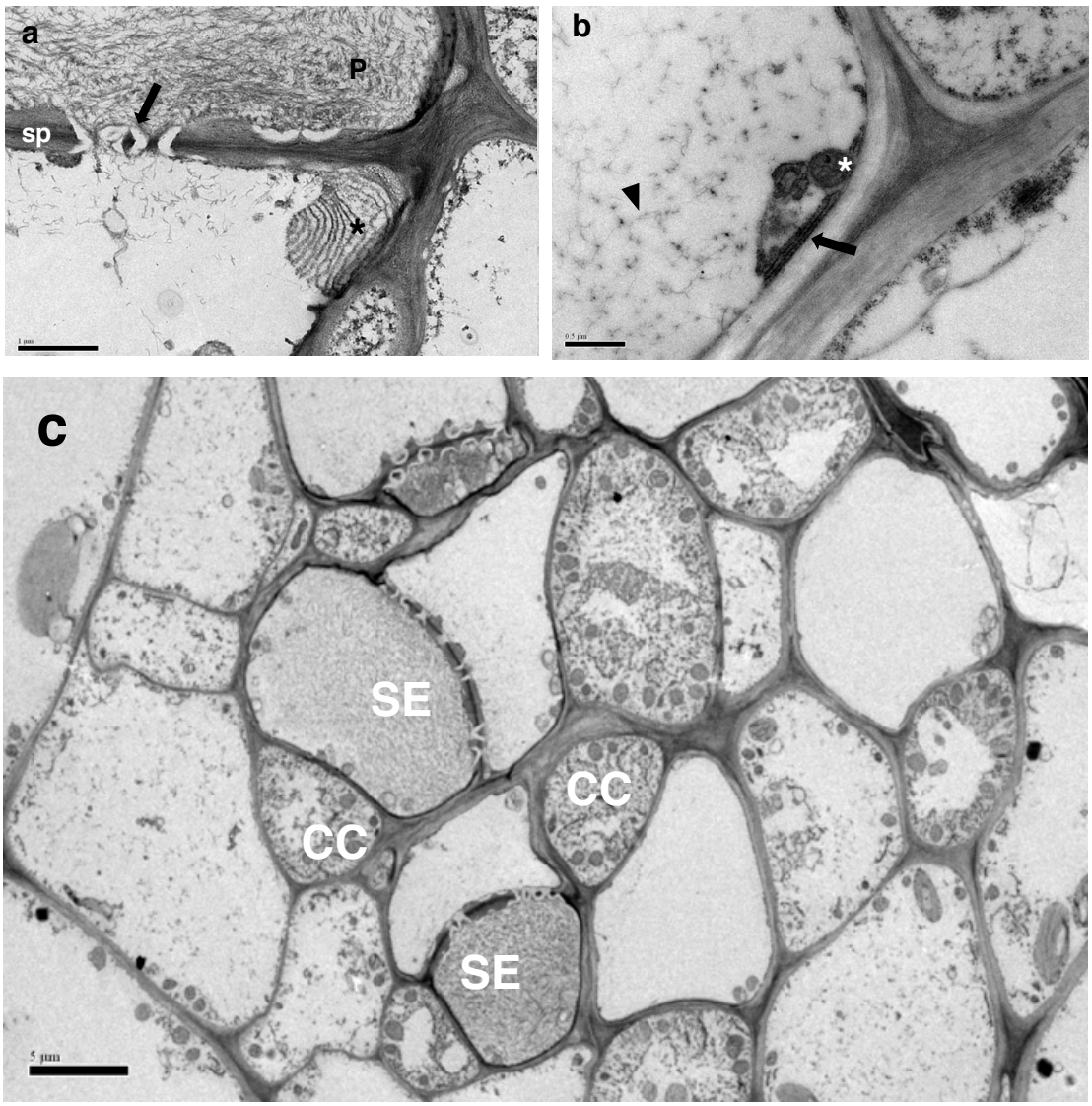

Figure 4.3.7 TEM of London Resin embedded vascular material

a) Sieve plate (sp) with callose collars (arrow resolved. P-protein filaments (P) throughout cytoplasm of upper most SE. Glancing section of SER apparent (*). Membrane preservation and contrast are good despite no osmication. Scale 1 μm b) Mitochondria (*) amidst parietal SER stack (arrow). P-protein dispersed throughout the cytoplasm (arrowhead) is evident. Scale 0.5 μm c) Transverse section of vasculature showing SE and CC Scale 5 μm.

Figure 4.3.7 shows that the phloem showed good structural preservation, despite the lack of osmication. This is probably because LR is less lipophilic than epoxy resins and so consequently less likely to disturb cell ultrastructure when an osmication step is omitted (Hawes, 1994). The membranes are well

preserved as are the mitochondria and plastids. The sections were very stable in the beam and withstood repeated imaging sessions over the course of several months.

4.3.3.3 Correlative light and electron microscopy

Having established that LR embedding was compatible with fluorescence retention and ultrastructure preservation, the ultimate test of this method was to examine the same sections sequentially by light and EM. Following observation of the block face in the confocal microscope, semi-thin (0.5 μm) for light microscopy and subsequently silver-grey sections (approximately 60 nm) were cut. Prior to heavy-metal staining several attempts were made to image the thin sections in the confocal microscope. Unfortunately, it was not possible to detect a GFP signal in such thin material (see figure 4.3.8; see also Keene et al., 2008).

Figure 4.3.8 – legend on next page.

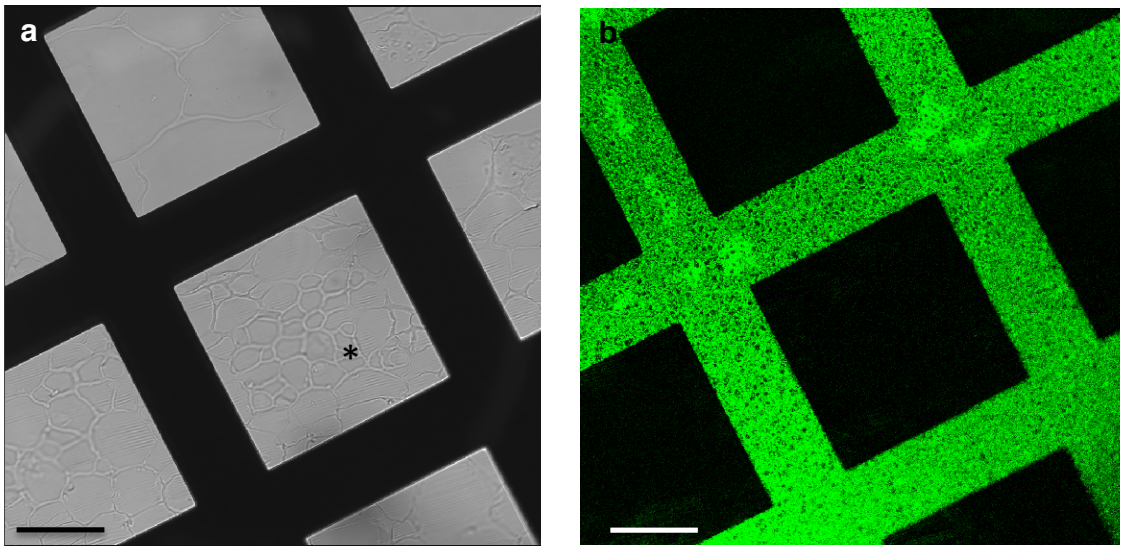

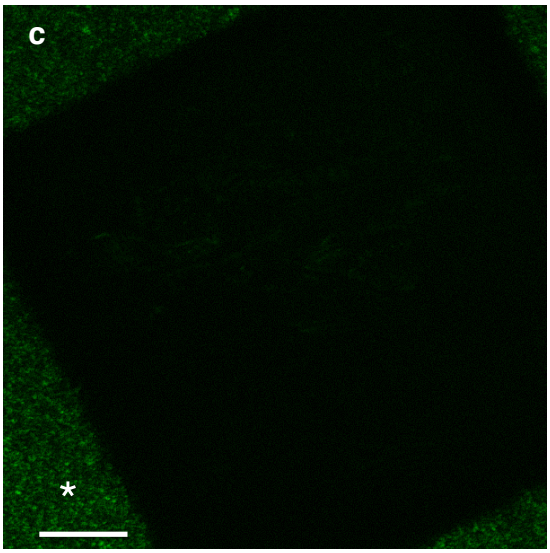

Figure 4.3.8 No GFP fluorescence in silver-grey sections of *pSEO*.HDEL:GFP expressing vasculature- see previous pages

a) Silver-grey (60 nm) section, taken from *Nicotiana tabacum* expressing *pSEO2*.HDEL:GFP (Knoblauch and Peters, 2010), mounted on a grid - apparent as black hatching in image. Bright-field image allows the section orientation and its position within the tissue to be checked. Vascular cells are evident (*). Scale 20 μm. b) Same section imaged with a 488nm laser to excite GFP. The copper grid generated autofluorescence. No GFP signal is detected in tissue. Scale 20 μm c) Same tissue imaged at a higher magnification (x63 lens). Still only faint non-specific fluorescence is apparent from the tissue. Autofluorescence from grid is marked with * Scale 5 μm

As SER distribution is consistent through the SE, it was possible to identify the SE in ultrathin sections. However, there was insufficient GFP signal for detection with the CSLM. Whilst not suitable for imaging the same cells in the same section, it was hoped that if the same cells could be identified in the block face, semi-thin and ultrathin could be correlated indirectly.

Several phloem bundles were imaged using the TEM and the same cells identified in the block face using the confocal microscope (Fig. 4.3.9 a and b). In c, note that in addition to the fluorescent SER, small vacuoles in the cytoplasm of parenchyma cells can be seen in both the TEM and confocal

images. In a number of sections, it was possible to identify fluorescent parietal SER aggregates (d) that could also be detected in ultrathin sections with the TEM (e, f).

Figure 4.3.9 – legend on page 93

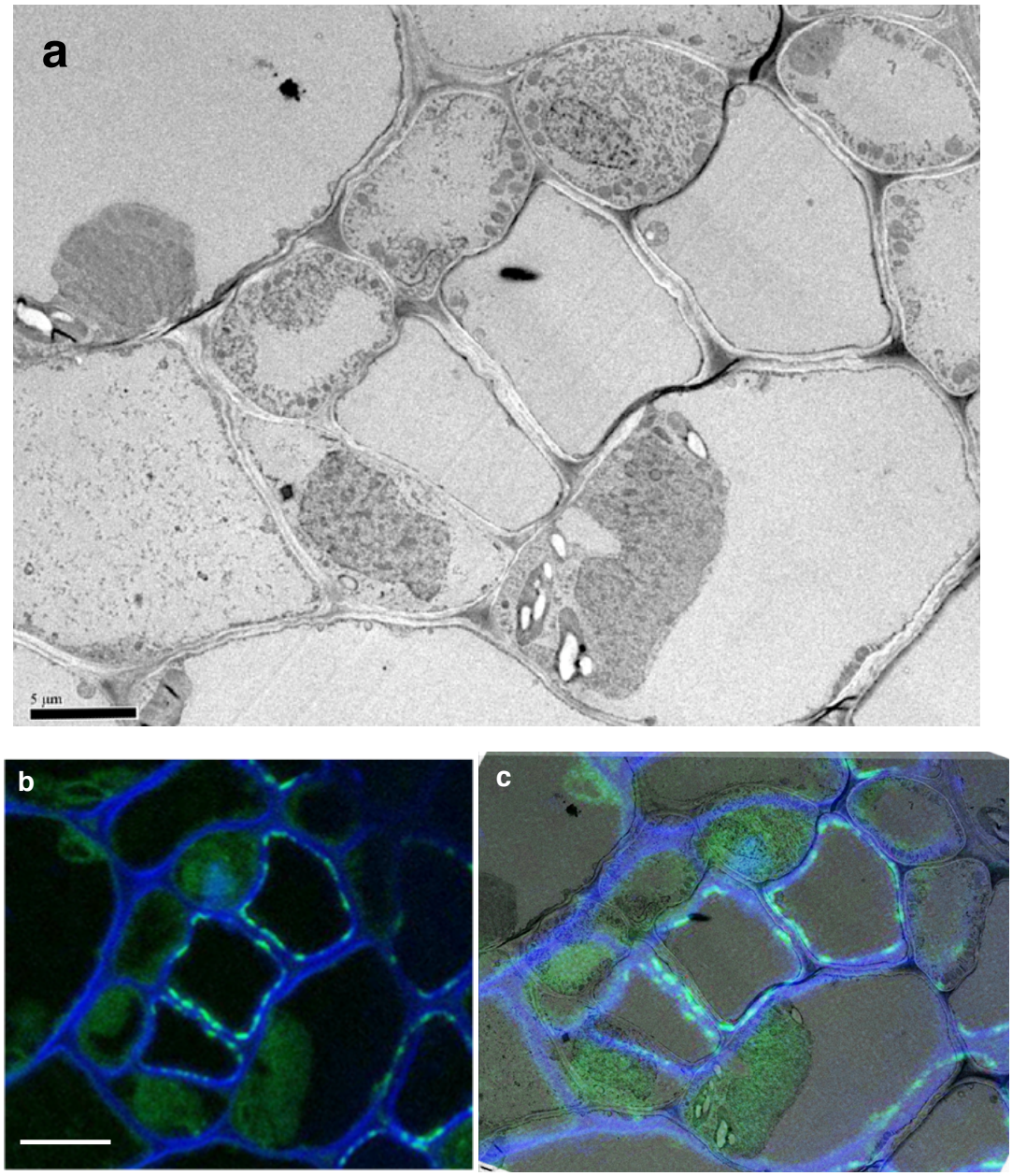

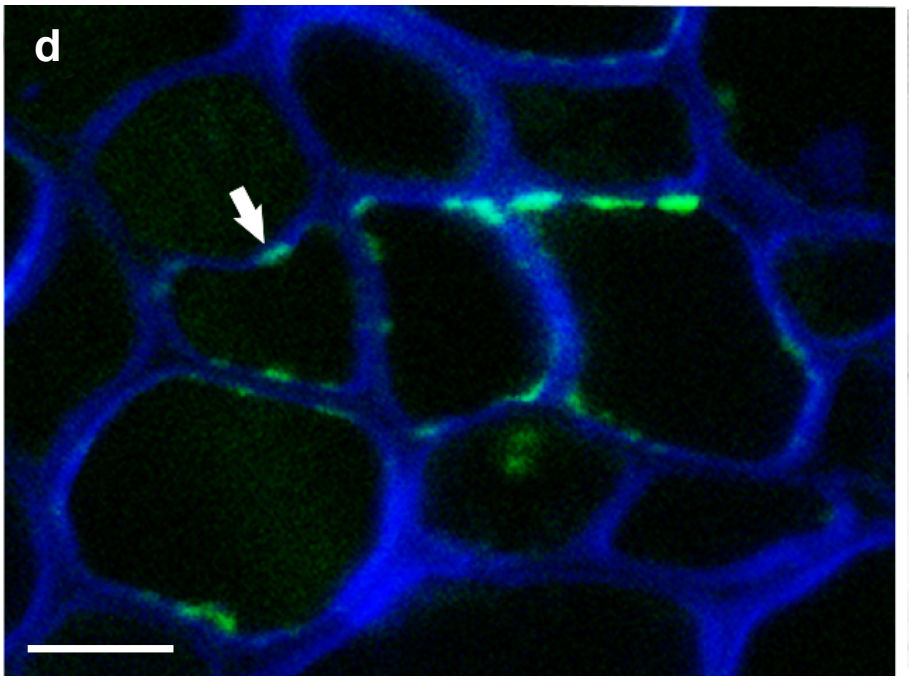
d

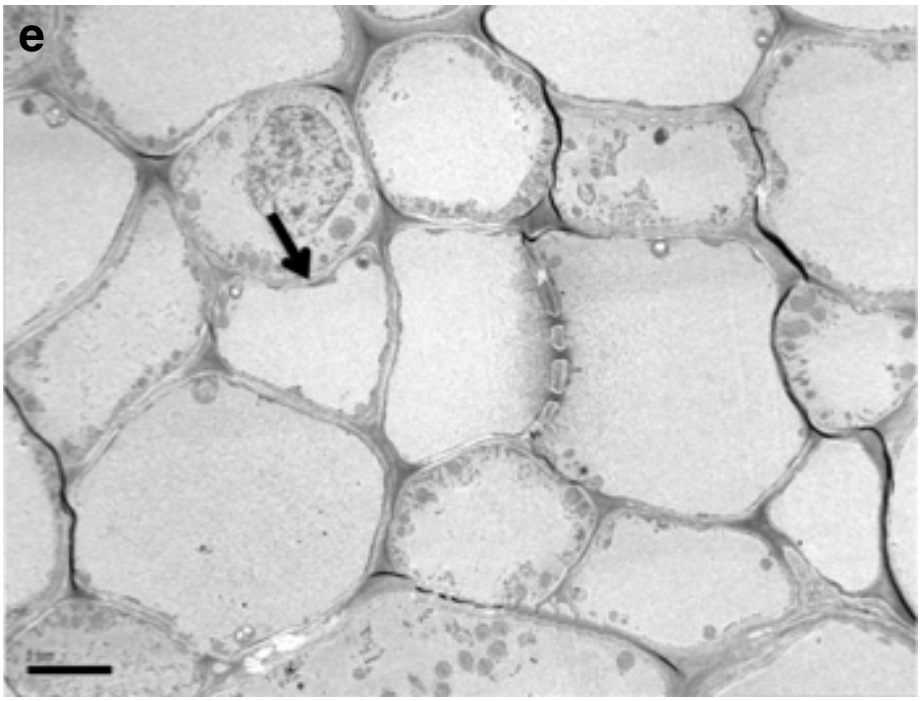
e

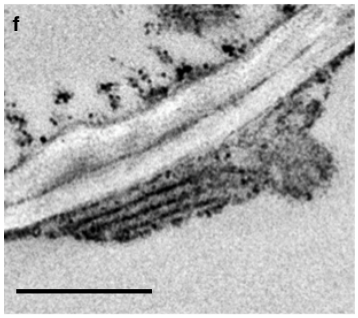

Figure 4.3.9 Correlative light and electron microscopy (CLEM) of *pSEO2*.HDEL:GFP – see previous pages. a) TEM image of an ultrathin section of petiole from *Nicotiana tabacum* expressing *pSEO2*.HDEL:GFP (Knoblauch and Peters, 2010) . The section was post-stained with uranyl acetate and lead citrate. Scale 5 µm b). A semi-thin section acquired immediately after the TEM section, imaged with the confocal microscope, showing the same field of view. Note that small vacuoles in the cytoplasm can be seen in both the TEM and confocal images. Scale = 5 µm c) Overlay image of a and b showing alignment of SE in the confocal and TEM images. d). A Semi-thin section of the phloem imaged in the confocal microscope shows conspicuous SER stacks (arrow). Scale = 10 µm e). The TEM image of the same field of view. The same SER stack arrowed in d is apparent in e (arrow). Scale = 5 µm f) An enlarged image of the SER stack arrowed in e Scale = 1µm Reproduced from Bell et al., 2013.

4.3.3.4 Correlative 3D-SIM, CSLM and TEM

Most super-resolution imaging approaches require that the cells of interest lie close to the coverslip to maximise spatial resolution (Huang, et al., 2009; Bell and Oparka, 2011). The retention of GFP in semi-thin sections meets these requirements to allow super-resolution imaging. After confocal imaging of the block face, ultrathin sections were cut, followed immediately by a semi-thin section from the same region of the block. 3D-SIM images of SP pores revealed spatial information not present under the confocal microscope or the TEM. For example, figure 4.3.10 (a-d) shows SP imaged sequentially by CLSM, 3D-SIM and TEM. Note that each method reveals different information on the structure of the SP.

Figure 4.3.10 – legend on page 96

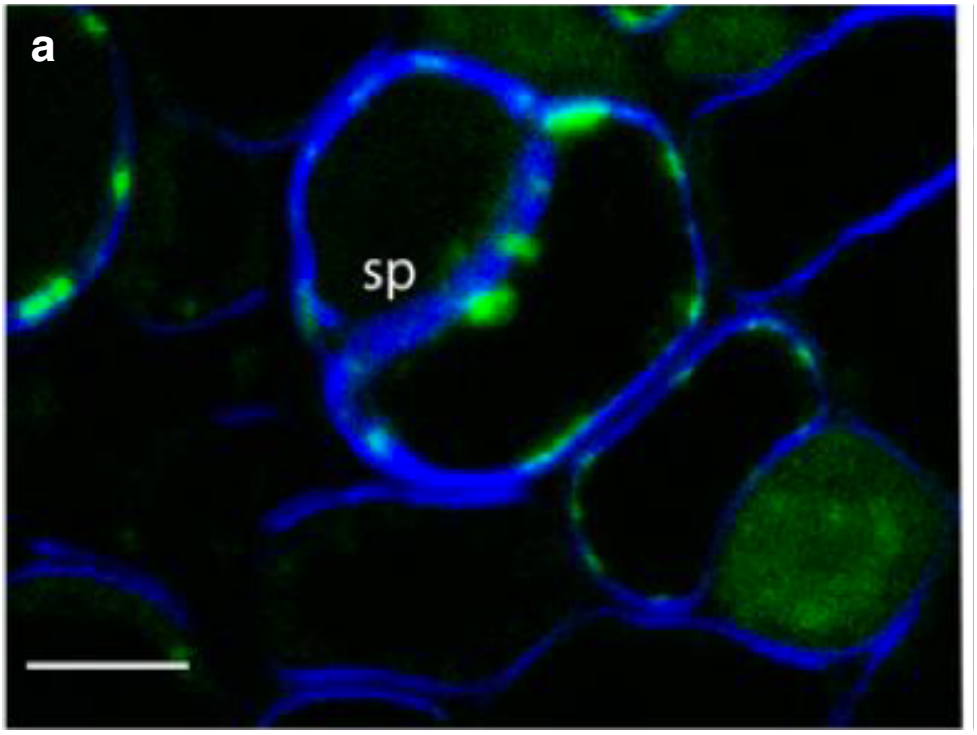

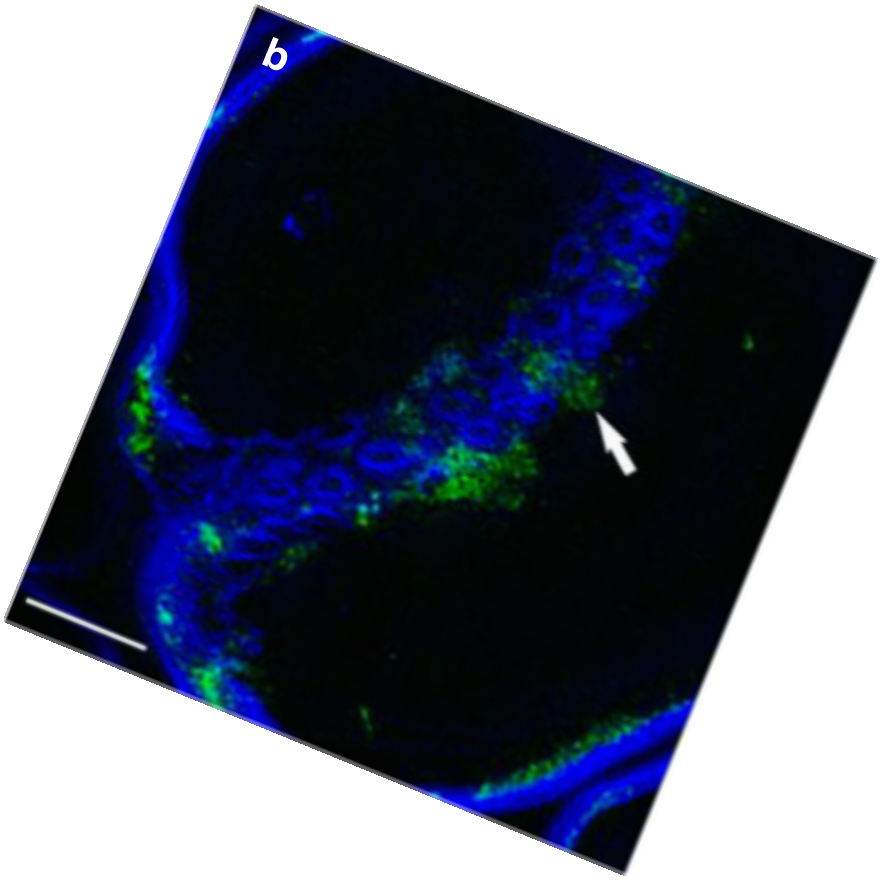

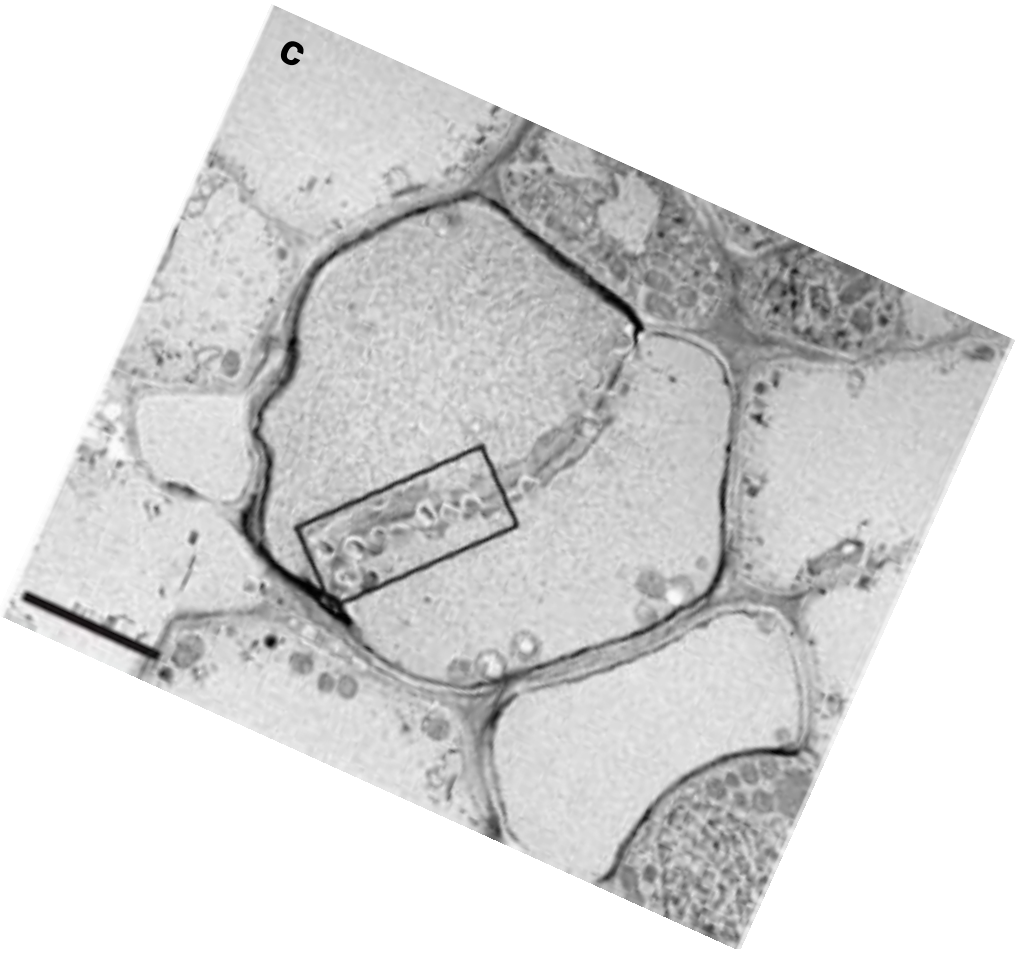
c

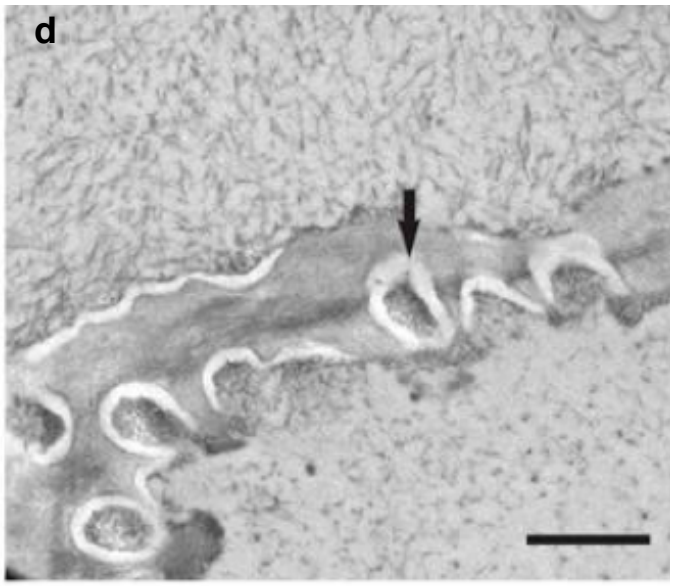
d

Figure 4.3.10 Correlative 3D-SIM, confocal microscopy, and TEM of the phloem
a) A semi-thin section of the phloem from a *Nicotiana tabacum* petiole expressing *pSEO2*.HDEL:GFP (Knoblauch and Peters, 2010) counterstained with calcofluor white to highlight cell walls and a SP. The SP and SER are visible but not resolved. Scale 5μm. b) A 3D-SIM image of the same SP was taken using the section shown in a. The 3D-SIM image was reconstructed from 20 serial Z-sections and, unlike the confocal image, resolves distinct cellulose collars around the SP pores. The SER is visible at the SP (arrow). Scale 1 μm. c) The TEM image of the same field reveals details of the SP and resolves SP pores. Scale 5 μm. d) Enlargement of the SP region boxed in c, revealing callose collars (arrow) around the pores. Scale 1μm. Figure reproduced from Bell et al., 2013.

With the CLSM, SP and the SER associated with them could be detected but not resolved (a). In the 3D-SIM image, which is a projection of sequential Z-sections taken every 125 nm, it was possible to reconstruct portions of the SP within the thickness of the section (b). In the thin-section TEM image, SP pores and their callose collars could be resolved but only partial pore transects were encountered due to the section thickness (c). The fixation protocol preserved the fine structure of the SER, which in glancing sections of SP appeared as a fine mesh of interconnected tubules (d). Using 3D-SIM imaging, similar fine tubules of fluorescent SER associated with SP could be detected (b). These correlative imaging approaches reveal that the three forms of microscopy adopted here (CLSM, 3D-SIM and TEM) are complementary, each revealing important information on subcellular structure.

4.3.3.5 Immunofluorescence

LR is known to be compatible with immunofluorescence (Luby-Phelps et al., 2003; Keene et al., 2008) so the next step was to assess the antigenicity of the embedded fluorescent samples by cutting 1-2 μm sections from the blocks and labelling these with an antibody against callose. Callose is a cell-wall constituent found at SP and at PPUs (Fitzgibbon et al., 2010). Using CLSM, callose was readily detected at the lateral sieve areas (highlighted by

Alexa 594 secondary antibody; false coloured red) along with the SER (HDEL:GFP; Fig. 4.3.11 a). Panel b is a 3D-SIM image of a SP in transverse orientation. The SP callose was immunolabeled and the cellulose highlighted using calcofluor white. The inset is an enlarged view of two of the pores and shows that the cellulose collars form outside the callose pore linings. Figure c shows a confocal image of an immunolabeled ST in longitudinal orientation. 3D-SIM was used to image the same ST following staining with calcofluor white (Fig d). This revealed the arrangements of the SER, callose and cellulose, respectively, on the SP (d i-iv).

Figure 4.3.11 – legend on page 98

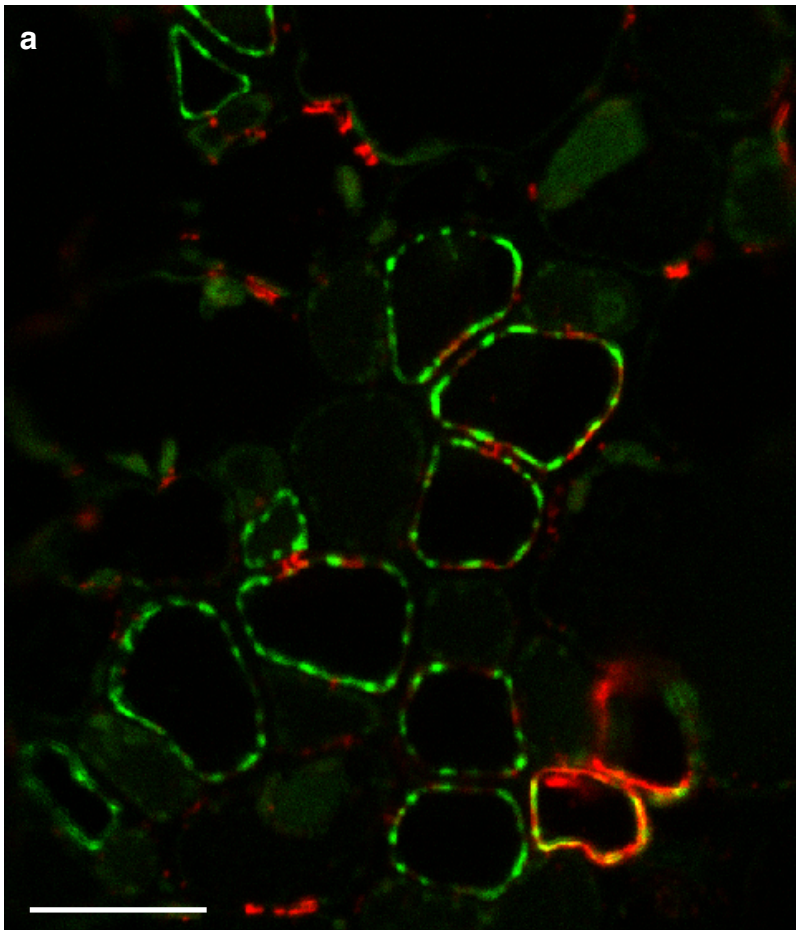

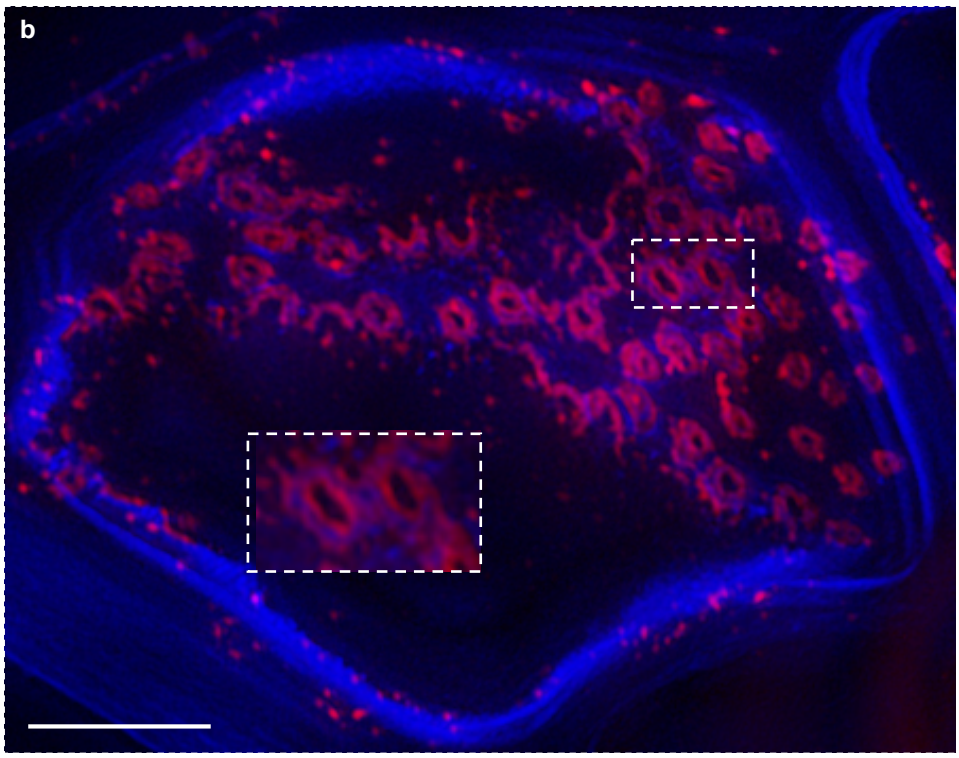

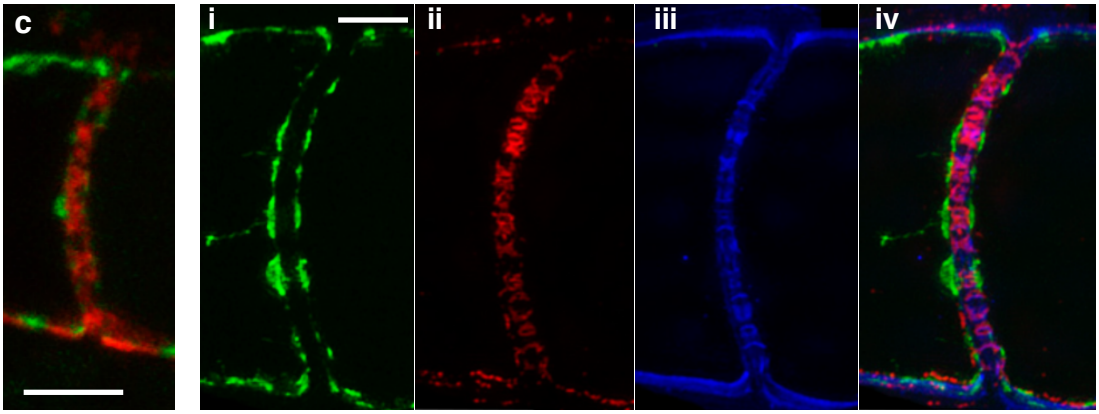

Figure 4.3.11 Immunodetection of callose in semi-thin sections of London resin-embedded material

a) SER stacks (*pSEO2*.HDEL:GFP) are seen in tranverse sections of SE. Alexa 594-conjugated secondary antibody reveals callose at the sites of lateral sieve areas (red; arrow). Scale 25μm.b) 3D-SIM image of a SP in transverse orientation. The SP callose was labelled with an anti-callose antibody and visualized using an Alexa 594 secondary antibody (red). The inset is an enlarged view of two of the pores and shows that the cellulose collars form outside the callose pore linings. Scale 2μm c) Confocal image of a SE in longitudinal orientation. Callose labeling appears at the SP as well as the lateral areas. Scale 10μm. d)

3D-SIM image of the same SP shown in c. The arrangements of the SER, callose, and cellulose are revealed. SER is shown in green (*pSEO2*.HDEL:GFP; i), callose in red (anti-callose antibody and Alexa 594 secondary; ii), cellulose in blue (calcofluor; iii). The merge of all three channels is shown (iv). Scale 5μm. Figure reproduced from Bell et al., 2013.

4.3.3.6 Osmication

Watanabe et al., (2011) found that by adding a small amount (0.001%) of osmium tetroxide they could further enhance membrane morphology in EM images. Osmium tetroxide is an oxidizer and so would not have been thought to be directly compatible with maintaining GFP fluorescence, which is known to be labile when exposed to oxidative stress (Chalfie et al., 1994). Used at 1% normally, when processing for TEM (Hayat, 1973), this much lower concentration presumably exerts a concomitantly lower oxidative stress whilst still stabilizing lipids and generating contrast. To see if a similar improvement could be achieved whilst still maintaining fluorescence and antigenicity, a one-hour incubation in 0.001% osmium tetroxide was performed after primary fixation with aldehydes and prior to dehydration and processing as before.

Figure 4.3.12 – legend on page 102.

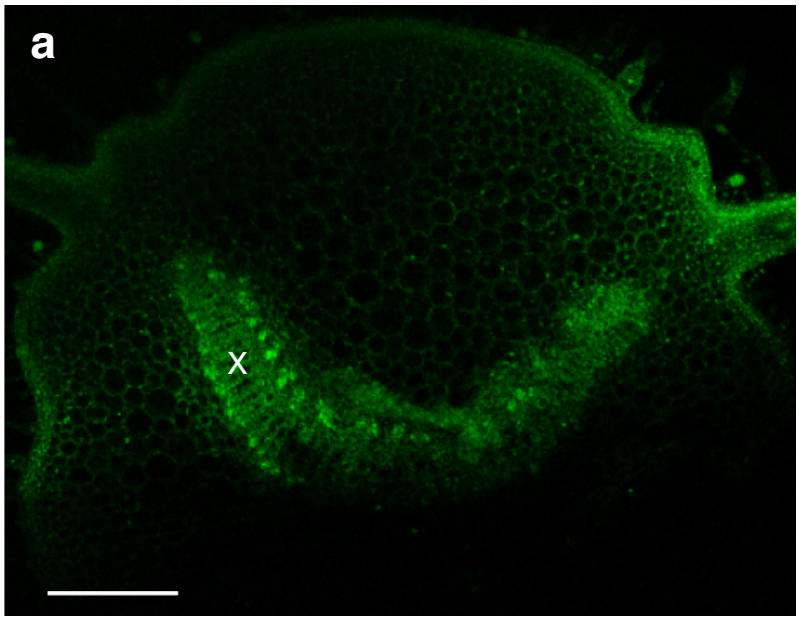

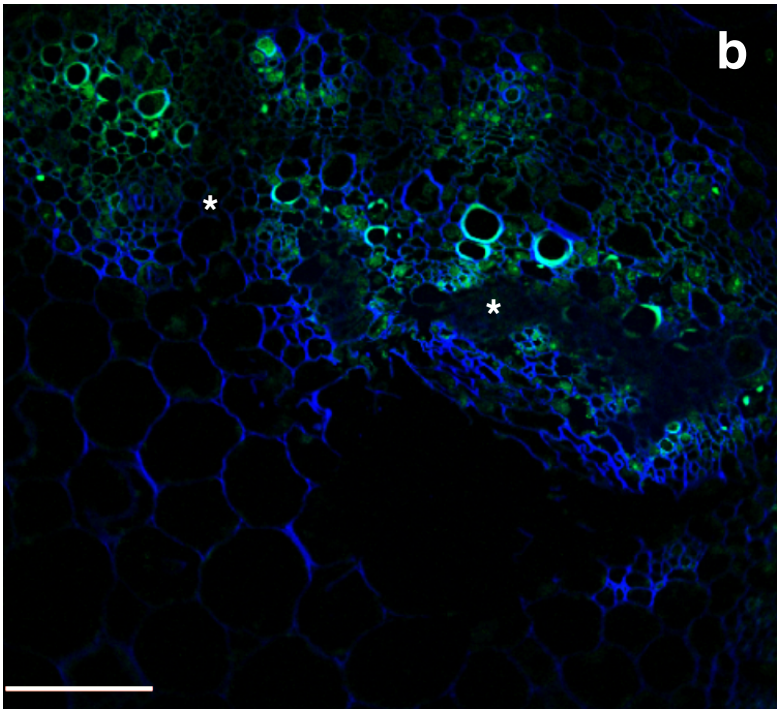
b
*
*

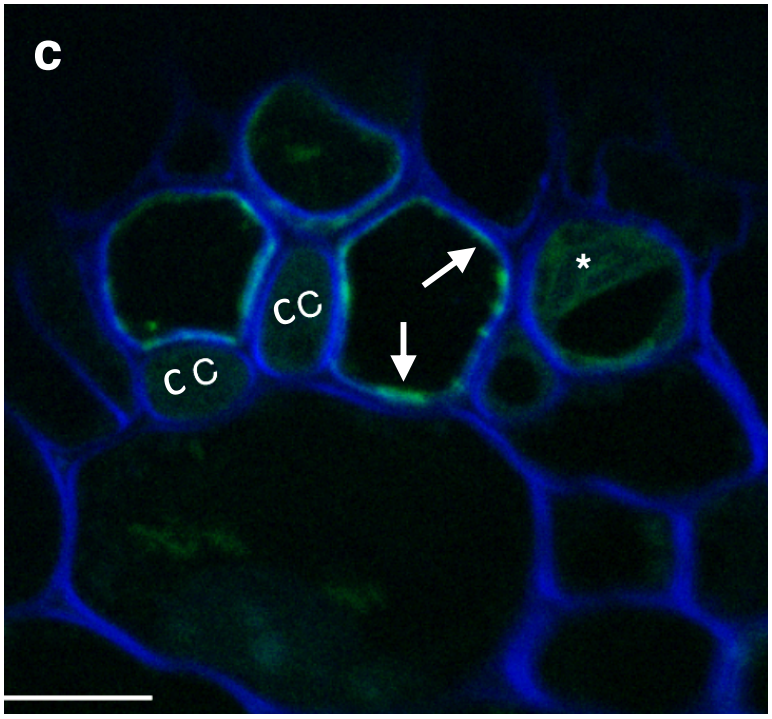
c
CC
CC
*

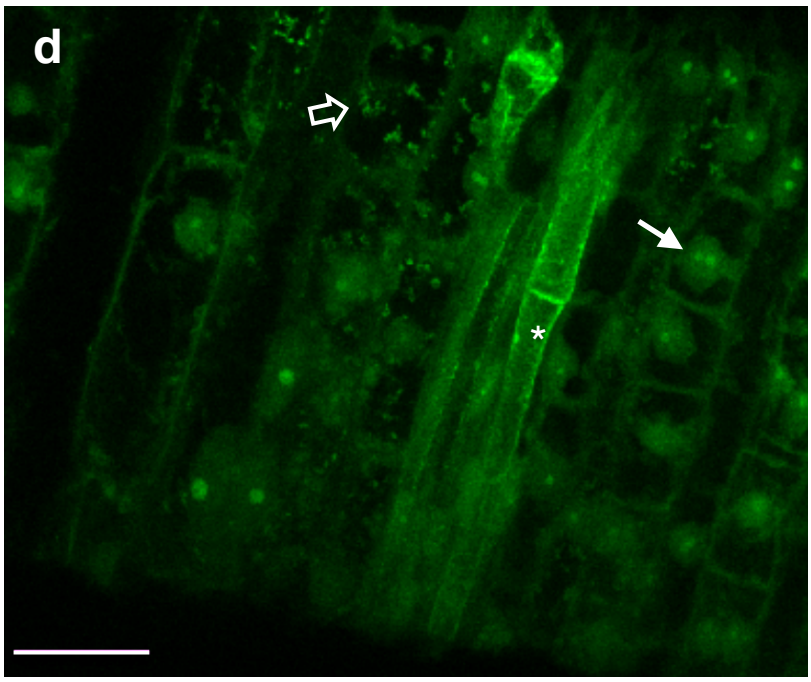
d
*

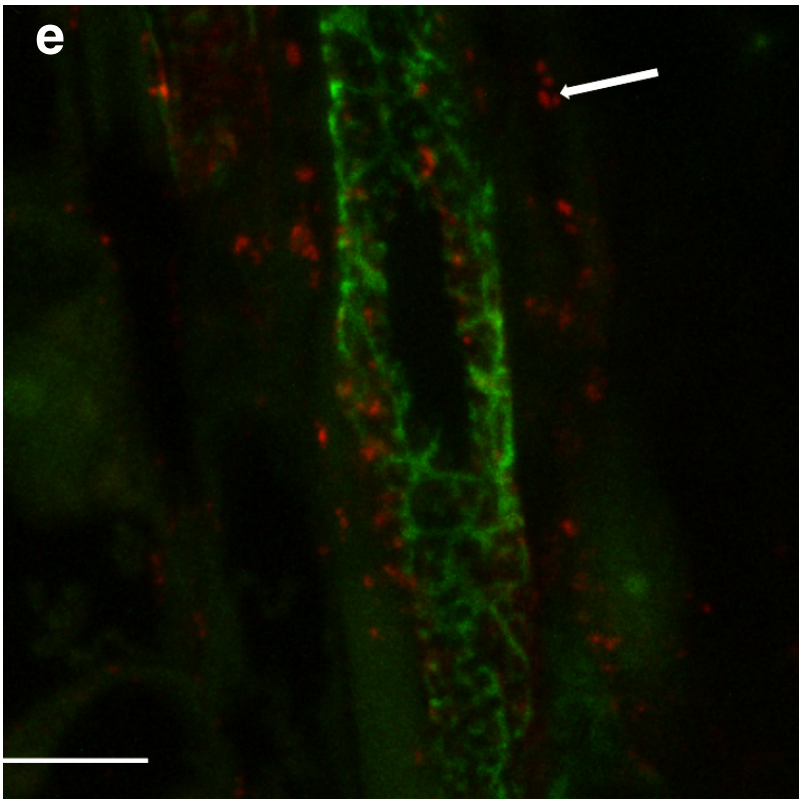
e

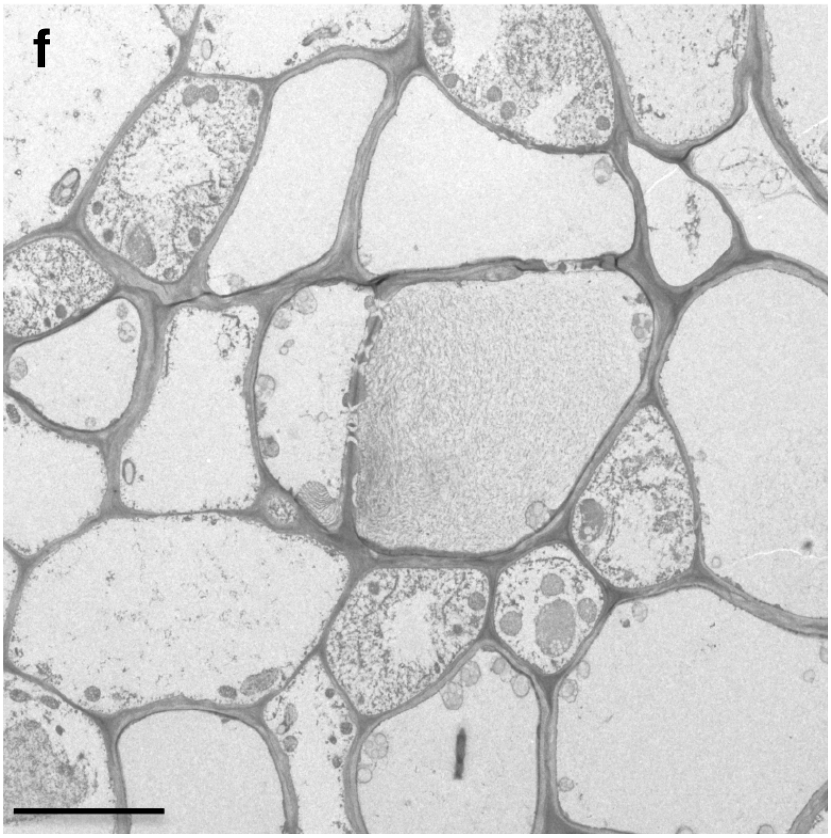

Figure 4.3.12 Incorporation of 0.001% osmium tetroxide is compatible with GFP fluorescence, and antigenicity

a) Block face of embedded *Nicotiana tobaccum* petiole expressing *pSEO2*.HDEL:GFP, shown in green (Knoblauch and Peters, 2010). At this magnification the general level of autofluorescence and the fluorescent signal is broadly the same as for non-osmified tissue – see Figure 4.3.5 d for comparison. Scale 600 μm. b) Semi-thin sections were stained with calcofluor to highlight cellose at the cell walls, shown in blue. The sections were brittle making it very difficult to tease out kinks produced when mounting on a slide. These are apparent as dark areas in the image (*). Information within these areas are lost. Scale 200 μm. c) SER is stacked and parietal. CC cytoplasm has an autofluorescent background (*). Scale 10 μm. d) A longitudinal section highlights the background autofluorescence in the surrounding tissues, apparent here in the nucleus and cytoplasm (closed and open arrow respectively). Scale 50 μm. e) Anti-callose antibody highlights callose (arrow) at PPUs, showing that its antigenicity is retained following incorporating osmium tetroxide. Scale 10 μm. f) Transmission electron micrograph showing a field of vascular cells (sieve tube, ST).

Lipid and membrane preservation is as good as for non-osmicated tissues (see Figure 4.3.7 c for comparison). Scale 5 μm.

Figure 4.3.12 shows that the incorporation of 0.001% osmium tetroxide is compatible with GFP fluorescence and antigenicity. Figure (a) shows that GFP fluorescence in the block face was essentially as with non-osmicated tissue (see figure 4.3.5 d for comparison). Figure 4.3.12 b shows that the section absorbed calcofluor, highlighting cellulose. However, the section was brittle so it was not possible to straighten out section folds, leaving these areas dark. Thus, information within these dark areas was lost. A closer view showed that the SER was stacked and parietal as expected. A longitudinal section (d) revealed high cytoplasmic autofluorescence. The tissue retained antigenicity and the anti-callose antibody highlighted the callose at PPUs (e). Note also that the delicate reticulate SER network was preserved. The increased background and problems with specimen handling (due to its brittle nature) would only be tolerated if the images captured in the TEM were significantly better than those found previously without osmication (see figure 4.3.7). The appearance of the field of cells in panel (f) is broadly similar to that imaged before (figure 4.3.9 a, e and f), so the secondary fixation with osmium tetroxide did not enhance the results delivered with the primary glutaraldehyde fixation alone. LR is less lipophilic than other resins and so less likely to disturb cell ultrastructure when osmication is omitted (Hawes, 1994). Watanabe et al., (2011) used a methacrylate resin for their embedding which perhaps is more disruptive to membranes, and osmication could potentially ameliorate this.

4.4 Summary and future directions

As discussed previously, the phloem is a tissue recalcitrant to conventional study. Regardless, microscopic investigations have proved vital in understanding the phloem. Whereas EM investigations have provided a structural context (Esau., 1969), light microscopy imaging has revealed much about movement into, through, and out from the phloem (Wright et al., 1996; Haupt et al., 2001). Super-resolution imaging has resolved the conformation of viral movement proteins in the phloem (Fitzgibbon et al., 2010), as well as the arrangement of the SER in ST (4.3.11 C; Bell et al., 2013).

By employing a CLEM imaging approach, it was possible to detect fluorescently labelled proteins in whole cells before sectioning, and after sectioning by probing for associated antigens. By developing a unified sample preparation method, a diversity of imaging approaches were brought to bear upon a single sample (illustrated in figure 4.3.13). This should be of great utility to researchers interested in studying plant cell biology.

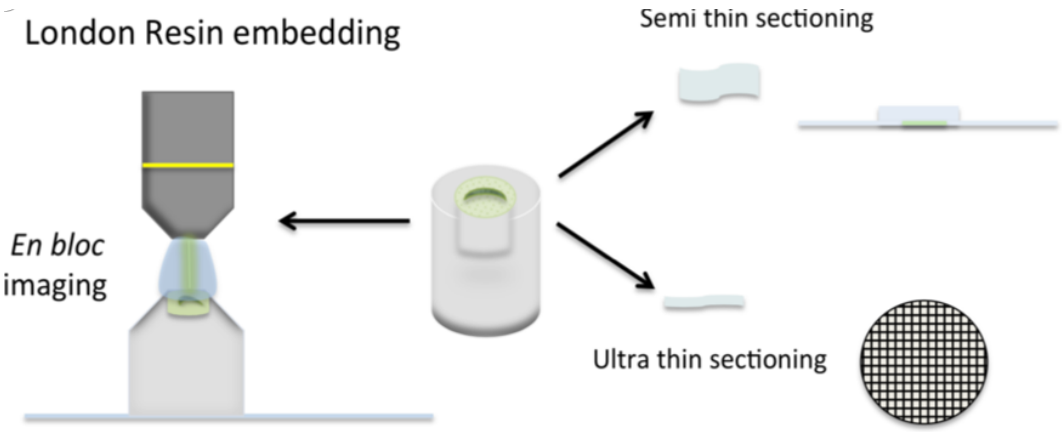

Figure 4.3.13 London Resin embedding

The embedded sample can be viewed *en bloc* or be sectioned further for fluorescence, immunofluorescence or 3D-SIM imaging (semi-thin sections) or ultrastructural analysis (ultra thin sectioning). This sample preparation method allows a direct comparison of these imaging technologies. Adapted from Bell and Oparka 2015.

5. A Survey of the Sieve Element Parietal Layer

5.1 Introduction

All land plants have a syncytial distribution network and a protoplasm that is arranged to maximise flow (Schulz, 1998). These conserved features indicate a common solution to distribute nutrients and signals along the plant body. The functions lost in the 'streamlining' of the SE are mitigated by the activities of the ontogenetically related sister CC (reviewed in White, 2013). This SE-CC complex is very stable and can persist for up to one hundred years in palms (Parthasarathy, 1974). The SE maturation process was established following the advent of the EM (Evert, 1990; *see* Introduction). Despite many of the vital aspects having been established, the cell biology of the SE is still subject to intense investigation (Froelich et al., 2011; Knoblauch et al., 2018; Furuta et al., 2014), with some authors continuing to challenge the basic fundamentals of its structure (Hafke et al., 2013). Using the novel approaches described in previous chapters, in combination with others, a new survey of the SE parietal layer is presented here.

5.2 Aims

5.2.1 To use zinc iodide osmium to highlight the SER and desmotubule in PPUs

5.2.2 To use FRAP to investigate lumenal transport in the SER

5.2.3 Use the xylem to deliver organelle-specific dyes to the SE

5.2.4 To examine the possibility that an actin cytoskeleton persists in the mature SE

5.3 Results and discussion

5.3.1 The SER

The smooth ER present in the differentiated SE is regarded as a functionally unique form (Sjolund, 1997). Reflecting this specificity, it is called the sieve element reticulum (SER; a term first used by Srivastava and O'Brien, 1966). Although its functional role is uncertain, biochemical evidence suggests that it sequesters calcium (Sjolund 1990), in general agreement with ER in animals and yeast (Rowland and Voeltz, 2012). A distinctive feature is that it emerges from the autolytic purge without an underlying actin cytoskeleton, although this has been challenged recently (Hafke et al., 2013). The ER is a dynamic and pleomorphic organelle (Hawes et al., 2015), and actin is understood to generate force and membrane movement (Gurel et al., 2014). In the absence of actin, it is interesting to consider what features of the SER remain in common with the ER in parenchyma cells. Freeze-fracture studies of *Streptanthus* estimated that the SER occupied nearly 100% of the total surface area of the SE (Sjolund, 1990). The SER is by far the most abundant organelle in the SE and, although arranged parietally, frictional interactions between it and mobile SE cargos will be considerable (Mullendore et al., 2010). It can therefore be assumed that the SER performs an essential role in the mature SE.

Zinc Iodide Osmium staining

Of all the imaging approaches used in this thesis (confocal, 3D-SIM and PALM, TEM) the latter has the resolving power to generate images with the greatest detail. The limitations of TEM have been discussed elsewhere in this thesis, but cognisant of these it has been used to conduct an ultrastructural survey of the SER. Conventionally, osmium tetroxide is used for secondary fixation but it has been observed that aldehyde/ osmium fixation techniques can result in ER membranes exhibiting low contrast (Hawes et al., 1981). Zinc iodide-osmium (ZIO) was used here instead as its reaction products are electron opaque and accumulate in ER cisternae and other double-membraned structures (Hawes, 1994). ZIO impregnation of tissues has been used to label autonomic nerves which were then viewed with the light microscope, and subsequently with the TEM (Pellegrino de Iraldi, 1977). It has been used in plants to selectively stain the cortical ER, Golgi and nuclear membranes, as well as thylakoids within chloroplasts (Barlow, 1984; Harris and Oparka, 1982; Hawes, 1994). However, it has not been used previously to study the arrangement of SER in the SE.

Froelich (2011) discussed the limitations of imaging the phloem with the TEM and how these could be ameliorated. Specifically, they highlighted the issue of pre-fixation artefacts. These are difficult to avoid when studying the phloem as chemical fixatives penetrate tissues slowly (discussed in chapter 3) and by the time they reach the vasculature, cells are likely to show signs of distress. Cutting tissues increases the surface area and, by extension, the speed of fixative delivery but this also has the potential to generate artefacts (Knoblauch and van Bel, 1998). To remedy this, entire plants were plunge frozen and freeze-substitution performed. This took approximately fifteen days to complete (Froelich et al., 2011). The fine structures of the SE and CC were preserved, the high sucrose content of the SE acting as a cryo-protectant. The structure of the surrounding parenchyma, however, was devastated. We previously published super-resolution images of vasculature

that had been fixed following xylem irrigation of fixative (discussed in chapter 3; Fitzgibbon et al., 2010). The ease and effectiveness of this method made it a standard protocol in our laboratory (Bell et al., 2013, Bell and Oparka, 2013, Bell et al., 2018). Whilst super-resolution microscopy produced the highest resolution images of the phloem to date from a light microscope (Fitzgibbon et al., 2010), examining vascular tissues with the TEM following xylem irrigation was also tested. Figure 5.3.1 shows images gathered following xylem-mediated delivery of primary fixative, using ZIO as a secondary fixative. In contrast to the images published by Froelich (Froelich et al., 2011) the phloem cells all showed good structural preservation.

Figure 5.3.1 – legend on page 110.

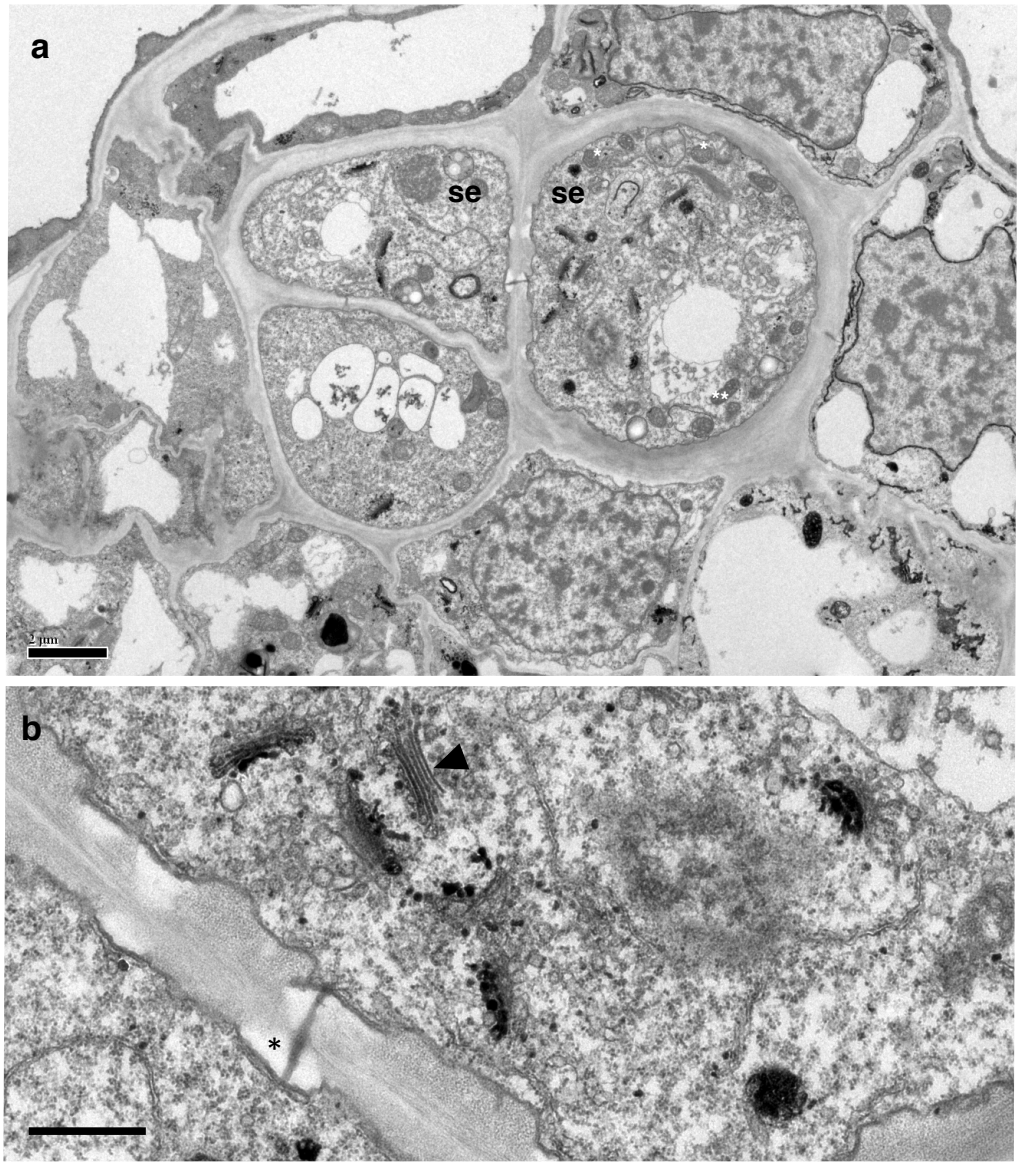

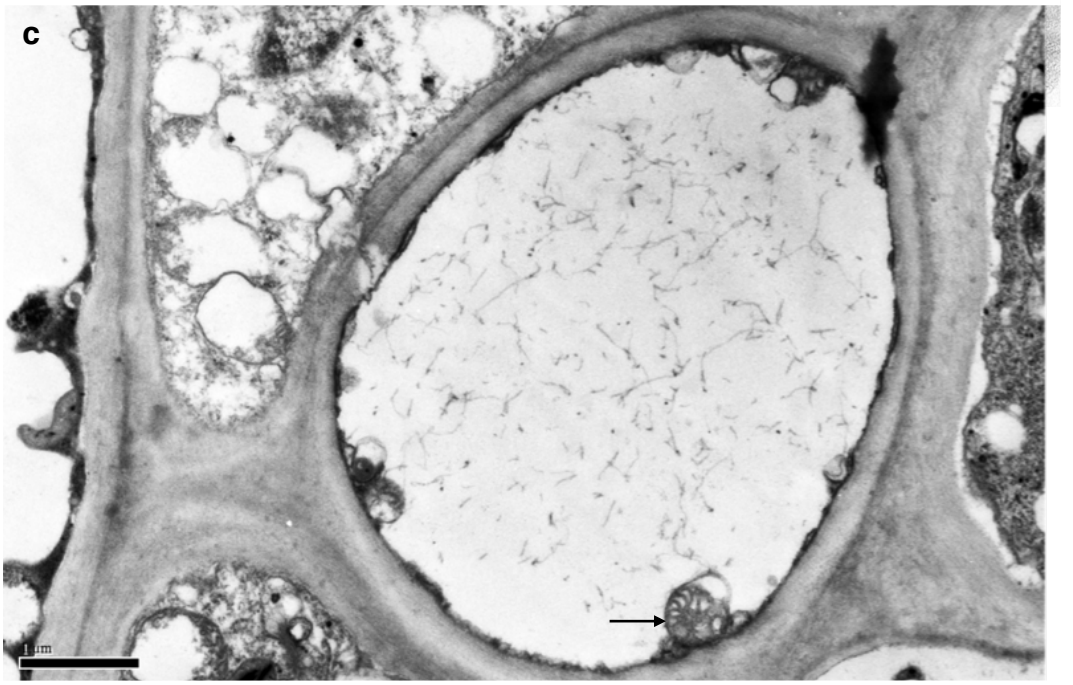
c
1 µm

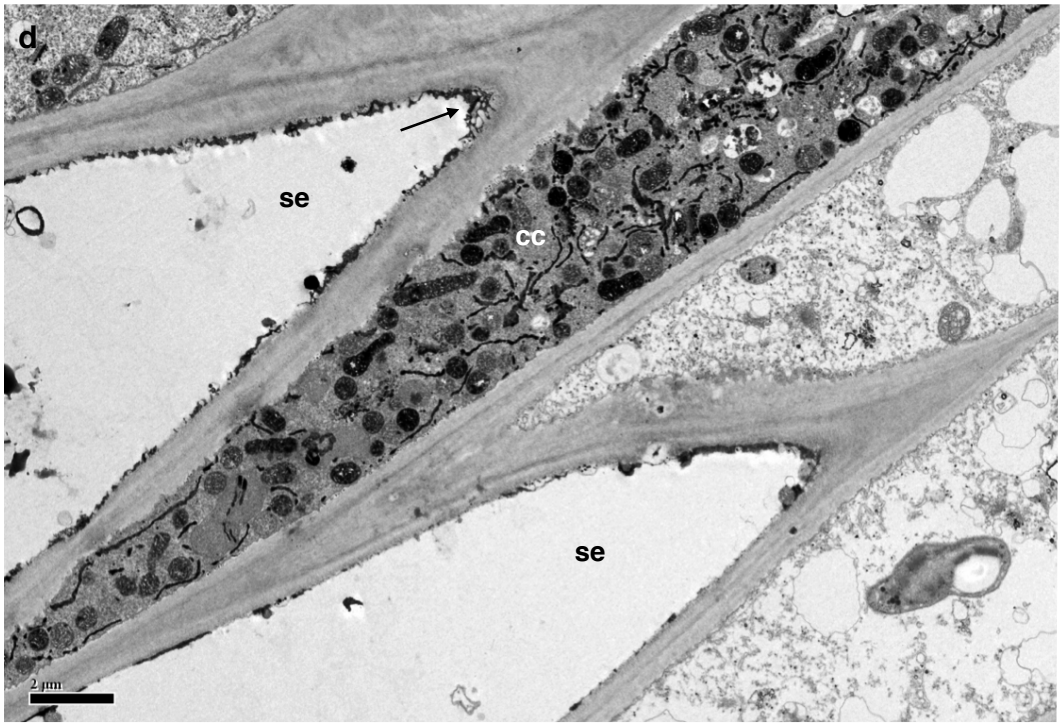
d
se
cc
se
2 µm

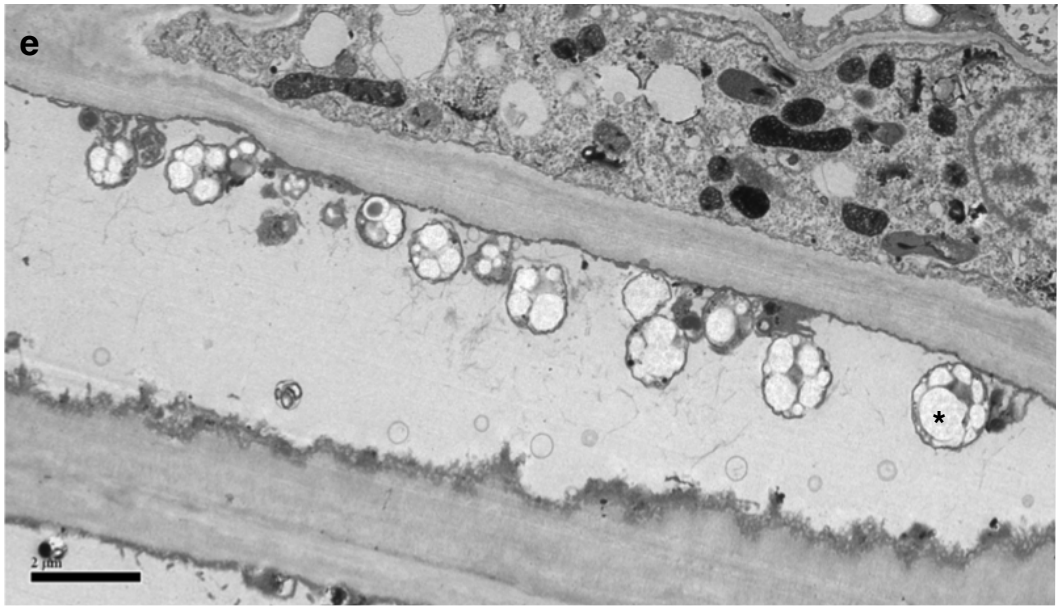

Figure 5.3.1 Xylem irrigation of fixative preserves fine structure in SEs and surrounding parenchyma

a) Transverse section of developing vasculature. Immature SE (se) are apparent due to wall thickening. Some mitochondria are rounded (*), whilst others (**) retain a rod-shape typical of the organelle in an undifferentiated cell. Scale 2 μm. b) Higher magnification image of SE from (a). ZIO has highlighted the Golgi apparatus (arrowhead). Desmotubule of a simple PD with electron lucent callose deposits associated (*). Scale 0.5 μm. c) Transverse cross-section through a mature SE. P-protein is dispersed throughout the lumen. Mitochondria sitting at periphery (arrow). Scale 1 μm. d) Longitudinal section shows contrast between dense lumen of CC and cleared lumen of mature SE where ER is at the periphery (arrow). Scale 2 μm e) Glancing longitudinal section of a differentiated SE with many plastids (e.g. *) Plastids contain starch, visible as electron lucent inclusions. There is no evidence of plastid rupture, nor of the release of free starch granules into SE lumen. Scale 2 μm.

With xylem irrigation the whole petiole is cut to allow fixative to enter the xylem. By disregarding the tissue immediately around the cut site, the TEM images above show that those distant to the entry site show no apparent signs of distress, suggesting that surge artefacts due to pressure release are limited, allowing the fixative to penetrate phloem cells very quickly and

preserve them in a near native state. The immediate proximity of the phloem to the conducting xylem facilitates this process. This success is underlined by the intact starch-containing plastids pictured in 5.3.1e. Plastids have been described as the 'most sensitive indicator of disturbance in the mature sieve element' (Barclay et al., 1977; Parthasarathy, 1974) and have been used to demonstrate the effects different fixation regimes have upon their structure (Esau, 1965). In the present study, these labile organelles showed no sign of a reaction to manipulation or inappropriate fixation (Barclay et al., 1977).

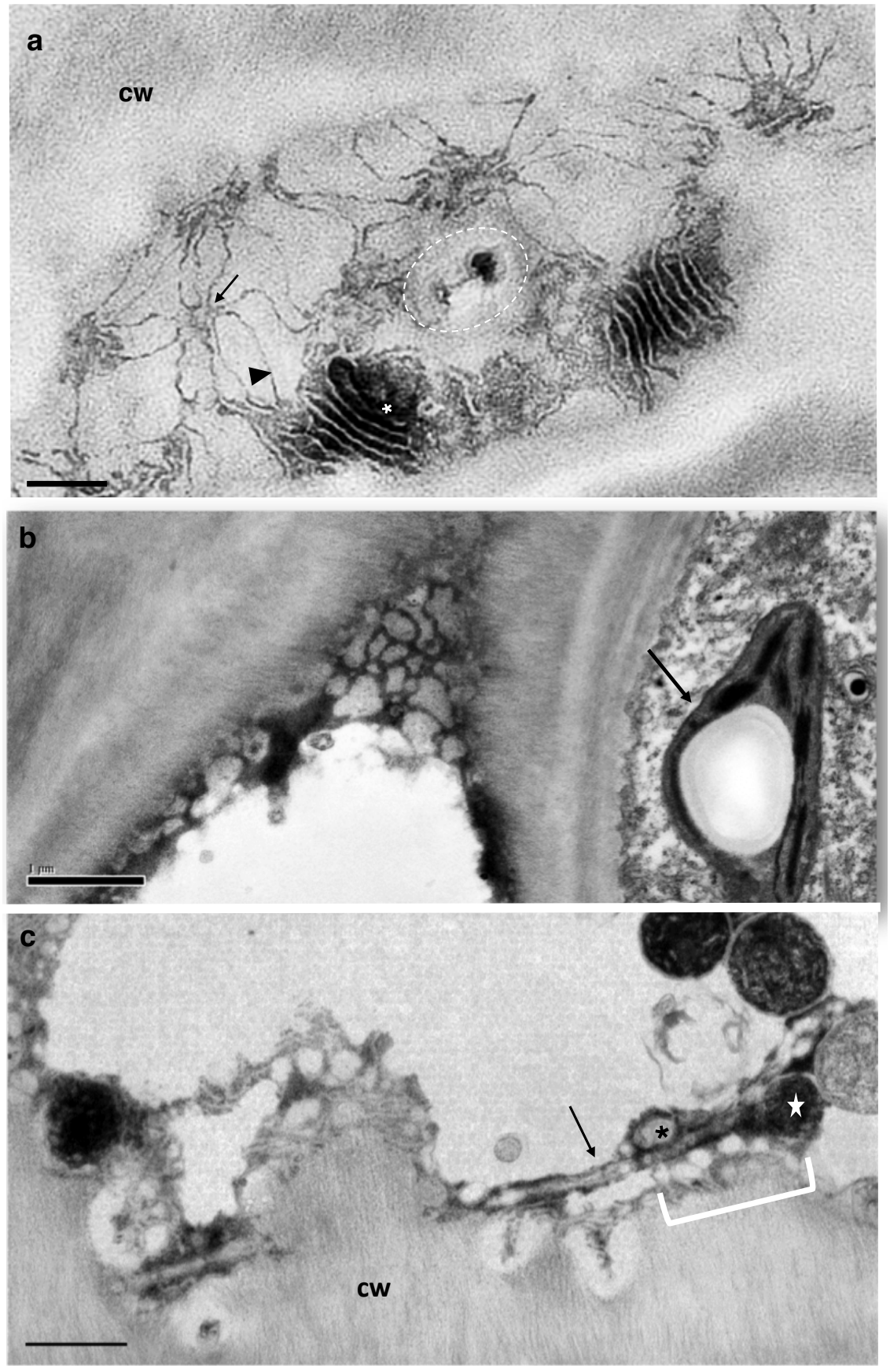

Figure 5.3.2 – legend on next page.

Figure 5.3.2 ZIO highlights different forms of SER

a) Glancing longitudinal section of the SE cell wall (cw) reveals different forms of SER and their connections. Thin tubules (arrowhead; 14 nm ± 5 n = 10) radiate from sites of dense stacking (*) to cisternae (arrow). Also captured is ZIO accumulated in the desmotubule (dashed circle) connecting this SE to its overlying CC. Scale 0.5 μm. b) Reticulate form of SER with many fenestrations. In the adjacent cell there is a chloroplast (arrow) with a starch inclusion. Scale 1 μm c) A rare view of two parallel SER tubules with an opaque central channel between them (arrow). These seemed to envelope a vesicular structure (*) and a mitochondrion (*). Fine tubular connections appear to radiate from the tubule to the SER at the PM (bracket). Scale 0.5 μm.

Figure 5.3.2 shows ZIO-stained longitudinal sections of vasculature with the characteristic polygonal and cisternal forms of SER but also, for the first time, two tubular forms not previously reported. Very fine anastomosing tubules were abundant, found at the periphery of the cell and associated with SER stacks and sheets. The other form was seen rarely and contained two parallel ER tubules with a central channel separating them. Figure 5.3.2 a) shows the fine anastomosing SER tubules (14 nm ± 5 n = 10). These are numerous and seem to extend from areas of denser stacking to other densely packed patches, or to cisternae (figure 5.3.2 a, star and arrow respectively). The SER stacks have an electron-dense intercisternal material sandwiched between them and were closely associated with the PM (5.3.2a). The lumenal spacing (23 nm ± 3 n =15) was quite consistent, as is the case for animal and yeast cells (Westrate et al., 2015). The classical polygonal form of SER is in close association with the plasma membrane (PM; figure 5.3.2 b) and is typical of that seen in other cell types (Boevink et al., 1998). Rarely, parallel tubules were seen that had a central channel (20 nm ±1.8 nm n = 6; figure 5.3.2 c) and these appeared to associate with vesicular structures and mitochondria. Fine tubular connections appear to emanate from these and join the PM.

The images show an assortment of very distinct membrane forms. These could represent different functional forms of the SER. Tubules have a higher

surface to volume ratio than sheets, making them more suited to surface-dependent functions, whereas sheets can provide a platform for lumenal processes (Westrate et al., 2015). In animal cells there is a correlation between the relative abundance of the tubular and stacked forms of ER and the functional output of that cell. In neurons, where few secretions are produced, the tubular form is abundant, whereas in the pancreas there is extensive enzyme secretion and the stacked form dominates (Westrate et al., 2015). There does not appear to be such a clear correlation in plants (Hawes et al., 2015). Biochemical analyses suggest the SER contains enzymes involved in autophagy (Oparka et al., 1981), as well as acting as a calcium store. As the coverage of the PM is almost complete, the SER could provide a route for circulation around the entire peripheral area of the SE. This extensive meshwork may play a role as a physical boundary separating the lumen from the PM, creating a peripheral membrane complex, whilst the fenestrations could allow water entry into the SE (Sjolund and Shih, 1983). An analogy is shared with the human kidney and small intestine where fenestrated blood vessel membranes facilitate filtration through PM and lumenal exchange. Fenestration size imposes specificity, where small fenestrations (60 – 70 nm diameter) are involved in exchange of water and small solutes and larger ones (up to 200 nm diameter) may allow passage of lipids and the removal of cellular debris (Satchell and Braet, 2009). SE 'housekeeping', e.g. local removal of cellular debris, must take place to allow these routes to operate as efficiently as possible, especially in those plants where the SEs persist for many years (e.g. palms > 100 years; Parthasarathy, 1974). However, a link between SER fenestration size and SE function clearly requires experimental verification.

3D-SIM

By extending the resolution of light microscopy, 3D-SIM begins to bridge the gap between light microscopy and EM. This enhanced resolution, allied with the ability to image in 3-D, made it a useful tool to conduct a structural survey of the SER. Presented here are images of transgenic *Nicotiana tabacum* plants expressing *pSEO2*.HDEL:GFP (Knoblauch and Peters, 2010; as used in chapter three (and published in Bell et al., 2013) that highlight the SER. Figure 5.3.3 shows volume projections reconstructed from several optical sections taken in Z. The channels, seen rarely with the TEM (figure 5.3.2 c), were very apparent and occur throughout the SER (5.3.3 a, arrow). The channels were found in membrane tubules, punctuated by fenestrations. The tubules split around the fenestrations (5.3.3 a, dashed rectangle), rejoining the main body of the tubule, in the same way a river splits and forms anabranches around small islands in a watercourse. In the next image (5.3.3 b) the reconstruction highlighted a patch of SER that showed nine fenestrations all of which appeared to connect with a channel. This is enlarged in (c) where the arrangement can be fully appreciated. The channel is 75 nm in diameter and the two largest fenestrations are 568 and 645 nm (** and arrowhead respectively). The smaller ones are between 75 and 90 nm, in good agreement with what has been reported previously by TEM (Sjolund and Shih, 1983). The TEM image in 5.3.2 d shows a mitochondrion associated with such a membrane tubule. The range of diameters of the fenestrations shown in figure 5.3.3 suggest they are not occupied by one structure in particular. In 5.3.3 d the parallel tubules are long (tubule arrowed is 6.69 μm) and connected membrane patches with single fenestrations. The abundant nature of these parallel ER tubules led us to call them ‘tramlines’ to distinguish them from the other types of SER in the cell. In another area of the cell (dashed circle) a “tramline” forms a “fly-over” across another “tramline” located in a different focal plane (arrow head). A closer look at this region is shown in 5.3.3 e. The very fine anastomosing tubules seen by TEM in figure 5.3.2 a) were not found using 3D-SIM but this was to be expected as

they are below the resolution of the 3D-SIM microscope. Also, lumenal GFP would not be a suitable marker for such fine tubules as it is excluded from such tightly constricted structures (Oparka et al., 1999; Tilsner and Oparka, 2010).

Through examining the extensive views generated by 3D-SIM it was possible to establish that SER “tramlines”, seen only rarely in the TEM (figure 5.3.2 c), are ubiquitous throughout the SE. Without further experimentation it is not possible to establish if the space between the SER tubules is occupied by another structure or is simply a space. The sarcoplasmic reticulum (SR) is a modified form of smooth ER that acts as a calcium reservoir in muscle cells and parallels have been drawn between it and the SER (Sjolund, 1990). The SR is permeated by transfer tubules (t-tubules; Sperelakis and Rubio, 1971) and these funnel calcium and transmit the action potential into the cell generating muscle contractions (Hong and Shaw, 2017). Action potentials are also understood to be propagated along the ST following calcium ion influx (van Bel et al., 2011). How this is achieved is not understood. As observed here the SER membrane channels are found throughout the SE and, if involved, these could help to synchronise electrical signals within the cell.

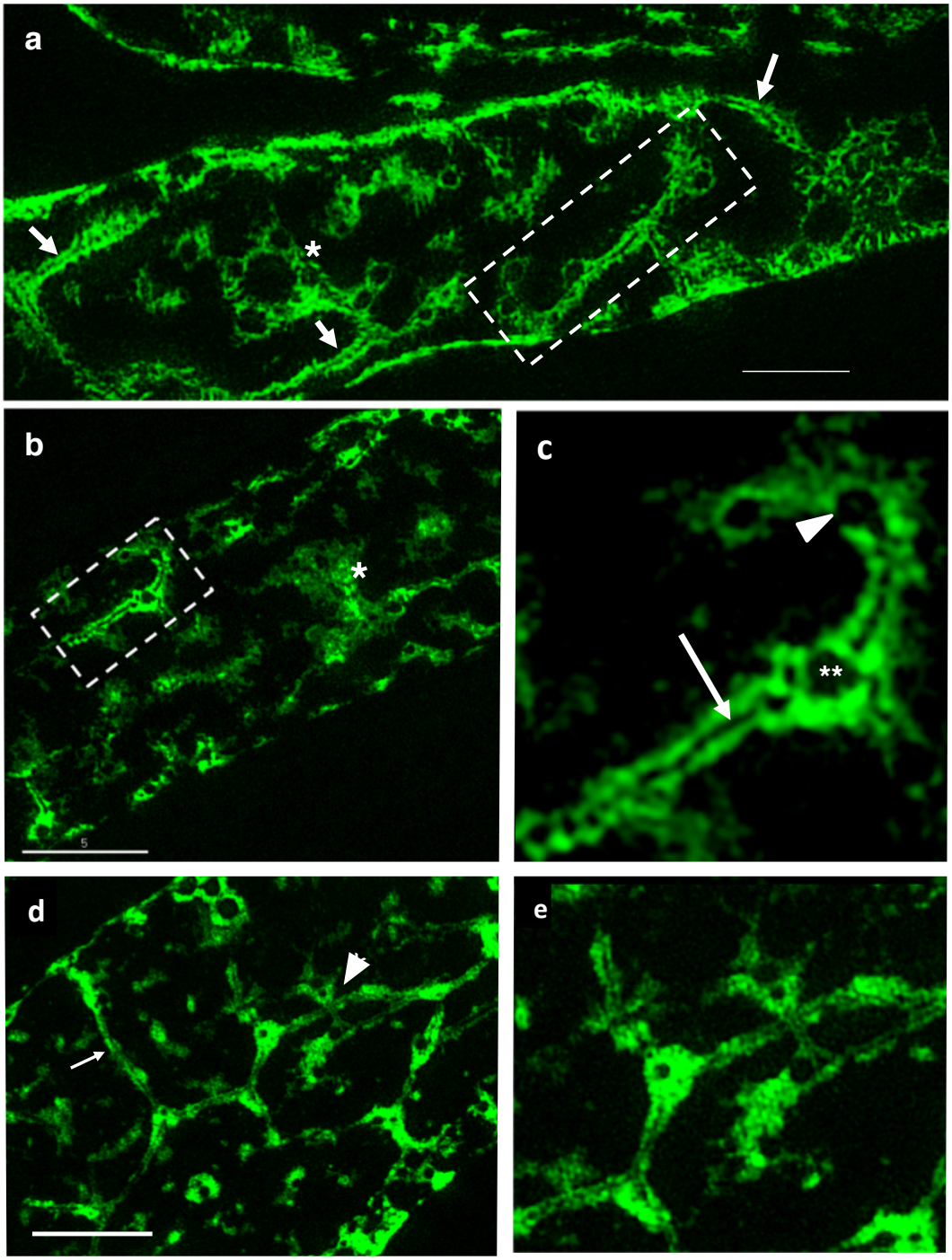

Figure 5.3.3 3D-SIM reveals SER tubules (tramlines) with central channels that are located throughout the SE parietal layer

a) Projected image of a SE expressing *pSEO2*.HDEL:GFP (Knoblauch and Peters, 2010). A dashed rectangle highlights a patch of SER with a central channel running between fenestrations of different sizes. SER tramlines with channels occur throughout the SE (arrows) Scale 5 μm. b) Although SER cisternae (*) are more apparent than tubules in this image a patch where clear associations between a “tramline” and fenestrations occur

(dashed rectangle). Scale 5 μm c) Enlargement of area highlighted in b. The channel (arrow) between ER tramlines is 75 nm in diameter. The largest fenestrations are 568 nm (*), 645 nm (arrowhead) in diameter. Scale 1 μm. d) SER tubules here are extended and not furcated around the fenestrations. The tubule arrowed is 6.69 μm long. One ER "tramline" is seen apparently running under another (arrowhead) Scale 5 μm. e) An enlargement of the area highlighted in d helps to confirm the 'fly-over' arrangement of "tramlines".

FRAP analysis of pSEO2.HDEL:GFP

FRAP was used to determine whether the lumenal *pSEO2*.HDEL:GFP marker was mobile within the SER. SE occupy a position deep amongst supporting tissues that exceeds the optical sectioning capacity of the confocal microscope. To overcome this, a method was published to observe intact SEs of *Vicia fava* (Knoblauch and van Bel, 1998). This was adapted here for the study of tobacco petioles. Briefly, large leaves (20 - 25 cm) were detached from the plant and the adaxial surface was held on a glass slide using double-sided tape. The cut petiole was threaded through the pierced cap of a 2ml Eppendorf tube filled with water and sealed with parafilm. This arrangement was shown to maintain viability for up to three days (Tilsner et al., 2009), greatly exceeding the duration of these observations. A few cortical cell layers were removed from the main vein using a new double-sided razor blade taking care not to compromise the underlying vasculature. Once cut, the imaging window was filled with water and a x20 water dipping lens (HCX APO; Leica Microsystems) used to check the tissue for obvious signs of damage. To assess if the SEs were translocating they were loaded with HPTS acetate (Invitrogen). HPTS acetate is a symplastic dye which, when cleaved by intracellular esterases, yields the membrane-impermeant 8-hydroxypyrene-l,3,6- trisulphonic acid (HPTS) (Wright and Oparka, 1996). Within ten minutes the dye front had reached the imaging window (figure 5.3.4) and the fluorescence then filled the SEs, which remained fluorescent during the imaging period, approximately ten minutes

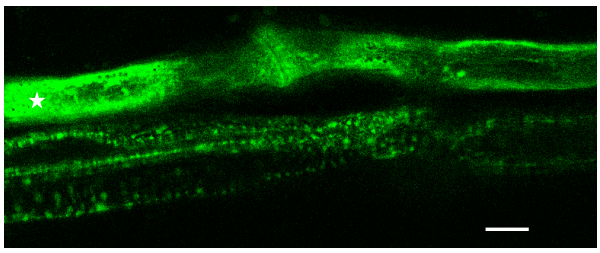

Figure 5.3.4 HPTS is translocated in uninjured SEs

CSLM snapshot of SE (star) translocating HPTS. The dye front moved visibly over the course of two minutes after which the SEs were completely fluorescent. *N. tabacum* expressing *pSEO2*.HDEL:GFP, reticulate arrangement apparent in SE not conducting HPTS (not starred). Scale 5 μm

Figure 5.3.5 – figure legend on following page.

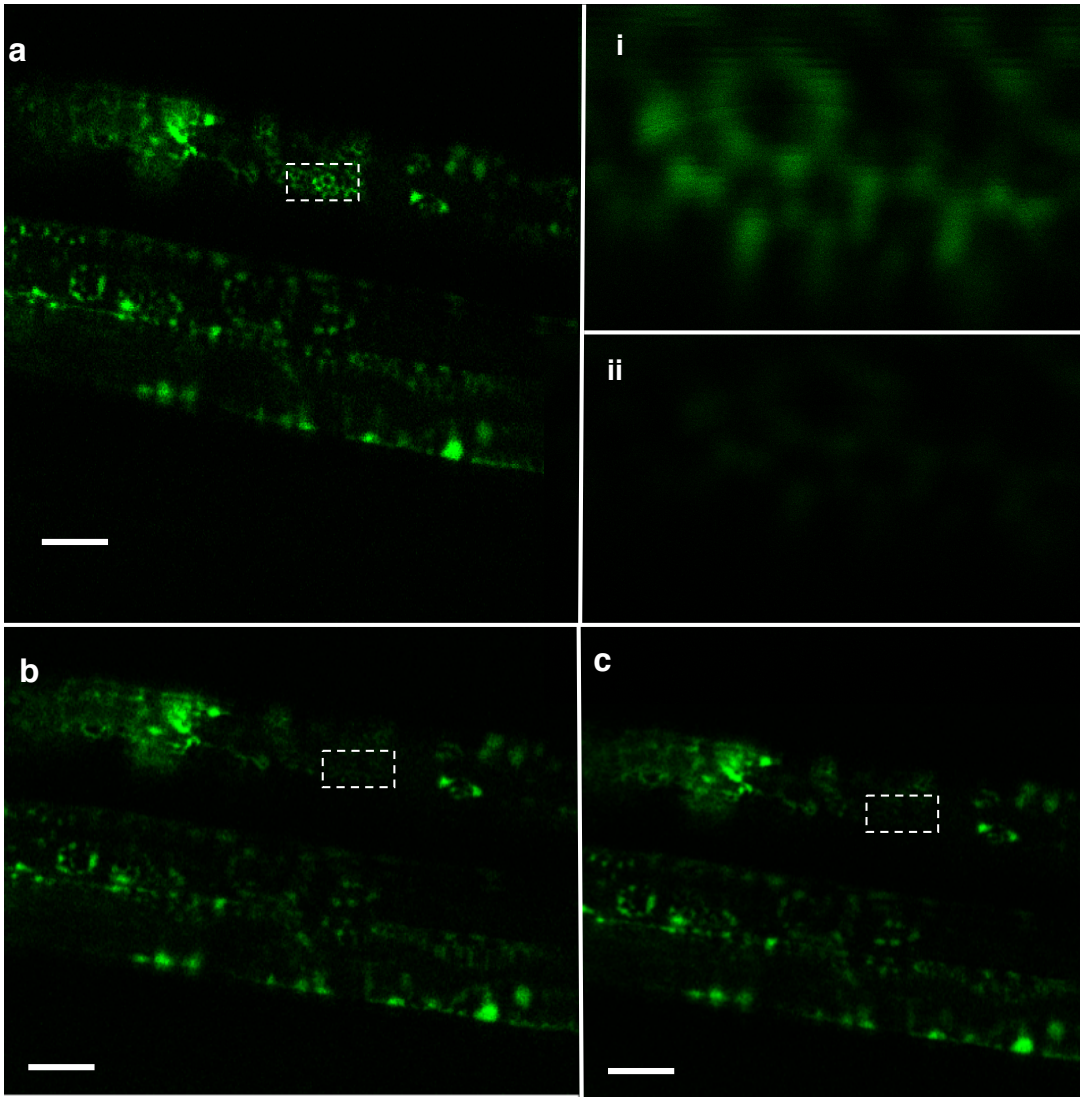

Figure 5.3.5 FRAP of SER lumen using lumenal GFP

a) Typical pre-bleach field of view where baseline fluorescence is established. A region of interest (ROI; dashed rectangle) is drawn around the most extensive area of SER in one plane of focus and this is subjected to FRAP. i) Snapshot generated by the Leica FRAP wizard showing the ROI zoomed in ahead of bleaching. ii) Snap shot from the same ROI following the last bleach step. Virtually all fluorescence is extinguished. b) Whole field, as in a, with the bleaching ROI highlighted. c) Whole-field image showing fluorescence after the recovery period. Scale 5 μm in each.

FRAP was performed as in chapter 3 (see also Fitzgibbon et al., 2010). Briefly, SEs were assessed to see if the SER was in the expected reticulate form and, if so, a ROI was drawn around a patch of tubules and these were then subjected to a FRAP imaging cycle of: establishing base fluorescence, bleaching, then monitoring recovery of fluorescence (see figure 5.3.5).

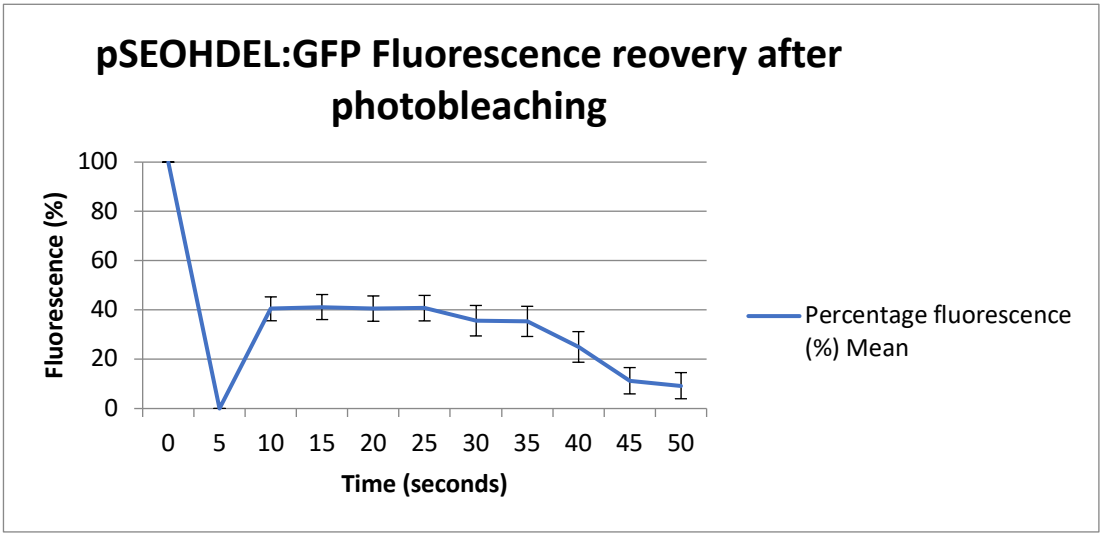

Figure 5.3.6 GFP fluorescence recovery after photobleaching

Fluorescence recovery averaged from 10 independent FRAP experiments on different SEs.

Due to persistent problems with sample drifting, recovery of fluorescence was monitored for 50 seconds. Across ten independent experiments, fluorescence initially recovered to 40% of the baseline then decayed to less than 10%. (Figure 5.3.5, 5.3.6). These data are only indicative as they were gathered from a poorly designed experiment. The drop in fluorescence

between 30 and 50 seconds is almost certainly due to photobleaching in the recovered area. Normalising the data gathered against a non-FRAPed region is required so that baseline values may be subtracted. Martens et al. (2006) examined the SER and ER of vascular cells using the membrane marker $DiOC_6$ and concluded that recovery from bleaching in intracellular FRAP was rapid, with a half-life (time from bleaching to when the fluorescent intensity reaches half of the final recovered intensity) of less than 60 seconds. Previously the reporter (HDEL:GFP) used here was useful when studying the ER using FRAP (Brandizzi et al., 2003; Stefano et al., 2014). The SER, however, is clearly different from those ER networks in nucleate paranchyma cells as it lacks an underlying cytoskeleton scaffold. It is not known how this might affect the SER and the extent to which functionality remains in common with the ER in parenchyma elements. Martens (Martens et al., 2006) used an actin depolymerising drug (cytochalasin D), at concentrations known to disrupt the network, and found that it did not affect FRAP of $DiOC_6$. Actin is known to be important in generating cytoplasmic streaming and movement in the cell (Deeks and Hussey, 2016), so perhaps its absence is likely to be of greater relevance to movement within the SER lumen rather than on the ER membranes.

It seems certain that an alternative to phloem mass flow must exist as non-mass flow patterns of assimilate movement have been noted (van Bel et al., 2011). Systemic resistance signals (Alvarez et al., 1998), for example, are not distributed according to phloem mass flow patterns. Source leaves receive systemic acquired resistance signals at a time they would have undergone the sink source transition, and so phloem unloading should have been rendered impossible by changes in vein organisation. Given its intimate association with PPUs and the parietal network in the SE continuum, it seems likely that the SER will play a role in influencing non-mass flow distribution within and around the SE. FRAP data (Martens et al., 2006) suggest that the ER membranes of the SE and CC are continuous and so

may provide a pathway for lateral movement between cells. Unfortunately, time and opportunity prevented a re-assessment of those observations as it would have been interesting to look at whether movement along the ST upon the SER membrane could be followed within a file of adjoining SEs.

5.3.2 Mitochondria and plastids

Mitochondria survive the autolytic purge having undergone the least structural change of the SE organelles (Evert, 1990). However, in mature *Nicotiana tabacum* SEs they are generally round, in contrast to the typically rod-shaped form prominent in undifferentiated SEs. In this study the mitochondria were found in close proximity to all forms of the SER (fenestrations, stacks and channels), or at the periphery amongst the 'ground matrix' that lies close to the PM (figure 5.3.2 d; figure 5.3.7 and Froelich et al., 2011). The plane of sectioning revealed a clear space of around 36 nm (± 8 nm, n = 10) around the mitochondrion (5.3.7 a, arrowed) where there appears to be no contact between its outer membrane and the enveloping SER. This could be a channel that allows signals or substances to be exchanged between the SER and mitochondrion, offering a means for specificity amidst the wider mass flow.

Plastids are either S-type or P-type depending on the ergastic material they contain (starch or protein, respectively). The plastids observed here were S-type as evidenced by the electron lucent inclusions within them. The role of plastids in differentiated SEs is unknown (Sjolund, 1997), but it is accepted that they are part of the wound response (Barclay et al., 1977). In figure 5.3.7 (d) a plastid appears to be tethered to a stack of SER (arrow) but is otherwise free in the lumen. This localisation was typical of what was observed and this thin tether may allow the plastid to detach quickly and form part of the surge that will plug the SE in the event of turgor loss. Untypical is the plastid opposite as it appears to lack a tether and is free within the cell

lumen. However, the membrane appears intact with no sign of starch grains escaping, a further reaction to disturbance (Barclay et al., 1977). Also, the SE is not full of P-protein, another recognised wound response. A large plastid (approximately 1 μm) would not have been able to pass through the SP pores (276 nm, Fitzgibbon et al., 2010).

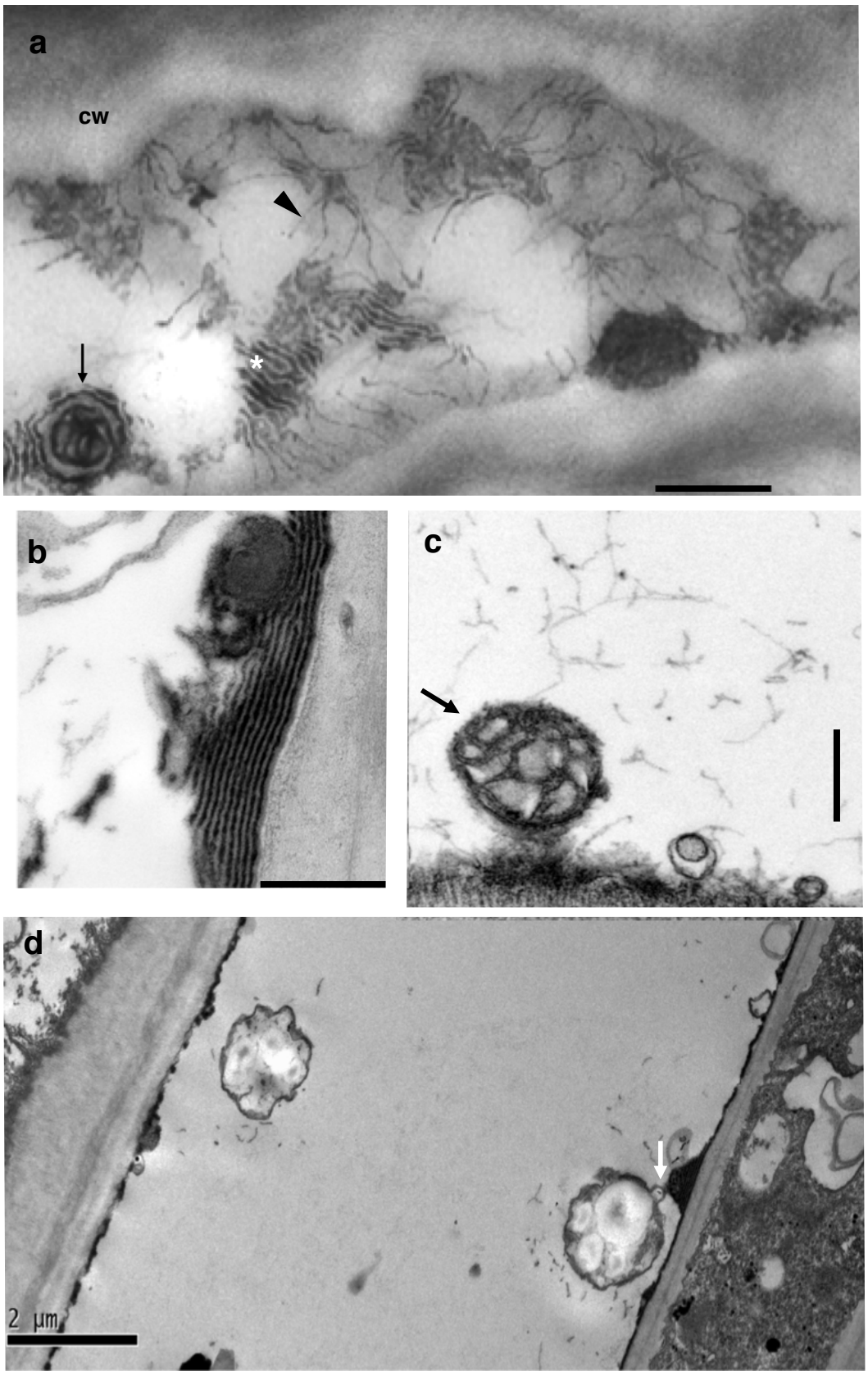

Figure 5.3.7 – legend on following page

Figure 5.3.7 Mitochondria and plastids are found at the cell periphery

a) Glancing section through the cell wall (cw) reveals the peripheral arrangement of SER stacks (*), tubules (arrowhead) and mitochondrion (arrow) embedded within. Scale 1 μm. b) Mitochondrion nestled amongst SER stack orientated parallel to lumen. Scale 0.5 μm c) Mitochondrion (arrow) associated with amorphous ground material. Scale 0.2 μm. c) Plastid appears tethered to a stack of SER (arrow). Plastid opposite is apparently free in the lumen. Scale 2 μm.

Flow velocity in *Nicotiana* petioles SEs has not been measured directly but has been estimated at 100 μm s^{-1} (Knoblauch et al., 2018). This would generate significant shearing forces between the SE sap and the cell periphery. Thus, the parietal layer must be secured to avoid being dragged along by mass flow. Protein clamps have been observed elsewhere (Ehlers et al., 2000; Froelich et al., 2011) and these appear to provide an effective anchoring system, keeping the SER close to the PM and stabilising peripheral membrane complexes. Both stacked sheets and reticulate tubules have mitochondria associated with them. Exploring the associations between ER and mitochondria has been of considerable recent interest (Rowland and Voeltz, 2012; Mehrshahi et al., 2014; Westrate et al., 2015) and the association of SER and mitochondria was examined here.

3D-SIM

It was hoped that by exploiting the 3D capabilities of 3D-SIM, we could observe the structural relationship between the SER and mitochondria. Considerable time was spent trying to label mitochondria immunologically without success.

Xylem delivery of dyes and live cell imaging of the SE

It was decided to try and exploit the xylem delivery route to see if it could translocate dyes and label a SE constituent *in vivo*. In our experience 3D-SIM did not work well with live plant samples. Confocal microscopy, however, has been used widely to image living plant tissues and has proved vital in

studies of the ER in parenchyma cells, establishing the saltatory movement of trans-Golgi network units on the actin ER network (Boevink et al., 1998) as well as tobacco mosaic virus attachment sites on the cortical ER (Christensen et al., 2009). Live tissues were prepared exactly as for FRAP of the SER. The integrity of the SER (as highlighted by *pSEO2*.HDEL:GFP; figure 5.3.8 a) was used as a proxy for wider cellular integrity and assessed using a x63 water dipping lens (HCX PLAPO CS; Leica Microsystems). The water in the 2 ml Eppendorf tube was replaced with the dye hexyl rhodamine B (Invitrogen), a cell-permeant, cationic, orange-red fluorescent probe that is readily sequestered by active mitochondria. Leaves were left to transpire the dye in a lit chemical flow-hood for 60 minutes and then paradermal cuts were made to create an imaging window in the main vein, as described above. Figure 5.3.8 show a SE exposed to hexyl rhodamine B.

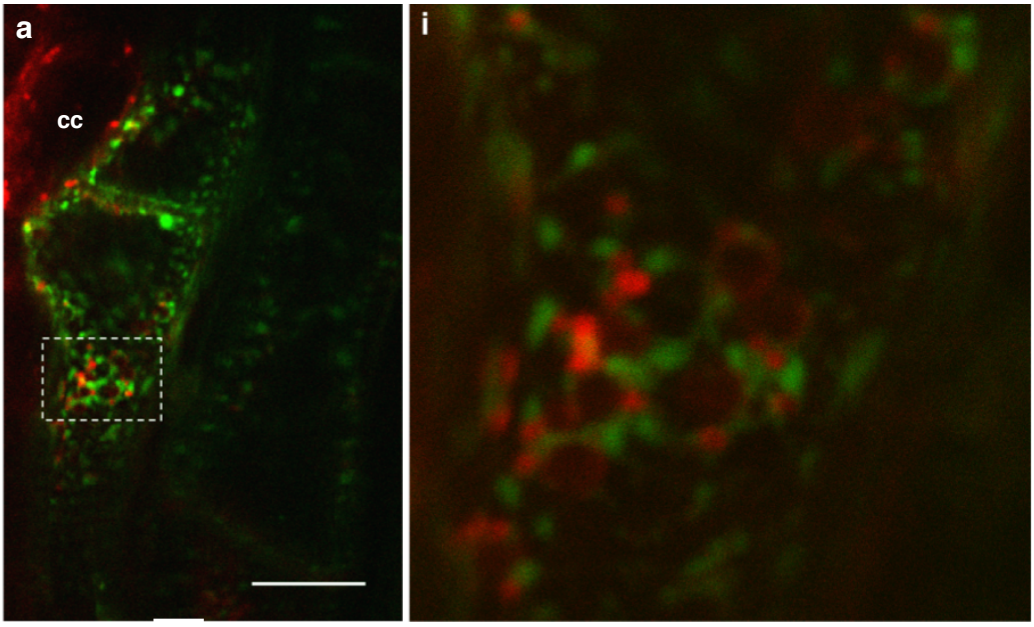

Figure 5.3.8 Hexyl rhodamine B labels mitochondria in live SE

a) Hexyl rhodamine B is transported in the xylem and labels mitochondria (false coloured red) in the SE as delineated by *pSEO2*.HDEL:GFP (shown in green; Knoblauch and Peters, 2010) and the CC. Scale 5 μm. b) Enlargement of area highlighted in a. Mitochondria are found at the vertices of the SER.

The images show that the dye reached the SE and accumulated in structures at the vertices of the tubular SER. Large fenestrations (1 μm ± 0.16 n = 6) remained empty. Mitochondria are numerous within mature SEs and as above, often found intimately associated with the SER (figure 4.2 a, c and d). The functional relevance of this relationship has not been established but through studies in other systems a role can be postulated. In animal cells, Ca^{2+} is released to mitochondria from the ER at discrete contact sites (Rowland and Voeltz, 2012). These contact sites have different structural features, being extensive or discrete, and this can define the ability of Ca^{2+} to be transferred (Rowland and Voeltz, 2012). If the contact sites are too close then the Ca^{2+} transporter cannot fit and transfer is not observed (Rowland and Voeltz, 2012). It could be that within the SE, mitochondria are immobilised by being held in tight association with SER, but that by relaxing these membrane links, e.g. at the vertices of the cortical SER, a functionality could be restored. Mitochondrial metabolic activity has been probed using dyes (Janus green B, rhodamine 123; Sjolund, 1990) that are taken up during respiration. This was also done here using hexyl rhodamine B. If this experiment was repeated, but with a dye that would persist in fixed sections, mitochondria could be examined with 3D-SIM and a relationship between SER type (fenestrated, channel or stack) and metabolic activity may become apparent.

5.3.3 Callose

Callose is found within mature SE at the SP and at the orifice where the connection from the CC enters the SE. Callose was surveyed to see where it was in relation to the SER as highlighted by *pSEO2*.HDEL:GFP (Knoblauch and Peters, 2010). Callose was immunolablled as before (see Methods). Figure 5.3.9 shows that the callose labelling was successful and that callose collars at the SE orifice were not associated with the SER fenestrations. Although this image was collected using the diffraction- limited CSLM, fenestrations are apparent that are of a size that correlate roughly with that of the callose structures so an association between the two would be expected to be appreciable.

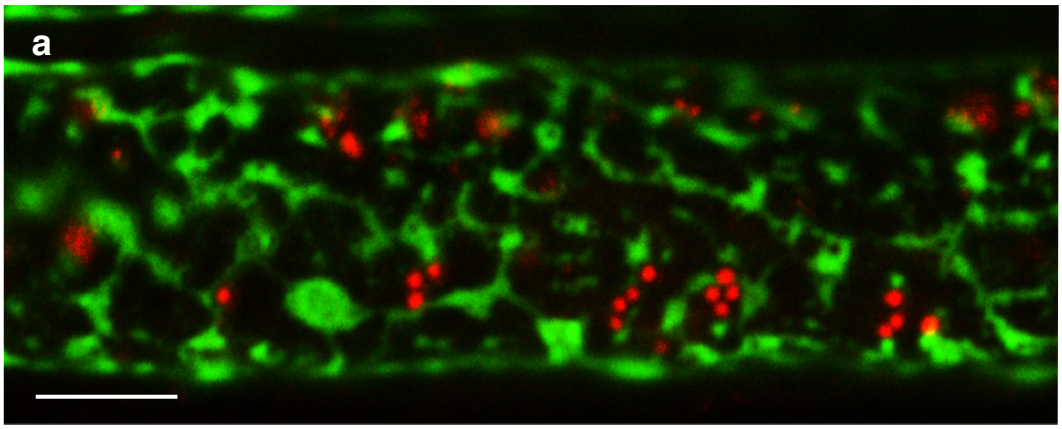

Figure 5.3.9 Callose does not occupy SER fenestrations

CSLM image of *pSEO2*.HDEL:GFP and callose indirectly imaged using the anti-callose antibody (BioSupplies) and the Alexa 594 secondary antibody (Invitrogen). Callose (false coloured red) is apparent as discrete spheres and is not found associated with SER (green) fenestrations or sheets. Scale 10 μm.

FRAP data (Martens et al., 2006) indicates that the SER is continuous between the CC and SE and so it would be expected that an association between the SER and the point at which the ER emerges into the SE to be seen. The CSLM would not offer sufficient resolution to show a definitive association but there was no overlap in the signals to suggest a connection in the tissues surveyed. Also, as discussed in chapter 5, a lumenal GFP

marker is not suitable to study this as it would be expected to be excluded from the highly constricted desmotubule (Oparka et al., 1999; Tilsner and Oparka, 2010).

5.3.4 PPUs

The interplay between CC and SE is fundamental. The CC underwrites much of the essential functions of the enucleate SE, so this link is of paramount importance for SE survival and, more broadly, the concerted growth and development of the plant. The SE and CC are connected symplasmically allowing ready exchange of materials up to 70 kDa (Paultre et al., 2016). The symplasmic connection between the CC and SE has a unique structure with up to one hundred branches from the CC emerging as a single orifice in the SE (Evert, 1990; Oparka and Turgeon, 1999). This unique symplastic connection is called a PPU (van Bel and Kempers, 1997) to reflect the compound nature of its structure. The desmotubule provides ER continuity between the CC and SE. Presented here are TEM images of glancing sections through *Nicotiana tobaccum* PPUs. The material was processed with ZIO (as above) which proved useful in highlighting the PPU desmotubule. Figure 5.3.10 a, is a glancing section that shows a CC, SE and the cell wall overlying. In this image it is possible to see rare views of all the PPU principle components: multiple entry sites from CC (dashed circle), dilations in desmotubule in the central cavity (arrow head) emerging as a single pore at SE (arrow). ZIO has helped these features stand out by staining the areas where it has accumulated darkly. Next, an overview showing the parietal layer of the SE has stacks of SER along its length and these sometimes sit next to PPU orifices. The SER stacks above the PPUs are darker, suggesting a greater distention and consequent accumulation of ZIO, but the membrane emerging from the PPU appear continuous with them. In the following three images (figure 5.3.10 c-e) the desmotubule within the PPU is examined. All show dilations in the membrane, as revealed by ZIO accumulation. No single image captures an entirely dilated desmotubule

which is why a panel of images is presented. This is probably due to the plane of sectioning not striking the true centre of a PPU. That these images collectively show dilations along the length of the desmotubule suggests that the lumen of the SER within PPUs is open, providing a potential route for movement. ZIO has been used to study the desmotubule of PD during their formation and development (Hepler, 1982). Helper (1982) showed that as the PD pores developed in the new cell wall, the electron-dense stain was gradually excluded from the desmotubule, as there was insufficient space between the ER membranes for ZIO accumulation. It is now understood that the desmotubule may not be a fixed structure, and may dilate in response to factors such as virus infection (Guenoune-Gelbart et al., 2008; Epel, 2009). Barton et al. (2011) provided evidence of cell-to-cell lumenal transport via the ER, but it has yet to be established if the ER conduits in the PPU are competent in this type of exchange. The results presented here would suggest that the lumen of the desmotubule is open, but only in the central portion of the pore. An earlier study by Martens (2006) found that there was discontinuity between the ER of the CC and the SER within the SE as lumenally located GFP did not cross from the CC to the SE. This arrangement appears to be reciprocal as lumenal GFP expressed from the SEO promoter, also did not cross to the CC-ER from the SER. It may be that a functional continuity does exist via the lumenal route but it has a size exclusion limit less than GFP (25 kDa; Buckley et al., 2015). This could be tested by labelling the lumen of either the CC-ER or the SER with a smaller fluorescent marker e.g. iLOV (12.1 kDa; Buckley et al., 2015) and looking for signs of iLOV diffusion between the CC and SE.

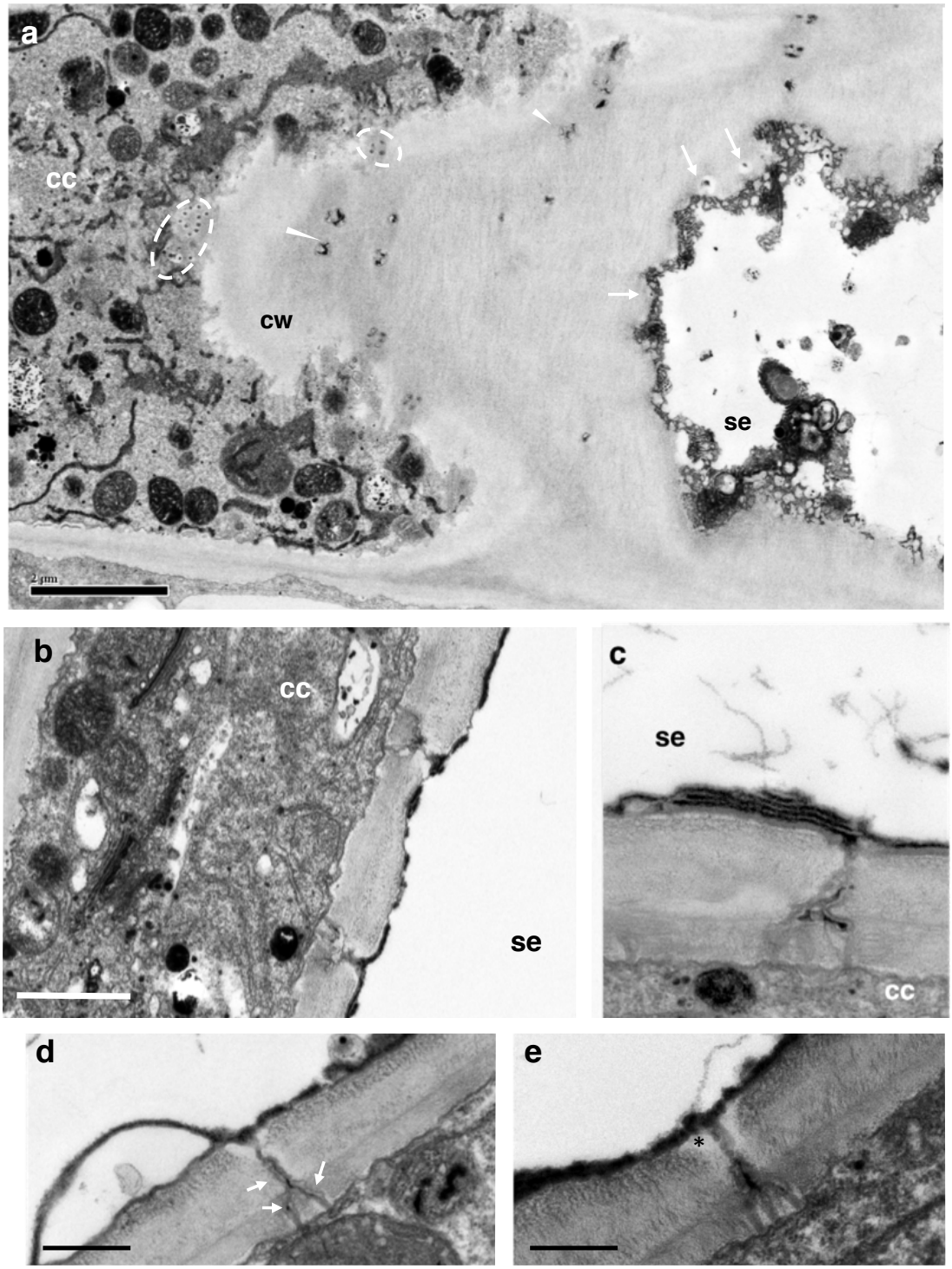

Figure 5.3.10 ZIO highlights dilations in the PPU desmotubule

a) An overview of the symplasmic connection between CC and SE. Face view of the multiple cavities in CC (dashed circles) that are the portal for passage to the SE. The central cavities are dilated (arrowhead) evidenced by the accumulated electron opaque ZIO precipitate. These then emerge as a single orifice into the SE (arrow). Scale 2 µm. b) Longitudinal section shows an overview of the CC-SE interface. The furcating arrangement of the PPU

from the CC is apparent. The branches then fuse, emerging at a single point in the SE. Scale 0.5 μm. c) Accumulated ZIO in dilated central cavity. Stack of SER sheets sitting over the SE orifice. Scale 0.5 μm d) ZIO accumulated in both tubules emerging from the CC, the point at which they seem to converge, and beyond towards the SE (arrows). Scale 0.5 μm. e) Three sites of entry to the PPU from the CC side. Callose (*) deposit around PPU SE oriface. Scale 0.5 μm.

5.3.5 Actin

Actin is a primary component of the plant cytoskeleton. It is involved in a number of diverse functions including; determining cell shape, driving cytoplasmic streaming and facilitating vesicle trafficking (Deeks and Hussey, 2016). It is understood to be absent from differentiated SEs (Schulz, 1998). Whereas components of the actin cytoskeleton have been found in phloem exudates (Lin et al., 2009), an intact actin network has not been reported. However, Hafke et al. (2013) published the results of a study that purported to show a fully developed parietal actin network in mature SEs. This assertion demanded experimental verification as it was contrary to all published studies of mature SEs. To this end, a transgenic *Nicotiana tabacum* expressing fimbrin fused to GFP from the 35s cauliflower mosaic virus promoter was fixed and sectioned with the vibrotome. Fimbrin is an actin cross-linking protein (Deeks and Hussey, 2016) and localises strongly to actin filaments. Figure 5.3.11 a) shows bundles of actin in a cross-section of cells in the vasculature. However, the SEs were devoid of actin filaments. Hafke et al. (2013) used a C4 actin antibody to indirectly visualise the actin network using TEM. The C4 antibody (Merck-Millipore) is a pan-actin antibody that binds to an epitope in a highly conserved region, and so would be expected to recognise actin seen in plants. I therefore also used the C4 antibody on fixed vasculature sections and visualised it using an Alexa secondary antibody (Invitrogen) imaged with the CSLM. In these experiments the SEs were demarcated by ER-lumenal GFP (expressed from the *pSEO2*.HDEL:GFP transgene) constitutively in *Nicotiana tabacum.* Figure 5.3.11 (b, c) shows images where the actin cytoskeleton is labelled in the CC

but is completely absent from the adjacent SE. The final image in the figure (5.3.11 d) has a wider field of view and shows actin labelling in the parenchyma cells surrounding the ST to further underline that the antibody can label actin in other tissues. These results failed to verify the observations made by Hafke et al.(2013), and are in agreement with the widely held view that mature SEs lack an intact actin cytoskeleton. These observations have since been published in an article describing the structure of mature SEs (Knoblauch et al., 2018).

Figure 5.3.11 – legend on next page

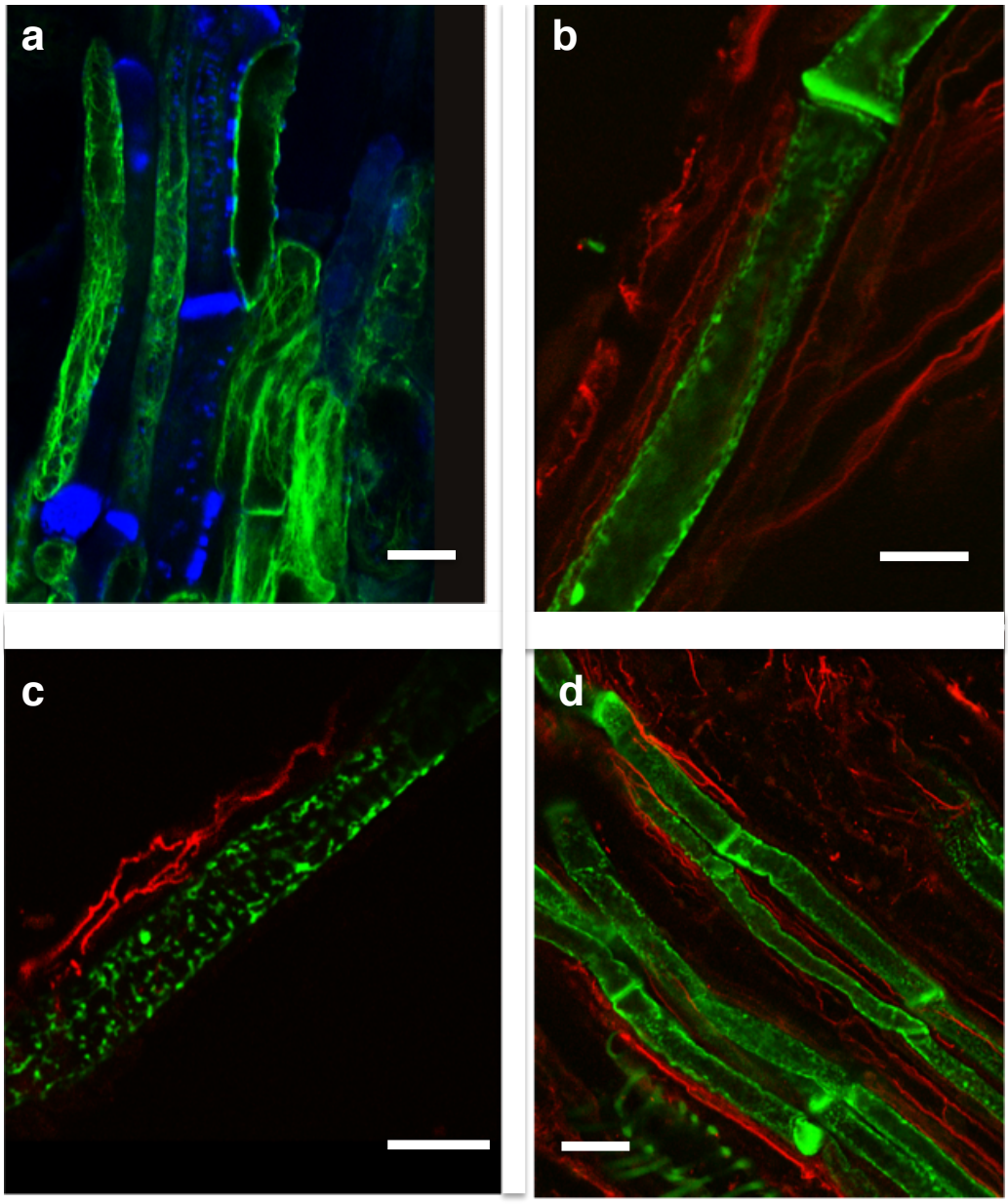

Figure 5.3.11 No actin found in differentiated SE

a) Longitudinal section of a transgenic *Nicotiana tabacum* expressing GFP fused to the actin-binding protein, fimbrin (green). Callose stained with aniline blue (blue). Tangles of GFP labelled actin are extensive in a CC and adjacent parenchyma cells but a SE is devoid of labelling. Scale 20 μm b - c) Sections from transgenic *Nicotiana tabacum* expressing *pSEO2*.HDEL:GFP to highlight the SER (green) immunolabelled with the anti-actin antibody C4 and visualised with an Alexa 594 anti - mouse secondary antibody (red). There is no overlap between the SER and actin signals. d) No actin apparent in the ST but staining apparent throughout the surrounding parenchmya cells. Scale b 15 μm, c 10 μm, and d 20 μm. (a, c modified from Knoblauch et al., 2018)

5.4 Summary and future directions

A variety of methods has been brought to bear upon the SE parietal layer and these have generated fresh insights. An ultrastructural assessment was conducted using conventional TEM but utilising a novel fixative delivery method that served to minimise preparation artefacts and preserve fine structures. Zinc iodide osmium impregnation proved very effective and clarified the distribution and forms of the SER. This, in combination with the minimally disruptive xylem fixative delivery method, produced views of the SER not seen before. Two new tubular forms were described. Very fine anastomosing tubules were abundant and seen to run between areas of stacked SER, offering the potential for membrane continuity throughout the SE. A second tubular form was seen only rarely in the TEM where parallel SER membranes seemed to follow a central channel for considerable lengths ("tramlines"). 3D-SIM correlated this form of parallel tubules. However, instead of them being an occasional feature they were seen to be abundant, additionally forming anabranches around fenestrations of different sizes. This highlights the need for conducting parallel imaging approaches to study the same cell type. A general feature of 3D-SIM imaging was the presence of dark, circular fenestrations at the ends of the SER tramlines (e.g. figure 5.3.3 a). Although we were unable to locate mitochondria using antibody labelling, the position of these 'holes' in the ER network corresponds well with

expected location of mitochondria, as seen with Hexyl Rhodamine B staining, namely at the 3-way junctions of the SER tramlines. Each mitochondrion appears to be ensheathed within the SER, with the tubular tramlines connecting all the mitochondria in the parietal layer. One could speculate that, as SE mitochondria are functional (Sjolund 1990), that ATP produced by these structures might be channelled around the cell in the spaces between the SER tramlines, providing a rapid route for disseminating metabolic energy within the mature SE. Now that these SER structures have been identified, the tramlines should be targeted for further investigation. They might also play a role in propagating electrical signals and might be enriched in calcium channels. Should such a population of channels be labelled constitutively, exploiting the SE promoter, *pSEO2*, (Knoblauch and Peters, 2010) to drive expression within mature SEs, 3D-SIM may offer the resolution to determine where on the membrane such channels were located.

SER function was explored using FRAP. Preliminary results are that lumenal GFP does not diffuse into bleached areas. Replicates are required with a longer recovery period after bleaching to confirm this inertia. A comparison between GFP and the dynamics of a smaller lumenal marker (iLOV; Buckley et al., 2015) could reveal whether lumenal movement occurs below a threshold. It has already been established that the SER membrane is competent for small dye movement (Martens et al., 2006). To obtain meaningful FRAP data it is important to use live, minimally disturbed tissues. This was achieved by tailoring a published method (Knoblauch and van Bel 1998) to *Nicotiana tabaccum* leaves. This method was then used in concert with xylem-mediated delivery to label metabolically active mitochondria using a fluorescent dye. This population was found at the vertices of the SER. These data demonstrate that the SE is amenable to live cell imaging and also that the xylem can be used to label a SE compartment.

By clearly delineating the SER with ZIO it was clear that it was in close association with the PPU orifice and that the desmotubule connecting the SER to the CC-ER was dilated along part of it length, as evidenced by ZIO accumulation. These observations require functional verification which could be achieved using FRAP. Intercellular CC-SE lumenal continuity could be investigated further using iLOV (Buckley et al., 2015) expressed from the *Arabidopsis* CC specific promoter *pAtSUC2* (Truernit and Sauer, 1995). Finally, attempts were made to corroborate the data presented by Hafke et al. (2013) that an intact actin cytoskeleton is present in mature SEs. Neither a transgenic plant constitutively expressing a fluorescently labelled actin-binding protein, nor the same pan-actin antibody used by Hafke et al. (2013), revealed the presence of such a network. This is in agreement with the prevailing opinion that SEs lose their cytoskeleton before maturity (see Knoblauch et al., 2018).

A summary of my observations, depicting the different forms of SER found in mature SEs, is shown in figure 5.4.1

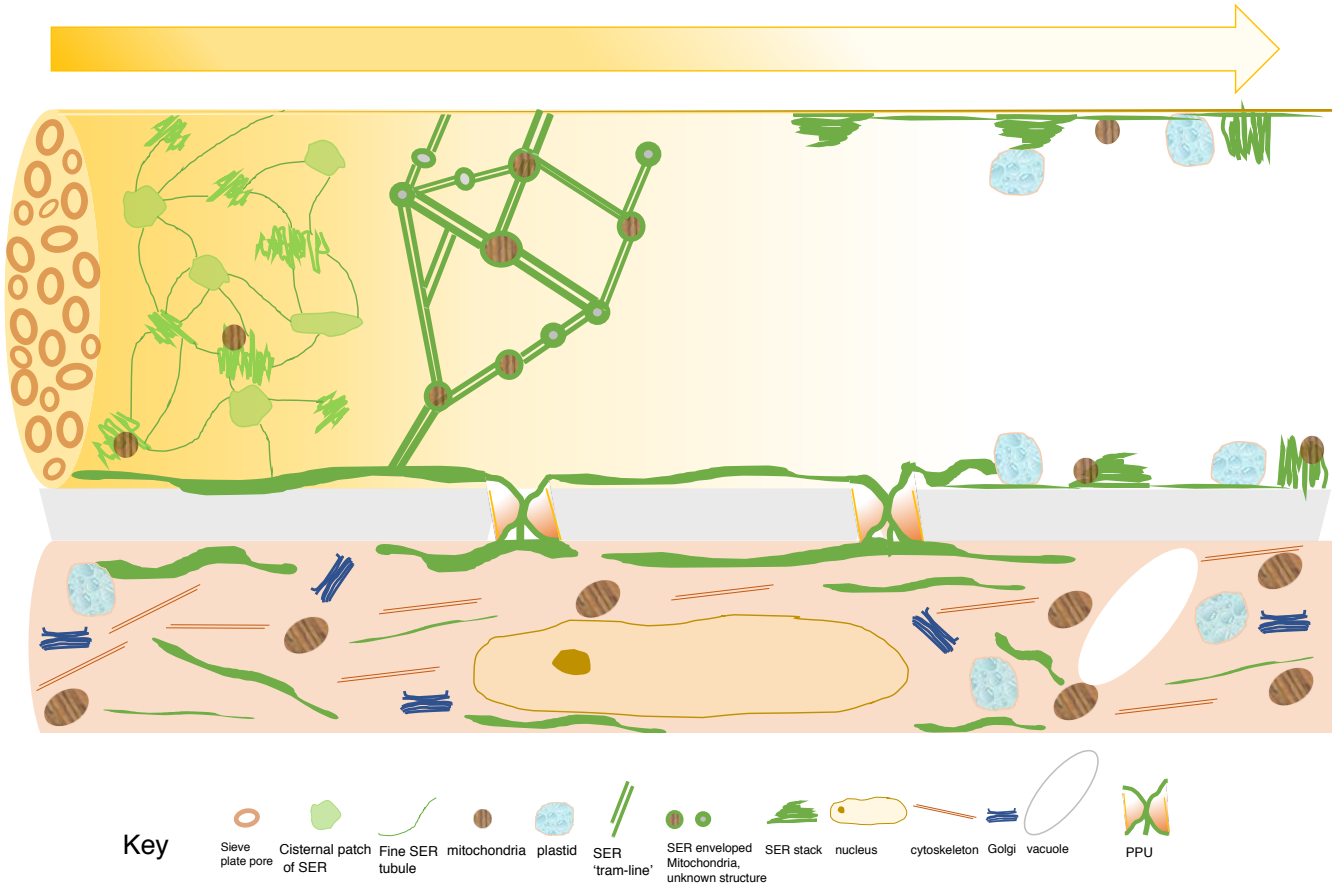

Figure 5.4.1 Diagrammatic representation of the parietal layer of the SE-CC complex .
The Image is drawn longitudinally with the SE on top and the CC underneath. The depth of sectioning increases (from left to right with the arrow) in the SE to illustrate the different arrangements of SE constituents, revealing; fine SER tubules and cisternal patches, SER 'tram-lines' and then SER stacks arranged perpendicular and parallel to the plasma membrane. The relative positions of plastids, mitochondria and unknown structures are shown.

6. Final Summary and Future Directions

The main aim of this project was to develop novel methods to image the SE. Through delivering fixative via the xylem it was possible to preserve the SE with minimal disruption to it and the surrounding tissues. This provided the basis upon which subsequent methods were developed. Through exploiting new super-resolution imaging technologies, the first sub-diffraction views of the SE were gathered. These were published in a 'break-through technologies' article in Plant Physiology with joint-first authorship (Fitzgibbon et al., 2010).

Next, a unified sample preparation method was developed. This produced material compatible with imaging at super-resolution, the conventional light microscope and the EM. Ultrastructural features were preserved, along with callose antigenicity. This was published with first authorship in The Plant Journal (Bell et al., 2013). The method garnered considerable interest and I was invited to discuss the technique further in the context of examining PD and the structure of tobacco BY2 cells in two separate Methods In Molecular Biology book chapters (Bell and Oparka, 2015; Bell et al., 2016).

Finally, a survey was conducted of the SE parietal layer. A variety of methods were brought to bear, and their synergy gave new insights into the form of the SER. ZIO as a secondary TEM stain was very useful in highlighting the SER. Two new tubular forms of SER were identified. First, an extensive network of very fine tubules was observed, running between areas of denser ER stacking. Second, parallel tubules, resembling 'tramlines', were seen at the SE periphery. Imaging with 3D-SIM confirmed the form of these 'tramlines' and showed them to be abundant throughout the SE periphery, an appreciation only possible through the resolving power of 3D-SIM and its optical sectioning capacity. Finally, as a part of the SE survey, I was able to

verify that the mature SE does not contain an actin cytoskeleton. These data were published in Current Opinion in Plant Biology (Knoblauch et al., 2018).

This is an exciting time for studying phloem cell biology. A suite of new techniques is available for its interrogation and this has opened up many new avenues of study. Below I speculate about the merit of a few others that could contribute to our understanding of the SE.

Optogenetics

Optogenetic tools have been developed to control protein interactions in living cells allowing them to be dynamically tuned with light (Shin et al., 2017). Such was its promise that this technique was named as method of the year by Nature Methods in 2010. The field has moved apace since then and the potential of one application is discussed here in the context of SE research. The core of this technology is the phytolyase homology region (PHR) of *Arabidopsis thaliana* Cry2, which is a light-sensitive protein that has been shown to self-associate upon blue-light exposure (Bugaj et al., 2013). Cry2 corrals fused proteins, and these assemblies are visualised using the fluorescent reporter mCherry. This allows sufficient spectral separation from the blue light used to generate the self-association (560 and 488 nm, respectively).

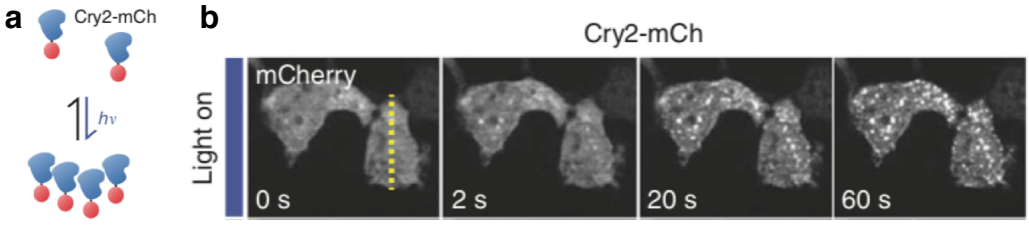

Figure 6.1 Optogenetics
a) Diagram showing light induced clustering of proteins. *Hv* light activation energy as given by Planck relation. b) Cry2-mCherry cluster formation in response to increased duration of 488 nm laser light pulses. Adapted from Bugaj et al., 2013.

An obvious candidate for investigation in this manner would be P-protein, which self-associates into a variety of physical forms, all of which are likely to have a consequence for mass flow. Froelich et al. (2011) examined the form of an *Arabidopsis* forisome (*Fabacae* P-protein) homologue (SEOR1) *in vivo* and noted that it varied from being condensed, oval, amorphous or filamentous. Whilst the condensed state was prominent in immature, non-conducting SEs and filaments typical in mature SEs, the appearance was highly variable. Accurate measurements of SEOR1 filaments made from TEM micrographs was used to inform a mathematical model of flow. The model assumes open channels in the SEOR1 agglomeration. If no open channels are present then critical parameters in the model change (Froelich et al., 2011). As agglomerations are rare, only one was found when examining 1500 serial sections taken from a single SE, and robust structural information is lacking. Growing transgenic *Arabidopsis* expressing SEOR1 fused to Cry2(WT) in micro-Rocs, which allow direct visualisation of the root system in a natural soil environment (Froelich et al., 2011), would allow an *in vivo* manipulation of SEOR1Cry2(WT). The laser of the CSLM can be directed with pixel-sized accuracy, allowing precise areas to be targeted. It is anticipated that blue- light activation would promote clustering of the Cry2(WT) domains of the SEOR1 fusion in a dose-dependent way, prolonged laser light exposure generating SEOR1 proteins in the most condensed state. These could then be observed *in vivo* or in the TEM for structural assessment. Both live-cell and TEM investigations are likely to inform models of phloem flow.

Golden Gate Cloning

Generating tools for optogenetics would require the creation of novel DNA constructs and this is typically a laborious multi-step process. The traditional cloning method involves joining two DNA fragments, flanked by restriction endonuclease (RE) generated overlaps, with DNA ligase (see figure 6.2).

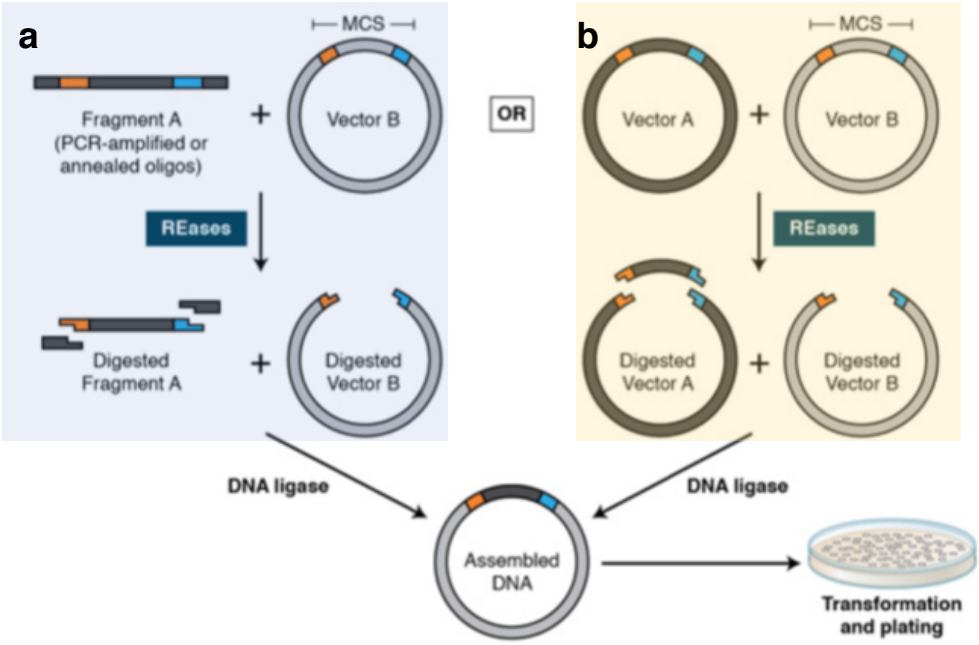

Figure 6.2 Traditional Cloning using restriction endonucleases and DNA ligation

a) Polymerase chain reaction (PCR) adds RE recognition sites to DNA. The same sites are found within the multiple cloning site (MCS) of the cloning vector B. Both can be cut with the same RE generating complementary ends. These can then be joined together using T4 DNA ligase. b) Alternatively, fragments can be moved between vectors following digestion by RE and T4 DNA ligation. The assembled DNA can then be propagated in competent bacteria allowing amplification and sequence verification. Adapted from NEB.com

Golden gate cloning provides an attractive alternative to the traditional cloning method outlined in figure 6.2. This method still uses RE and DNA ligase but using type IIS RE as opposed to type IIP used typically. Type IIS RE differ as they cleave at a defined point shifted from their recognition sequence, meaning that the original cleavage site is not reconstituted in the final vector (see figure 6.3).

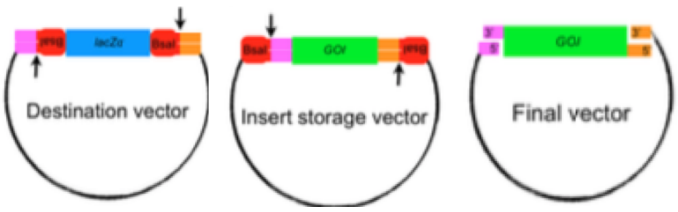

Figure 6.3 Golden Gate Cloning

Golden gate compatible destination vector has the lacZa cassette flanked by *Bsa1I* (a type IIS RE) restriction sites. The RE recognises these but cleaves outside at points marked with an arrow. The insert storage vector contains a gene of interest (GOI) also flanked by *Bsa1* recognition sites, Point of cleavage again indicated by arrows. The final vector produced following a digestion and ligation reaction does not contain *Bsa1* sites.
Adapted from Emami et al., 2013.

This ensures that once assembled the final vector is resistant to digestion. This allows the digestion and ligation reactions to take place in the same tube, by alternating between their permissive temperatures (37 °C and 16 °C respectively), which is readily achieved in a PCR thermocycler. This saves time and increases efficiency through avoiding consecutive reactions and the intervening clean-up steps.

Emami et al. (2013) described *Agrobacterium* vectors that are competent with golden gate cloning and constitutively express a plasma membrane mCherry fluorescent marker. This marker allows facile selection of T_1 transgenic plants through screening for red fluorescence in the dry seeds (see figure 6.4)

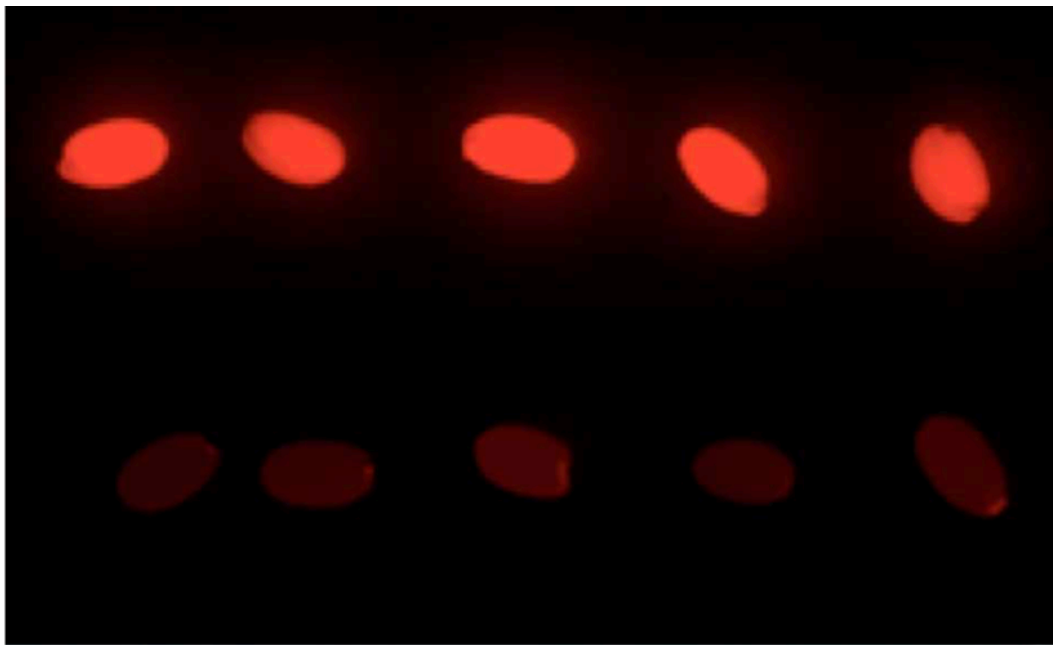

Figure 6.4 Screening transformed seeds using mCherry

Seeds are screened for mCherry expression using a stereo fluorescence microscope. Those in the top row are expressing mCherry and contain the transgene. These can then be grown on for downstream analysis. Adapted from Emami et al., 2013.

Preliminary work is underway to develop a suite of phloem-specific markers that can be examined *in planta* to further dissect the structure and function of the SE-CC complex. Specifically, the form and function of the SER will be studied, as well as the continuity between the CC and SE. Dronpa (Andro et al., 2004) is expressed from the CC- specific promoter, AtSuc2 (Truernit and Sauer, 1995) and from the SE-specific promoter (*pSEO2*; Knoblauch and Peters, 2010). By activating Dronpa (Andro et al., 2004) in developing SEs it will be possible to determine at what time these cells liberate their cellular contents and become competent to translocate. This pulse of fluorescence will also reveal the extent to which the contents of immature SE pass throughout the plant. In addition, it should be possible to tag a range of SE constituents and examine the fate of these during SE-differentiation. Such a study would greatly facilitate future studies of SE biology. To facilitate this, I have generated a range of constructs for targeting either the SE or CC, using golden-gate cloning (Table 6.1)

Table 6.1 List of constructs generated using golden-gate cloning

Promoter	**Transgene**	**Reporter**
AtSuc2 (CC)	Calnexin	PAGFP
AtSuc2 (CC)	LifeAct	YFP
AtSuc2 (CC)	RTN6	eGFP
pSEO2 (SE)		Dronpa
pSEO2 (SE)	Calnexin	PAGFP
pSEO2 (SE)	LifeAct	YFP
pSEO2 (SE)	RTN6	eGFP

pAtSuc2, Truernit and Sauer, 1995; *pSEO2*, Knoblauch and Peters, 2010; Calnexin; Runions et al., 2006 LifeAct; Riedl J et al., 2008; RTN6: Fernandez-Calvino et al., 2011, Knox et al., 2015

Creating transgenic plants expressing ER membrane markers constitutively will allow facile observations of membrane dynamics. It is anticipated that the SER surface provides a functional continuum throughout the ST, but this requires experimental verification. Whilst conclusive evidence has been produced that there is no actin cytoskeleton in mature SE (Knoblauch 2018), by expressing an actin marker under the SE promoter it would be possible to follow its disassembly in the developing SE and observe the fate of the monomers, should they remain detectable, in the translocation stream.

Reticulons (RTNs) are ER-localised proteins, understood to be involved in inducing membrane tubulation (Knox et al., 2015; Kriechbaumer et al., 2018). Twenty-one isoforms have been found in *Arabidopsis,* and a tissue specific expression pattern is emerging (Kriechbaumer et al., 2018). No studies have been published of potential RTNs in the SE. It appears that the SER in mature SEs persists without an underlying actin cytoskeleton. It lacks the dynamism associated with the ER in other cell types but retains a superficially similar form. The absence of actin in the SE could account for this stasis, whereas the presence of RTNs could support the tightly tubulated

SER structure. RTN6 was identified in a proteomic study and found to have a role in primary PD formation (Knox et al., 2015). It is the subject of study in our laboratory, and as such is a good starting point for SE localisation studies. Should it be localised to the SE it would be a very good candidate for expression using the optogenetic tools described above. *In vitro* assays have shown that RTN spacing determines the degree of dilation between the RTN insertion points (Hu et al., 2008) It should be possible to induce clustering of RTN *in planta* of the different RTN isoforms and observe the effect that this had upon the shape of the SER. The above tools should be available to the phloem community in the near future.

Lattice light sheet microscopy

In 2014 Eric Betzig, along with Stefan Hess and William Moerner, won the Nobel prize for chemistry for the development of super-resolved fluorescence microscopy. Specifically, this prize recognised Professor Betzig's development of PALM which was published in 2006 (Betzig et al., 2006) the theory and application of to plant vascular tissues is discussed in chapter 3 of this thesis. By the time the Nobel Prize was awarded however, Professor Betzig had developed a new imaging platform, the lattice light-sheet microscope (LLSM; Chen et al.,2014). LLSM illuminates a sample using two-dimensional optical lattices which are scanned plane-by-plane through the sample to generate a 3D image. The highest acquisition speeds (100 frames per second) are achieved in a diffraction limited mode which can produce a lateral resolution of 230 nm and an axial resolution of 370 nm (Whitehead et al., 2017). A super-resolution structured illumination microscopy mode can resolve 150 nm laterally and 280 nm axially. In both modes the sample exhibits very little evidence of phototoxicity (Whitehead et al., 2017). Of particular relevance to phloem research is that the orthogonal beam can penetrate up to 100 μm into the sample (Chen et al., 2017). It is known that the phloem in young seedlings is around 50 μm from the surface (Froelich et al., 2011) bringing it comfortably within LLSM range. This combined with

intrinsic low phototoxicity makes LLSM ideal for performing *in situ* observations of phloem, in particular following SE differentiation through using the golden gate generated tools described above.

7. References

Alvarez, M. E., Pennell, R. I., Meijer, P. J., Ishikawa, A., Dixon, R. A. and Lamb, C. (1998) Reactive oxygen intermediates mediate a systemic signal network in the establishment of plant immunity. Cell 92: 773-784.

Andresen, M., Stiel, A. C., Fölling, J., Wenzel, D., Schönle, A., Egner, A., Eggling, C., Hell, S. W. and Jakobs. (2008) Photoswitchable fluorescent proteins enable monochromatic multilabel imaging and dual color fluorescence nanoscopy. Nature Biotechnology 26: 1035-1040.

Andro, R., Mizuno, H. and Miyawaki, A. (2004) Regulated fast reversible protein highlighting. Science 306: 1370-1373.

Axelrod, D., Burghardt, T. P., and Thompson, R. (1984) Total internal reflection fluorescence. Annual Reviews of Biophysics and Bioengineering 13: 247-268.

Barclay, G. F., Oparka, K. J. and Johnson, R. P. C. (1977) Induced disruption of sieve element plastids in *Heracleum mantegazzianum* L. Journal of Experimental Botany 28: 709-717.

Barlow, P. W. (1984) Positional controls in root development. In *Positional controls in plant development*, P. W. Barlow & D. J. Carr (eds). 281–318. Cambridge: Cambridge University Press.

Barton, D. A., Cole, L., Collings, D. A., Liu, D. Y. T., Smith, P. M. C., Day, D. A. and Overall, R. L. (2011) Cell to cell transport via the lumen of the endoplasmic reticulum. Plant Journal 66: 806-817.

Baskin, T. I., Busby, C. H., Fowke, L. C., Sammut, M. and Gubler, F. (1992) Improvements in immunostaining samples embedded in methacrylate: localisation of microtubules and other antigens throughout developing organs in plants of diverse taxa. Planta 187: 405-413.

Baskin, T. I., Miller, D. D., Vos, J. W., Wilson, J. E. and Hepler, P. K. (1996) Cryofixing single cells and multicellular specimens enhances structure and immunocytochemistry for light microscopy. Journal of Microscopy 182: 149-161.

Bates, M., Huang, B., Dempsey, G. T. and Zhuang, X. (2007) Multicolour super-resolution imaging with photo-switchable fluorescent probes. Science 317: 1749-1753.

Baulcombe, D. C., Chapman, S. and Santa Cruz, S. (1995) Jellyfish green fluorescent protein as a reporter for virus infections. Plant Journal. 7: 1045-1053.

Bayer, E., Sparkes, I., Vanneste, S. and Rosado, A. (2017) From shaping organelles to signalling platforms:the emerging functions of plant ER–PM contact sites. Current Opinion in Plant Biology 40: 89-96.

Behnke, H. D. and Schulz, A. (1983) The development of specific sieve-element plastids in wound phloem of *Coleus blumei* (S-type) and *Pisum sativum* (P-type), regenerated from amyloplast containing parenchyma cells. Protoplasma 114: 125-132.

Behnke, H. D., and Sjolund, R. D. (1990) Preface. In Sieve Elements: Comparative Structure and Development, H.D. Behnke and R. D. Sjolund, eds (Springer-Verlag), pp v- vi.

Bell, K. and Oparka, K. J. (2011) Imaging plasmodesmata. Protoplasma 248: 9-25.

Bell, K. and Oparka, K. (2015). Preparative methods for imaging plasmodesmata at super-resolution. Methods in Molecular Biology 1217: 67-79.

Bell, K., Mitchell, S., Paultre, D., Posch, M. and Oparka, K. (2013) Correlative imaging of fluorescent proteins in resin-embedded plant material. Plant Physiology 161: 1595-1603.

Bell, K., Oparka, K. and Knox, K. (2016) Super-resolution imaging of live BY2 cells using 3D-structured illumination microscopy. Bio-protocol 6: e1697

Bell, K., Oparka, K. and Knox, K. (2018) Preparation and imaging of specialised ER using super-resolution and TEM techniques. Methods in Molecular Biology 1691: 33-42.

Betzig, E., Patterson, G. H., Sougrat, R., Lindwasser, O. W., Olenych, S., Bonifacino, J. S., Davidson, M. W., Lippincott-Schwartz, J. and Hess, H. F. (2006) Imaging intracellular fluorescent proteins at nanometer resolution. Science 313: 1643-1645.

Billinton, N. and Knight, A. W. (2001). Seeing the wood through the trees: A review of techniques for distinguishing green fluorescent protein from endogenous autofluorescence. Analytical Biochemistry 291: 175-197.

Blackman, L.M., Boevink, P., Santa Cruz, S., Palukaitis, P. and Oparka, K.J. (1998) The movement protein of cucumber mosaic virus traffics into sieve elements in minor veins of *Nicotiana clevelandii*. Plant Cell 10: 525-537.

Boevink, P., Oparka, K. Santa Cruz, S., Martin, B., Betteridge, A. and Hawes, C. (1998) Stacks on tracks: the plant Golgi apparatus traffics on an actin/ER network. Plant Journal 15: 441-447.

Brandizzi, F., Irons, S. L., Johansen, J., Kotzer, A. and Neumann, U. (2004) GFP is the way to glow: bioimaging of the plant endomembrane system. Journal of Microscopy 214: 138-158.

Buckley, A. M., Petersen, J., Roe, A. J., Douce, G. R. and Christie, J. M. (2015) LOV-based reporters for fluorescence imaging. Current Opinion in Chemical Biology 27: 39-45.

Bugaj, L., Choksi, A. T., Medusa, C. K., Kane, R. S. and Schaffer, D. V. (2013) Optogenetic protein clustering and signalling activation in mammalian cells. Nature Methods 10: 249-252.

Chalfie, M., Tu, Y., Euskirchen, G., Ward, W. W. and Prasher D. C. (1994) Green fluorescent protein as a marker for gene expression. Science 263: 802-805.

Chapman, S., Oparka, K. J. and Roberts, A. G. (2005) New tools for in vivo fluorescence tagging. Current Opinion in Plant Biology 8: 565-573.

Cheadle, V. I. (1956) Research on xylem and phloem: Progress in fifty years. American Journal of Botany 43: 719-731.

Chen, B., Legant, W. R., Wang, K., Shao, L., Milkie, D. E., Davidson, M. W., Janetopoulos, C., Wu, X. S., Hammer III, J. A., Liu, Z., English, B. P., Mimori-Kiyosue, Y., Romero, D. P., Ritter, A. T., Lippincott-Schwarz, J., Fritz-Laylin, L., Mullins, R. D., Mitchell, D. M., Bembeneck, J. N., Reymann, A., Böhme, R., Grill, S. W., Wang, J. T., Seydoux, G., Tulu, U. S., Kiehart, D. P. and Betzig, E. (2014) Lattice light-sheet microscopy: Imaging molecules to embryos at high spatiotemporal resolution. Science 346: 439-351.

Christensen, N. M., Faulkner, C. and Oparka, K. (2009) Evidence for Unidirectional Flow through Plasmodesmata. Plant Physiology 150: 96-104.

Cortese, K., Diaspro, A. and Tacchetti, C. (2009) Advanced correlative light/ electron microscopy: current methods and new developments using Tokuyasu cryosections. Journal of Histochemistry and Cytochemistry 57: 1103-1112.

Crawford, K. M. and Zambryski, P. C. (2001) Non-targeted and targeted protein movement through plasmodesmata in leaves in different developmental and physiological states. Plant Physiology 125: 1802-1812.

Cronshaw, J. and Esau, K. (1967) Tubular and fibrillar components of mature and differentiating sieve elements. Journal of Cell Biology 34: 801-815.

Deeks, M. J. and Hussey, P. J. (2016) Plant Actin Biology eLS doi.org/10.1002/9780470015902.a0021255.pub2

Dickson, R. M., Cubitt, A. B., Tsien, R. Y. and Moerner, W. E. (1997) On/off blinking and switching behaviour of single molecules of green fluorescent protein. Nature 388: 355-358.

Dobbie, I. M., King, E., Parton, R. M., Carlton, P. M., Sedat, J. W., Swedlow, J. R. and Davis, I. (2011) OMX: a new platform for multimodal, multichannel wide-field imaging. Cold Spring Harbour Protocols 8: 899-909.

Ehlers, K., Knoblauch, M. and van Bel, A. J. E. (2000) Ultrastructural features of well-preserved and injured sieve elements: minute clamps keep the phloem transport conduits free for mass flow. Protoplasma 214: 80-92.

Emami, S., Yee, M. and Dinney, J. R. (2013) A robust family of Golden Gate *Agrobacterium* vectors for plant synthetic biology. Frontiers in Plant Science 4: 1-6.

Epel, B. (2009) Plant viruses spread by diffusion on ER-associated movement-protein-rafts through plasmodesmata gated by viral induced host beta-1, 3-glucanases. Seminars in Cell and Developmental Biology 20: 1074-1081.

Esau, K. (1965) Fixation images of sieve element plastids in *Beta*. Proceedings of the National Academy of Science of the United States of America 54: 429-437.

Esau, K. (1972) Changes in the nucleus and endoplasmic reticulum during differentiation of a sieve element in *Mimosa pudica* L. Annals of Botany 36: 703-710.

Esau, K. and Gill, R. H. (1973) Correlations in differentiation of protophloem sieve elements of *Allium cepa* root. Journal of Ultrastructure Research 44: 310-328.

Evert, R. F. (1977) Phloem structure and histochemistry. Annual Reviews of Plant Physiology 28: 199-222.

Evert, R. F. (1990) Dicotyledons. In Sieve Elements: Comparitive Structure, Induction and Development, H. D. Behnke and R. D. Sjolund, eds (Springer-Verlag), pp. 103-130.

Faulkner, C., Akman, O.E., Bell, K., Jeffree, C. and Oparka, K. (2008) Peeking into pit fields: A multiple twinning model of secondary plasmodesmata formation in tobacco. Plant Cell 20: 1504-1518.

Fernandez-Suarez, M. and Ting, A. Y. (2008) Fluorescent probes for super-resolution imaging in living cells. Nature Review Molecular Cell Biology 9: 929-943.

Fitzgibbon, J., Bell, K., King, E. and Oparka, K. (2010) Super-resolution imaging of plasmodesmata using three-dimensional structured illumination microscopy. Plant Physiology 153: 1453-1463.

Froelich, D. R., Mullendore, D. L., Jensen, K. H., Ross-Elliott, T. J., Anstead, J. A., Thompson, G. A., Pélissier, H. C. and Knoblauch M. (2011) Phloem ultrastructure and pressure flow: sieve-element-occlusion-related agglomerations do not affect translocation. Plant Cell 23: 4428-4445.

Furuta, K. M., Yadav, S. R., Lehesranta, S., Belevich, I., Miyashima, S., Heo, J. O., Vatén, A., Lindgren, O., De Rybel, B., Van Isterdael, G., Somervuo, P., Lichtenberger, R., Rocha, R., Thitamadee, S., Tähtiharju, S., Auvinen, P., Beeckman, T., Jokitalo, E. and Helariutta, Y. (2014) Arabidopsis NAC45/86 direct sieve element morphogenesis culminating in enucleation. Science 345: 933-937.

Geipmans, B. N. G., Adams, S. R., Ellisman, M. H. and Tsein, R.Y. (2006) The fluorescent toolbox for assessing protein location and function. Science 312: 217-224.

Gibson, T. (2009) Cell regulation: determined to signal discrete cooperation. Trends in Biochemical Sciences 34: 471-482.

Gillespie, T., Boevink, P., Haupt, S., Roberts, A. G., Toth, R., Valentine, T., Chapman, S. and Oparka, K. J. (2002) Functional analysis of a DNA-shuffled movement protein reveals that microtubules are dispensable for the cell- to-cell movement of tobacco mosaic virus. Plant Cell 14: 1207-1222.

Grabenbauer, M., Geerts, W. J., Fernandez-Rodriguez, J., Hoenger, A., Koster, A. J. and Nilsson, T. (2005) Correlative microscopy and electron tomography of GFP through photooxidation. Nature Methods 2: 8570-862.

Guenoune-Gelbart, D., Elbaum, M., Sagi, G., Levy, A. and Epel, B. L. (2008) Tobacco mosaic virus (TMV) replicase and movement protein function synergistically in facilitating TMV spread by lateral diffusion in the plasmodesmal desmotubule of *Nicotiana benthamiana*. Molecular Plant Microbial Interactions 21: 335-345.

Gurel, P. S., Hatch, A. and Higgs, H. N. (2014) Connecting the cytoskeleton to the endoplasmic reticulum and Golgi. Current Biology 24: R660- R672.

Gustafsson, M. G. (2005) Nonlinear structured-illumination microscopy: wide-field fluorescence imaging with theoretically unlimited resolution. Proceedings of the National Academy of Sciences of the United States of America 102: 13081-13086.

Gustafsson, M. G. L. (2000) Surpassing the lateral resolution limit by a factor of two using structured illumination microscopy. Journal of Microscopy 198: 82-87.

Gustafsson, M. G. L., Shao, L., Carlton, P. M., Wang, C. J. R., Golubovskaya, I. N., Cande, W. Z., Agard, D. A. and Sedat, J. W. (2008) Three-dimensional resolution doubling in wide-field fluorescence microscopy by structured illumination. Biophysical Journal 94: 4957-4970.

Gustafsson, M.G.L., Agard, D.A. and Sedat, J.W. (1999) I^5M: 3D widefield light microscopy with better than 100 nm axial resolution. Journal of Microscopy 195: 10-16.

Habuchi, S., Ando, R., Dedecker, P., Verheijen, W., Mizuno, H., Miyawaki, A. and Hofkens, J. (2005) Reversible single-molecule photoswitching in the GFP-like fluorescent protein Dronpa. Proceedings of the National Academy of Science of the United States of America 102: 9511-9516.

Hafke, J. B., Ehlers, K., Foller, J., Holl, S. R., Becker, S. and van Bel, A. J. E. (2013) Involvement of the sieve element cytoskeleton in electrical responses to cold shocks. Plant Physiology 162: 707-719.

Harrar, E. S. (1928) A stain combination for phloem tissues of woody plants. Botanical Gazette. 86: 111-12.

Harris, N. and Oparka, K. J. (1983) Connections between dictyosomes, ER and GERL in cotyledons of mung bean (*Vigna radiate* L.) Protoplasma 114: 93-102.

Haseloff, J. and Amos, B. (1995) GFP in plants. Trends in Genetics 11: 328-329.

Haseloff, J., Siemering, K. R., Prasher, D.C. and Hodge, S. (1997) Removal of a cryptic intron and subcellular localization of green fluorescent protein are required to mark transgenic *Arabidopsis* plants brightly. Proceedings of the National Academy of Science of the United States of America. 94: 2122-2127.

Haupt, S., Oparka., K. Sauer, N. and Neumann, S. (2001) Macromolecular trafficking between *Nicotiana tabacum* and the holoparasite *Cuscuta reflexa*. Journal of Experimental Botany 52: 173-177.

Hawes, C. (1994) Electron microscopy. In: Harris, N. and Oparka K. J. (eds) Plant cell biology: a practical approach. IRL, Oxford, pp 69-96.

Hawes, C. R., Juniper, B. E. and Horne, J. C. (1981) Low and high voltage electron microscopy of mitosis and cytokinesis in maize roots. Planta 152: 397-407.

Hawes, C., Kiviniemi, P. and Kriechbaumer, V. (2015) The endoplasmic reticulum: A dynamic and well-connected organelle. Journal of Integrative Plant Biology 57: 50-62.

Hayat, M. A. (1973) Principles and Techniques of Electron Microscopy. Biological Applications. Volume 3 (Van Nostrand Reinhold Company)

Hell, S. and Stelzer, E. H. K. (1992) Fundamental improvement of resolution with a 4Pi-confocal fluorescence microscope using two-photon excitation. Optics Communications 93: 277-82.

Hell, S.W. and Wichmann, J. (1994) Breaking the diffraction resolution limit by stimulated-emission: stimulated-emission-depletion fluorescence microscopy. Optics Letters 19: 780-82.

Heo, J., Bernhard, B. and Helariutta, Y. (2017) Differentiation of conductive cells: a matter of life and death. Current Opinion in Cell Biology. 35: 23-29.

Hepler, P. K. (1982) Endoplasmic reticulum in the formation of the cell plate and plasmodesmata. Protoplasma 111: 121-133.

Hepton, C. E. L., Preston, F. R. S. and Ripley, G. W. (1955) Electron microscopic observations on the structure of the sieve plates in *Cucurbita*. Nature 176: 868-870.

Hong, T.T. and Shaw, R. M. (2017) Cardiac t-tubule microanatomy and function. Physiological Reviews 97: 227-252.

Hu, J., Shibata, Y., Voss, C., Shemesh, T., Li, Z., Coughlin, M., Kozlov, M. M., Rapoport, T. A. and Prinz, W. A. (2008) Membrane proteins of the endoplasmic reticulum induce high-curvature tubules. Science 319: 1247-1250.

Huang, B., Bates, M. and Zhuang, X. W. (2009) Super-resolution fluorescence microscopy. Annual Review of Biochemistry 78: 993-1016.

Huang, B., Wang, W., Bates, M. and Zhuang, X. (2008) Three-dimensional super-resolution imaging by stochastic optical reconstruction microscopy. Science 319: 810-813.

Huang, F., Sirinakis, G., Allgeyer, E. S., Schroeder, L. K., Duim, W. C., Kromann, E. B., Phan, T., Rivera-Molina, F. E., Myers, J. R., Irnov, I., Lessard, M., Zhang, Y., Handel, M. A., Jacobs-Wagner, C., Lusk, C. P., Rothman, J. E., Toomre, D., Booth, M. J. and Bewersdorf, J. (2016) Ultra-High resolution 3D imaging of whole cells. Cell 166: 1028-1040.

Imlau, A., Truernit, E. and Sauer, N. (1999) Cell-to-cell and long-distance trafficking of the green fluorescent protein in the phloem and symplastic unloading of the protein into sink tissues. Plant Cell 11: 309-322.

Jahn, K. A., Barton, D.A., Kobayashi, K., Ratinac, K.R., Overall, R.L. and Braet, F. (2012) Correlative microscopy: providing new understanding in the biomedical and plant sciences. Micron 43: 565-582.

Jefferson, R. A., Kavanagh, T. A. and Bevan, M. W. (1987) Beta-Glucuronidase (Gus) as a sensitive and versatile gene fusion marker in plants. EMBO Journal 6: 3901-3907.

Johnson, A., and Vert, G. (2017) Single event resolution of plant plasma membrane protein endocytosis by TIRF microscopy. Frontiers in Plant Science 8: article 612

Juergensen, K., Scholz-Starke, J., Sauer, N., van Bel, A. J. E. and Grundler, F. M. W. (2003) The companion cell-specific *Arabidopsis* disaccharide carrier *AtSUC2* is expressed in nematode-induced syncytia. Plant Physiology 131: 61-69.

Keene, D. R., Tulfa, S. F., Lunstrum, G. P., Holden, P. and Horton, W. A. (2008) Confocal/TEM overlay microscopy: A simple method for correlating confocal and electron microscopy of cells expressing GFP/YFP fusion proteins. Microscopy and Microanalysis 14: 342-348.

Kempers, R., Ammerlaan, A. and van Bel, A.J.E. (1998) Symplasmic constriction and ultrastructural features of the sieve element/companion cell complex in the transport phloem of apoplasmically and symplasmically phloem-loading species. Plant Physiology 116: 271-278.

Klar, T. A., Jakobs, S., Dyba, M., Egner, A. and Hell, S.W. (2000) Fluorescence microscopy with diffraction resolution limit broken by stimulated emission. Proceedings of the National Academy of Sciences of the United States of America 97: 8206-8210.

Kleine-Vehn, J., Wabnik, K., Martinie, A., Langowski, L., Willig, K., Naramoto, N., Leitner, J., Tanaka, H., Jakobs, S., Robert, S., Luschnig, C., Govaerts, W., Hell, S. W., Runions, J. and Friml, J. (2011) Recycling, clustering, and endocytosis jointly maintain PIN auxin carrier polarity at the plasma membrane. Molecular Systems Biology 7: 540-

Knoblauch, M. (2014) Exploring a tree one cell at a time. The New York Times. https://www.nytimes.com/2014/09/02/science/trees-plants-nutrient-flow.html

Knoblauch, M. and Oparka, K. (2012) The structure of the phloem—still more questions than answers. Plant Journal 70: 147-156.

Knoblauch, M. and Peters, W. S. (2010) Münch, morphology, microfluidics – our structural problem with the phloem. Plant, Cell and Environment 33: 1439-1452.

Knoblauch, M., Stubenrauch, M., van Bel., A. J. E. and Peters, W. S. (2012) Forisome performance in artificial sieve tubes. Plant, Cell and Environment. 35: 1419-1427.

Knoblauch, M. and Peters, W. S. (2017) What actually is the Münch hypothesis? A short history of assimilate transport by mass flow. Journal of Integrative Plant Biology 59: 292-310.

Knoblauch, M. and van Bel, A. J. E. (1998) Sieve tubes in action. Plant Cell 10: 35-50.

Knoblauch, M., Peters, W. S., Bell, K., Ross-Elliott, T. and Oparka, K. (2018) Sieve-element differentiation and phloem sap contamination. Current opinion in Plant Biology 43: 43-49.

Knox, K., Wang, P., Kriechbaumer, V., Tilsner, J., Frigerio, L., Sparkes, I., Hawes, C. and Oparka, K. (2015) Putting the squeeze on plasmodesmata: A role for reticulons in primary plasmodesmata formation. Plant Physiology 168: 1563-1572.

Kodama, Y. (2016) Time gating of chloroplast autofluorescence allows clearer fluorescence imaging *In Planta*. PLOSone 11: e0152484

Köhler, R. (1998) GFP for *in viv*o imaging of subcellular structures in plant cells. Trends in Plant Science 3: 317-320.

Komis, G., Samajova, O., Ovecka, M. and Samaj, J. (2015). Super-resolution microscopy in plant cell imaging. Trends in Plant Science 20: 834-843.

Koster, A. J. and Klumperman, J. (2003) Electron Microscopy in cell biology: integrating structure and function. Nature Cell Biology 4 (Supplement): SS6-SS10.

Kriechbaumer, V., Maneta-Peyret, L., Fouillen, L., Botchway, S. W., Upson, J., Hughes, L., Richardson, J., Kittleman, M., Moreau, P. and Hawes, C. (2018) The odd one out: *Arabidopsis* reticulon 20 does not bend ER membranes but has a role in lipid regulation. Scientific Reports 8: 2130-2145.

Lee, J. Y., Wang, X., Cui, W., Sager, R., Modla, S., Czymmek, K., Zybaliov, B., van Wijk, K., Zhang, C., Lu, H. and Lakshmanan, V. (2011) A plasmodesmata-localized protein mediates crosstalk between cell-to-cell communication and innate immunity in *Arabidopsis*. Plant Cell 23: 3353-3373.

Levy, A., Erlanger, M., Rosenthal, M. and Epel, B. L. (2007) A plasmodesmata-associated β-1,3-glucanase in *Arabidopsis*. Plant Journal 49: 669-682.

Lin, M. K., Lee, Y. J., Lough, T. J., Phinney, B. S. and Lucas, W. (2009) Analysis of the pumpkin phloem proteome provides insights into angiosperm sieve tube function. Molecular and Cellular Proteomics 8: 343-356.

Lippincott-Schwartz, J. and Manley, S. (2009) Putting super-resolution fluorescence microscopy to work. Nature Methods 6: 21-30.

Lippincott-Schwartz, J. and Patterson, G. H. (2009) Photoactivatable fluorescent proteins for diffraction-limited and super-resolution imaging. Trends in Cell Biology 19: 555-565.

Loussert-Fonta, C. and Humbel, B. M. (2015) Correlative microscopy. Archives of Biochemistry and Biophysics 581: 98-110.

Luby-Phelps, K., Ning, G., Fogerty, J. and Besharse, J. C. (2003) Visualization of identified GFP-expressing cells by light and electron microscopy. Journal of Histochemistry and Cytochemistry 51: 271-274.

Maranto, A. R. (1982) Neuronal mapping: a photooxidation reaction makes lucifer yellow useful for electron microscopy. Science 217: 953-955.

Martens, H. J., Roberts, A. G., Oparka, K. J. and Schulz, A. (2006) Quantification of plasmodesmatal endoplasmic reticulum coupling between sieve elements and companion cells using fluorescence redistribution after photobleaching. Plant Physiology 142: 471-480.

McIntosh, R., Nicastro, D. and Mastronarde, D. (2005) New views of cells in 3D: An introduction to electron microscopy. Trends in Cell Biology 15: 43-51.

Mehrshahi, P., Johnny, C. and DellaPenna, D. (2014) Redefining the metabolic continuity of chloroplasts and ER. Trends in Plant Science 19: 501-507.

Meisslitzer-Ruppitsch, C., Rohrl, C., Neumuller, J., Pavelka, M. and Ellinger, A (2009) Photooxidation technology for correlated light and electron microscopy. Journal of Microscopy 235: 322-335.

MicroscopyU, by Nikon. Microscopy Basics > Numerical Aperture www.microscopyu.com

Mullendore, D. L., Windt, C. W. and Van As, H. and Knoblauch, M. (2010) Sieve tube geometry in relation to phloem flow. Plant Cell 22: 579-593.

Oparka, K., Duckett, C. M., Prior, D. A. M. and Fisher, D. B. (1994) Real-time imaging of phloem unloading in the root-tip of Arabidopsis. Plant Journal 6: 759-766.

Oparka, K. J. and Roberts, A. G. (2001) Plasmodesmata. A not so open-and-shut-case. Plant Physiology 125: 123-126.

Oparka, K. J. and Turgeon, R. (1999) Sieve elements and companion cells – Traffic control centers of the phloem. Plant Cell 11: 739-750.

Oparka, K. J., Johnson, R. P. C. and Bowden, I. D. (1981) Sites of acid phosphatase in the differentiating root protophloem of *Nymphoides peltata* (S.G. Gmel) O. Kuntze. Plant, Cell and Environment. 4: 27-35.

Oparka, K. J., Roberts, A. G., Boevink, P., Santa Cruz, S., Roberts, I. M., Pradel, K. S., Imlau, A., Kotlizky, G., Sauer, N. and Epel, B. L. (1999) Simple, but not branched, plasmodesmata allow the nonspecific trafficking of proteins in developing tobacco leaves. Cell 97**:** 743-754.

Otero, S. and Helariutta, Y. (2017) Companion cells: a diamond in the rough. Journal of Experimental Botany. 68: 71-78.

Parthasarathy, M. V. (1974) Ultrastructure of phloem in palms. III. Mature phloem. Protoplasma 79: 265-315.

Paultre, D. S. G., Gustin, M. P, Molnar, A. and Oparka, K. J. (2016) Lost in transit: long-distance trafficking and phloem unloading of protein signals in *Arabidopsis* homografts. Plant Cell 28: 2016-2025.

Peleg, G., Malter, D. and Wolf, S. (2007) Viral infection enables phloem loading of GFP and long-distance trafficking of the phloem. Plant Journal 51: 165-172.

Pélissier, H. C., Peters, W. S., Collier, R., van Bel, A.J.E. and Knoblauch, M. (2008) GFP tagging of sieve element occlusion (SEO) proteins results in green fluorescent forisomes. Plant Cell Physiology 49: 1699-1710.

Pellegrino de Iraldi, A. (1977) Significance of the Maillet method (ZIO) for cytochemical studies of subcellular structures. Experientia 33: 1-10.

Perinetti, G., Müller, T., Spaar, A., Polishchok, R., Luini, A. and Egner, A. (2009) Correlation of 4Pi and electron microscopy to study transport though Golgi stacks in living cells with super resolution. Traffic 10: 379-391.

Pfeiffer, S., Beese, M., Boettcher, M., Kawaschinski, K. and Krupinska, K. (2003) Combined use of confocal laser scanning microscopy and transmission electron microscopy for visualisation of identical cells processed by cryotechniques. Protoplasma 222: 129-137.

Prior, D. A. M., Oparka, K. J. and Roberts, I. M. (1999) *En bloc* optical sectioning of resin-embedded specimens using a confocal laser scanning microscope. Journal of Microscopy 193: 20-27.

Radford, J.E., Vesk, M. and Overall, R.L. (1998) Callose deposition at plasmodesmata. Protoplasma 201: 30-37.

Reichel, C. and Beachy, R. N. (2000) Degradation of tobacco mosaic virus movement protein by the 26S proteasome. Journal of Virology 74: 3330-3337.

Restriction Endonucleases: Molecular cloning and beyond. www.neb.com

Robards, A. W. and Humpherson, P. G. (1967) Phytoferrin in plastids of the cambial zone of Willow. Planta 76: 169-178.

Roberts, I. M., Boevink, P., Roberts, A. G., Sauer, N., Reichel, C. and Oparka, K. J. (2001) Dynamic changes in the frequency and architecture of plasmodesmata during the sink-source transition in tobacco leaves. Protoplasma 218: 31-44.

Robinson, J. M. and Takizawa, T. (2008) Correlative fluorescence and electron microscopy in tissues: immunocytochemistry. Journal of Microscopy 235: 259-272.

Ross-Elliott, T. J., Jensen, K. H., Haaning, K. S., Wager, B. M., Knoblauch, J., Howell, A. H., Mullendore, D. L., Monteith, A. G., Paultre, D., Yan, D., Otero, S., Bourdon, M., Sager, R., Lee, J., Helariutta., Knoblauch, M. and Oparka., K. (2017) Phloem unloading in *Arabidopsis* roots is convective and regulated by the phloem pole pericycle. eLife 6: e24125.

Rowland, A. A. and Voeltz, G. K. (2012) Endoplasmic reticulum-mitochondria contacts: function of the junction. Nature Reviews Molecular Cell Biology 13: 607-615.

Sahl, S. J., Hell, S. W. and Jakobs, S. (2017) Fluorescence nanoscopy in cell biology. Nature Reviews Molecular Cell Biology 18: 685-701.

Satchell, S. C. and Braet, F. (2009) Glomerular endothelial cell fenestrations: an integral component of the glomerular filtration barrier. American Journal of Renal Physiology 296: F947-F956.

Schermelleh, L., Carlton, P. M., Haase, S., Shao, L., Winoto, L., Kner, P., Burke, B., Cardoso, M. C., Agard, D. A., Gustafsson,M. G. L., Leonhardt, H. and Sedat, J. W. (2008) Subdiffraction multicolor imaging of the nuclear periphery with 3D structured illumination microscopy. Science 320: 1332-1336.

Schmidt, R., Wurm, C. A., Punge, A., Egner, A., Jakobs, S. and Hell, S. W. (2009). Mitochondrial cristae revealed with focused light. Nano Letters 9: 2508-2510.

Schneider, C. A., Rasband, W. S., and Eliceiri, K. W. (2012) NIH Image to ImageJ: 25 years of image analysis. Nature Methods 9: 671-675

Schulz, A. (1998) Phloem. Structure related to function. Progress in Botany 59: 429-475.

Schulz, A. (1992) Living sieve cells of conifers as visualised by confocal, laser-scanning fluorescence microscopy. Protoplasma 166: 153-164.

Shaner, N. C., Steinbach, P. A., and Tsein, R. Y. (2005) A guide to choosing fluorescent proteins. Nature Methods 2: 905-916.

Shin, Y., Berry, J., Pannucci, N., Haataja, M. P., Toettcher, J. E. and Brangwynne. (2017) Spatiotemporal control of intracellular phase transitions using light-activated optodroplets. Cell 168: 1-13.

Shroff, H., Galbraith, G. C., Galbraith, J. A. and Betzig, E. (2008) Live-cell photoactivated localisation microscopy of nanoscale adhesion dynamics. Nature Methods 5: 417-423.

Simpson, C., Thomas, C., Findlay, K., Bayer, E. and Maule, A. J. (2009) An *Arabidopsis* GPI-anchor plasmodesmal neck protein with callose binding activity and potential to regulate cell-to-cell trafficking. Plant Cell 21: 581-594.

Sjolund, R. and Jensen, K. (1985) EGTA-soluble antimonate precipitates are formed in phloem sieve element reticulum (SER) membranes. Plant Physiology 77: 147.

Sjolund, R. D. (1990) Sieve elements in plant tissue cultures: Development, freeze-fracture, and isolation., In Sieve Elements: Comparative Structure and Development, H.D. Behnke and R. D. Sjolund, eds (Springer-Verlag), pp 179-198.

Sjolund, R. D. (1997) The phloem sieve element: A river runs through it. Plant Cell 9: 1137-1146.

Sjolund, R.D. and Shih., C. Y. (1983) Freeze-fracture analysis of phloem structure in plant tissue cultures. I. The sieve element reticulum. Journal of Ultrastructural Research 82: 111-121.

Sperelakis, N., and Rubio R. (1971) An orderly lattice of axial tubules which interconnect adjacent transverse tubules in guinea-pig ventricular myocardium. Journal of Molecular and Cellular Cardiology 2: 211-214.

Srivastava, L. and O'Brien, T. (1966) On the ultrastructure of cambium and its vascular derivatives II. Secondary phloem of *Pinus strobus* L. Protoplasma 61: 277-293.

Staehelin, L.A. (1997) The plant ER: a dynamic organelle composed of a large number of discrete functional domains. Plant Journal 11: 1151-1165.

Stefano, G., Hawes, C. and Brandizzi, F. (2014) ER – the key to the highway. Current Opinion in Plant Biololgy 22: 30-38.

Thaine, R., Probine, M. C. and Dyer, P. Y. (1967) Existence of Transcellular Strands in Mature Sieve Elements. Journal of Experimental Botany 18: 110-127.

Thompson, M. V. and Holbrook, N. M**. (**2003). Application of a single-solute non-steady-state phloem model to the study of long-distance assimilate transport. Journal of Theoretical Biology 220**:** 419-455.

Thompson, M. V. and Wolniak, S. M. (2008) A plasma membrane-anchored fluorescent protein fusion illuminates sieve element plasma membranes in *Arabidopsis* and tobacco. Plant Physiology 146: 1599-1610.

Thorsch, J. and Esau, K. (1982) Microtubules in differentiating sieve elements of *Gossypium hirsutum*. Journal of Ultrastructural Research 78: 73-83.

Tilsner, J. and Oparka, K. J. (2010) Tracking the green invaders: Advances in imaging virus infection in plants. Biochemical Journal 430: 21-37.

Tilsner, J., Linnik, O., Christensen, N. M., Bell, K., Roberts, I. M., Lacomme, C. and Oparka, K. J. (2009) Live-cell imaging of viral RNA genomes using a Pumilio-based reporter. Plant Journal 57: 758-770.

Toth, K. F., Wang, Q. and Sjölund, R. D. (1994) Monoclonal antibodies against phloem P-protein from plant tissue cultures: I. Microscopy and biochemical analysis. American Journal of Botany 81: 1370-1377.

Truernit, E. and Sauer, N. (1995) The promoter of the *Arabidopsis thaliana* SUC2 sucrose-H^+ symporter gene directs expression of b-glucuronidase to the phloem: evidence for phloem loading and unloading by SUC2. Planta 196: 564-570.

Tsien, R. Y. (1998) The green fluorescent protein. Annual Reviews of Biochemistry 67: 509-544.

van Bel, A. J. E. (2003) The phloem, a miracle of ingenuity. Plant Cell and Environment. 26: 125-149.

van Bel, A. J. E. and Kempers, R. (1996) The pore/plasmodesm unit; key element in the interplay between sieve element and companion cell. Progress in Botany 58: 278-291.

van Bel, A. J. E. and Koops, A. J. (1985) Uptake of [^{14}C]sucrose in isolated minor-vein networks of *Commelina benghalensis* L. Planta 164: 362-369.

van Bel, A. J. E., Knoblauch, M., Furuch, A. C. U. and Hafke, J. B. (2011) (Questions)^{n} on phloem biology. 1. Electropotential waves, Ca^{2+} fluxes and cellular cascades along the propagation pathway. Plant Science 181: 210-218.

van Bel, A.J.E., Ehlers, K. and Knoblauch, M. (2002) Sieve elements caught in the act. Trends in Plant Science 7: 126-132.

Vangindertael, V., Camacho, R., Semples, W., Mizuno, H., Dedecker, P. and Janssen, K. P. F. (2018) An introduction to optical super-resolution microscopy for the adventurous biologist. Methods and Applications in Fluorescence 6: 022003.

Vasilchenko, A. S., Yuryev, M., Ryazantsev, D. Y., Zavriev, S. K., Feofanov, A. V., Grishin, E. V. and Rogozhin, E. A. (2016) Studying of cellular interaction of hairpin-like peptide EcAMP1 from barnyard grass (*Echinochloa crusgalli* L.) seeds with plant pathogenic fungus *Fusarium solani* using microscopy techniques. Scanning 38: 591-598.

Vogel, F., Hofius, D. and Sonnewald, U. (2007) Intracellular trafficking of potato leaf roll virus movement protein in transgenic *Arabidopsis*. Traffic 8: 1205-121.

Watanabe, S., Punge, A., Hollopeter, G., Willig, K. I., Hobson, R. J, Davi., M. W., Hell, S.W. and Jorgensen, E. M. (2011) Protein localization in electron micrographs using fluorescence microscopy. Nature Methods 8: 80-84.

Weatherley, P. E. and Johnson, R. P. C. (1968) The form and function of the sieve tube: A problem in reconciliation. International Review of Cytology 24: 149-192.

Westrate, L. M., Lee, J. E., Prinz, W. A. and Voeltz, G. K. (2015) Form follows function: the importance of endoplasmic reticulum shape. Annual Review of Biochemistry 84: 791-811.

White, R. G. (2013) Cell biology of sieve-element companion cell complexes. In Phloem: Molecular Cell Biology, Systemic Communication, Biotic Interactions**.** Thompson, G. A. and van Bel, A. J. E. eds (Wiley and Sons) pp 8-29.

White, T. G., Amos, W. B. and Fordham, M. (1987) An evaluation of confocal versus conventional imaging of biological structures by fluorescence light microscopy. Journal of Cell Biology 105: 41-46.

Whitehead, L. W., McArthur, K., Geoghegan, N. D. and Rogers, K. L. (2017) The reinvention of twentieth centuary microscopy for three-dimensional imaging. Immunology and Cell Biology 95: 520-524.

Wright, K. M. and Oparka, K. J. (1996) The fluorescent probe HPTS as a phloem- mobile, symplastic tracer: an evaluation using confocal laser scanning microscopy. Journal of Experimental Botany 47: 439-445.

Wright, K. M., Roberts, A. G., Martens, H. J., Sauer, N. and Oparka, K. (2003) Structural and functional vein maturation in developing tobacco leaves in relation to *AtSUC2* promoter activity. Plant Physiology 131: 1555-1565.

Zeiss application notes. Introduction to Photoactivated Localization Microscopy
www.zeiss-campus.magnet.fsu.edu/articles/superresolution/palm/introduction.html

Publications from this thesis

Fitzgibbon, J., Bell, K., King, E. and Oparka, K. (2010) Super-resolution imaging of plasmodesmata using three-dimensional structured illumination microscopy. Plant Physiology 153: 1453-1463.

Bell, K. and Oparka, K. J. (2011) Imaging plasmodesmata. Protoplasma 248: 9-25.

Bell, K., Mitchell, S., Paultre, D., Posch, M. and Oparka, K. (2013) Correlative imaging of fluorescent proteins in resin-embedded plant material. Plant Physiology 161: 1595-1603.

Bell, K. and Oparka, K. (2015). Preparative methods for imaging plasmodesmata at super-resolution. Methods in Molecular Biology 1217: 67-79.

Bell, K., Oparka, K. and Knox, K. (2016) Super-resolution imaging of live BY2 cells using 3D-structured illumination microscopy. Bio-protocol 6: e1697

Bell, K., Oparka, K. and Knox, K. (2018) Preparation and imaging of specialised ER using super-resolution and TEM techniques. Methods in Molecular Biology 1691: 33-42.

Knoblauch, M., Peters, W. S., Bell, K., Ross-Elliott, T. and Oparka, K. (2018) Sieve-element differentiation and phloem sap contamination. Current opinion in Plant Biology 43: 43-49.

3D-structured illumination microscopy (3D-SIM) and photoactivation localisation microscopy (PALM): new tools in the study of plasmodesmal structure (2010) Bell, K., Fitzgibbon, J., King, E., Flors, C., Tilsner, J. and Oparka. K. Presented at *Plasmodesmata 2010. Sydney, Austrailia*.

3D-structured illumination microscopy (3D-SIM) and photoactivation localisation microscopy (PALM): new tools in the study of plasmodesmal structure (2010) Bell, K., Fitzgibbon, J., King, E., Flors, C., Tilsner, J. and Oparka. K. Presented at *International Conference on Plant Vascular Biology 2010. Columbus, Ohio USA. Awarded second prize in 'Best Poster' category.*

Super-Resolution Imaging of Plasmodesmata Using Three-Dimensional Structured Illumination Microscopy[1][W]

Jessica Fitzgibbon[2], Karen Bell[2], Emma King[3], and Karl Oparka*

Institute of Molecular Plant Sciences, University of Edinburgh, Edinburgh EH9 3JR, United Kingdom (J.F., K.B., K.O.); and Light Microscopy Facility, College of Life Sciences, University of Dundee, Dundee DD1 5EH, United Kingdom (E.K.)

We used three-dimensional structured illumination microscopy (3D-SIM) to obtain subdiffraction ("super-resolution") images of plasmodesmata (PD) expressing a green fluorescent protein-tagged viral movement protein (MP) in tobacco (*Nicotiana tabacum*). In leaf parenchyma cells, we were able to resolve individual components of PD (neck and central cavities) at twice the resolution of a confocal microscope. Within the phloem, MP-green fluorescent protein filaments extended outward from the specialized pore-PD that connect sieve elements (SEs) with their companion cells (CCs) along the tubular sieve element reticulum (SER). The SER was shown to interconnect individual pore-PD at the SE-CC interface. 3D-SIM resolved fine (less than 100 nm) endoplasmic reticulum threads running into individual pore-PD as well as strands that crossed sieve plate pores, structurally linking SEs within a file. Our data reveal that MP entering the SE from the CC may remain associated with the SER. Fluorescence recovery after photobleaching experiments revealed that this MP pool is relatively immobile compared with the membrane probe 3,3′-dihexyloxacarbocyanine iodide, suggesting that MP may become sequestered by the SER once it has entered the SE. The advent of 3D-SIM offers considerable potential in the subdiffraction imaging of plant cells, bridging an important gap between confocal and electron microscopy.

Fluorescence-based imaging has revolutionized cell biology, allowing the localization of proteins to specific cells and organelles (Shaner et al., 2007; Frigault et al., 2009). However, conventional fluorescence microscopy is limited by the diffraction of light to approximately 200 nm in the lateral (*x-y*) plane and to about 500 nm in the axial (*z*) plane (Fernandez-Suarez and Ting, 2008; Huang et al., 2009). This is because light traveling through a lens cannot be focused to a point, only to an airy disc with a diameter of about half the wavelength of the visible emitted light (Huang et al., 2009). Confocal laser scanning microscopy has produced improvements in axial resolution due to the removal of out-of-focus flare, but it is also limited by diffraction (Huang et al., 2009). Thus, objects closer than about 200 nm cannot be resolved but appear merged into one. Many subcellular structures of interest to cell biologists lie below this resolution limit and have remained below the diffraction barrier. Such structures can be seen but not resolved.

Recently, major innovations in biological imaging have broken the diffraction barrier. These include photoactivation localization microscopy (PALM) and stimulated emission and depletion (STED; for review, see Fernandez-Suarez and Ting, 2008; Huang et al., 2009). Most subdiffraction or "super-resolution" approaches have improved resolution in either the lateral (*x-y*) plane or the axial (*z*) plane, but usually not both (Schermelleh et al., 2008). Many of the structures of interest within plant cells lie some distance from the cell wall, posing problems for some super-resolution approaches (e.g. PALM) where the subject of interest must lie close to the coverslip (Huang et al., 2009). Recently, Schermelleh et al. (2008) described a subdiffraction multicolor imaging protocol using three-dimensional structured illumination microscopy (3D-SIM). In this method, objects beyond the diffraction limit are illuminated with multiple interfering beams of light transmitted through a series of diffraction gratings, producing a resolution of 100 nm in *x-y* and 200 nm in *z* (Schermelleh et al., 2008; Huang et al., 2009). These substantial increases in resolution are significant for plant cell imaging. The thickness of the plant cell wall is typically in the region of about 700 nm, allowing limited optical sectioning capacity with a confocal

[1] This work was supported by the Biotechnology and Biological Sciences Research Council (studentship to J.F.).

[2] These authors contributed equally to the article.

[3] Present address: Advanced Microscopy Unit, School of Biomedical Sciences, University of Nottingham Medical School, Queen's Medical Centre, Nottingham NG7 2UH, UK.

* Corresponding author; e-mail karl.oparka@ed.ac.uk.

The author responsible for distribution of materials integral to the findings presented in this article in accordance with the policy described in the Instructions for Authors (www.plantphysiol.org) is: Karl Oparka (karl.oparka@ed.ac.uk).

[W] The online version of this article contains Web-only data.
www.plantphysiol.org/cgi/doi/10.1104/pp.110.157941

microscope (about 500 nm in *z*). A further advantage of 3D-SIM is that it permits the imaging of conventional fluorescent reporters and dyes that are compatible with confocal imaging, allowing a direct correlation of 3D-SIM and confocal images (Schermelleh et al., 2008).

The phloem of higher plants is a major conduit for the long-distance transport of solutes (Oparka and Turgeon, 1999) and also functions as a "superhighway" for macromolecular trafficking (Lucas and Lee, 2004; Kehr and Buhtz, 2008; Lee and Cui, 2009). However, the phloem is difficult to image with conventional optical microscopy (Knoblauch and van Bel, 1998; Oparka and Turgeon, 1999; van Bel et al., 2002). Sieve elements (SEs), the conducting cells of the phloem, are enucleate yet contain a plethora of proteins and RNAs associated with long-distance signaling and defense (van Bel and Gaupels, 2004; Lee and Cui, 2009). Many of these macromolecules are synthesized in the companion cell (CC) and passed into the SE via the specialized pore-plasmodesmata (PD) that connect the two cell types (Oparka and Turgeon, 1999; van Bel et al., 2002). Pore-PD have been suggested to be a major "lifeline" from CC to SE (van Bel et al., 2002), but the exact nature of this pathway remains unresolved.

Our current understanding of PD substructure is derived largely from electron microscope studies (Roberts, 2005). Such methods are time-consuming and do not permit facile protein localization within PD. Recent proteomics approaches have been successful in identifying new proteins associated with PD (Maule, 2008). Localization of these proteins with confocal microscopy results in the appearance of discrete punctae at the cell wall, consistent with the location of pit fields (Faulkner et al., 2008), but does not pinpoint specific protein locations within PD. In general, there is a growing gap between proteomics studies of plant organelles, including PD, and the ability to ascribe accurate addresses to these proteins (Millar et al., 2009; Moore and Murphy, 2009). The advent of 3D-SIM prompted us to explore the potential of subdiffraction imaging in plant cells, with a view to obtaining improved florescence resolution of PD. We used 3D-SIM to examine PD in a transgenic tobacco (*Nicotiana tabacum*) line expressing the viral movement protein (MP) of *Tobacco mosaic virus* (TMV) fused to GFP. Using a specific antibody to callose, a wall constituent located at the PD collar, we were able to resolve clearly the structure of single, simple PD in epidermal cells at 100-nm resolution, discriminating between the neck region of the pore and the central cavity to which it connects (Roberts and Oparka, 2003; Faulkner et al., 2008). 3D-SIM also revealed details of the central cavities of complex PD seen previously only with the electron microscope (Ding et al., 1992; Ehlers and Kollmann, 2001; Faulkner et al., 2008).

Using 3D-SIM, we were able to image PD sequentially from the epidermis to the phloem within vascular bundles, producing unparalleled images of sieve plate pores and the specialized pore-PD that connect SEs with their CCs. In the SEs, MP was no longer restricted to the central cavities of PD but became distributed along the SE parietal layer, connecting all the pore-PD along the SE-CC interface. We were able to detect fine threads of MP-GFP that extended for up to 40 μm along the SE and also crossed individual sieve plate pores. Fluorescence recovery after photobleaching (FRAP) experiments revealed that this MP-GFP pool was relatively immobile within the SE parietal layer, suggesting that the SE may sequester TMV MP on or within the sieve element reticulum (SER).

Our data reveal that 3D-SIM is especially suited to the subdiffraction imaging of plant cells and yields spatial information not previously possible with conventional fluorescence-based imaging. The unique optical sectioning capacity of 3D-SIM and the ability to produce multicolor imaging with conventional fluorophores offer enormous potential in plant cell biology.

RESULTS

Simple PD

To obtain comparisons of PD using different imaging techniques, we first examined PD using confocal microscopy and subsequently with 3D-SIM. We were unable to locate directly the same PD pores with both techniques but were able to collect images from the same regions of tissue for comparison. In the 3D-SIM microscope, we were able to collect conventional wide-field images in parallel with the 3D-SIM images, providing a direct resolution comparison of the same PD at the same optical depth within the tissue.

In the leaf epidermis, MP-labeled PD showed the characteristic punctae in the cell wall described previously using confocal imaging (Roberts et al., 2001; Faulkner et al., 2008). When leaf tissue was labeled with callose antibody, we obtained strong signals from both GFP (488 nm) and callose (Alexa 594; Fig. 1A), and these signals overlapped to produce characteristic yellow punctae within the cell wall. However, we were unable to resolve the signals clearly or to identify individual PD pores. Comparisons of the same PD viewed by conventional wide-field fluorescence imaging and 3D-SIM are shown in Figure 1 (C–G). Wide-field imaging revealed a significant overlap of the callose/GFP signals in the cell wall (Fig. 1, E and G). However, using 3D-SIM, we were able to resolve individual simple PD and to separate the GFP and Alexa 594 signals clearly (Fig. 1, C, D, and F). Measurements of individual PD estimated the callose signal to extend laterally in the cell wall for about 187 ± 6 nm ($n = 32$), slightly larger than the dimension of the raised wall collar that surrounds the PD pore (100 nm; Faulkner et al., 2008). While the dimensions of the callose signal were consistent for each simple

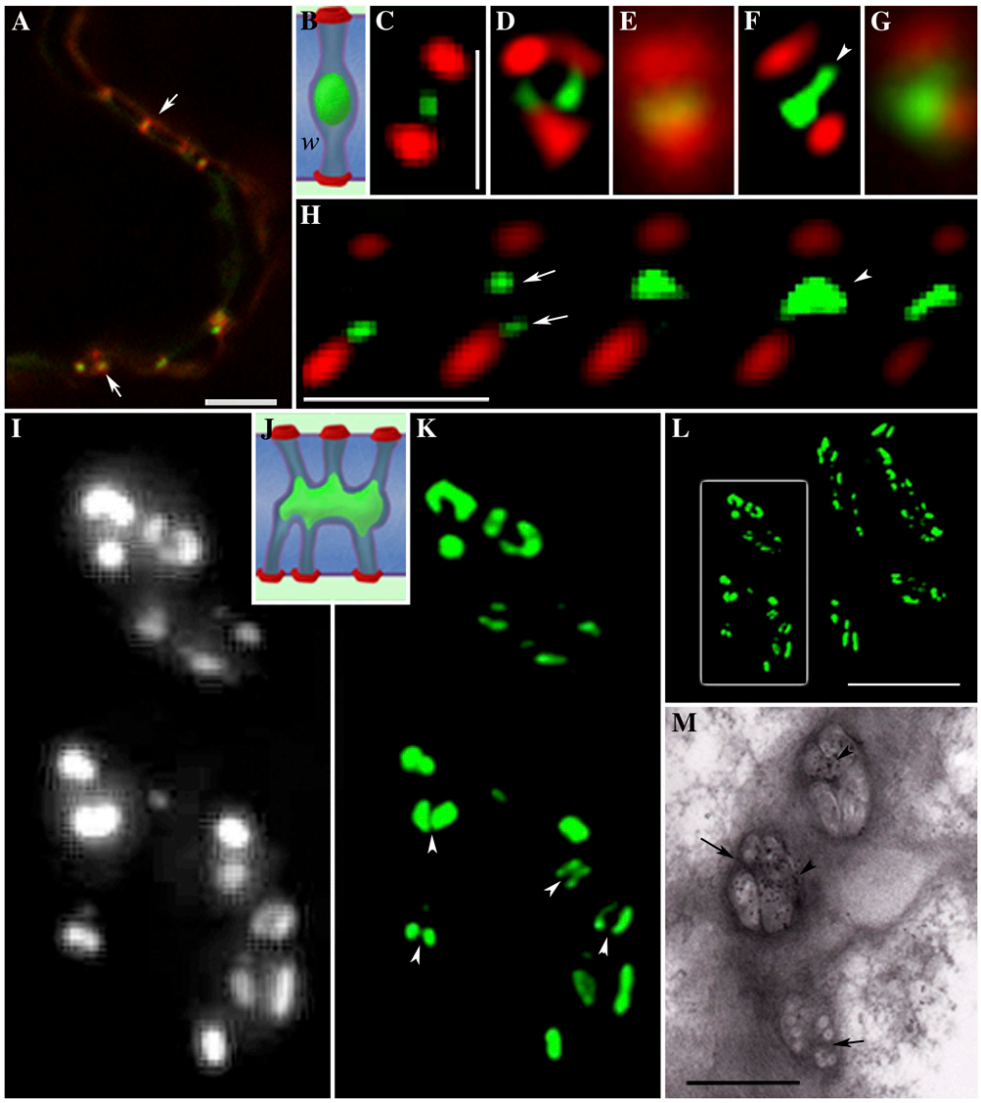

Figure 1. Simple and branched PD viewed with confocal, wide-field, and 3D-SIM imaging. A, Conventional confocal image showing PD containing MP-GFP (green) labeled with callose antibody (Alexa 594; red). Overlapping signals appear yellow (arrows), but individual PD are not resolved. Bar = 5 μm. B to G, 3D-SIM images of simple PD. B, Diagram of a single PD pore, showing callose collars (red) separated from a single central cavity (green). C to F, 3D-SIM spatially resolves the callose collars of individual PD from the central cavity. The corresponding wide-field images of the same pores pictured in D and F are shown in E and G, respectively. A Y-shaped PD configuration is shown in D. An extension of the central cavity is seen in F (arrowhead). W, Cell wall. Bars = 1 μm. H, A *z* series taken using 3D-SIM of a single PD pore. The individual images are 125 nm apart. Note that two pores can be seen (arrows), each leading to a shared central cavity (arrowhead). Bar = 1 μm. I to M, Comparative images of PD central cavities obtained with wide-field illumination (I), 3D-SIM (K and L), and EM (M). L shows a *z* stack of an entire pit field, with the boxed region, enlarged in K, revealing fine wall partitions (arrowheads) that separate individual central cavities. Similar partitions are shown in the EM image in M (arrows), in which the viral MP within central cavities is immunolabeled with gold (arrowheads). J shows a diagrammatic representation of a branched PD pore. Bars = 5 μm (L) and 1 μm (M).

pore, those of the central cavities varied considerably. In many pores, the central cavity appeared spherical (Fig. 1C), while in others, it extended laterally in the region of the middle lamella (Fig. 1F). Significantly, 3D-SIM revealed an unlabeled region of about 136 $\pm$ 6 nm (n = 15) between the central cavity and the callose collars. This region lacked viral MP and most likely corresponds to the region of pore that connects the PD entrance to the underlying cavity (Fig. 1B). In many cases, we observed two callose collars in one cell face and a single collar in the adjoining cell face (Fig. 1D), consistent with the images of Y-shaped PD often reported in transmission electron microscopy (TEM) studies (Faulkner et al., 2008). Using optical sectioning, we were able to image successive longitudinal "slices" of single PD within the cell wall, locating the two distinct pores that connect to the same central cavity (Fig. 1H).

Branched PD

While the PD that connect epidermal cells are predominantly simple in architecture, those that connect the epidermis-mesophyll and mesophyll-mesophyll boundaries are branched and arranged in discrete pit fields (Fig. 1, I–L). Using wide-field imaging of the epidermis-mesophyll interface, we could detect characteristic pit fields within which MP-GFP was detected in discrete punctae (Fig. 1I; Faulkner et al., 2008). Imaging these pit fields with 3D-SIM revealed a remarkable complexity in central cavity structure that could not be resolved with wide-field imaging (Fig. 1K) and showed that many of the punctae seen with wide-field imaging could be resolved into two or more closely associated central cavities (Fig. 1K, arrowheads). Some of these central cavities extended for up to 600 nm within the cell wall (Fig. 1K; the complete pit field is shown in Fig. 1L). Many had a horseshoe-shaped cross-section (Fig. 1K), also seen in glancing sections of the wall using comparative EM (Fig. 1M; for interpretation, see Fig. 1J). In the EM, such cavities are separated by narrow wall partitions (Fig. 1M; Faulkner et al., 2008) that could also be resolved with 3D-SIM (Fig. 1K). We were also able to image the complex PD that connect the epidermis with trichomes (Faulkner et al., 2008). By imaging the basal cell wall of the trichome in face view, we were able to optically section in z through all PD at a single wall interface (Fig. 2A). Figure 2B shows a z series, each section 125 nm apart, of an individual complex PD at the trichome-epidermis interface. Note that the channels leading from individual PD pores at the surface become progressively fused in the region of the middle lamella. Following pectinase treatment, we were able to image PD in elongated parenchyma cells surrounding vascular bundles. Here, the central cavities became increasingly elaborate, and optical sections of the cell wall revealed many closely adjacent cavities that had fused to form one extended cavity in the middle lamella region of wall (Fig. 2, C–E). The callose signals revealed that these cavities were shared by numerous overlying PD pores. These central cavities extended for over 1 μm in the middle lamella region of wall (Fig. 2, D and E).

Phloem PD

In pectinase-treated tissues, we were able to separate out phloem strands from surrounding tissues (van Bel and Koops, 1985) and to examine the PD that connect different phloem cell types. As above, we compared wide-field fluorescence and 3D-SIM images of the same cells using the same oil-immersion objective. Callose labeling of SEs with Alexa 594 revealed an exception-

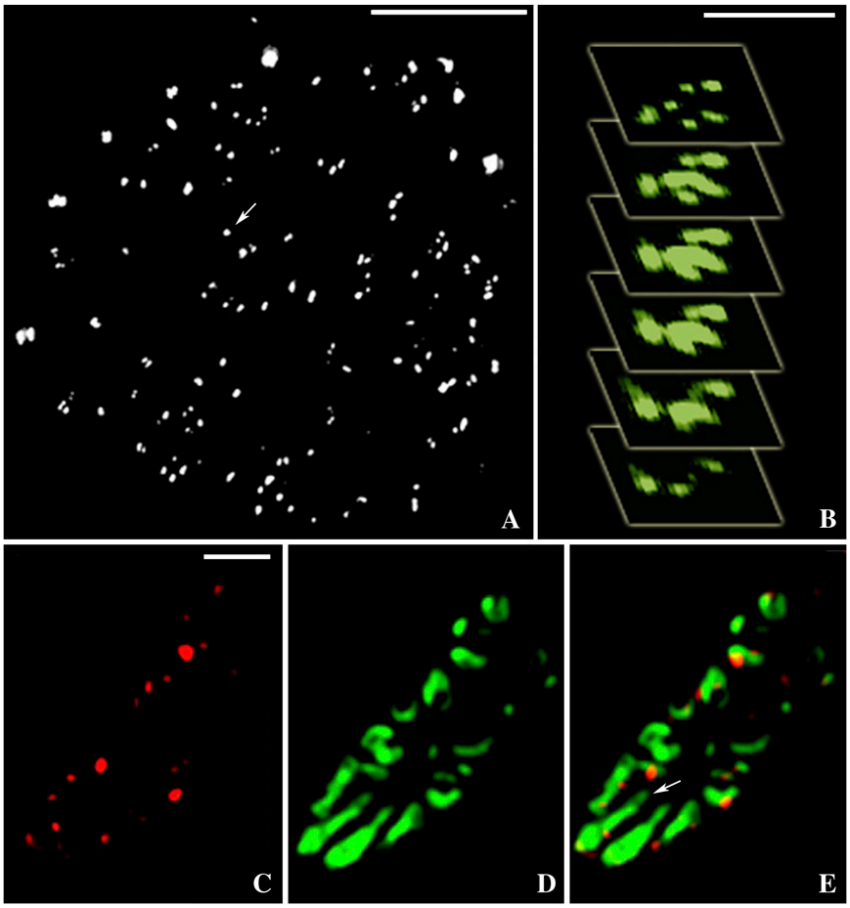

Figure 2. 3D-SIM images of branched PD. A, A z stack of all the branched PD (MP-GFP) at the trichome-epidermis interface. A single branched pore is shown (arrow). Bar = 5 μm. B, Single images (125 nm apart) of a single branched PD. Note that six branches can be detected entering from the trichome and only three entering from the epidermis. Single pores entering from the epidermis and trichome become fused in the middle lamella region of the wall. Bar = 1 μm. C to E, 3D-SIM images of pit fields in a phloem parenchyma cell. Callose is labeled with Alexa 594 (red; C), and central cavities are labeled with MP-GFP (D). Note that the central cavities extend for over 1 μm from the collars that lead into them (arrow; merged image in E). Bar = 1 μm.

ally strong signal from sieve plates (Fig. 3). Using conventional imaging, we could detect small red spots on the sieve plates, consistent with the location of callose around the sieve plate pores, but were unable to resolve clearly the individual pores (Fig. 3A). By contrast, 3D-SIM resolved the individual sieve plate pores clearly (Fig. 3B). The average diameter of the pores was 276 ± 16 nm (n = 21), and the callose collars extended this diameter to 568 ± 22 nm (n = 21).

Using 3D-SIM, we were also able to generate optical stacks through entire SE-CC complexes. For example, Figure 3C shows an optical stack of 67 separate sections, each 125 nm apart. The rotation of this image can be viewed in Supplemental Movie S1. Using optical stacking, we were also able to resolve the individual lateral sieve area pores connecting adjacent SEs (Fig. 3D; Supplemental Movie S2) and the pore-PD that connect SEs and CCs at their shared interface (Figs. 3C and 4, C–E).

Fine Strands of MP Interconnect Pore-PD at the SE-CC Interface

In confocal images of the phloem, we noticed that MP-GFP was no longer located exclusively in the central cavities of PD but extended longitudinally within the SEs (Fig. 4A). Using 3D-SIM, we could resolve MP-decorated strands of about 144 ± 6 nm (n = 30) diameter that could be traced for up to 40 μm along the SE parietal layer, specifically at the SE-CC junction, and noticed that these strands connected individual pore-PD (Fig. 4B). In surface views of the SE-CC interface, we were able to resolve the callose collars of the individual pore-PD leading into the SE (Figs. 4, C–E, and 5A). Measurements showed the pores to have a diameter of 188 ± 8 nm (n = 26), significantly smaller than the sieve plate pores. The callose collars extended the pore diameter to 510 ± 19 nm (n = 26). The intricate association of the MP strands with the pores is shown in Fig. 4 (C–E) and in Supplemental Movie S3. Optical sectioning of the SE-CC interface revealed that the strands were linked into a network, often running into the center or around the perimeters, of the pore-PD (Figs. 4, C–E, and 5A). Such fine strands could not be resolved with wide-field fluorescence imaging (Fig. 4F).

In many SEs, we observed up to four fine strands extending from each pore (Fig. 5A). The average diameter of these strands was 89 ± 6 nm (n = 6), at

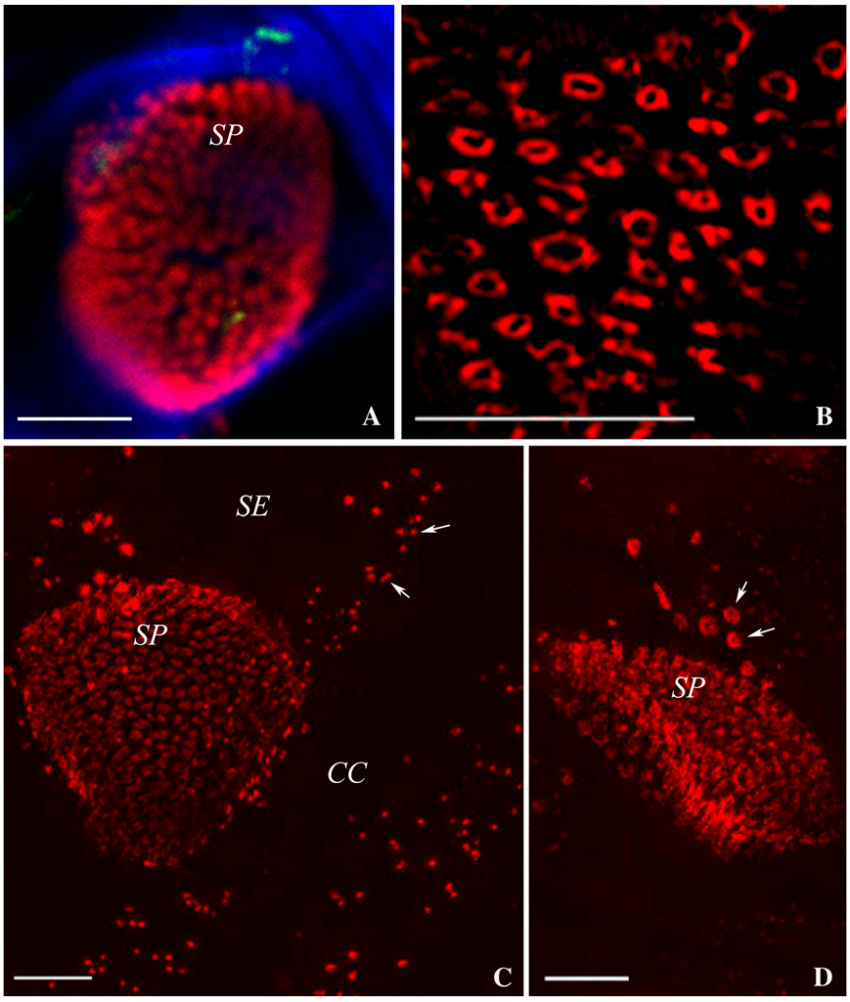

Figure 3. 3D-SIM images of SEs. A, A sieve plate (SP) imaged using confocal microscopy (callose, red; cellulose, blue). Sieve plate pores are seen as red dots but cannot be resolved. Bar = 5 μm. B, Comparative 3D-SIM image. Note that the individual sieve plate pores, and the callose collars lining them, are resolved clearly. Bar = 5 μm. C, SE-CC complex. The image is a stack of 67 images taken with 3D-SIM. Callose (red) is associated with sieve plate pores and with pore-PD (arrows). Bar = 5 μm. D, SE showing lateral sieve area pores (arrows) near the sieve plate. Bar = 5 μm.

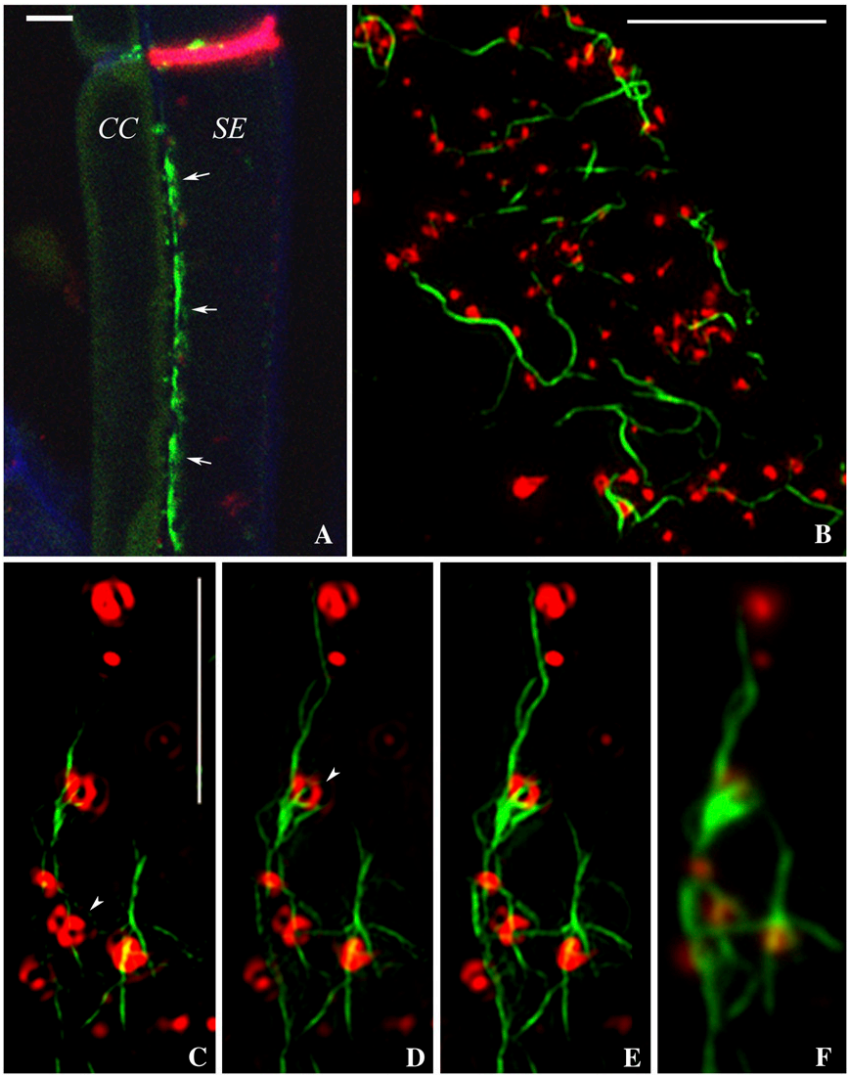

Figure 4. Viral MP decorates the SER. A, Confocal image showing MP-GFP associated with the SE-CC interface (arrows). Bar = 5 μm. B, 3D-SIM image of the surface of the SE parietal layer revealing strands of MP-decorated SER (green) associated with pore-PD (red). Bar = 5 μm. C to E, 3D-SIM images (125 nm apart) showing individual strands of MP-decorated SER associated with pore-PD. Note that the callose collars of the pore-PD are resolved (arrowheads). Bar = 5 μm. F, The corresponding wide-field image to E fails to resolve the structure of the pore-PD.

the limit of resolution of 3D-SIM. However, we were unable to detect equivalent strands of MP in the adjoining CC (data not shown). The SER is composed of an elaborate system of tubular elements and stacked cisternae that, together with the plasma membrane, mitochondria, and plastids, form the SE parietal layer (Evert, 1990; van Bel et al., 2002). The cytoskeleton is absent from enucleate SEs (Evert, 1990), making the tubular SER a likely candidate for MP targeting. To confirm this, we stained SEs with the red vital ER stain, hexyl rhodamine B (Fig. 6, A and B). As this dye photobleaches rapidly and has an emission of 574 nm, we were unable to use the 594-nm line of the 3D-SIM microscope. Using confocal microscopy, we found that MP colocalized with the tubular component of the SER (Fig. 6, A and B) but not with the stacked parietal cisternae. Also, while MP labeled the ER at the SE-CC interface only (Fig. 6B), hexyl rhodamine B stained the entire SER (data not shown). To obtain comparative TEM images, tissue was postfixed in osmium and embedded in resin. The TEM images showed good preservation of SEs, as judged by a lack of plasmolysis and the intact appearance of SE plastids, organelles acutely sensitive to SE turgor loss (Supplemental Fig. S1, A and B; Barclay et al., 1976; Ehlers et al., 2000). Using the MP-GFP tobacco line, we were able to image the SER using TEM for comparison with the 3D-SIM images. In glancing sections of the SE wall, the SER was visible as a fine, tubular network identical to that seen with 3D-SIM (Supplemental Fig. S1, B and C). Measurements of the tubular SER revealed an average diameter of 77 $\pm$ 3 nm (n = 11).

100-nm Strands of ER Traverse Sieve Plate Pores

Next, we examined the surfaces of sieve plates connecting individual SEs. Here, we also found tubular elements of MP-decorated SER (Fig. 5B). In optical stacks of sieve plates, the sieve plate pores had the appearance of "cotton reels" due to the callose cylinders lining them (Fig. 5, B and E–H; Supplemental Movie S4). In many of these pores, we noticed that the

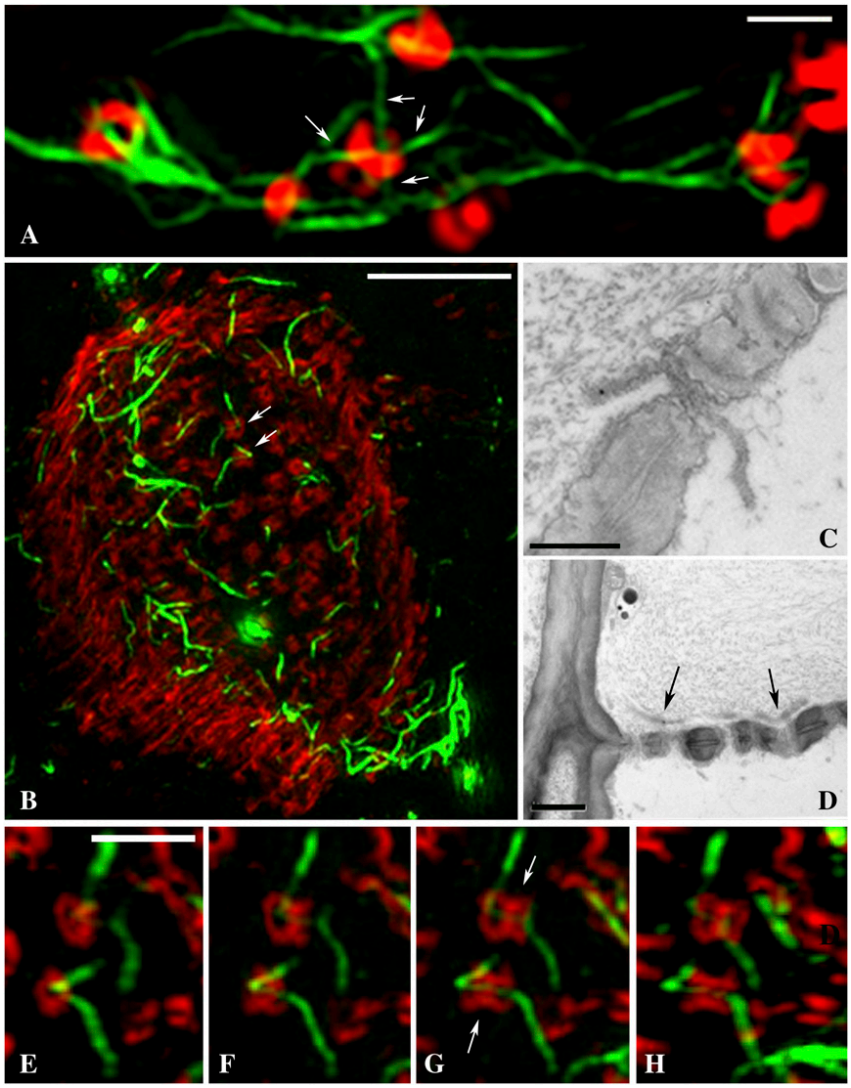

Figure 5. High-magnification views of pore-PD and sieve plate pores. A, High-magnification view of the pore-PD shown in Figure 4E. Four individual SER strands (less than 100 nm diameter; arrows) can be seen to enter a single pore. Bar = 1 μm. B, A *z* stack of a sieve plate (callose, red) showing fine strands of MP-decorated SER (green) traversing the sieve plate pores (arrows). Bar = 5 μm. C and D, EM images of petiole phloem fixed using the same protocol as for 3D-SIM. C depicts a single ER profile traversing a sieve plate pore, and D shows ER elements (arrows) lying adjacent to a sieve plate. Bars = 0.5 μm (C) and 1 μm (D). E to H, Details of the sieve plate pores shown in B. The images are from a rotated *z* series of the sieve plate. Note that the SER strands (arrows in G) can be traced from one SE to another through the pores. Bar = 1 μm.

tubular SER became thinned down into fine strands of about 103 ± 3 nm (n = 30) in diameter that appeared to traverse the sieve plates (Fig. 5B). To examine this further, we rotated the optical stack to obtain 3D images of single sieve plate pores. This confirmed that the fine strands were running longitudinally across individual pores from one SE to the next (Fig. 5, E–H). By TEM, we were able to detect similar ER strands of about 80 nm traversing sieve plate pores (Fig. 5C) and lying against sieve plates (Fig. 5D).

FRAP of Enucleate SEs

To determine if the MP-GFP located on the SER was mobile, we imaged phloem strands from intact petioles and photobleached the SER using high-intensity illumination at 488 nm with the confocal microscope. MP-GFP showed little recovery into the photobleached area (Fig. 6C). To determine if tissue isolation had disrupted the SER, we also performed FRAP on SEs stained with 3,3′-dihexyloxacarbocyanine iodide ($DiOC_6$), a membrane potential probe that selectively stains the ER (Martens et al., 2006). In contrast to MP-GFP, $DiOC_6$ showed a rapid recovery into the photobleached area (Fig. 6C), indicating that the SER was continuous between the bleached and unbleached regions of the SE.

DISCUSSION

Despite a historical acceptance that resolution is limited by diffraction (for review, see Huang et al., 2009), there has been a rapid expansion of imaging techniques that break the diffraction barrier. Many of these have achieved improved resolution in either the *x-y* or *z* axes, but 3D-SIM is currently the only method that achieves 2-fold increases in resolution in both dimensions (Schermelleh et al., 2008). The relative ease of 3D-SIM and its improved capacity for optical *z* stacking over confocal microscopy made it an ideal choice for imaging PD, structures below the limit of

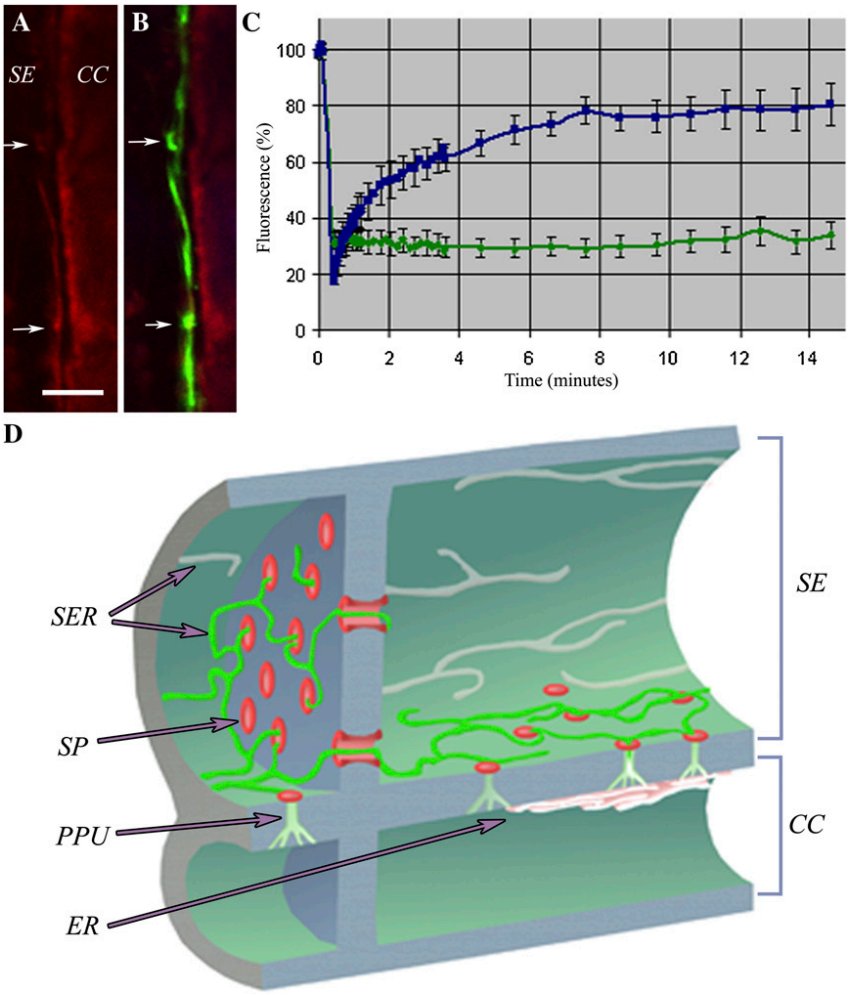

Figure 6. A and B, Confocal images of the SE-CC interface stained with the red ER-specific dye, hexyl rhodamine B (arrows; A). The corresponding MP-GFP image (B) shows that MP decorates the SER specifically within the SE (arrows). Bar = 5 μm. C, FRAP data in which the GFP-labeled SER was photobleached with high-intensity illumination at 488 nm. The recovery profiles for $DiOC_6$ (blue) and GFP (green) are shown for the same bleach conditions. D, Diagrammatic representation of the relationship of the SER with sieve plate pores (SP) and pore-PD (PPU) as revealed by 3D-SIM. MP-GFP (green) highlights the SER at the SE-CC interface only and labels the SER strands that connect individual pore-PD. The SER forms a continuum between SE and CC. Callose associated with pore-PD and sieve plate pores is shown in red.

resolution of conventional fluorescence imaging. At present, 3D-SIM, in common with many of the other super-resolution approaches, does not achieve live-cell imaging and is restricted to samples that must remain static during imaging. TEM remains the highest resolution technique for imaging plant cells, although the major advantages of 3D-SIM over TEM are the ability to localize a wide range of proteins rapidly using conventional fluorophores and its ability to rapidly produce 3D information. Unlike confocal imaging, 3D-SIM cannot yet be used to image protein dynamics using photoactivatable probes, although recent reports suggest that super-resolution techniques will enter the domain of live-cell imaging in the near future (Huang et al., 2009).

Although the membrane-lined pore of PD is about 50 nm (Roberts, 2005), the width of the raised wall collars extends the structural diameter of tobacco PD to about 100 nm (Faulkner et al., 2008), within the resolution limit of 3D-SIM (Schermelleh et al., 2008). We have shown that different components of PD (collar and central cavity) can be spatially resolved with accuracy. Within the phloem, a tissue recalcitrant to conventional imaging, 3D-SIM resolved sieve plate pores, lateral sieve areas, and the pore-PD that connect CC and SE. In the last of these, we were able to image individual strands of ER entering the pore from the SE side of the cell wall. Recently, Truernit et al. (2008) described a clearing method for measuring a range of phloem parameters in three dimensions using confocal imaging. This method is still limited by diffraction, but used in combination with 3D-SIM it may offer an approach to studying phloem architecture at super-resolution.

Previously, we showed that the MP of *Cucumber mosaic virus* (CMV) entered SEs during virus infection, and we noted a fibrillar structure within SEs that was below the limit of resolution (Blackman et al., 1998). We show here that this structure is likely to be the tubular SER and that the TMV MP also enters SEs via PD to become distributed throughout the SER (shown diagrammatically in Fig. 6D). Although MP-GFP must enter the enucleate SE from the CC (Oparka and Turgeon, 1999), our FRAP data suggest that MP is relatively immobile in the SE parietal layer compared with the ER membrane probe ($DiOC_6$). TMV MP has been shown previously to accumulate as a fibrillar material in the central cavities of PD, possibly within

the extended desmotubule lumen (Ding et al., 1992). However, we have been unable to determine the exact location (membrane or lumen) of MP-GFP that decorates the SER. The lack of mobility of MP in the SER may reflect the fact that it is sequestered on this unique structure. Electron micrographs depicting SER in surface views are extremely rare, but those that do (Esau, 1978; Warmbrodt, 1986) reveal an intricate strand-like network identical to that reported here using 3D-SIM (Supplemental Fig. S1C). This fine SER network is quite unlike that of nucleate parenchyma cells (Brandizzi et al., 2002; Runions et al., 2006). The SER may be involved in a range of functions (van Bel et al., 2002) and has recently been suggested to be a Ca^{2+} reservoir essential for the maintenance of long-distance electrical signals in the phloem (Furch et al., 2007). Only a limited number of organelles remain in the mature SE (Evert, 1990; Oparka and Turgeon, 1999; van Bel et al., 2002), but despite the selective autolysis of the cell, the SE parietal layer contains several biosynthetic enzymes (Bird et al., 2003; Wang et al., 2003), transporters (Meyer et al., 2004), protein signals (Khan et al., 2007), and transcripts (for review, see Lee and Cui, 2009). These raw materials are supplied by the CC and passed selectively into the SE (Oparka and Turgeon, 1999; van Bel et al., 2002). To achieve this feat, the SE must anchor these components in the face of mass flow occurring through the sieve tube lumen (Sjolund, 1997; Ehlers et al., 2000).

Many viral ribonucleoprotein complexes enter SEs for long-distance transport and exit the phloem at distant sites in the plant (Kehr and Buhtz, 2008; Lee and Cui, 2009). We showed recently that infectious TMV RNA becomes anchored to the cortical ER within seconds of its injection into a single trichome cell (Christensen et al., 2009). The TMV MP remodels the cortical ER during infection (Heinlein et al., 1998; Gillespie et al., 2002) and transfers the viral genome through PD (Guenoune-Gelbart et al., 2008). The continuous ER network through PD in the form of the central desmotubule (Roberts, 2005), as well as the maintained continuity of ER within and between SEs (Evert, 1990), suggest that some viruses may require to locate the ER only once during infection, subsequently depending on the cortical ER to "hitch a ride" to the SE (Christensen et al., 2009). At present, we have been unable to determine why MP is restricted to the SE-CC interface, as the SER encircles the entire SE parietal layer (Evert, 1990; Martens et al., 2006). The radial distances for MP diffusion on the SER within the SE are small compared with the axial dimensions, so there appears to be no a priori reason why MP should not associate with the entire SER. One possibility is that a functionally unique form of SER occurs at the SE-CC interface, making it possible for selective protein transport to occur between these two cell types.

Previously, we showed using FRAP that ER coupling between CCs and SEs is extensive compared with other cell types (Martens et al., 2006). It has been suggested that the TMV MP may also diffuse between infected and noninfected cells via the membrane of the desmotubule (Guenoune-Gelbart et al., 2008). Our data here suggest that small membrane-bound molecules (e.g. $DiOC_6$), in addition to moving between CC and SE, may also diffuse along the SER, although the lateral diffusion of the TMV MP appears to be restricted. During natural TMV infection, it is thus possible that the SER represents the "end of the line" for viral MP once invasion of the SE has occurred. The appearance of MP on the SER begs the question of why MP is not normally retained on the ER of nonvascular parenchyma cells during TMV infection. During early TMV infection, MP decorates the ER but is subsequently removed by the host cell, later appearing on microtubules (Gillespie et al., 2002). The most likely explanation for the removal of MP from the ER is that nucleate parenchyma cells have a cytoskeleton-based degradation pathway (Gillespie et al., 2002; Reichel et al., 2006) that is absent from the enucleate SEs.

Over 40 years ago, using conventional light microscopy, Thaine and colleagues (Thaine, 1961; Thaine et al., 1967) described fine "transcellular strands" in enucleate SEs and suggested that these were involved in phloem translocation. These membranous strands were later dismissed as diffraction artifacts (Esau, 1963) or bundles of P-protein filaments created by wounding (Johnson et al., 1976). Thaine and colleagues would have been unable to resolve the fine strands that we observed here using subdiffraction imaging. However, their images may have represented larger bundles of SER strands running longitudinally along the SE-CC interface.

Using 3D-SIM, we have been able to resolve several structures seen previously only with the electron microscope. Significantly, we were able to use standard cytological methods and fluorophores compatible with confocal imaging. The fields of cell biology and molecular plant pathology are likely to benefit enormously from the application of 3D-SIM.

MATERIALS AND METHODS

Plant Material

Tobacco (*Nicotiana tabacum* 'Xanthi') plants expressing TMV MP-GFP (Roberts et al., 2001) and cv Samsun nn plants were grown from seed in a heated glasshouse and used for experiments between 30 and 55 d old.

Confocal Microscopy

For imaging GFP, longitudinal sections of petiole were prepared using a Vibroslice Tissue Slicer HA752 (Camden Instruments). Petioles were embedded in 5% Phytoagar (Duchefa Biochemie) to stabilize before cutting into approximately 100-μm sections. The excess Phytoagar was trimmed before the tissue was briefly counterstained with aniline blue to visualize callose at sieve plates. The tissue was mounted in water and viewed through a coverslip.

To image the ER in SEs, tissue sections were prepared as above and then stained with hexyl rhodamine B (Invitrogen) at 0.1 μg mL^{-1}.

The tissues were imaged using a Leica SP2 confocal laser scanning microscope (Leica Microsystems) with a ×63 water-immersion lens (HCX PLAPO CS; Leica Microsystems). Aniline blue was excited using a 405-nm

laser, GFP with a 488-nm laser, and hexyl rhodamine B with 561-nm laser source.

Immunolocalization

Longitudinal petiole tissue sections were prepared as above and then fixed in 4% paraformaldehyde/0.25% glutaraldehyde in PME buffer (50 mM PIPES, 2 mM EGTA, and 2 mM $MgSO_4$, pH 6.8). The tissue was washed with PME before the vasculature was separated following a 15-min pectinase treatment at 37°C: pectinase (2%; Invitrogen) in 1% (w/v) phosphate-buffered saline (PBS) with 1% (w/v) bovine serum albumin and 5 mM EDTA. The sections were then rinsed in PME with 10% (v/v) glycerol and 0.02% (v/v) Triton X-100 before washing further with 1% (w/v) PBS. Nonspecific binding sites were blocked using 3% (w/v) PBS and 50 mM Gly in 1% (w/v) PBS for 20 min. The tissue was then incubated overnight in mouse anti-callose (Biosupplies) antibody at a 1:400 dilution. Sections were rinsed briefly in the blocking solution before incubating with secondary antibody, anti-mouse Alexa 594 (Invitrogen) diluted 1:500, for 3 h. All antibodies were diluted in 1% (w/v) bovine serum albumin, 0.02% (v/v) Tween in 1% (w/v) PBS and incubated at 37°C. The petiole sections were mounted in Citifluor AF1 antifade agent (Agar Scientific) under a coverslip and then sealed with nail varnish. Tissues were then imaged with a Leica SP2 confocal scanning microscope, as described above using a 591-nm laser source for the Alexa 594, or with 3D-SIM as described below.

TEM

For TEM, tissue was fixed as described above in 3% glutaraldehyde in 0.1 M sodium cacodylate buffer followed by postfixation in 1% osmium tetroxide in 0.1 M sodium cacodylate buffer prior to embedding in Araldite (Oparka and Turgeon, 1999). EM immunolocalization of viral MP within PD was performed exactly as described by Faulkner et al. (2008).

Structured Illumination

The protocol applied was based on that described by Schermelleh et al. (2008). Images were acquired using a UPlanSApochromat 100×, numerical aperture 1.4, oil-immersion objective lens (Olympus) and back-illuminated Cascade II 512 × 512 EMCCD camera (Photometrics) on the OMX version 2 system (Applied Precision) equipped with 405, 488, and 593 solid-state lasers.

Samples were illuminated by a coherent scrambled laser light source that had passed through a diffraction grating to generate the structured illumination by interference of light orders in the image plane to create a 3D sinusoidal pattern, with lateral stripes approximately 0.2 μm apart. The pattern was shifted laterally through five phases and through three angular rotations of 60′ for each *z* section, separated by 0.125 μm.

Exposure times were typically between 50 and 250 ms, and the power of each laser was adjusted to achieve optimal intensities of between 2,000 and 4,000 counts in a raw image of 16-bit dynamic range, at the lowest possible laser power to minimize photobleaching. Where required, the cameras were run in EMCCD mode and gain was applied. Each frame acquisition was separated by a 300-ms pause.

Image Processing

Raw images were processed and reconstructed to reveal structures with greater resolution (Gustafsson et al., 2008). The channels were then aligned in *x*, *y*, and rotationally using predetermined shifts as measured using a target lens and 100-nm Tetraspeck fluorescent microspheres (Invitrogen) in the Softworx alignment tool (Applied Precision).

FRAP

Large petiole pieces were immersed in PBS and cut into fine longitudinal sections with a scalpel. Sections from MP-GFP plants were incubated in 0.25 mg mL^{-1} aniline blue solution, while sections from wild-type tobacco (cv Samsun nn) plants were incubated in a 0.25 mg mL^{-1} aniline blue/2 μg mL^{-1} $DiOC_6$ solution for 10 min. Sections were then immersed in clean PBS and washed for 5 min with agitation before being mounted on slides with coverslips.

FRAP was performed using the Leica Confocal Suite FRAP Wizard. Five prebleach images were collected with a 488-nm laser at 20% intensity (×63 water objective, unidirectional scan, zoom ×3, resolution 512 × 512), and then a 10-μm region was specifically bleached using 10 scans with the 488-nm laser at 100% intensity. Postbleach images were then collected using the same settings as the prebleach images for approximately 15 min in total. Scans were taken every 1 s for the first 30 s, then every 10 s for the next 150 s, and then every 1 min for the subsequent 12 min.

The background fluorescence was subtracted from all values, and each series was corrected for bleaching during the postbleach acquisition phase using an area of fluorescence outside of the cell containing the region of interest for reference. Fluorescence readings were then normalized to percentage values of the prebleach fluorescence, and the normalized measurements were averaged.

Supplemental Data

The following materials are available in the online version of this article.

Supplemental Figure S1. SEs and CCs.

Supplemental Movie S1. Movie showing the rotation of a single SE (from Fig. 3C).

Supplemental Movie S2. Movie showing the rotation of two adjacent sieve plates (one shown in Fig. 3D).

Supplemental Movie S3. Movie of Figure 4B, showing the MP-decorated SER and its relationship with pore-PD

Supplemental Movie S4. Movie of Figure 5E, showing the rotation of sieve plate pores.

ACKNOWLEDGMENTS

We are grateful to Danae Paultre for technical assistance and to the Scottish Universities Life Sciences Alliance and the Light Microscopy Facility, University of Dundee, for access to the 3D-SIM microscope.

Received April 20, 2010; accepted May 25, 2010; published May 27, 2010.

LITERATURE CITED

Barclay G, Oparka KJ, Johnson RPC (1976) Induced disruption of sieve-element plastids in *Heracleum mantegazzianum* L. J Exp Bot **28:** 709–717

Bird DA, Franceschi VR, Facchini PJ (2003) A tale of three cell types: alkaloid biosynthesis is localized to sieve elements in opium poppy. Plant Cell **15:** 2626–2635

Blackman LM, Boevink P, Santa Cruz S, Palukaitis P, Oparka KJ (1998) The movement protein of cucumber mosaic virus traffics into sieve elements in minor veins of *Nicotiana clevelandii*. Plant Cell **10:** 525–537

Brandizzi F, Snapp EL, Roberts AG, Lippincott-Schwartz J, Hawes C (2002) Membrane protein transport between the endoplasmic reticulum and the Golgi in tobacco leaves is energy dependent but cytoskeleton independent: evidence from selective photobleaching. Plant Cell **14:** 1293–1309

Christensen NM, Faulkner C, Oparka KJ (2009) Evidence for unidirectional flow through plasmodesmata. Plant Physiol **150:** 96–104

Ding B, Haudenshield JS, Hull RJ, Wolf S, Beachy RN, Lucas WJ (1992) Secondary plasmodesmata are specific sites of localization of the tobacco mosaic virus movement protein in transgenic tobacco plants. Plant Cell **4:** 915–928

Ehlers K, Knoblauch M, van Bel AJE (2000) Ultrastructural features of well-preserved and injured sieve elements: minute clamps keep the phloem conduits free for mass flow. Protoplasma **214:** 80–92

Ehlers K, Kollmann R (2001) Primary and secondary plasmodesmata: structure, origin, and functioning. Protoplasma **216:** 1–30

Esau K (1963) Ultrastructure of differentiated cells in higher plants. Am J Bot **50:** 495–506

Esau K (1978) Developmental features of the primary phloem in *Phaseolus vulgaris* L. Ann Bot (Lond) **42:** 1–13

Evert RF (1990) Dicotyledons. *In* H-D Behnke, RD Sjolund, eds, Sieve

Elements: Comparative Structure, Induction and Development. Springer-Verlag, Berlin, pp 103–137

Faulkner C, Akman OE, Bell K, Jeffree C, Oparka K (2008) Peeking into pit fields: a multiple twinning model of secondary plasmodesmata formation in tobacco. Plant Cell **20:** 1504–1518

Fernandez-Suarez M, Ting AY (2008) Fluorescent probes for super-resolution imaging in living cells. Nat Rev Mol Cell Biol **9:** 929–943

Frigault MM, Lacoste J, Swift JL, Brown CM (2009) Live-cell microscopy: tips and tools. J Cell Sci **122:** 753–767

Furch ACU, Hafke JB, Schulz A, van Bel AJE (2007) Ca^{2+}-mediated remote control of reversible sieve tube occlusion in *Vicia faba*. J Exp Bot **58:** 2827–2838

Gillespie T, Boevink P, Haupt S, Roberts AG, Toth R, Valentine T, Chapman S, Oparka KJ (2002) Functional analysis of a DNA-shuffled movement protein reveals that microtubules are dispensable for the cell-to-cell movement of tobacco mosaic virus. Plant Cell **14:** 1207–1222

Guenoune-Gelbart D, Elbaum M, Sagi G, Levy A, Epel BL (2008) Tobacco mosaic virus (TMV) replicase and movement protein function synergistically in facilitating TMV spread by lateral diffusion in the plasmodesmal desmotubule of *Nicotiana benthamiana*. Mol Plant Microbe Interact **21:** 335–345

Gustafsson MG, Shao L, Carlton PM, Wang CJ, Golubovskaya IN, Cande WZ, Agard DA, Sedat JW (2008) Three-dimensional resolution doubling in wide-field fluorescence microscopy by structured illumination. Biophys J **94:** 4957–4970

Heinlein M, Padgett HS, Gens JS, Pickard BG, Casper SJ, Epel B, Beachy RN (1998) Changing patterns of localization of the tobacco mosaic virus movement protein and replicase to the endoplasmic reticulum and microtubules during infection. Plant Cell **10:** 1107–1120

Huang B, Bates M, Zhuang XW (2009) Super-resolution fluorescence microscopy. Annu Rev Biochem **78:** 993–1016

Johnson RPC, Freundlich A, Barclay GF (1976) Transcellular strands in sieve tubes: what are they? J Exp Bot **27:** 1117–1136

Kehr J, Buhtz A (2008) Long distance transport and movement of RNA through the phloem. J Exp Bot **59:** 85–92

Khan JA, Wang Q, Sjolund RD, Schulz A, Thompson GA (2007) An early nodulin-like protein accumulates in the sieve element plasma membrane of Arabidopsis. Plant Physiol **143:** 1576–1589

Knoblauch M, van Bel AJE (1998) Sieve tubes in action. Plant Cell **10:** 35–50

Lee JY, Cui WE (2009) Non-cell autonomous RNA trafficking and long-distance signaling. J Plant Biol **52:** 10–18

Lucas WJ, Lee JY (2004) Plasmodesmata as a supracellular control network in plants. Nat Rev Mol Cell Biol **5:** 712–726

Martens HJ, Roberts AG, Oparka KJ, Schulz A (2006) Quantification of plasmodesmatal endoplasmic reticulum coupling between sieve elements and companion cells using fluorescence redistribution after photobleaching. Plant Physiol **142:** 471–480

Maule AJ (2008) Plasmodesmata: structure, function and biogenesis. Curr Opin Plant Biol **11:** 1–7

Meyer S, Lauterbach C, Niedermeier M, Barth I, Sjolund RD, Sauer N (2004) Wounding enhances expression of AtSUC3, a sucrose transporter from Arabidopsis sieve elements and sink tissues. Plant Physiol **134:** 1–10

Millar AH, Carrie C, Pogson B, Whelan J (2009) Exploring the function-location nexus: using multiple lines of evidence in defining the subcellular location of plant proteins. Plant Cell **21:** 1625–1631

Moore I, Murphy A (2009) Validating the location of fluorescent protein fusions in the endomembrane system. Plant Cell **21:** 1632–1636

Oparka KJ, Turgeon R (1999) Sieve elements and companion cells: traffic control centers of the phloem. Plant Cell **11:** 739–750

Reichel C, Ruehland C, Reiser COA, Hess J (2006) Protein-based nanosystems: virus-like-particles in modern vaccine development. Journal of Biomedical Nanotechnology **2:** 186–200

Roberts AG (2005) Plasmodesmal structure and development. *In* KJ Oparka, ed, Plasmodesmata: Annual Plant Reviews, Vol 18. Blackwell Publishing, Oxford, pp 1–32

Roberts AG, Oparka KJ (2003) Plasmodesmata and the control of symplasmic transport. Plant Cell Environ **26:** 103–124

Roberts IM, Boevink P, Roberts AG, Sauer N, Reichel C, Oparka KJ (2001) Dynamic changes in the frequency and architecture of plasmodesmata during the sink-source transition in tobacco leaves. Protoplasma **218:** 31–44

Runions J, Brach T, Kuhner S, Hawes C (2006) Photoactivation of GFP reveals protein dynamics within the endoplasmic reticulum membrane. J Exp Bot **57:** 43–50

Schermelleh L, Carlton PM, Haase S, Shao L, Winoto L, Kner P, Burke B, Cardoso MC, Agard DA, Gustafsson MGL, et al (2008) Subdiffraction multicolor imaging of the nuclear periphery with 3D structured illumination microscopy. Science **320:** 1332–1336

Shaner NC, Patterson GH, Davidson MW (2007) Advances in fluorescent protein technology. J Cell Sci **120:** 4247–4260

Sjolund RD (1997) The phloem sieve element: a river runs through it. Plant Cell **9:** 1137–1146

Thaine R (1961) Transcellular strands and particle movement in mature sieve tubes. Nature **192:** 772–773

Thaine R, Probine MC, Dyer PY (1967) Existence of transcellular strands in mature sieve elements. J Exp Bot **18:** 110–127

Truernit E, Bauby H, Dubreucq B, Grandjean O, Runions J, Barthelemy J, Palauqui JC (2008) High-resolution whole-mount imaging of three-dimensional tissue organization and gene expression enables the study of phloem development and structure in *Arabidopsis*. Plant Cell **20:** 1494–1503

van Bel AJE, Ehlers K, Knoblauch M (2002) Sieve elements caught in the act. Trends Plant Sci **7:** 126–132

van Bel AJE, Gaupels F (2004) Pathogen-induced resistance and alarm signals in the phloem. Mol Plant Pathol **5:** 495–504

van Bel AJE, Koops AJ (1985) Uptake of [^{14}C]sucrose in isolated minor-vein networks of *Commelina benghalensis* L. Planta **164:** 362–369

Wang W, Hause B, Peumans WJ, Smagghe G, Mackie A, Fraser R, Van Damme EJM (2003) The Tn antigen-specific lectin from ground ivy is an insecticidal protein with an unusual physiology. Plant Physiol **132:** 1322–1334

Warmbrodt RD (1986) Structural aspects of the primary tissues of the *Cucurbita pepo* L. root with special reference to the phloem. New Phytol **102:** 175–192

Protoplasma (2011) 248:9–25
DOI 10.1007/s00709-010-0233-6

REVIEW ARTICLE

Imaging plasmodesmata

Karen Bell · Karl Oparka

Received: 6 September 2010 / Accepted: 22 October 2010 / Published online: 12 November 2010

Abstract At only 50 nm in diameter, plasmodesmata (PD) are below the limit of resolution of conventional light microscopy. Consequently, much of our current interpretation of the substructure of PD is derived from transmission electron microscopy. However, PD can be imaged with alternative techniques, including field emission scanning electron microscopy and 'super-resolution' imaging approaches such as 3D-structured illumination microscopy. This review considers the methods currently available for studying PD and focuses on the boundary between light- and electron-based imaging approaches.

Keywords Plasmodesmata · Transmission electron microscopy · 3D-structured illumination microscopy

Introduction

Plasmodesmata (PD), the small pores that interconnect most types of plant cells, are about 50 nm in diameter and are therefore difficult to image using conventional optical-based methods. Despite their very small size, PD can be seen but not resolved with a conventional light microscope. The minute dimensions of PD did not deter many of the light microscopists of the nineteenth century from making painstaking observations of living plant cells that have seldom been surpassed in their attention to detail. Tangl (1879) first described 'open communications' between endosperm cells, and Strasburger (1901) later called these channels 'plasmodesmata', challenging the widely held cell theory of Schleiden and Schwann (1804) that each cell functioned as an autonomous unit (as cited by Roberts 2005).

The advent of electron microscopy in the 1950s brought a new level of attention to PD ultrastructure and remains the method by which current models of PD structure are derived. However, new advances in fluorescence imaging have broken the 'diffraction barrier', long held to limit the resolution of optical microscopy (Huang et al. 2009; Huang 2010; Patterson et al. 2010), and are beginning to blur the boundary between light and electron microscopy, bringing PD into a new imaging 'window' that was previously thought impossible. This review will consider a range of imaging approaches for studying PD, encompassing more conventional methods alongside emerging technologies that are likely to find their way into mainstream imaging in the near future.

Transmission electron microscopy

There is no doubting the impact of transmission electron microscopy (TEM) on the field of PD biology. Virtually all we know of PD structure is derived from this approach (Roberts 2005; Fig. 1). TEM was instrumental in demonstrating that PD are plasma membrane (PM)-lined pores containing a central desmotubule connected to the cortical ER of adjacent cells (Roberts 2005; Fig. 1).

In the 1980s and 1990s, there was a significant interest in the fine structure of PD from a wide range of evolutionary groups. Notable contributions were magnificent descriptions of PD by Esau (e.g. Esau and Thorsch 1985), Kollmann (see Ehlers and Kollmann 2001) and

Handling Editor: Manfred Heinlein

K. Bell · K. Oparka (✉)
Institute of Molecular Plant Sciences, University of Edinburgh,
Mayfield Road,
Edinburgh EH9 3JR, UK
e-mail: karl.oparka@ed.ac.uk

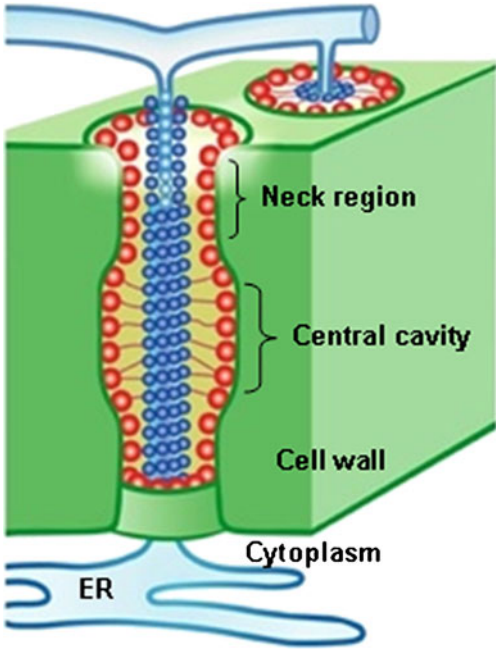

Fig. 1 Diagrammatic representation of the PD pore as derived from TEM studies. The central desmotubule (*pale blue*) is continuous with the cortical ER. Proteinaceous particles (*dark blue*), sometimes helically arranged, are associated with the outer leaflet of the desmotubule. Additional particles (*red*) are associated with the inner leaflet of the plasma membrane (*dark green*). Spoke-like extensions of unknown origin connect the desmotubule with the plasma membrane. In some species, a prominent raised wall collar is present around the neck region of the pore. Diagram courtesy of Alison Roberts

Evert (e.g. Robinson-Beers and Evert 1991). In our view, the quality of these TEM images of PD has not been surpassed, despite significant improvements in resolution. Example images of PD are shown in Fig. 2 and reveal significant substructural details of the PD pore, including the desmotubule and central rod, together with 'spokes' that extend from the desmotubule to the PM (Fig. 2a, b). Small particles, often showing ninefold symmetry, and possibly arranged in a spiral fashion, (Ding et al. 1992a, Blackman and Overall 2001), have been observed to be associated with the outer leaflet of the desmotubule and the inner leaflet of the PM (Figs. 1 and 2f). These particles are about 4–5 nm in diameter, slightly smaller than the width of the cytoplasmic sleeve (5–6 nm), while the radial gaps between the spiralling particles may be as small as 3 nm (reviewed in Robards and Lucas 1990). PD may have a simple or complex architecture (see Burch-Smith et al. this issue) and may become highly specialised at specific interfaces. In the case of the PD that connect the sieve element (SE) with its companion cell (CC), a single callose-lined pore leads into the SE while branched pores occur in the CC wall (Fig. 1c). In Strasburger cells within the phloem of pine needles, large complex PD form, each containing several pores derived from the adjoining cells. Such complex PD often show conspicuous central cavities shared by each of the contributing pores (Fig. 2d). Many PD, when sectioned across the neck region of the pore, often display a densely staining cytoplasmic sleeve (Fig. 2f) while those sectioned below this region often show the sleeve to be electron lucent (e.g. Fig. 2b). There has been much speculation as to the nature of the structural components of PD, including suggestions that they may be cytoskeletal elements (Aaziz et al. 2001; Blackman and Overall 2001; Oparka 2004; Roberts 2005). However, for reasons of molecular constraint, cytoskeletal elements would be difficult to incorporate into the cytoplasmic sleeve of PD (Tilsner et al. 2010).

Chemical fixatives may cause structural artefacts due to poor sample penetration and the relatively slow rate at which the cellular matrix is crosslinked (Gilkey and Staehelin 1986). However, rapid low-temperature fixation, followed by cryo-EM, allows imaging at a near-native state (McIntosh et al. 2005). In this procedure, heat is quickly removed from the sample before ice crystals can form, preserving the cellular architecture. High-pressure freezing, followed by freeze substitution, has revealed the basic structure of PD, confirming that many of the structures seen in conventional TEM images are not artefacts associated with aldehyde fixation (Ding et al. 1992a). However, it is worth noting that despite the fixation/freezing protocol

Fig. 2 Images of PD derived from TEM. Simple PD connecting mesophyll cells in a sugarcane leaf are shown in longitudinal (**a**) and transverse sections (**b**). Note the prominent neck constrictions in **a**. In **b**, the PD are sectioned below the neck region, revealing an electron-lucent cytoplasmic sleeve. Spoke-like extensions are apparent in some of the pores. **a**, **b** are from Robinson-Beers and Evert (1991) and reproduced with permission from the authors and the publisher. Scale in **a**=200 nm; scale in **b**=100 nm. **c** The specialised pore-PD connecting a sieve element (*SE*) with its companion cell (*CC*). Prominent callose collars (*C*) line the pores leading into the SE. The PD are branched within the CC wall. From Evert and Mierzwa (1989) with permission of the authors and the publisher. Scale=150 nm. **d** A longitudinal section through a complex PD structure connecting Strasburger cells in the phloem of a pine needle. Multiple PD pores connect into a shared central cavity (*Ca*). *Arrows* indicate neck constrictions and *darts* show open desmotubule structures. From Glockmann and Kollmann (1996) with permission from the authors and the publisher. Scale=1 μm. **e** PD connecting the trichome with the epidermis in a tobacco leaf. The PD are sectioned across the neck region and show conspicuous wall collars (*WC*). From Faulkner et al. (2008) with permission from the publisher. Scale=100 nm. **f** Single PD pore from the trichome/epidermis interface of a tobacco leaf. Individual components can be discerned, including the plasma membrane (*PM*), desmotubule (*Dt*) and central rod (*CR*). The wall collar (*WC*) is also visible. Note that the cytoplasmic sleeve (*CS*) in the neck region contains electron-dense material. Scale=100 nm. Oparka unpublished data. **g**–**i** PD imaged after tannic acid fixation (from Olesen 1979). Wall collars are visible in **g**. **h** A single PD after rotational enhancement. Note that the particles within the wall collar show a ninefold symmetry. **i** A model derived from the TEM images, showing the wall collar and the dimensions of the different regions in the neck of the pore. Reproduced with permission from the author and the publisher

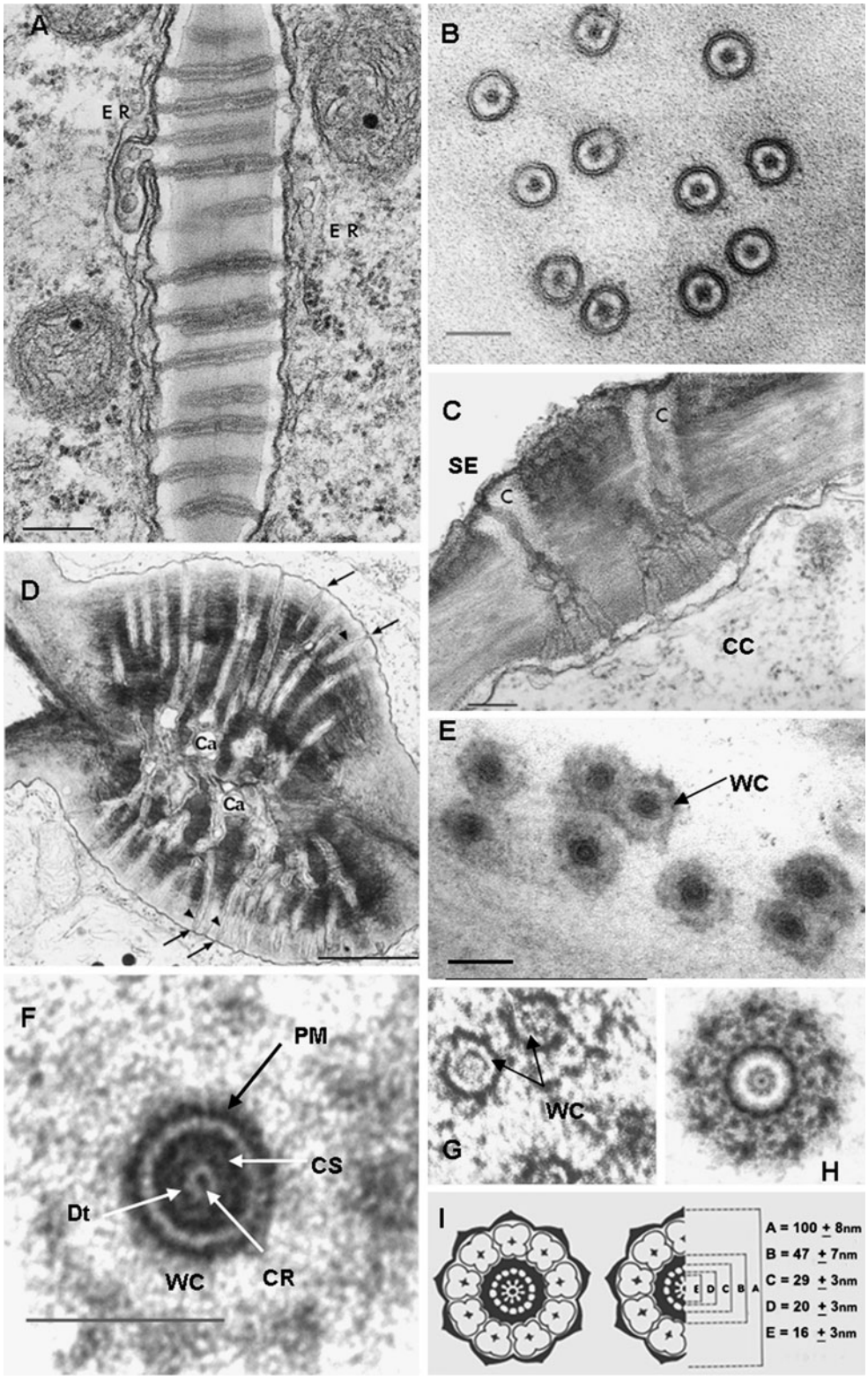

used, conventional resin-embedding procedures may lead to tissue shrinkage, potentially underestimating the dimensions of structures within PD. In most studies of PD, postfixation in osmium, followed by conventional staining with uranyl acetate and lead citrate has been the norm. However, a number of staining techniques have revealed additional details of PD structure and these will be dealt with briefly.

Tannic acid fixation

Many PD display a conspicuous wall collar around the neck of the pore (Fig. 2e–i). Olesen (1979) used high-contrast ultrathin sections following tannic acid fixation (2% tannic acid added to the primary fixative) to demonstrate the presence of large particles (20–30 nm diameter) immediately below the plasma membrane, in the wall collar around the neck constriction (Fig. 2g–i). Rotational enhancement of the images revealed a ninefold symmetry of the external collar particles (Fig. 2h, i). The overall dimensions of the external ring structure described by Olesen and others (about 100–130 nm in diameter, Robards and Lucas 1990) correspond well to the raised wall collar seen in field emission scanning electron microscopy (FESEM) images (Fig. 4e, f; see below). However, the nature of the particles within the raised collar remains to be determined. Olesen (1979) suggested that these external particles might be components of a hypothetical 'sphincter', involved in the regulation of solute transport through PD. This remains a possibility as a number of proteins, including a class I β 1,3-glucanase (Levy et al. 2007), a viral movement protein-interacting host factor that affects callose deposition (Fridborg et al. 2003), and a novel PD-localised callose-binding protein (PDCB1; Simpson et al. 2009) have all been shown to be associated with the neck region of PD. However, it remains to be determined whether the entire machinery necessary for callose deposition at PD resides exclusively within the raised wall collar.

Zinc iodide osmium impregnation

Zinc iodide osmium (ZIO) impregnation of tissues, sometimes known as the 'Maillet method' (Maillet 1959; Pellegrino de Iraldi 1977), was used effectively for the demonstration of autonomic nerves at the light microscope level and subsequently at the TEM level. This stain accumulates as an electron-dense product between double-membraned structures (for recipe see Hawes 1994). In plants, it has been used to selectively stain the cortical ER, Golgi and nuclear membranes, as well as thylakoids within chloroplasts (Barlow et al. 1984; Hawes 1994). A single maize root cell stained with ZIO is shown in Fig. 3a and reveals a significant contrast within the endomembrane system. A variation of the ZIO method utilised osmium ferricyanide (White et al. 1979), which like ZIO accumulates between double membranes. This method was used by Hepler (1982) to demonstrate the entrapment of ER within the phragmoplast to form the future PD of the cell plate. Images of ZIO-fixed maize roots showing the entrapment of ER strands in a developing cell plate are shown in Fig. 3b, c. Interestingly, in the Hepler (1982) study, as the PD pores continued to develop in the new cell wall, the electron-dense stain was gradually excluded from the desmotubules, suggesting that the closely appressed ER membranes of this structure had insufficient lumenal space to allow accumulation of the ZIO. There has been a general consensus that the ER membranes forming the desmotubule are always in close contact. However, this is not always the case (e.g. Glockmann and Kollmann 1996; Fig. 2d; see also Tilsner et al. this issue). In our lab, we have found that ZIO stain accumulates within the desmotubule in PD from a range of tissues, for example in the PD that connect the protophloem sieve elements with surrounding pericycle cells in the *Arabidopsis* root tip (Fig. 3d). As it now appears that the desmotubule may not be a fixed structure and may dilate in response to factors such as virus infection (Guenoune-Gelbart et al. 2008; Epel 2009), the use of ZIO staining may find uses in confirming that under certain conditions the membranes that form the desmotubule may indeed become separated.

Field emission scanning electron microscopy

Scanning electron microscopy, which is normally restricted to exposed surfaces, would appear superficially, to be unsuitable for imaging PD. However, FESEM is potentially a powerful tool in imaging PD (Vesk et al. 2000), provided that they can be suitably exposed on the cell surface. In addition, cryo-FESEM, in which the tissue is rapidly frozen and fractured within the specimen chamber, is likely to reveal details of PD close to their functioning state. We have been exploiting this method to obtain new images of the neck region of PD and on the ways in which secondary PD develop within a single wall interface (Faulkner et al. 2008). Leaf trichomes are a suitable model for FESEM as they comprise a linear chain of cells that contain PD only at their end walls (see also Burch-Smith et al. this issue). Using tobacco, small pieces of leaf were frozen rapidly in sub-cooled liquid nitrogen and rapidly transferred to the freezing stage of the microscope. While still frozen, the trichomes were removed with a scalpel, exposing the cell–wall interface between the basal trichome cell and the epidermis. Using this approach, all the PD at a single wall interface can be exposed (Fig. 4a, b; see also Faulkner et al. 2008). A second approach involves placing the leaf surface into colloidal graphite and prising the leaf surface away from the frozen graphite, revealing predominantly the PM surface between the basal cell and the epidermis (see diagram in Fig. 4). We have also used fracturing, followed by FESEM, to examine the interfaces between vascular parenchyma cells, revealing extensive PD pit fields in areas of shared wall interface (Fig. 4d). Such large groupings of PD are seen only rarely in TEM images when the wall has

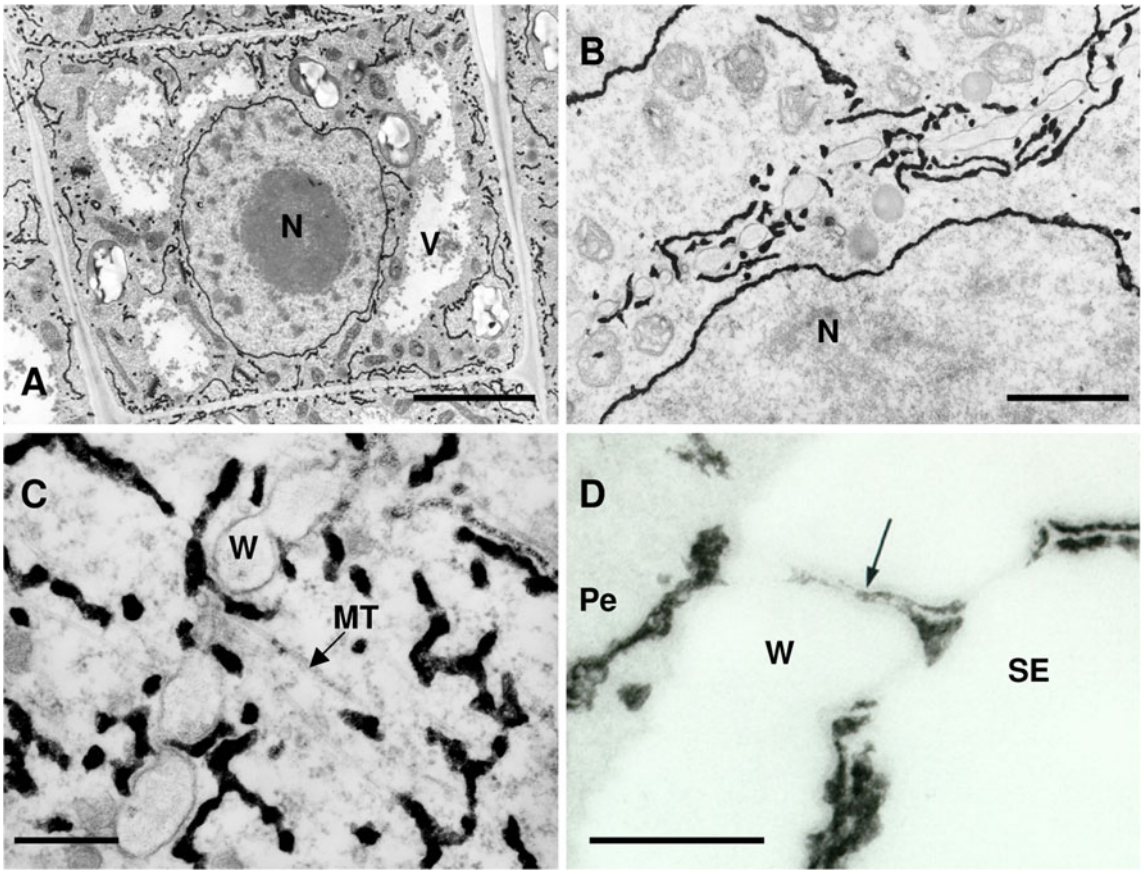

Fig. 3 Zinc iodide osmium (*ZIO*) impregnation of plant tissues. **a** Maize root tip cells after ZIO postfixation. The endomembrane system is clearly delineated, including ER, Golgi bodies and the nuclear envelope. Scale=10 μm. **b**, **c** Differentiating cell plates viewed after ZIO postfixation. Cortical ER strands have become trapped in the developing cell wall (*W*). Microtubules (*MT*) are also visible in **c**. Scale in **b**=5 μm. Scale in **c**=1 μm. Images **a**–**c**, courtesy of C. Hawes (unpublished data). **d** PD between a protophloem sieve element (*SE*) and a neighbouring pericycle cell (*Pe*) in the *Arabidopsis* root show accumulation of ZIO in the desmotubule (*arrow*). Scale= 1 μm. Oparka, unpublished data

been sectioned tangentially (c.f. Fig. 4c). These freeze-fracturing approaches have revealed new details of the neck region of PD. As chemical fixation and embedding are absent from this procedure, and the PD are imaged while still frozen, the images represent PD in as close to their functioning state as possible (Fig. 4e, f).

Images of fractured wall faces reveal prominent wall collars and significant 'twinning' of PD pores (see Faulkner et al. 2008; Fig. 4e). Given the rapidity of freezing, it is significant that the wall collars are clearly defined in FESEM images, suggesting that they are an integral component of PD in the functioning state, and not an artefact of chemical fixation. Measurements of tobacco and *Arabidopsis* PD using these methods have revealed significant differences in pore diameter between these species (Bell and Oparka, unpublished data) and are likely to reveal interesting differences in the dimensions of PD connecting different cell types. Fractures in which the PM is exposed reveal a unique view of the neck of PD, namely from the outer leaflet of the PM looking into the cell (Fig. 4e; Faulkner et al. 2008). In these images, the imprint of the wall collar on the PM can be seen (Fig. 4e), and in suitable views, the desmotubule entering the neck of the pore can be discerned (Fig. 4f, inset). Similar to TEM, high-magnification FESEM views of trichome PD have revealed radially arranged particles on the PM in contact with the wall collar (Fig. 4f inset, c.f. Fig. 2h, i).

FESEM was also used recently by Mullendore et al. (2010) to obtain remarkably clear images of sieve plates from a range of species. Sieve-plate pores are derived from PD (Esau and Thorsch 1985) and as such represent an extreme form of modification of the basic PD structure in which the PD pore becomes enlarged and lined by callose, while the central desmotubule is lost during development (Esau and Thorsch 1985). Mullendore et al. (2010) developed an intricate enzymatic clearing method devised to remove the occluding cytoplasm from sieve tubes following freezing, revealing details of the sieve-plate pores and the callose collars lining them. Significantly, in the absence of rapid freezing, the callose collars occupied a

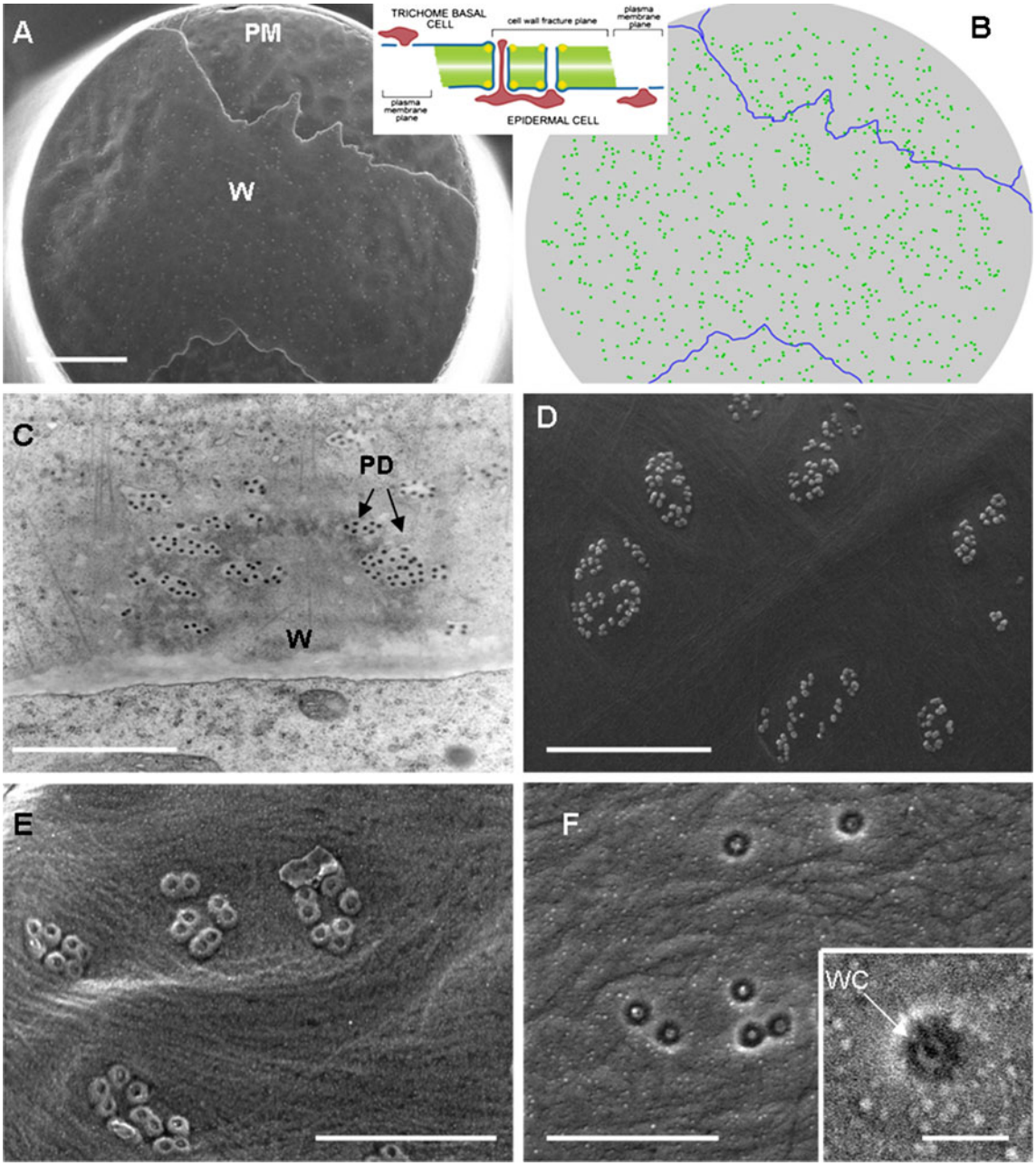

Fig. 4 FESEM images of PD. **a** The trichome/epidermis interface in a tobacco leaf after freeze fracturing and FESEM. Note that the fracture plane has occurred across the cell wall (*W*) and also along the plasma membrane (*PM*) of the underlying cell. Individual PD are visible in both the wall and membrane faces. **b** A diagram of the fracture, with the positions of all PD at this interface marked in *green*. The *inset diagram* shows the different wall/membrane faces exposed during freeze fracturing. Scale=5 μm. From Faulkner et al. (2008) with permission from the publisher. **c** A rare glancing TEM section across the neck region of several PD in a pigment strand cell of a developing rice grain. Note that the wall collars have an electron-lucent appearance. Scale=10 μm. Oparka, unpublished data. **d** Freeze fracture of a tobacco vascular parenchyma element viewed by FESEM. Numerous PD with raised collars are visible and are aggregated into distinct pit fields. Scale=5 μm. Oparka, unpublished data. **e** High-magnification FESEM view of PD pores with raised wall collars (wall fracture, see **a**). Note that many of the pores are twinned. Scale=1 μm. From Faulkner et al. (2008) with permission from the publisher. **f** Equivalent PM view to that shown in **e** reveals PD in the surface of the membrane. Here, the wall collars appear as dark imprints. The central desmotubule can be seen in some of the pores. Note also the imprints of cellulose microfibrils on the surface of the frozen membrane. Scale=1 μm. From Faulkner et al. (2008) with permission from the publisher. *Inset* shows a single PD pore in the plasma membrane. A desmotubule is apparent, as well as radially arranged particles within the wall collar (*WC*; c.f. Fig. 2). Scale= 100 nm. Oparka, unpublished data

large proportion of the pore diameter (Fig. 5a–d). The scanned surface of the frozen and cleared tissue was then used to empirically derive the width of sieve plates and the diameter of their pores, and these data were subsequently used to derive a new model of phloem flux.

Fluorescent tags for PD

Viral movement proteins (MPs), fused to green fluorescent protein (GFP), provided the first in vivo tags for imaging PD (Epel et al. 1996). However, it is not yet clear if MPs from different viral groups label exactly the same components of the PD pore, due to fluorescence resolution constraints. For *Tobacco mosaic virus* (TMV) MP, it seems likely that this MP accumulates, both during infection (Tomenius et al. 1987) and in transgenic plants expressing MP (Moore et al. 1992), in the central cavities of complex PD (Ding et al. 1992b; Roberts et al. 2001). As pointed out by Burch-Smith et al. (this issue), a consensus appears to have arisen that TMV MP labels only secondary PD. However, the labelling pattern of this MP may not be as specific as this, and it is likely that TMV MP is more accurately a marker for those PD, either primary or secondary, within which central cavities have developed. The MP of *Potato leafroll virus* (MP17) appears to label PD in a different manner to that of TMV, being absent almost entirely from the PD in young, developing tissues whilst predominating in the PD found in older mature tissues (Vogel et al. 2007; Fig. 6a; Burch-Smith et al. this issue). Regardless of the precise localisation of viral MPs within PD, there is no doubting their usefulness in a range of studies of PD (see Lucas 2006).

Stains for PD

Aniline blue Decolourised aniline blue has been used extensively for labelling the callose associated with PD

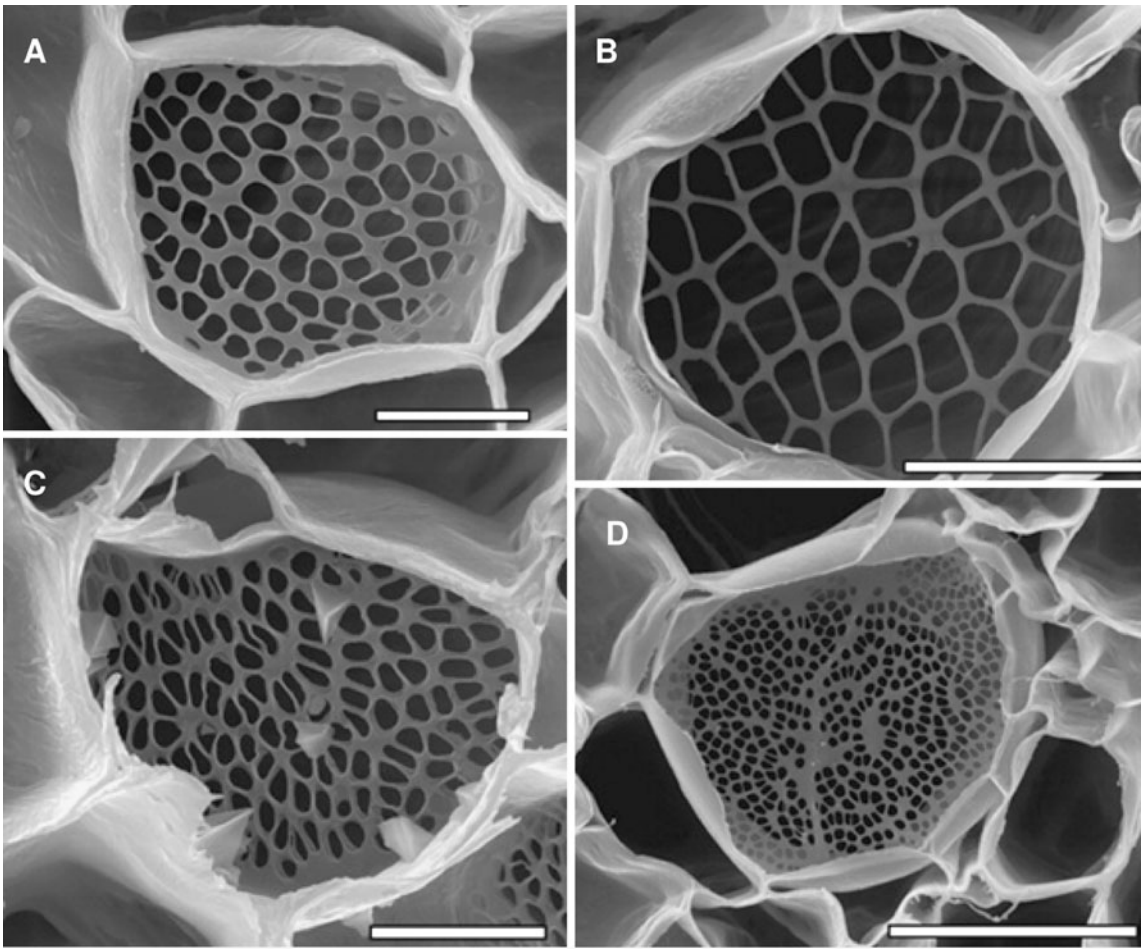

Fig. 5 FESEM images of sieve plates after removal of their cell contents. **a** *Proteus vulgaris*, scale=5 μm. **b** *Cucurbita maxima*, scale=20 μm. **c** *Solanum lycopersicum*, scale=5 μm. **d** *Ricinus communis*, scale=20 μm. From Mullendore et al. (2010). Reproduced with permission from the authors and the publisher

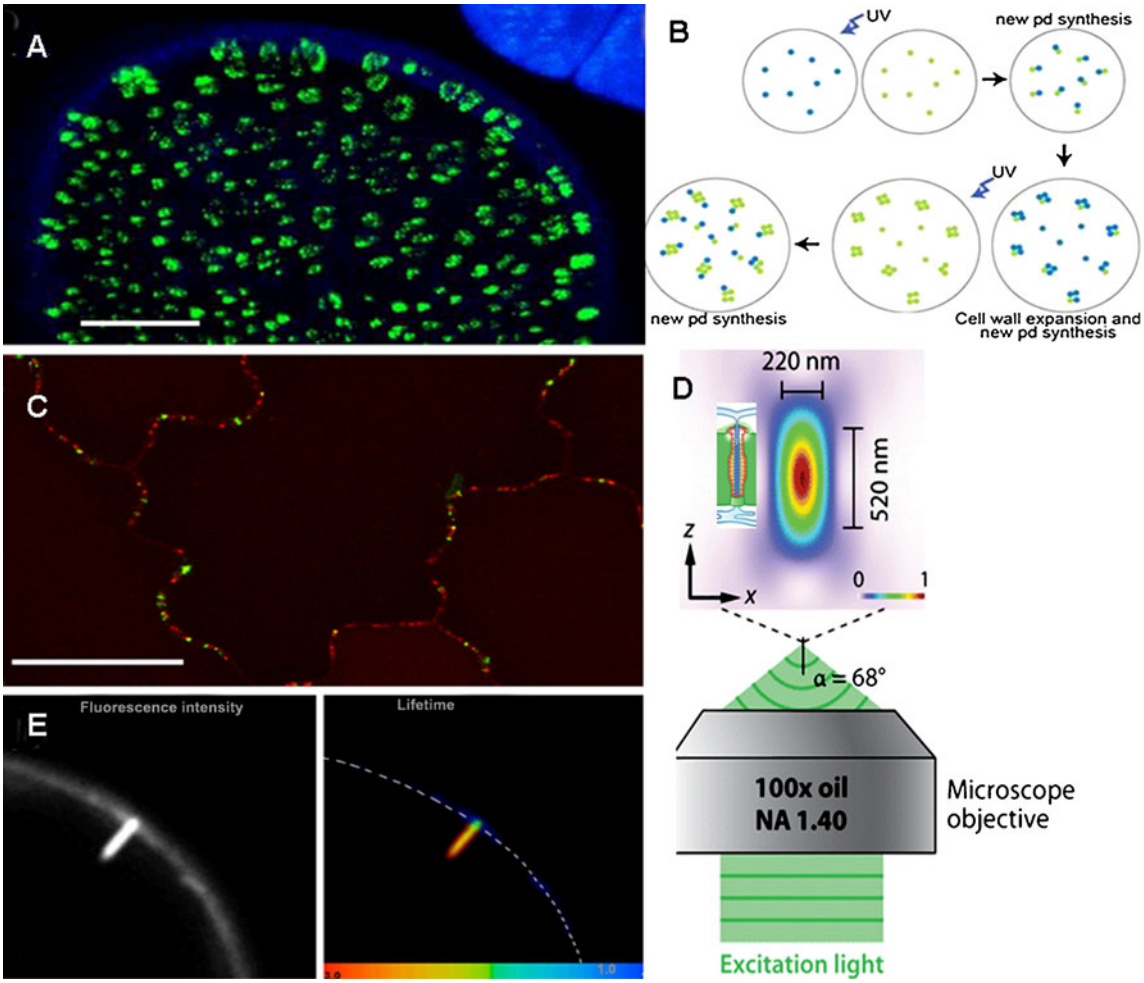

Fig. 6 **a** MP-GFP associated with PD in a surface view of the tobacco epidermis/trichome interface. Scale=10 μm. Oparka, unpublished data. **b** A schematic showing the photoswitching of PD labelled with photoswitchable cyan fluorescent protein. On exposure to UV, the PD are switched from *cyan* to *green*. New PD then develop during wall extension (labelled *green* at 488 nm), resulting in two distinct labelled populations. Later in development, all the PD are again switched to *green* using UV light. Using this approach, the appearance of new PD can be monitored over relatively long time periods (days). **c** The leaf epidermis of an *Arabidopsis* transgenic expressing both PDLP1-mRFP and MP17-GFP. Two distinct populations of PD are present, simple (*red*) and complex (*green*). Scale=20 μm. Fitzgibbon, Faulkner and Oparka, unpublished data. **d** Point spread function (*PSF*) from an oil immersion lens. The dimensions of a single PD pore are shown to scale. Note that the entire PD pore falls within the PSF. Modified from Huang et al. 2009 with permission from the author and the publisher. **e** Interaction between PDLP1 and the MP of GFLV assessed using FLIM. The tubule structure induced by the MP extends from PD and interaction with PDLP1 is strongest within the PD pore. Fluorescence lifetime measurements are illustrated using a false colour code, ranging from 1 (*blue*) to 3 ns (*orange*). Ritzenthaler, unpublished data

(Currier 1957). However, aniline blue tends to fade rapidly and is cytotoxic to plant cells (Oparka and Read 1994). Aniline blue has been used both qualitatively and quantitatively to image PD (Guenoune-Gelbart et al. 2008) and to determine the amount of callose associated with PD in response to viral pathogen attack (e.g. Iglesias and Meins 2000).

DiOC6 This stain has been used extensively in plant tissues to stain both mitochondria and ER (Oparka and Read 1994). It also stains PD under suitable conditions. For example, in plasmolysed cells, DiOC6 clearly labels the ER that is associated with the PD pore (Oparka et al. 1994). DiOC6 has also been used to stain PD in isolated cell walls derived from *Arabidopsis* cell suspension cultures (Ritzenthaler et al. 2000).

PD tags arising from proteomics studies

For several years, callose labelling and/or viral MPs remained the only *bona fide* tags for labelling PD. However, a number of proteomics approaches have begun to yield valuable, previously unknown PD proteins whose

functions are the subject of much recent study. For these proteins, fusion to GFP has revealed their unequivocal localisation to PD (Thomas et al. 2008; Simpson et al. 2009) and provided a new suite of PD markers for developmental and physiological studies of PD (Maule 2008). Plasmodesma-localised protein 1 (PDLP1) was isolated from the walls derived from *Arabidopsis* cultured cells and is a member of a large family of PDLP proteins (Thomas et al. 2008; Fig. 6c). Subsequently, a family of PD callose-binding (PDCB) proteins was isolated using this approach (Simpson et al. 2009; Fig. 7h–j). Interestingly, both PDLP1 and PDCB1 appear to label all PD, including the primary PD present in newly formed cell walls. The presence of different classes of proteins within PD offers the intriguing possibility that these proteins might interact functionally in situ within the PD pore. Such interactions could potentially be monitored using fluorescence resonance energy transfer or fluorescence lifetime imaging (FLIM). It has been shown recently, using FLIM, that PDLP1 interacts at the PD pore with the MP of a tubule-forming virus, *Grapevine fan leaf virus* (GFLV), perhaps acting as a PD receptor for the viral MP (Fig. 6d; see Amari et al. 2010). Interestingly, the PDLP1 did not interact with the MP of TMV within PD although it did interact with the MP of *Cauliflower mosaic virus* (CaMV), a second tubule-forming virus. These data suggest that PDLP1 may be a receptor-like protein usurped specifically by viruses whose passage through PD is guided by tubules.

Imaging different populations of PD

The growing repertoire of PD proteins holds great promise in imaging PD development. Recently, we crossed *Arabidopsis* plants expressing PDLP1-mRFP with a second transgenic line expressing the MP17 protein of PLRV (Vogel et al. 2007). In the leaves of these plants, all of the simple PD in immature cells were labelled red. As the epidermal cells differentiated, new branched PD, expressing both red and green signals, were detected in a discrete developmental pattern (Fig. 6c; Fitzgibbon and Oparka, unpublished data). It seems likely that as increasing numbers of PD proteins are isolated, some of these will prove to be valuable tags for both primary and secondary PD and some for different PD morphotypes (e.g. simple and complex PD). Another intriguing possibility is that some PD proteins may prove to be unique to specific cellular interfaces within the plant, for example for the specialised PD that occur between the sieve element and companion cell. The identification of such proteins awaits the isolation of PD from specific wall interfaces.

Pulse-chasing PD using photoswitchable probes

In the last 5 years, a large number of photoswitchable and photoconvertible fluorescent reporters have been introduced that hold great promise in the study of PD dynamics and development (reviewed in Lippincott-Schwartz and Patterson 2009; Tilsner and Oparka 2010). This approach will require the selection of specific wall interfaces (e.g. the trichome/epidermis boundary) where all the PD can be imaged in a single plane (Fig. 6a). For example, photoswitchable cyan fluorescent protein (PSCFP) is cyan when imaged at 488 nm laser light and is converted to a green form by a short burst of illumination at 405 nm (see also Chapman et al. 2005). Subsequent imaging at 488 nm reveals two populations of protein, cyan from the unswitched region of the cell and green from within the switched region. The use of transgenic lines expressing PSCFP fused to known PD proteins offers the opportunity of selectively photoswitching populations of PD and tracking their fate over time during wall extension. By photoconverting all of the PD in the same cell wall (cyan to green), the areas of wall within which new PD develop (cyan only) can, in principle, be determined over time (Fig. 6b).

Super-resolution imaging of plasmodesmata

Regardless of the number of new PD proteins that are isolated, the resolution imposed by the diffraction barrier of the emitted light (Abbe 1873) represents a serious limitation to bridging the imaging gap between fluorescence and electron microscopy. Since 2005, however, there has been an explosion in imaging approaches that break the diffraction barrier (reviewed in Huang et al. 2009 and Huang 2010), collectively referred to as ‘super-resolution imaging’ or ‘nanoscopy’.

The diffraction limit

Due to diffraction, light from a point in the object does not converge to an exact point in the image and so is blurred. Blur represents information lost from the final image. Ernst Abbe (1873) formalised the limits of resolution attainable in a diffraction-limited system in the nineteenth century. The mathematical expression for this is $d=\lambda/2n \sin \alpha$ where (d) is the minimum distance between objects required to resolve them as single entities and is a product of the wavelength (λ) of light divided by the numerical aperture of the lens ($n \sin \alpha$) multiplied by 2. A minimum value for d is reached as it is not possible to arbitrarily increase the numerical aperture because light will no longer be able to

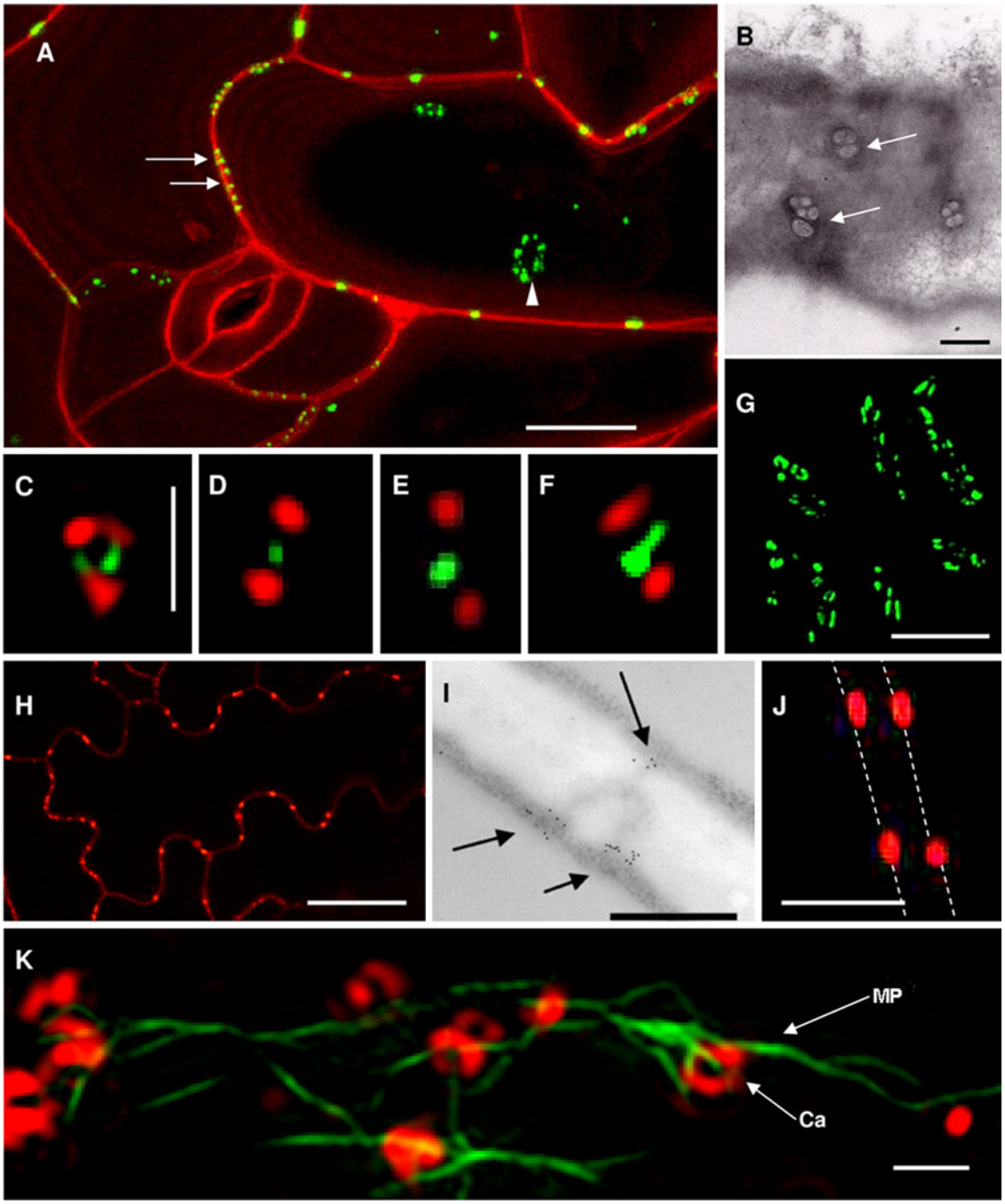

Fig. 7 Super-resolution imaging of PD using 3D-SIM. **a** A conventional confocal image of an *Arabidopsis* leaf expressing a MP-GFP fusion (MP17; see Vogel et al. 2007). The epidermal walls have been stained red with propidium iodide. PD connecting individual epidermal cells can be seen (*arrow*) as well as PD grouped into pit fields between the epidermis and the mesophyll (*dart*). Scale= 15 μm. Fitzgibbon and Oparka, unpublished data. **b** Glancing TEM section of pit fields showing central cavities separated by small wall partitions. Scale=1 μm. Oparka, unpublished data. **c–f** 3D-SIM images of individual PD. MP-GFP (*green*) is visible in the central cavities and callose (*red*) has been stained with a callose antibody. Paired callose platelets are clearly visible. Scale=5 μm. **g** 3D-SIM image of a single pit field reveals MP-GFP within central cavities similar to those observed using TEM (c.f. **b**). Scale=5 μm. **h** Confocal image of a callose-binding PD protein (PDCB1-mCherry; see Simpson et al. 2009). Epidermal PD can be seen but not resolved. Scale=20 μm. Oparka and Faulkner, unpublished data. **i** Immunogold localisation of PDCB1 to the neck region of PD. Scale=500 nm. From Simpson et al. 2009. Reproduced with the permission from the authors and the publisher. **j** A 3D-SIM image of PD labelled with PDCB1-mCherry. The association of the protein with individual callose collars can now be resolved. Scale=5 μm. Oparka and Faulkner, unpublished data. **k** 3D-SIM image of the parietal layer of a sieve element. The callose collars (*red*) associated with individual PD pores are resolved, along with MP-decorated strands (MP, *green*) that interconnect the PD. 3D-SIM images are from Fitzgibbon et al. (2010) and reproduced with permission from the publisher. Scale=1 μm

enter the lens. Nor is it feasible to use wavelengths of light shorter than 400 nm as this can damage biological samples. Abbe's theorem predicted that objects closer than approximately 200 nm laterally (*x*–*y*) and 500 nm axially (*z*) cannot be resolved.

Whilst the lateral resolution limit is a direct consequence of light diffraction, the much higher axial limit is due to microscope design. Anisotropy results as light is collected from only one side of the specimen, causing an elongation of the point spread function (PSF) in the axial plane (point spread function is the 3D intensity distribution of a point object). Optical sectioning using a confocal or multiphoton microscope allows greater sample penetration and increased resolution by creating an effectively smaller PSF, but the axial resolution remains comparatively poor. Whilst frustrating for cell biologists generally, this is of particular disadvantage to plant scientists who, unless using protoplasts, have to contend with the cell wall. Figure 6e shows the PSF of a light microscope fitted with a high numerical aperture (NA) oil lens. For comparison, the dimensions of a typical PD pore are shown. Note that the entire PD structure falls within the PSF and so cannot be resolved. However, the locations of PD in the wall can be seen due to the fluorescence they emit (e.g. Fig. 7a). Unfortunately, it is not possible to distinguish the number of PD present, nor their architecture, within a single point of fluorescence.

I^5M and 4Pi microscopy boost axial resolution by using opposing objective lenses with high NAs. In this scheme, a much greater portion of the full spherical angle is covered and a common focal area is imaged coherently. I^5M is a wide field system in which an arc lamp illuminates the sample (Gustafsson et al. 1999). In 4Pi microscopy, a laser is used and the samples are optically sectioned (Hell and Stelzer 1994) producing a 3D resolution of 200 nm. Leica launched a commercial 4Pi confocal microscope in 2005. Due to the optical sectioning capacity, 4Pi is likely to be of most use to plant biologists who are interested in imaging cells within tissues but, as yet, no 4Pi publications using plants have been published. Whilst the increased NA of the coherent objectives boosts axial resolution significantly, it does so within the limits of diffraction set by Abbe's theorem. To break that limit requires more than a change in microscope design.

3D-structured illumination microscopy (3D-SIM) achieves a resolution of 100 nm in the *x*–*y* dimension and 200 nm in *z* dimension. In optical microscopy, the image produced is a product of the incident light that interacts with the sample, as represented by the distribution of the dye/fluorescent protein. Gustafsson (2000) proposed that by introducing spatial structure to the incident light, it is possible to reveal a greater level of detail in the unknown sample structure. The interaction between the structured incident light and the structure of the sample produces emitted light that contains interference fringes (Gustafsson 2000, 2005). The interference fringes can be much courser than either of the original structural patterns and as such are more readily observable even if one, or both, of the original patterns are too fine to resolve. Through processing a series of images, it is possible to extract additional information about the sample, thereby generating an image with improved resolution. Originally demonstrated in 2D, 3D imaging capacity soon evolved. To achieve this, laser light is first diffused and polarised before passing it through a diffraction grating where it is split into two parallel beams. These beams then enter the objective where they are focused to interfere at the sample plane. This interference generates a sinusoidal illumination pattern. Multiple images are taken by scanning and rotating the excitation pattern, and these are processed linearly to reconstruct an image with up to twice the normal resolution of a conventional light microscope. In addition to providing extended resolution, 3D-SIM is also compatible with standard fluorochromes (e.g. GFP, mCherry, DAPI) and with the sample preparation methods commonly used for light microscopy. In 2008, the application of 3D-SIM was first reported in a multi-colour 3D study of the nuclear periphery (Schermelleh et al. 2008). Concomitantly, a commercial 3D-SIM platform was released by Deltavision, called OMX (Optical Microscope eXperimental).

3D-SIM of plasmodesmata

We recently used 3D-SIM in a study of *Nicotiana tabacum* PD constitutively expressing the TMV MP (Fitzgibbon et al. 2010). By double labelling the PD with a red callose antibody, we were able to show that these two signals (callose and MP) could be resolved easily (Fig. 7c–f). The width of the callose collar was estimated to be about 150 nm, slightly larger than the raised wall collar seen in FESEM images (c.f. Fig. 4e). We were also able to resolve an unlabelled region of the pore, about 135 nm in length, between the callose collar and the MP within the central cavity (Fig. 7c–f). 3D-SIM also offered unique views of central cavities when PD pit fields were optically sectioned (Fig. 7g). Here, central cavities closely resembled those images seen only rarely in the TEM in glancing sections of the cell wall (c.f. Fig. 7b). More recently, we have used 3D-SIM to image the localisation of the putative callose-binding protein, PDCB1. Immunogold labelling of this protein showed it to be localised to the neck region of PD (Fig. 7i; Simpson et al. 2009), a feature confirmed using 3D-SIM (Fig. 7j). Within the phloem, we were able to resolve sieve-plate pores and the specialised pore-PD that interconnect the companion cell with the sieve element. Significantly, we were able to image individual callose-

lined pores leading into the sieve element parietal layer. In this region, we noticed that the TMV MP was no longer associated only with the central cavities of PD but became distributed on a tubular material that interconnected all the pore-PD in the sieve element parietal layer (Fig. 7k). These unique views of the sieve element–companion cell interface cannot be obtained using confocal microscopy and are seen only rarely in fortuitous glancing sections of this interface.

Although lacking the capacity of 3D-SIM to resolve fine detail, confocal microscopy is used routinely to ascribe subcellular locations of proteins fused to GFP (Escobar et al. 2003). Liu et al. (2008) recently highlighted an important limitation when using confocal microscopy to identify PD-associated proteins. A dramatic distortion of the PSF occurs when imaging close to the cell wall due to the different refractive indices of the cell wall and the cytosol. A consequence of this is that a single point of fluorescence may reflect across the cell wall resulting in the appearance of paired punctae. Liu et al. (2008) proposed a simple polarisation method to recognise reflected signals that would allow fluorescent artefacts to be identified. The increased axial resolution and optical sectioning capacity of 3D-SIM ensures that it is more robust in identifying plasmodesmal associated proteins than confocal microscopy. Thus, 3D-SIM offers great potential in bridging the gap between confocal and electron microscopy.

Other super-resolution imaging approaches also offer potential but have yet to be tested on plant tissues. Saturating structured illumination microscopy (SSIM; Gustafsson 2005) retains compatibility with conventional fluorophores and achieves true super resolution. SSIM uses structured light but of very high intensity to saturate the emission of stimulated fluorochromes. As the saturation level is approached, the fluorescence emission is no longer proportional to the excitation light intensity. The effective resolution is thus limited only by the fluorescent lifetime of the probe and not by the exciting light. SSIM is not yet available commercially.

Stimulated emission depletion microscopy

Stimulated emission depletion (STED) was the first far-field super-resolution imaging technique to be applied to cell biology (Klar and Hell 1999). Like SSIM, it saturates fluorochrome emission but does so using a second, STED laser. Unlike SSIM, which is a wide field technique, STED uses point scanning. Through the introduction of a polymeric phase plate, the STED laser can be modified to contain a focal doughnut (Hein et al. 2010). This features an intensity zero at its focal centre and strong intensities at the periphery. The excitation laser is then precisely co-aligned to occupy the STED zero point. The STED beam is shifted towards the red end of the fluorochrome emission spectrum and so can de-excite potentially excited molecules through stimulated emission. Stimulated emission occurs when an excited state fluorochrome encounters a photon that contains the energy difference between the excited and ground state. Consequently, the fluorochrome is brought back to the ground state before emission occurs. Although reliant upon the pattern generated by two diffraction-limited laser light sources, STED is truly super resolution as the size of the STED pattern is limited only by the power of the STED laser. Furthermore, it is theoretically possible to use any fluorochrome in a STED study (Willig et al. 2006). Whilst organic dyes typically offer the greatest photostability under STED conditions, imaging parameters have been optimised for fluorescent protein imaging (Willig et al. 2006). By coupling STED with 4Pi microscopy, super resolution has been achieved in all three dimensions (Schmidt et al. 2008). Using STED, synaptic vesicle movement has been dissected at video rate (Westphal et al. 2008), and more recently, connexon-43 clusters were imaged crossing the cell membrane (Hein et al. 2010). Significantly, Leica Microsystems has recently launched a STED module that can upgrade its existing SP5 confocal platform. A super-resolution 'bolt-on' to an existing imaging system that is integrated with a familiar user interface is likely to prove popular amongst researchers.

The STED microscope has evolved significantly since it was first described (Hell and Stelzer 1994). Table 1 highlights its capacity to image in 3D, to achieve exceptionally high lateral resolution and image at a video rate. Whilst no published STED platform has integrated all these specifications, any one has the potential to contribute significantly to plasmodesmal research. For example, the capacity to image in 3D at high resolution could allow structural dissection of the PD pore, in a similar vein to that described by Fitzgibbon et al. (2010) whereas super-resolution imaging at a biologically relevant temporal resolution could be a powerful tool in unravelling plant virus dynamics.

Single molecule imaging

STED and SSIM are super-resolution techniques that image an ensemble of molecules. It is worth noting that super resolution can also be attained by imaging single molecules (reviewed in Patterson et al. 2010). The principle underlying single molecule detection is that the position of a single emitter can be localised with a high degree of accuracy if enough photons are collected. This allows the centre of the fluorescent emission to be determined by fitting the photon output to the ideal PSF. Photoactivation localisation microscopy (PALM), stochastic optical reconstruction microscopy (STORM) and fluorescence photoactivation

Table 1 A comparison of the spatial and temporal resolutions of biological imaging techniques

	x–y resolution (nm)	*z* resolution (nm)	Temporal resolution
Wide field (a)	230	800	Milliseconds
CSLM (b)	200	550	Milliseconds
4Pi or I^5M (a)	100	100	Milliseconds
3D-SIM (c)	100	200	N/A
SSIM (d)	50	N/A	N/A
STED (e)	20	N/A	N/A
Video rate STED (f)	62	62	Milliseconds
4Pi STED (g)	40	40	N/A
PALM/STORM (h)	20	N/A	N/A
3D STORM (i)	30	60	N/A
Time lapse PALM (j)	40	N/A	Seconds

(a) Stemmer et al. (2008), (b) White et al. (1987), (c) Schermelleh et al. (2008), (d) Gustafsson (2005), (e) Donnert et al. (2007), (f) Westphal et al. (2008), (g) Schmidt et al. (2008), (h) Bates et al. (2007), (i) Huang et al. (2008), (j) Biteen et al. (2008)

localisation microscopy are all examples of techniques that use this same principle. All independently conceived, publications introducing these technologies first appeared in 2006, and although not yet used on plant cells, it is worth considering these techniques briefly.

To detect a single emitter from a sample containing many fluorescent molecules requires a probe with requisite photophysical properties (Lippincott-Schwartz and Patterson 2009) and a sensitive detection system, usually a CCD camera. Dronpa is a monomeric fluorescent protein used in single molecule detection experiments (Andro et al. 2004; Habuchi et al. 2005). It photoconverts from a green fluorescence to a dark state in response to prolonged 488 nm laser irradiation, with a sharp burst of 405 nm laser light restoring the initial green fluorescence. In single molecule studies, activation is stochastic, and the light–dark cycling allows imaging and localisation without overlap. Through iteration of activation and imaging, a super-resolution image is constructed from the coordinates of many molecules. Resolution is directly dependent upon the total number of photons collected, and to that end, it is essential to maximise the signal to noise ratio. In addition to using probes with a high dynamic range and contrast ratio, the imaging platform is frequently integrated with a total internal reflection (TIRF) microscope. In TIRF (Axelrod et al. 1984), the angle of incident light is such that it cannot cross the sample refractive index and so is deflected back into the objective. When the incident light hits the coverslip, an evanescent wave is generated that decays exponentially, and so TIRF penetrates to only around 100 nm. Imaging in a limited focal volume limits background fluorescence from the bulk tissue increasing the signal to noise ratio by reducing noise. A lateral (*x–y*) resolution of 20 nm has been reported for PALM (Bates et al. 2007).

The developers of STORM were the first to generate a 3D image using single molecule detection (Huang et al. 2008). They did so by using a cylindrical lens to generate an elliptical image of a single fluorophore. From this, it was possible to measure the axial (*z*) position from the ellipticity and the lateral (*x–y*) position from the centroid. A resolution of 25 nm laterally (*x–y*) and 50 nm axially (*z*) was achieved (Huang et al. 2008).

Although capable of imaging live cells (Biteen et al. 2008) and in 3D (Huang et al. 2008), single molecule detection techniques are currently of limited practical use. The requirement for fluorescent probes with specific photophysical capacities (Lippincott-Schwartz and Patterson 2009) would require most labs to reengineer their suite of reporter proteins. Also, the necessity to have samples that produce low or no background provides another challenge to plant scientists (Moreno et al. 2006). Whilst TIRF limits bulk tissue auto-fluorescence, through reducing the focal volume, it does require areas of interest to be within approximately 100 nm of the coverslip.

A comparison of the spatial and temporal resolutions achievable with different types of optical-based microscopy is shown in Table 1. Note that whilst some have greatly improved *x–y* resolution, others show great improvements in *z* resolution. The final choice of system is likely to be dictated by the experimental system under study. Of the plethora of super-resolution approaches currently being developed, it will be interesting to see which of these will enter mainstream plant cell biology. Undoubtedly, many of these emerging techniques are applicable to the study of PD. However, it will require inventive tissue preparation and imaging conditions to achieve this goal.

Image processing

Although conventional imaging systems (CSLM and wide field) produce images with inherently less detail than their super-resolution counterparts, it is possible to extend the resolution significantly using imaging processing techniques. Through removing optical distortions, present in all images (regardless if they are collected by a super-resolution or a

'conventional' platform), it is possible to gain greater information about the sample. Many different image processing methods are available, and these differ largely in the algorithm used to process the raw data (Conchello and Lichtman 2005). One example of particular relevance is near neighbour subtraction (NNS). NNS is beneficial when the fluorescent signal is concentrated in thin filaments or discrete patches, as in PD (Conchello and Lichtman 2005). Using a 2D PSF, calculated for a miss-focus distance equal to the distance between the optical sections, NNS blurs the adjacent sections and then subtracts them from the section of interest to remove the out-of-focus light (Conchello and Lichtman 2005). This is then repeated for each of the remaining sections in turn before projecting the final image, minus much of the extraneous light. As computing powers increase, it will be possible to derive ever more accurate methods to process images using less simplifying assumptions. A limit is reached, however, as it is not possible to estimate frequency components of the specimen that are not passed by the objective (Conchello and Lichtman 2005).

Correlative light and electron microscopy

Because the boundaries between light and electron microscopy are blurring, there is a growing need to confirm that structures seen in the light microscope are indeed identical to those observed by TEM. Accordingly, a new area of biological imaging, correlative light and electron microscopy (CLEM), is emerging in which the same samples are viewed sequentially by light and electron microscopy (Koster and Klumperman 2003, reviewed in Tilsner and Oparka 2010). This approach was used to image mitochondria expressing a fluorescent reporter using both PALM and TEM (Betzig et al. 2006). To retain fluorescence, the cells were frozen and cryosectioned before imaging. The PALM images were found to superimpose exactly on the TEM images, confirming the resolution of the PALM technique and accurately ascribing the correct protein localisation.

Photo-oxidation is a method that translates a fluorescent signal to an electron-dense one. Upon illumination, virtually all fluorochromes produce singlet oxygen. Photo-oxidation harnesses singlet oxygen to convert the chromogen DAB (3,3′-diaminobenzidine tetrachloride) to a highly localised osmiophilic granular precipitate (Maranto 1982). The conversion takes place in fixed tissues that have been incubated in an oxygenated DAB solution (Meisslitzer-Ruppitsch et al. 2009). Upon illumination with high intensity excitation light, reaction products develop, visualised as a gradual browning under bright field. Following treatment with osmium tetroxide, the samples can then be processed for EM as normal (Maranto 1982). The success of the photo-oxidation reaction depends largely upon the capacity of the fluorochrome to generate sufficient singlet oxygen. Lucifer Yellow was the first fluorochrome used (Maranto 1982), but subsequent studies have used other fluorochromes due principally to their greater singlet oxygen yield (Geipmans et al. 2006; Meisslitzer-Ruppitsch et al. 2009). The omnipresent GFP has been used successfully to catalyse the photo-oxidation reaction but only in a few studies (Grabenbauer et al. 2005; Meisslitzer-Ruppitsch et al. 2009). Aside from conventional TEM imaging, photoconverted samples have also been used in electron tomography studies (Cortese et al. 2009).

A method that relies on conventional fluorescent labels and a light catalysed reaction to generate an electron-dense product is appealing. It would therefore seem worthwhile to invest time in testing the suite of markers already available for their photo-oxidising potential. As the capacity for generating singlet oxygen varies and DAB precipitate is best preserved when concentrated within an organelle or a limited area, this approach might be particularly suited to PD.

Many findings based on fluorescent protein imaging need support from EM (Lippincott-Schwartz and Patterson 2009). By using a super-resolution method in a correlative approach, a direct comparative analysis of imaging capabilities is possible. Perinetti et al. (2009) correlated 4Pi images of Golgi stacks with TEM serial sections and 3D reconstruction. They first mapped the positions of separated Golgi stacks with a wide field microscope before imaging them in 3D using confocal and then 4Pi microscopy. The correlation was achieved by detecting a fluorescent Golgi protein using a nanogold conjugated antibody, followed by careful TEM serial sectioning and recording. Whilst this approach required a second step to make the fluorescent signal visible in the EM, a bifunctional probe allows the sample to be directly detectable at both the light and EM level.

FluoroNanogold is an example of a dual labelling reagent that contains fluorescent and electron-dense particles. It is a Fab probe that is covalently bound to a fluorochrome and gold particle. As it is an immunoglobulin fragment (the fragment of antigen binding), it is smaller, and as such can yield enhanced labelling efficiency. Greater penetration is also afforded by the comparatively small gold conjugate (between 0.8 and 1.4 nm; Robinson and Takizawa 2009). A consequence of this is that silver enhancements may be needed to increase the size of the gold particles to allow ready light microscope visualisation. As immunological microscopy is already a routine lab technique, with an ever-expanding toolbox of antibodies, using bifunctional probes in place of standard secondary antibodies is a potentially high-return imaging investment.

As studies of PD advance, there will be a growing need to ascribe the location of newly discovered PD proteins

with accuracy to their native location within the PD pore. EM immunogold labelling is one approach to achieving this, but will require the production of antibodies for each new protein detected. Given the small size of PD, immunogold labelling is subject to its own suite of problems, including the need for stringent controls and the inherent problems associated with different gold particle sizes. A simpler solution would be to conduct correlative imaging in which fluorescent PD protein fusions are imaged first using a super-resolution instrument, followed by correlative TEM in which the protein is rendered electron dense. We have shown that using 3D-SIM, proteins can be ascribed to different locations within PD. The challenge for the future is to accurately ascribe PD proteins to their correct location and to conduct meaningful functional studies on the role of these proteins within PD.

Conflict of interest The authors declare that they have no conflict of interest.

References

Aaziz RD, Dinant A, Epel BL (2001) Plasmodesmata and plant cytoskeleton. Trends Plant Sci 6:326–330

Abbe E (1873) Beitrage zur theorie das mikroskops und der mikroskopischen wahrnehmung. Arch Mikrosk Anat 9:413–468

Amari K, Boutant E, Hofmann C, Schmitt-Keichinger C, Fernandez-Calvino L, Dider P, Lerich A, Mutterer J, Thomas CL, Heinlein M, Mely Y, Maule AJ, Rizenthaler C (2010) A family of plasmodesmal proteins with receptor-like properties for plant viral movement proteins. PLoS Pathog 6:1–10

Andro R, Mizuno H, Miyawaki A (2004) Regulated fast reversible protein highlighting. Science 306:1370–1373

Axelrod D, Burghardt TP, Thompson R (1984) Total internal reflection fluorescence. Ann Rev Biophys Bioeng 13:247–268

Barlow PW, Hawes CR, Horne JC (1984) Structure of amyloplasts and endoplasmic reticulum in the root caps of *Lepidium sativum* and *Zea mays* observed after selective membrane staining and by high-voltage electron microscopy. Planta 160:363–371

Bates M, Huang B, Dempsey GT, Zhuang X (2007) Multicolour super-resolution imaging with photo-switchable fluorescent probes. Science 317:1749–1753

Betzig E, Patterson GH, Sougrat R, Lindwasser OW, Olenych S, Bonifacino JS, Davidson MW, Lippincott-Schwartz J, Hess HF (2006) Imaging intracellular fluorescent proteins at nanometer resolution. Science 313:1643–1645

Biteen JS, Thompson MA, Tselentis NK, Bowman GR, Shapiro L, Moerner WE (2008) Super-resolution imaging in live *Caulobacter crescentus* cells using photoswitchable EYFP. Nat Meth 5:947–949

Blackman LM, Overall RL (2001) Structure and function of plasmodesmata. Aust J Plant Physiol 28:709–727

Chapman S, Oparka KJ, Roberts AG (2005) New tools for in vivo fluorescence tagging. Curr Opin Plant Biol 8:565–573

Conchello J-A, Lichtman JW (2005) Optical sectioning microscopy. Nat Meth 2:920–931

Cortese K, Diaspro A, Tacchetti C (2009) Advanced correlative light/electron microscopy: current methods and new developments using Tokuyasu cryosections. J Histochem Cytochem 57:1103–1112

Currier H (1957) Callose substance in plant cells. Amer J Bot 44:478–488

Ding B, Turgeon R, Parthasarathy MV (1992a) Substructure of freeze-substituted plasmodesmata. Protoplasma 169:28–41

Ding B, Haudenshield JS, Hull RJ, Wolf S, Beachy RN, Lucas WJ (1992b) Secondary plasmodesmata are specific sites of localization of the tobacco mosaic virus movement protein in transgenic tobacco plants. Plant Cell 4:915–928

Donnert G, Keller J, Wurm CA, Rizzoli SO, Westphal V, Schonle A, Jahn R, Jakobs S, Eggeling C, Hell SW (2007) Two-color far-field fluorescence. Nanoscopy Biophys J 92:L67–L69

Ehlers K, Kollmann R (2001) Primary and secondary plasmodesmata: structure, origin and functioning. Protoplasma 216:1–30

Epel B (2009) Plant viruses spread by diffusion on ER-associated movement-protein-rafts through plasmodesmata gated by viral induced host beta-1, 3-glucanases. Semin Cell Dev Biol 20:1074–1081

Epel BL, Padgett HS, Heinlein M, Beachy RN (1996) Plant virus dynamics probed with GFP–protein fusion. Gene 173:75–79

Esau K, Thorsch J (1985) Sieve plate pores and plasmodesmata, the communication channels of the symplast—ultrastructural aspects and developmental relations. Amer J Bot 72:1641–1653

Escobar NM, Haupt S, Thow G, Boevink P, Chapman S, Oparka K (2003) High-throughput viral expression of cDNA–green fluorescent protein fusions reveals novel subcellular addresses and identifies unique proteins that interact with plasmodesmata. Plant Cell 15:1507–1523

Evert RF, Mierzwa RJ (1989) The cell wall–plasmalemma interface in sieve tubes of barley. Planta 177:24–34

Faulkner C, Akman OE, Bell K, Jeffree C, Oparka K (2008) Peeking into pit fields: a multiple twinning model of secondary plasmodesmata formation in tobacco. Plant Cell 20:1504–1518

Fitzgibbon J, Bell K, King E, Oparka K (2010) Super-resolution imaging of plasmodesmata using three-dimensional structured illumination microscopy. Plant Physiol 153:1453–1463

Fridborg I, Grainger J, Page A, Coleman M, Findlay K, Angell S (2003) TIP, a novel host factor linking callose degradation with the cell-to-cell movement of potato virus X. Mol Plant Microb Interact 16:132–140

Geipmans BNG, Adams SR, Ellisman MH, Tsein RY (2006) The fluorescent toolbox for assessing protein location and function. Science 312:217–224

Gilkey JC, Staehelin LA (1986) Advances in ultrarapid freezing for the preservation of cellular ultrastructure. J Electron Microsc Tech 3:177–210

Glockmann C, Kollmann R (1996) Structure and development of cell connections in the phloem of *Metasequoia glyptostroboides* needles. I. Ultrastructural aspects of modified primary plasmodesmata in Strasburger cells. Protoplasma 193:191–203

Grabenbauer M, Geerts WJ, Fernandez-Rodriguez J, Hoenger A, Koster AJ, Nilsson T (2005) Correlative microscopy and electron tomography of GFP through photooxidation. Nat Meth 2:857–862

Guenoune-Gelbart D, Elbaum M, Sagi G, Levy A, Epel BL (2008) Tobacco mosaic virus (TMV) replicase and movement protein function synergistically in facilitating TMV spread by lateral diffusion in the plasmodesmal desmotubule of *Nicotiana benthamiana*. Mol Plant Microb Interact 21:335–345

Gustafsson MGL (2000) Surpassing the lateral resolution limit by a factor of two using structured illumination microscopy. J Microsc 198:82–87

Gustafsson MGL (2005) Nonlinear structured-illumination microscopy: wide-field fluorescence imaging with theorectically unlimited resolution. Proc Natl Acad Sci USA 2:13081–13086

Gustafsson MGL, Agard DA, Sedat JW (1999) I5M: 3D widefield light microscopy with better than 100 nm axial resolution. J Microsc 195:10–16

Habuchi S, Ando R, Dedecker P, Verheijen W, Mizuno H, Miyawaki A, Hofkens J (2005) Reversible single-molecule photoswitching in the GFP-like fluorescent protein dronpa. Proc Natl Acad Sci USA 102:9511–9516

Hawes C (1994) Electron microscopy. In: Harris N, Oparka KJ (eds) Plant cell biology: a practical approach. IRL, Oxford, pp 69–96

Hein BH, Willig KI, Wurm CA, Westphal V, Jakobs S, Hell SW (2010) Stimulated emission depletion nanoscopy of living cells using SNAP-tag fusion proteins. Biophys J 98:158–163

Hell SW, Stelzer EHK (1994) Confocal microscopy with an increased detection aperture: type-B 4Pi confocal microscopy. Opt Lett 19:222–224

Hepler PK (1982) Endoplasmic reticulum in the formation of the cell plate and plasmodesmata. Protoplasma 111:121–133

Huang B (2010) Super-resolution optical microscopy: multiple choices. Curr Opin In Chem Biol 14:10–14

Huang B, Wang W, Bates M, Zhuang X (2008) Three-dimensional super-resolution imaging by stochastic optical reconstruction microscopy. Science 319:810–813

Huang B, Bates M, Zhuang XW (2009) Super-resolution fluorescence microscopy. Ann Rev Biochem 78:993–1016

Iglesias VA, Meins F Jr (2000) Movement of plant viruses is delayed in a β-1, 3-glucanase-deficient mutant showing a reduced plasmodesmatal size exclusion limit and enhanced callose deposition. Plant J 21:157–166

Klar TA, Hell SW (1999) Subdiffraction resolution in far-field fluorescence microscopy. Opt Lett 24:954–956

Koster AJ, Klumperman J (2003) Electron microscopy in cell biology: integrating structure and function. Nat Cell Biol 4 (Supplement): SS6–SS10

Levy A, Erlanger M, Rosenthal M, Epel B (2007) A plasmodesmata-associated β-1, 3-glucanase in *Arabidopsis*. Plant J 49:669–682

Lippincott-Schwartz J, Patterson GH (2009) Photoactivatable fluorescent proteins for diffraction-limited and super-resolution imaging. Trends Cell Biol 19:555–565

Liu DYT, Kuhlmey BT, Smith PMC, Day DA, Faulkner CR, Overall RL (2008) Reflection across plant cell boundaries in confocal laser scanning microscopy. J Microsc 231:349–357

Lucas WJ (2006) Plant viral movement proteins: agents for cell-to-cell trafficking of viral genomes. Virology 344:169–184

Maillet M (1959) Modification de la technique de Champy au tetraoxyde d'osmium-iodure de K. Resultats de son application a l'etude des fibres nerveuses. C R Soc Biol 153:939–941

Maranto AR (1982) Neuronal mapping: a photooxidation reaction makes lucifer yellow useful for electron microscopy. Science 217:953–955

Maule AJ (2008) Plasmodesmata:structure, function and biogenesis. Curr Opin Plant Biol 11:680–686

McIntosh R, Nicastro D, Mastronarde D (2005) New views of cells in 3D: an introduction to electron microscopy. Trends Cell Biol 15:43–51

Meisslitzer-Ruppitsch C, Rohrl C, Neumuller J, Pavelka M, Ellinger A (2009) Photooxidation technology for correlated light and electron microscopy. J Microsc 235:322–335

Moore PJ, Fenczik CA, Deom CM, Beachy RN (1992) Developmental changes in plasmodesmata in transgenic tobacco expressing the movement protein of tobacco mosaic virus. Protoplasma 170:115–127

Moreno N, Bougourd S, Haselhoff J, Feijo JA (2006) Imaging plant cells. In: Pawley JP (ed) Handbook of biological confocal microscopy, 3rd edn. Springer, New York, pp 769–787

Mullendore DL, Windt CW, Van As H, Knoblauch M (2010) Sieve tube geometry in relation to phloem flow. Plant Cell 22:579–593

Olesen P (1979) The neck constriction in plasmodesmata. Planta 144:349–358

Oparka KJ (2004) Getting the message across: how do plant cells exchange macromolecular complexes? Trends Plant Sci 9:33–41

Oparka KJ, Read ND (1994) The use of fluorescent probes for studies of living plant cells, Plant cell biology: a practical approach. IRL, Oxford, pp 27–50

Oparka KJ, Prior DAM, Crawford JW (1994) Behaviour of plasma membrane, cortical ER and plasmodesmata during plasmolysis of onion epidermal cells. Plant Cell Environ 17:163–171

Patterson GH, Davidson M, Manley S, Lippincott-Schwartz J (2010) Super-resolution imaging using single-molecule localization. Annu Rev Phys Chem 61:345–367

Pellegrino de Iraldi A (1977) Significance of the Maillet method (ZIO) for cytochemical studies of subcellular structures. Experientia 33:1–10

Perinetti G, Muller T, Spaar A, Polishchuk R, Luini A, Egner A (2009) Correlation of 4Pi and electron microscopy to study transport through single Golgi stacks in living cells with super resolution. Traffic 10:379–391

Ritzenthaler C, Finlay K, Roberts K, Maule AJ (2000) Rapid detection of plasmodesmata in purified cell walls. Protoplasma 211:165–171

Robards AW, Lucas WJ (1990) Plasmodesmata. Annu Rev Plant Physiol 41:369–419

Roberts AG (2005) Plasmodesmal structure and development. In: Oparka KJ (ed) Plasmodesmata. Blackwell, Oxford, pp 1–23

Roberts IM, Boevink P, Roberts AG, Sauer N, Reichel C, Oparka KJ (2001) Dynamic changes in the frequency and architecture of plasmodesmata during the sink-source transition in tobacco leaves. Protoplasma 218:31–44

Robinson JM, Takizawa T (2009) Correlative fluorescence and electron microscopy in tissues: immunocytochemistry. J Microsc 235:259–272

Robinson-Beers K, Evert RF (1991) Fine structure of plasmodesmata in mature leaves of sugarcane. Planta 184:307–318

Schermelleh L, Carlton PM, Haase S, Shao L, Winoto L, Kner P, Burke B, Cardoso MC, Agard DA, Gustafsson MGL, Leonhardt H, Sedat JW (2008) Subdiffraction multicolor imaging of the nuclear periphery with 3D structured illumination microscopy. Science 320:1332–1336

Schmidt R, Wurm CA, Jakobs S, Engelhardt J, Egner A, Hell SW (2008) Spherical nanosized focal spot unravels the interior of cells. Nat Meth 5:539–544

Simpson C, Thomas C, Findlay K, Bayer E, Maule AJ (2009) An Arabidopsis GPI-anchor plasmodesmal neck protein with callose binding activity and potential to regulate cell-to-cell trafficking. Plant Cell 21:581–594

Stemmer A, Beck M, Fiolka R (2008) Widefield fluorescence microscopy with extended resolution. Histochem Cell Biol 130:807–817

Thomas CL, Bayer EM, Ritzenthaler C, Fernandez-Calvino L, Maule AJ (2008) Specific targeting of a plasmodesmal protein affecting cell-to-cell communication. PLoS Biol 6:180–190

Tilsner J, Oparka KJ (2010) Tracking the green invaders: advances in imaging virus infection in plants. Biochem J 430:21–37

Tilsner J, Amari K, Torrance L (2010) Plasmodesmata viewed as specialised membrane adhesion sites. Protoplasma. doi:10.1007/s00709-010-0217-6

Tomenius K, Clapham D, Meshi T (1987) Localization by immunogold cytochemistry of the virus-coded 30K protein in plasmodesmata of leaves infected with tobacco mosaic virus. Virology 160:363–371

Vesk M, Dibbayawan TP, Vesk PA, Egan EA (2000) Field emission scanning electron microscopy of plant cells. Protoplasma 210:138–155

Vogel F, Hofius D, Sonnewald U (2007) Intracellular trafficking of potato leaf roll virus movement protein in transgenic *Arabidopsis*. Traffic 8:1205–1214

Westphal V, Rizzoli SO, Lauterbach MA, Kamin D, Jahn R, Hell SW (2008) Video-rate far-field optical nanoscopy dissects synaptic vesicle movement. Science 320:246–249

White DL, Mazurkiewicz JE, Barrnett RJ (1979) A chemical mechanism for tissue staining by osmium tetroxide-ferrocyanide mixtures. J Histochem Cytochem 27:1084–1091

White J, Amos W, Fordham M (1987) An evaluation of confocal versus conventional imaging of biological structures by fluorescence light microscopy. J Cell Biol 105:41–48

Willig KI, Kellner RR, Medda R, Hein B, Jakobs S, Hell SW (2006) Nanoscale resolution in GFP-based microscopy. Nat Meth 9:721–723

Correlative Imaging of Fluorescent Proteins in Resin-Embedded Plant Material[1]

Karen Bell, Steve Mitchell, Danae Paultre, Markus Posch, and Karl Oparka*

Institute of Molecular Plant Sciences, University of Edinburgh, Edinburgh EH9 3JR, United Kingdom (K.B., S.M., D.P., K.O.); and Light Microscopy Facility, College of Life Sciences, University of Dundee, Dundee DD1 5EH, United Kingdom (M.P.)

Fluorescent proteins (FPs) were developed for live-cell imaging and have revolutionized cell biology. However, not all plant tissues are accessible to live imaging using confocal microscopy, necessitating alternative approaches for protein localization. An example is the phloem, a tissue embedded deep within plant organs and sensitive to damage. To facilitate accurate localization of FPs within recalcitrant tissues, we developed a simple method for retaining FPs after resin embedding. This method is based on low-temperature fixation and dehydration, followed by embedding in London Resin White, and avoids the need for cryosections. We show that a palette of FPs can be localized in plant tissues while retaining good structural cell preservation, and that the polymerized block face can be counterstained with cell wall probes. Using this method we have been able to image green fluorescent protein-labeled plasmodesmata to a depth of more than 40 μm beneath the resin surface. Using correlative light and electron microscopy of the phloem, we were able to locate the same FP-labeled sieve elements in semithin and ultrathin sections. Sections were amenable to antibody labeling, and allowed a combination of confocal and superresolution imaging (three-dimensional-structured illumination microscopy) on the same cells. These correlative imaging methods should find several uses in plant cell biology.

The localization of fluorescent proteins (FPs) in cells and tissues has become one of the major tools in cell biology (Tsien, 1998; Shaner et al., 2005). Advances in confocal microscopy have meant that many proteins can be tagged with appropriate fluorescent markers and tracked as they move within and between cells (Chapman et al., 2005). Additional approaches involving photobleaching and photoactivation of FPs have opened up new avenues for exploring protein dynamics and turnover within cells (Lippincott-Schwartz et al., 2003). However, not all cells are amenable to live-cell imaging, which in plants is usually restricted to surface cells such as the leaf epidermis. An example is the phloem. The delicate nature of sieve elements and companion cells, which are under substantial hydrostatic pressure, has made studies of the fine structure of these cells particularly difficult (Knoblauch and van Bel, 1998). Despite this, significant advances have been made in imaging the phloem through inventive use of imaging protocols that allow living sieve elements to be observed as they translocate assimilates (for review, see Knoblauch and Oparka, 2012). However, determining the precise localization of the plethora of proteins located within the sieve element (SE)-companion cell (CC) complex remains a technical challenge. The phloem is the conduit for long-distance movement of macromolecules in plants, including viral genomes. For several viruses, the entry into the SE-CC complex is a crucial step that determines the capacity for long-distance movement. Identifying the cell types within the phloem that restrict the movement of some viruses is technically challenging due to the small size of phloem cells and their location deep within plant organs (Nelson and van Bel, 1998).

The problems associated with imaging proteins in phloem tissues prompted us to explore methods for retaining the fluorescence of tagged proteins within tissues not normally amenable to confocal imaging. Previously, we used superresolution imaging techniques on fixed phloem tissues sectioned on a Vibroslice, providing information on the association between a viral movement protein (MP) and plasmodesmata (PD) within the SE-CC complex (Fitzgibbon et al., 2010). However, we wished to explore the same cells using correlative light and electron microscopy (CLEM), necessitating the development of methods that would allow sequential imaging of cells using fluorescence microscopy and transmission electron microscopy (TEM). To this end, we developed a protocol that retains fluorescent proteins through aldehyde fixation and resin embedding.

In the last 10 years there has been significant interest in imaging fluorescent proteins in semithin sections (for review, see Cortese et al., 2009). Luby-Phelps and colleagues (2003) first described a method for retaining GFP fluorescence after fixation and resin embedding, but their method has not seen widespread application. The advent of superresolution imaging techniques (for review, see Bell and Oparka, 2011) has stimulated considerable interest in this field as the retention of

[1] This work was supported by the Biotechnology and Biological Sciences Research Council and the Scottish Universities Life Sciences Alliance.

* Corresponding author; e-mail karl.oparka@ed.ac.uk.

The author responsible for distribution of materials integral to the findings presented in this article in accordance with the policy described in the Instructions for Authors (www.plantphysiol.org) is: Karl Oparka (karl.oparka@ed.ac.uk).

www.plantphysiol.org/cgi/doi/10.1104/pp.112.212365

fluorescence in thin sections means that cells can be imaged using techniques such as photoactivation light microscopy and stochastic optical reconstruction microscopy, allowing a lateral resolution of less than 10 nm to be achieved (Subach et al., 2009; Xu et al., 2012). A number of studies have described CLEM on the same cells (Luby-Phelps et al., 2003; Betzig et al., 2006; Watanabe et al., 2011). Advances in this field were reviewed recently (Jahn et al., 2012; see contributions in Muller-Reichert and Verkade, 2012). For example, Pfeiffer et al. (2003) were able to image SEs and CCs using high-pressure freezing, followed by freeze substitution in acetone and resin embedding. They then used thick optical sections of the tissue to locate cells of interest, and these were subsequently imaged using TEM. However, there have been few attempts to retain FPs in resin-embedded plant tissues. Thompson and Wolniak (2008) described the retention of mCitrine fused to an SE-plasma membrane protein in glycol methacrylate sections. The fluorescent signal was stable using wide-field microscopy but bleached rapidly under the confocal microscope.

To date, cryosections have been the preferred choice for CLEM in mammalian tissues (Watanabe et al., 2011). Recently, Lee et al. (2011) chemically fixed Arabidopsis (*Arabidopsis thaliana*) seedlings, cut 50-μm sections, and examined these with a confocal microscope. After confocal mapping the sections were embedded in resin and thin sectioned. These authors were able to locate the same PD pit fields using confocal and TEM, providing important information on the localization of a novel PD protein. As general rule, cryosectioning is a time-consuming process, and subcellular details may be obscured in cryosections because of poor tissue contrast (Watanabe et al., 2011). A major problem with imaging FPs in resin sections has been that GFP and its derivatives are quenched by the acidic, oxidizing conditions required for fixation, dehydration, and embedding of delicate specimens (Tsien, 1998; Keene et al., 2008). Recently, however, Watanabe et al. (2011) explored the retention of FPs in *Caenorhabditis elegans* cells after fixation by different aldehydes and embedding media. These authors tested a range of resins and found that Citrine and tandem dimer Eos (tdEos) could be retained in methacrylate plastic sections. This material was difficult to cut thinly (<70 nm) compared to epoxy-based resins, but the authors obtained valuable correlative images using stimulated emission depletion microscopy and photoactivation light microscopy followed by low-voltage scanning electron microscopy.

Because the retention of fluorescent proteins may differ between plant and animal cells, we explored a number of approaches for retaining fluorescent proteins in resin. Using low-temperature conditions (<8°C) during fixation and dehydration, we could retain strong fluorescence prior to tissue embedding. We also explored different embedding media and found that tissue could be effectively polymerized in London Resin (LR) White while retaining sufficient fluorescence for confocal imaging. Using water-dipping lenses, we were able to detect fluorescent proteins in optical sections up to 40 μm below the surface of the block face. Ultrathin sections from the same blocks showed good structural preservation and allowed CLEM. Subsequently, we cut 1- to 2-μm sections and examined these using confocal microscopy and three-dimensional-structured illumination microscopy (3D-SIM). Sections could be counterstained with a number of conventional fluorophores and antibodies, allowing colocalization studies. These simple methods allow successive imaging of FPs with the light and electron microscope, combining the strengths of both imaging platforms. We believe this approach will have significant utility for tissues that are recalcitrant to conventional confocal imaging.

RESULTS

Fixation and Dehydration

Because a variety of methods have been used to retain FPs in semithin sections, we conducted a series of tests on tobacco (*Nicotiana tabacum*) and Arabidopsis plants expressing different FPs. For these tests we used a transgenic tobacco line in which HDEL:GFP was expressed under the *SEO2* promoter (Knoblauch and Peters, 2010), which is active only in sieve elements. In this line, GFP is targeted to the sieve element reticulum (SER), a specialized form of endoplasmic reticulum that exists as an anastomosing network of tubules and parietal stacked aggregates (Knoblauch and Peters, 2010). This line has discrete GFP fluorescence readily visible in freehand sections (Fig. 1A). This signal was monitored through fixation and embedding and allowed fluorescence levels to be assessed during optimization of the method. Previously we showed that GFP fluorescence, antigenicity, and structural integrity were well preserved in tissue fixed using a combination of 4% paraformaldehyde and 0.25% glutaraldehyde (Fitzgibbon et al., 2010). The aim here was to preserve the tissue sufficiently so that it could withstand the rigors of both light and electron microscopy. As expected, we found that fixation and dehydration at room temperature eliminated fluorescence before the samples were embedded (Keene et al., 2008). However, fixation and dehydration at low temperature (<8°C) successfully retained fluorescence. We were able to increase the glutaraldehyde concentration as high as 2%, while still retaining good fluorescence preservation. However, we noticed a concomitant increase in the autofluorescence of the tissues, particularly the xylem, at this higher glutaraldehyde concentration. However, the fluorescent signal from GFP was easily visible above background (Fig. 1B). To limit background autofluorescence during processing we included dithiothreitol (DTT) during dehydration and infiltration. When used in combination with low temperature processing, DTT reduces background autofluorescence (Brown et al., 1989), preserves antigenicity during chemical fixation (Baskin et al., 1992, 1996), and may prevent quenching of fluorescent proteins (Thompson and Wolniak, 2008).

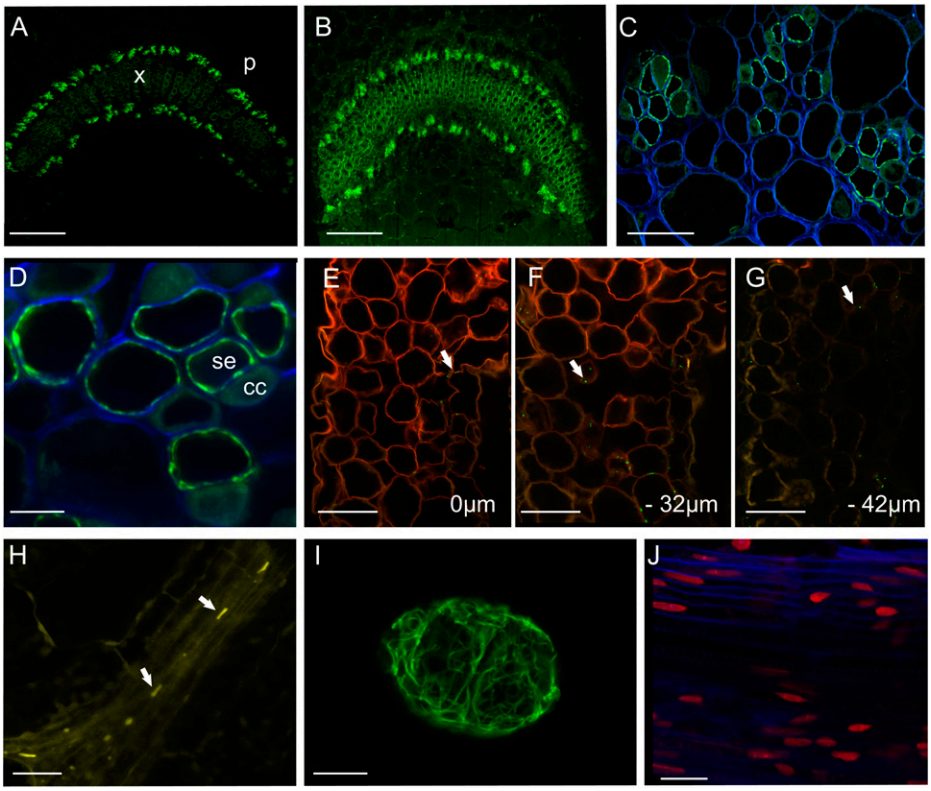

Figure 1. En bloc imaging of FPs using confocal microscopy. A, Unprocessed, free-hand section of a tobacco petiole expressing pSEO2.HDEL:GFP (shown in green; Knoblauch and Peters, 2010). In this construct, GFP highlights the SER but at this magnification reveals general fluorescence from phloem bundles. p, Phloem, x, xylem. Scale = 600 μm. B, Petiole expressing pSEO2.HDEL:GFP imaged in a polymerized block of LR. Scale = 600 μm. C, An embedded petiole expressing pSEO2.HDEL:GFP imaged with a 63× water-dipping lens. The SER is clearly visible at this magnification. Cell walls (blue) were highlighted with calcofluor white, which was added directly to the block face. Scale = 40 μm. D, A region of the phloem at higher magnification. SEs (se) show conspicuous labeling of the SER, while CCs (cc) show background autofluorescence. Scale = 10 μm. E–G, Imaging of an Arabidopsis line expressing a viral movement protein fused to GFP (MP17:GFP; Vogel et al., 2007). GFP signal is evident from plasmodesmata (arrow) in mesophyll cells of the leaf. Cell walls were counterstained en bloc with propidium iodide (red). The block was optically sectioned and images captured at the block surface (0 μm; E), at −32 μm (F), and at −42 μm (G) below the block surface. Note that GFP fluorescence from PD is apparent to a depth greater than the penetration of the propidium iodide stain. Scale = 50 μm. H, En bloc imaging of SEOR1 protein (arrows) tagged with YFP (see Froelich et al., 2011) in the phloem of the midvein of an Arabidopsis leaf. Scale = 25 μm. I, En bloc reconstruction of a viral X-body produced by a PVX vector modified to express GFP fused to its coat protein (CP:GFP; Santa-Cruz et al.,1996). Scale = 25 μm. J, Nuclei in the hypocotyl of Arabidopsis expressing a histone 2B fused to RFP (H2B:RFP; Federici et al., 2012). Cell walls were counterstained with calcofluor. Scale = 25 μm.

Resin Embedding

We tested a number of resins including LR White, methacrylate, and Durcupan, a water-miscible resin. Following dehydration, we attempted low-temperature, ultraviolet-, and heat-polymerizing protocols. Material embedded in Durcupan did not section well in our hands. Methacrylate retained fluorescence well after low-temperature/ultraviolet polymerization, but significant tissue collapse was evident (data not shown). Our best results were obtained by polymerizing samples at 50°C in LR White following low-temperature fixation and dehydration. We monitored loss of fluorescence from tissue sections using ImageJ software and found a 27.5% (±6, n = 11) loss of fluorescence relative to fresh tissue during fixation and embedding. We deemed this to be an acceptable loss and pursued optimization of subsequent steps. It is likely that plant tissues respond differently to fixatives and embedding media. However, the protocol detailed in the methods section was suitable for most of the tissues we examined.

Imaging FPs en Bloc and in Semithin Sections

We showed previously that plant cell walls can be imaged successfully en bloc following polymerization of tissues in Araldite (Prior et al., 1999). After fixation and embedding in LR White, we imaged the polymerized block face using confocal microscopy. In tobacco phloem tissues expressing HDEL:GFP, we could detect fluorescent phloem bundles en bloc at magnifications as

low as 5× (Fig. 1B). We were able to counterstain the cell walls en bloc by adding 10 μg mL^{-1} calcofluor white (Hahne et al., 1983) or 1 μg mL^{-1} propidium iodide (Pighin et al., 2004) directly to the block face as droplets. Using a 63× lens, we obtained a strong GFP signal from the SER while the calcofluor staining clearly delineated the cell walls (Fig. 1C). We found that glutaraldehyde fixation caused a faint background autofluorescence from the cytoplasm, allowing CCs to be identified (Fig. 1D). When we used propidium iodide as a wall stain, we found that the cell walls became labeled to a depth of more than 30 μm into the tissue, allowing deep confocal imaging using water-dipping lenses. In a transgenic line expressing a viral MP fused to GFP (MP17-GFP; Vogel et al., 2007), we were able to image fluorescent PD in leaf mesophyll cells to a depth of more than 40 μm into the resin block (Fig. 1E–G). At this depth, the propidium iodide signal had faded significantly, but the MP17-GFP signal remained strong (Fig. 1G).

SEs in Arabidopsis are extremely small (Mullendore et al., 2010), making SE substructures difficult to detect in semithin sections. Using an Arabidopsis line expressing yellow fluorescent protein (YFP) fused to the sieve-element occlusion related (SEOR1) protein (Froelich et al., 2011), we were able to image phloem protein bodies within individual sieve elements en bloc (Fig. 1H). Next we embedded tobacco leaf petioles infected with a Potato Virus X (PVX) vector in which GFP is fused to the viral coat protein (PVX.CP-GFP; Santa Cruz et al., 1996). In this virus, the GFP forms a virion "overcoat," allowing the virus to be tracked as it moves. As expected, we found large aggregates of virus particles associated with the viral X-bodies, structures that harbor a range of viral and host components (Tilsner et al., 2012). Using en bloc imaging we could reconstruct individual X-bodies using optical sectioning and reconstruction (Fig. 1I). We also embedded an Arabidopsis line expressing a histone 2B-red fluorescent protein (RFP) fusion (Federici et al., 2012). Here we were able to image RFP-labeled nuclei in resin sections of the hypocotyl (Fig. 1J).

CLEM

Following observation of the block face in the confocal microscope, we cut ultrathin sections (60 nm) for electron microscopy and stained these with uranyl acetate and lead citrate. We attempted to image these thin sections in the confocal microscope, prior to heavy-metal staining, but were unable to detect a GFP signal (see also Keene et al., 2008). Ultrathin sections of the phloem expressing HDEL:GFP showed good structural preservation, despite the lack of osmication (Fig. 2A). We imaged several phloem bundles in the petiole using TEM and were able to identify the same cells in the block face in the confocal microscope (Fig. 2B). In Figure 2C, note that in addition to the fluorescent SER, small vacuoles in the cytoplasm of parenchyma cells can be seen in both the TEM and confocal images. In a number of sections, we were able to identify fluorescent parietal SER aggregates (Fig. 2D) that could also be detected in ultrathin sections with the TEM (Fig. 2, E and F).

Correlative 3D-SIM, Confocal Microscopy, and TEM

Most superresolution imaging approaches require that the cells of interest lie close to the coverslip to maximize spatial resolution (Huang et al., 2009; Bell

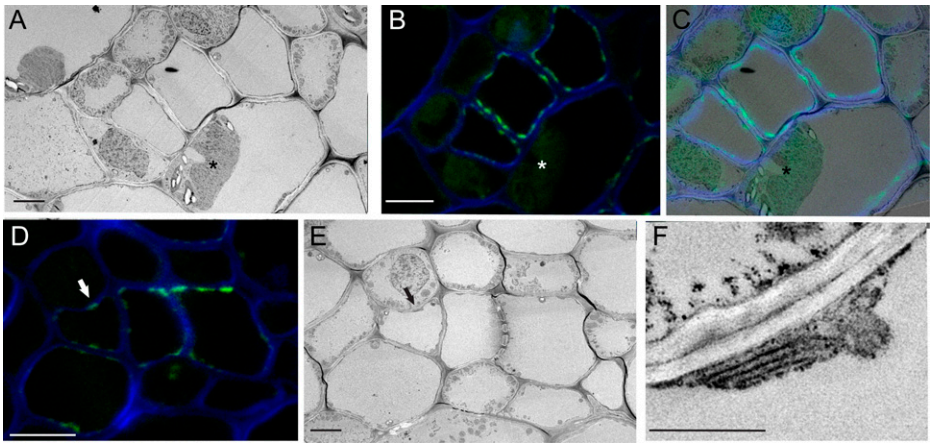

Figure 2. CLEM of pSEO2.HDEL:GFP. A, TEM image of an ultrathin section of petiole from a plant expressing pSEO2.HDEL:GFP. The section was poststained with uranyl acetate and lead citrate. Scale = 5 μm. B, A semithin section acquired immediately after the TEM section, imaged with the confocal microscope, showing the same field of view. Note that small vacuoles in the cytoplasm can be seen in both the TEM and confocal images (stars in A and B). Scale = 5 μm. C, Overlay image of A and B showing alignment of sieve elements in the confocal and TEM images. D, A Semithin section of the phloem imaged in the confocal microscope shows conspicuous SER stacks (arrow). Scale = 10 μm. E, The TEM image of the same field of view. The same SER stack arrowed in D is apparent in E (arrow). Scale = 5 μm. F, An enlarged image of the SER stack arrowed in E. Scale = 1 μm.

and Oparka, 2011). The retention of GFP in semithin sections meets these requirements and allows super-resolution imaging. After confocal imaging of the block face, we cut ultrathin sections and a semithin section from the same region of the block. Using 3D-SIM, we obtained images of sieve plate pores that revealed spatial information not present using confocal microscopy or TEM. Figure 3, A–D, shows sieve plates imaged sequentially by confocal laser scanning microscopy (CLSM), TEM, and 3D-SIM. Note that each method reveals different information on the structure of the sieve plate. Using CLSM we could detect, but not resolve, sieve plate pores and the SER associated with them (Fig. 3A). In the thin-section TEM image, we could resolve sieve plate pores and their callose collars, but only partial pore transects were encountered due to the section thickness (Fig. 3, B and C). In the 3D-SIM image, in which we were able to take sequential Z-sections at 125-nm spacing, we were able to reconstruct portions of the sieve plate within the thickness of the section (Fig. 3D). 3D-SIM resolved the sieve plate pores and revealed distinct cellulose collars that were not apparent in either the TEM or CLSM images (Fig. 3D). Our fixation protocol preserved the fine structure of the SER, which in glancing at sections of sieve plates appeared as a fine mesh of interconnected tubules (Fig. 3E). Using 3D-SIM imaging, we could detect similar fine tubules of fluorescent SER associated with sieve plates (Fig. 3D). These correlative imaging approaches reveal that the three forms of microscopy adopted here (CLSM, 3D-SIM, and TEM) are complementary, each revealing important information on subcellular structure.

We also examined sections of tissue infected by PVX.CP-GFP using 3D-SIM. We were able to image fine bundles of virus filaments that could be resolved to about 100 nm in diameter (Fig. 3F). Significantly, we saw very little bleaching of the GFP signal during the multiple acquisitions required to generate 3D-SIM images.

Immunofluorescence

LR is compatible with fluorescent antibody labeling, so we were able to achieve triple labeling of sieve elements by cutting 1- to 2-μm sections from the blocks and labeling these with an antibody against callose. Callose is a cell wall constituent found at the neck of PD (Simpson et al., 2009) and sieve plates (Fitzgibbon et al., 2010). Using the confocal microscope, we could detect callose at the lateral sieve plates (Alexa 594 secondary antibody) along with the SER (HDEL:GFP; Fig. 4A). Figure 4B is a 3D-SIM image of a sieve plate in transverse orientation. The sieve plate callose was

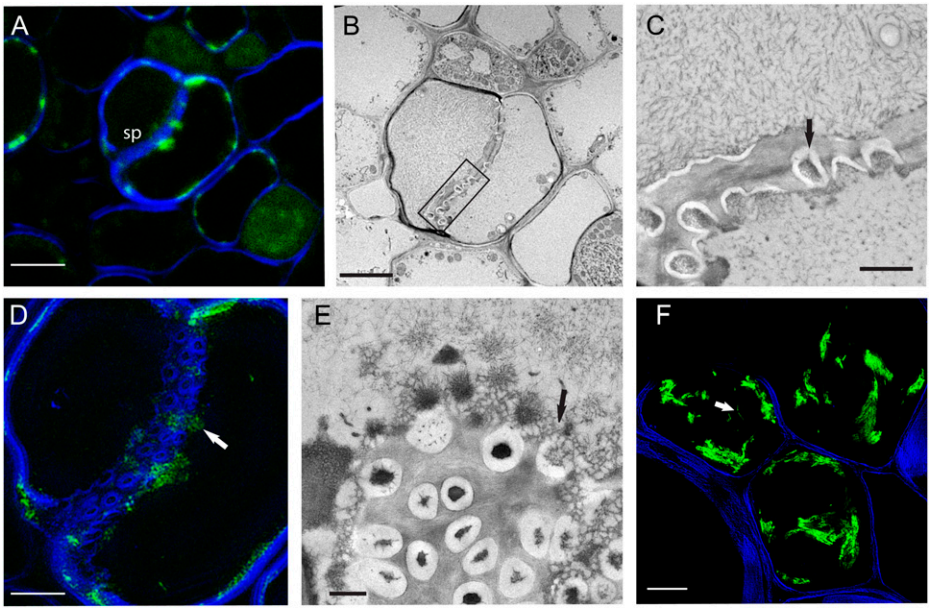

Figure 3. Correlative 3D-SIM, confocal microscopy, and TEM of the phloem. A, A semithin section of the phloem from a tobacco petiole expressing pSEO2.HDEL:GFP counterstained with calcofluor white to highlight cell walls and a sieve plate (SP). The sieve plate and SER are visible but not resolved. Scale = 5 μm. B, The TEM image of the same field reveals details of the sieve plate and resolves sieve plate pores. Scale = 5 μm. C, Enlargement of the sieve plate region boxed in B, revealing callose collars (arrow) around the pores. Scale = 1 μm. D, A 3D-SIM image of the same sieve plate was taken using the section shown in A. The 3D-SIM image was reconstructed from 20 serial Z-sections and, unlike the confocal image, resolves distinct cellulose collars around the sieve plate pores. The SER is visible at the sieve plate (arrow). Scale = 5 μm. E, The fine structure of the tubular SER (arrow) is apparent in a glancing transverse section of a sieve plate imaged using TEM. Scale = 1 μm. F. 3D-SIM image of PVX X-body (see also en bloc image in Fig. 1). 3D-SIM resolves fine viral filaments at around 100 nm in diameter (arrow). Scale = 5 μm.

immunolabeled and the cellulose highlighted using calcofluor white. The inset is an enlarged view of two of the pores and shows that the cellulose collars (see Fig. 3D) form outside the callose pore linings. Figure 4C shows a confocal image of an immunolabeled sieve tube in longitudinal orientation. We used 3D-SIM to image the same sieve tube following staining with calcofluor white (Fig. 4D). This revealed the arrangements of the SER, callose, and cellulose, respectively, on the sieve plate (Fig. 4D, i–iv).

DISCUSSION

The field of correlative microscopy has undergone considerable expansion in recent years (Muller-Reichert and Verkade, 2012). Correlative microscopy is the application of two or more microscopy techniques to the same region of a sample, generating complementary structural and chemical information that would not be possible using a single technique (Jahn et al., 2012). In this field, new superresolution imaging instruments have bridged the gap between light and electron microscopy (Watanabe et al., 2011). While confocal microscopy has become the mainstay of modern cell biology, there is a growing need to image the localization of proteins with increasing subcellular accuracy (Betzig et al., 2006). Two distinct types of correlative microscopy approaches have been identified; "combinatorial labeling," in which two or more labels are identified using different forms of microscopy (e.g. confocal and TEM) and "noncombinatorial labeling," in which the label appears in only one type of imaging method but allows identification of the same cells using a second method (Jahn et al., 2012). Generally, noncombinatorial labeling involves faster and simpler sample preparation. The technique we have described here, in which FPs are retained in fixed and embedded plant cells, is an example of a noncombinatorial approach that allows the same FP-containing cells to be identified using TEM. However, our method could be adapted to a combinatorial one if the proteins of interest were first labeled with a probe (e.g. fluoronanogold or quantum-dot complexes) that would produce fluorescent and electron-dense signals in both confocal microscopy and TEM, respectively.

A major goal has been to determine precisely the structures within which fluorescent proteins reside. The technique we have described here retains fluorescent proteins in resin blocks and semithin sections, and allows imaging of those plant tissues that are

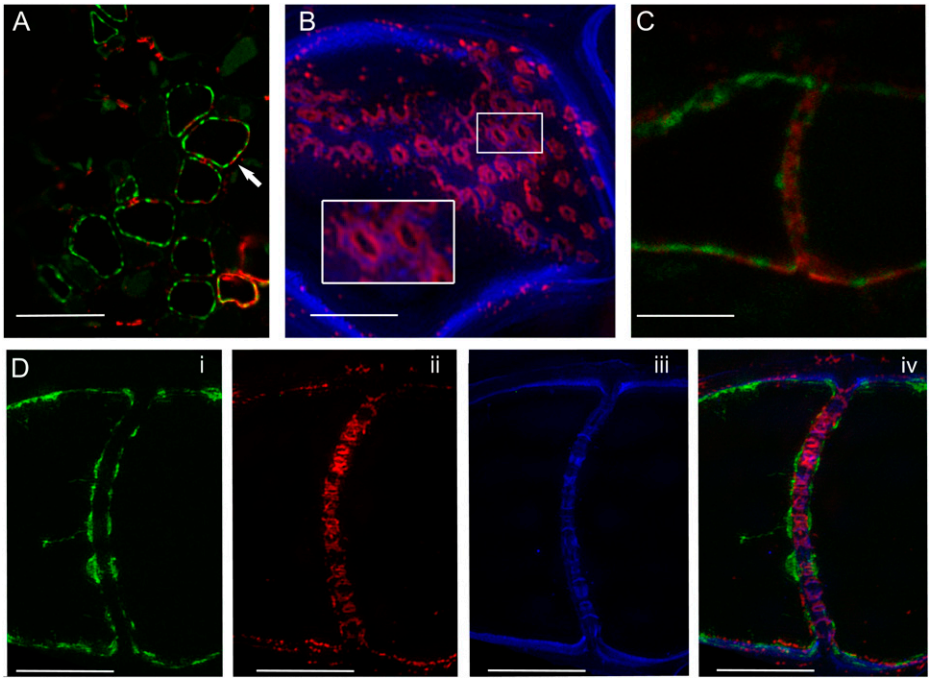

Figure 4. Immunodetection of callose in semithin sections of resin-embedded material. A, SER stacks (pSEO2.HDEL:GFP) are seen in tranverse sections of sieve elements. Alexa 594-conjugated secondary antibody reveals callose at the sites of lateral sieve areas (red; arrow). Scale = 25 μm. B, 3D-SIM image of a sieve plate in transverse orientation. The sieve plate callose was labeled with anticallose antibody and visualized using an Alexa 594 secondary antibody (red). The inset is an enlarged view of two of the pores and shows that the cellulose collars form outside the callose pore linings. C, Confocal image of a sieve element in longitudinal orientation. Callose labeling appears at the sieve plate as well as the lateral areas. Scale = 10 μm. D, 3D-SIM image of the same sieve plate shown in C. The arrangements of the SER, callose, and cellulose are revealed. SER is shown in green (pSEO2.HDEL:GFP; i), callose in red (anticallose antibody and Alexa 594 secondary; ii), cellulose in blue (calcofluor; iii). The merge of all three channels is shown (iv). Scale = 5 μm.

problematic with conventional live-cell fluorescence microscopy. To achieve CLEM we first examined the block face, ahead of cutting a semithin section, followed by ultrathin sections for TEM. These sections showed good structural preservation when fixed with a combination of glutaraldehyde and paraformaldehyde. As in previous studies (Keene et al., 2008), we were unable to retain sufficient fluorescence in the ultrathin sections to achieve correlative imaging on the same ultrathin section. However, using sequential sectioning we were able to locate the same cells and fluorescently tagged structures using confocal imaging and TEM. The retention of fluorescent proteins in semithin sections also allowed us to use superresolution imaging on the same sections as those used for confocal imaging, extending the range of imaging protocols that can be brought to bear on a single sample. Interestingly, sequential imaging did not simply extend the resolution range but also provided new information on subcellular structure. For example, using 3D-SIM we were able to resolve distinct cellulose collars surrounding sieve plate pores. These collars were situated outside the central callose collar but were not visible in either the confocal or TEM images. They may have been generated by the formation of sieve plate callose that, as it expanded, compressed the cellulose microfibrils around the pore.

Autofluorescence

In the material we used here, the FP signal was strong and detected easily above background autofluorescence. With increasing glutaraldehyde concentrations we found that the autofluorescence of cells increased. This was particularly true of the xylem, but other cells showed a degree of cytoplasmic fluorescence. In confocal images this was useful in identifying different cell types in the phloem, such as companion cells (e.g. Fig. 1D). It is unlikely that our method will work on cells that show a low and/or diffuse FP signal. Ultimately, the method requires a trade off between fixation and fluorescence that will depend on the questions being addressed.

Variability in LR White pH

Watanabe et al. (2011) noted that the pH of batches of LR White varied considerably. Generally, FPs are quenched at low pH (<6; Tsien, 1998). We noted also that the pH of LR White batches was variable but obtained good FP retention in plant tissues embedded in a LR White pH range extending from 4.6 to 6.5 (data not shown). Higher-pH resin batches are to be preferred because of potential quenching of fluorophores. LR White may be buffered to higher pH using ethanolamine (Watanabe et al., 2011). However, this may cause the blocks to become brittle and difficult to section (data not shown). Checking the pH of the resin before attempting FP localization is advisable.

CONCLUSION

The greatest utility of our method is likely to be in the imaging of FP-labeled structures that are difficult to image using conventional fluorescence microscopy. Such imaging is usually conducted on surface cells, or to a depth that can be accommodated by serial optical imaging. While multiphoton microscopy may extend the depth to which such sectioning is possible (Zipfel et al., 2003), resolution becomes limited. We have shown that by imaging plant tissues en bloc using appropriate counterstains, small structures such as PD (<50 nm) can be viewed to a depth of more than 40 μm in leaf cells. Such deep imaging is helpful when trying to locate structures in the block for subsequent electron microscope imaging (Prior et al., 1999) and also permits optical reconstruction of cells without painstaking serial sectioning. When required, semithin sections of the tissue can be cut, and these can be stained with conventional fluorophores and antibodies. Despite multiple imaging steps on both confocal and 3D-SIM microscopes, the fluorescent proteins we studied retained strong fluorescence and showed little photobleaching. We have been able to return to the same blocks over a period of several months, and so the method is likely to allow long-term preservation of fluorescent proteins in resin when sectioning is required at a later date.

MATERIALS AND METHODS

Plant Material

Tobacco (*Nicotiana tabacum*) plants expressing pSEO2.HDEL:GFP (Knoblauch and Peters, 2010) and *Nicotiana benthamiana* were grown from seed in a heated glasshouse and used in experiments between 30 and 55 d old. Arabidopsis (*Arabidopsis thaliana*) seedlings expressing SEOR1:YFP (Froelich et al., 2011), MP17:GFP (Vogel et al., 2007), and H2B:RFP (Federici et al., 2012) were germinated and grown on Murashige and Skoog media. Arabidopsis plants were used between 3 and 5 d post germination.

Fixation and Embedding

For tobacco, the petiole was cut and immediately submerged in 4% (w/v) formaldehyde (Agar Scientific), 2% (w/v) glutaraldehyde (TAAB), 50 mM PIPES, and 1 mM $CaCl_2$ and then trimmed further under fixative to eliminate any potential airlocks. The petioles were allowed to transpire the fixative solution via the xylem for 60 min at room temperature in an illuminated fume hood (see Fitzgibbon et al., 2010). The petiole was then sectioned transversely into about 2-mm transverse slices using a double-edged razor blade. The sections were then returned to the fixative and incubated for 16 h on a rolling-bed platform in the dark at 8°C. Further tissue processing was done at 8°C in the dark unless stated otherwise. The sections were then washed in buffer (50 mM PIPES, 1 mM $CaCl_2$) three times for 10 min before dehydration in a graded ethanol series (50% [v/v], 70% [v/v], and 90% [v/v] twice, each for 15 min). The ethanol solutions also contained 1 mM DTT to reduce tissue autofluorescence (Brown et al., 1989). The tissue sections were then infiltrated in medium grade LR (London Resin Company) at 1:1, 1:2, and 1:3 ratios of 90% ethanol (supplemented by 1 mM DTT) to resin for 45 min each before two 60-min changes in 100% LR. The final embedding step was done at ambient temperature. The samples were then polymerized in gelatin capsules (TAAB) at 50°C for 24 h.

In the case of Arabidopsis, the seedlings were processed intact and embedded as described above. The only deviation was that the H2B:RFP seedlings were fixed with 1% glutaraldehyde to maximize RFP fluorescence.

Loss of Tissue Fluorescence

To measure losses in FP fluorescence during the above steps, tissue slices were removed at each stage of the fixation and embedding process and their

fluorescence compared with fresh hand sections of the petiole. For each section of the line expressing pSEO2.HDEL:GFP, a region of the phloem was photographed at 5× under identical settings on the confocal microscope. For each stage of fixation and embedding the fluorescence was measured in 11-phloem bundles, using ImageJ (Schneider et al., 2012), and the mean fluorescence value calculated as a percentage of the initial fluorescence.

En Bloc Staining

En bloc staining of cell walls was done with 1 μg mL^{-1} propidium iodide (Invitrogen) and 10 μg mL^{-1} calcofluor white (Sigma) by adding a drop of dyes to trimmed block faces and allowing them to penetrate into the tissue for 20 min. The remaining dye was then rinsed from the block face by immersing it in distilled water for 2 min.

Confocal Microscopy

Semithin sections (1 to 2 μm) were cut using a glass knife on a Leica Ultracut UCT ultramicrotome (Leica Microsystems). These, and also the intact block faces, were imaged using a Leica SP2 confocal laser scanning microscope (Leica Microsystems) with either a 5× (HC PL FLUOTAR; Leica Microsystems) or a 63× water-immersion lens (HCX PLAPO CS; Leica Microsystems). Calcofluor was excited at 405 nm, GFP at 488 nm, YFP at 514 nm, RFP at 561 nm, and Alexa 594 at 591 nm.

Transmission Electron Microscopy

Ultrathin sections (60 nm) were cut using a Diatome diamond knife, stained in 1% (w/v) aqueous uranyl acetate and Reynolds lead citrate (Reynolds, 1963) and viewed in a Philips CM120 transmission electron microscope (FEI). Representative images were taken on a Gatan Orius CCD camera (Gatan).

Immunolocalization of Callose

Semithin sections were cut as above and then affixed to a slide using a coating of poly-L-Lys (Invitrogen) and heated briefly (1 to 2 min) on a slide warmer. Sections were then incubated for 10 min in blocking solution (3% [w/v] bovine serum albumin; 50 mM Gly in 1% [w/v] phosphate buffered saline [PBS]) before being rinsed with 1% PBS three times for 1 min each. They were then incubated for 90 min in mouse anticallose antibody (Biosupplies) at a 1:400 dilution. Sections were rinsed three times for 1 min in the blocking solution before incubation with secondary antibody, anti-mouse Alexa 594 (Invitrogen) diluted 1:500, for 1 h. All antibodies were diluted in 1% bovine serum albumin, 0.02% (v/v) Tween in 1% (w/v) PBS and incubated at 37°C. The sections were rinsed in 1% PBS three times for 1 min each before staining with 10 mM calcofluor (Invitrogen). After 2 min, excess stain was rinsed off using 1% PBS. The sections were then allowed to air dry before mounting with Citifluor AF1 antifade agent (Agar Scientific) under a number 1 coverslip and then sealed with nail varnish. Tissue sections were then imaged with a Leica SP2 confocal scanning microscope, using 59-nm excitation for Alexa 594 and 405-nm excitation for Calcofluor, as described above.

PVX Infections

Infections were initiated in *N. benthamiana* using a 35S promoter-driven PVX.GFP-CP bombardment construct (C. Lacomme, unpublished data). Microprojectile bombardments were carried out with a custom-built gene gun similar to the one described in Gaba and Gal-On (2005).

3D-SIM

3D-SIM was conducted as described by Fitzgibbon et al. (2010), using the protocol initially described by Schermelleh et al. (2008). Images were acquired on an OMX microscope (Applied Precision) equipped with 405-, 488-, and 593-nm solid-state lasers and a UPlanSApochromat 100× 1.4 numerical aperture, oil immersion objective lens (Olympus). Samples were illuminated by a coherent scrambled laser light source that had passed through a diffraction grating to generate the structured illumination by interference of light orders in the image plane to create a three-dimensional sinusoidal pattern, with lateral stripes approximately 0.2 μm apart. The pattern was shifted laterally through five phases and through three angular rotations of 60° for each Z-section, separated by 0.125 μm. Exposure times were typically between 100 and 200 ms, and the power of each laser was adjusted to achieve optimal intensities of between 2,000 and 4,000 counts in a raw image of 16-bit dynamic range, at the lowest possible laser power to minimize photo bleaching. Raw images were processed and reconstructed to reveal structures with greater resolution (Gustafsson et al., 2008) implemented on SoftWorx, version 6.0 (Applied Precision). The channels were then aligned in x, y, and rotationally using predetermined shifts as measured using 100-nm TetraSpeck (Invitrogen) beads with the SoftWorx alignment tool (Applied Precision).

ACKNOWLEDGMENTS

We thank Dr. Christophe Lacomme for the use of the 35S promoter-driven PVX.GFP-CP bombardment construct. We thank Dr. Michael Knoblauch for providing the SEO lines used in this study and Dr. Jim Haseloff for providing the histone 2B:RFP line.

Received December 7, 2012; accepted February 19, 2013; published March 1, 2013.

LITERATURE CITED

Baskin TI, Busby CH, Fowke LC, Sammut M, Gubler F (1992) Improvements in immunostaining samples embedded in methacrylate: localisation of microtubules and other antigens throughout developing organs in plants of diverse taxa. Planta **187:** 405–413

Baskin TI, Miller DD, Vos JW, Wilson JE, Hepler PK (1996) Cryofixing single cells and multicellular specimens enhances structure and immunocytochemistry for light microscopy. J Microsc **182:** 149–161

Bell K, Oparka KJ (2011) Imaging plasmodesmata. Protoplasma **248:** 9–25

Betzig E, Patterson GH, Sougrat R, Lindwasser OW, Olenych S, Bonifacino JS, Davidson MW, Lippincott-Schwartz J, Hess HF (2006) Imaging intracellular fluorescent proteins at nanometer resolution. Science **313:** 1642–1645

Brown RC, Lemmon BE, Mullinax JB (1989) Immunofluorescent staining of microtubules in plant tissues: improved embedding and sectioning techniques using polyethylene glycol (PEG) and Steedman's wax. Bot Acta **102:** 54–61

Chapman S, Oparka KJ, Roberts AG (2005) New tools for *in vivo* fluorescence tagging. Curr Opin Plant Biol **8:** 565–573

Cortese K, Diaspro A, Tacchetti C (2009) Advanced correlative light/electron microscopy: current methods and new developments using Tokuyasu cryosections. J Histochem Cytochem **57:** 1103–1112

Federici F, Dupuy L, Laplaze L, Heisler M, Haseloff J (2012) Integrated genetic and computation methods for *in planta* cytometry. Nat Methods **9:** 483–485

Fitzgibbon J, Bell K, King E, Oparka K (2010) Super-resolution imaging of plasmodesmata using three-dimensional structured illumination microscopy. Plant Physiol **153:** 1453–1463

Froelich DR, Mullendore DL, Jensen KH, Ross-Elliott TJ, Anstead JA, Thompson GA, Pélissier HC, Knoblauch M (2011) Phloem ultrastructure and pressure flow: sieve-element-occlusion-related agglomerations do not affect translocation. Plant Cell **23:** 4428–4445

Gaba V, Gal-On A (2005). Inoculation of plants using bombardment. Curr Protoc Microbiol **16:** B3.1–B3.14

Gustafsson MGL, Shao L, Carlton PM, Wang RCJ, Golubovskaya IN, Cande ZW, Agard DA, Sedat JW (2008) Three-dimensional resolution doubling in wide-field fluorescence microscopy by structured illumination. Biophys J **94:** 4957–4970

Hahne G, Herth W, Hoffman F (1983) Wall formation and cell-division in fluorescence-labelled plant protoplasts. Protoplasma **115:** 217–221

Huang B, Bates M, Zhuang XW (2009) Super-resolution fluorescence microscopy. Annu Rev Biochem **78:** 993–1016

Jahn KA, Barton DA, Kobayashi K, Ratinac KR, Overall RL, Braet F (2012) Correlative microscopy: providing new understanding in the biomedical and plant sciences. Micron **43:** 565–582

Keene DR, Tufa SF, Lunstrum GP, Holden P, Horton WA (2008) Confocal/TEM overlay microscopy: a simple method for correlating confocal and electron microscopy of cells expressing GFP/YFP fusion proteins. Microsc Microanal **14:** 342–348

Knoblauch M, Oparka K (2012) The structure of the phloem: still more questions than answers. Plant J **70:** 147–156

Knoblauch M, Peters WS (2010) Münch, morphology, microfluidics: our structural problem with the phloem. Plant Cell Environ **33:** 1439–1452

Knoblauch M, van Bel AJE (1998) Sieve tubes in action. Plant Cell **10:** 35–50

Lee JY, Wang X, Cui W, Sager R, Modla S, Czymmek K, Zybaliov B, van Wijk K, Zhang C, Lu H, et al (2011) A plasmodesmata-localized protein mediates crosstalk between cell-to-cell communication and innate immunity in *Arabidopsis*. Plant Cell **23:** 3353–3373

Lippincott-Schwartz J, Altan-Bonnet N, Patterson GH (2003) Photobleaching and photoactivation: following protein dynamics in living cells. Nat Cell Biol **5**(Suppl): S7–S14

Luby-Phelps K, Ning G, Fogerty J, Besharse JC (2003) Visualization of identified GFP-expressing cells by light and electron microscopy. J Histochem Cytochem **51:** 271–274

Mullendore DL, Windt CW, Van As H, Knoblauch M (2010) Sieve tube geometry in relation to phloem flow. Plant Cell **22:** 579–593

Muller-Reichert T, Verkade P, editors (2012) Correlative Light and Electron Microscopy. Methods in Cell Biology, Vol 111. Academic Press, Oxford

Nelson RS, van Bel AJE (1998) The mystery of virus trafficking into, through and out of vascular tissue. Prog Bot **59:** 476–533

Pfeiffer S, Beese M, Boettcher M, Kawaschinski K, Krupinska K (2003) Combined use of confocal laser scanning microscopy and transmission electron microscopy for visualisation of identical cells processed by cryotechniques. Protoplasma **222:** 129–137

Pighin JA, Zheng HQ, Balakshin LJ, Goodman IP, Western TL, Jetter R, Kunst L, Samuels AL (2004) Plant cuticular lipid export requires an ABC transporter. Science **306:** 702–704

Prior DAM, Oparka KJ, Roberts IM (1999) *En bloc* optical sectioning of resin-embedded specimens using a confocal laser scanning microscope. J Microsc **193:** 20–27

Reynolds ES (1963) The use of lead citrate at high pH as an electron-opaque stain in electron microscopy. J Cell Biol **17:** 208–212

Santa Cruz S, Chapman S, Roberts AG, Roberts IM, Prior DAM, Oparka KJ (1996) Assembly and movement of a plant virus carrying a green fluorescent protein overcoat. Proc Natl Acad Sci USA **93:** 6286–6290

Schermelleh L, Carlton PM, Haase S, Shao L, Winoto L, Kner P, Burke B, Cardoso MC, Agard DA, Gustafsson MGL, et al (2008) Subdiffraction multicolor imaging of the nuclear periphery with 3D structured illumination microscopy. Science **320:** 1332–1336

Schneider CA, Rasband WS, Eliceiri KW (2012) NIH Image to ImageJ: 25 years of image analysis. Nat Methods **9:** 671–675

Shaner NC, Steinbach PA, Tsien RY (2005) A guide to choosing fluorescent proteins. Nat Methods **2:** 905–909

Simpson C, Thomas C, Findlay K, Bayer E, Maule AJ (2009) An *Arabidopsis* GPI-anchor plasmodesmal neck protein with callose binding activity and potential to regulate cell-to-cell trafficking. Plant Cell **21:** 581–594

Subach FV, Patterson GH, Manley S, Gillette JM, Lippincott-Schwartz J, Verkhusha VV (2009) Photoactivatable mCherry for high-resolution two-color fluorescence microscopy. Nat Methods **6:** 153–159

Thompson MV, Wolniak SM (2008) A plasma membrane-anchored fluorescent protein fusion illuminates sieve element plasma membranes in Arabidopsis and tobacco. Plant Physiol **146:** 1599–1610

Tilsner J, Linnik O, Wright KM, Bell K, Roberts AG, Lacomme C, Santa Cruz S, Oparka KJ (2012) The TGB1 movement protein of potato virus X reorganizes actin and endomembranes into the X-body, a viral replication factory. Plant Physiol **158:** 1359–1370

Tsien RY (1998) The green fluorescent protein. Annu Rev Biochem **67:** 509–544

Vogel FD, Hofius D, Sonnewald U (2007) Intracellular trafficking of potato leafroll virus movement protein in transgenic Arabidopsis. Traffic **8:** 1205–1214

Watanabe S, Punge A, Hollopeter G, Willig KI, Hobson RJ, Davi MW, Hell SW, Jorgensen EM (2011) Protein localization in electron micrographs using fluorescence microscopy. Nat Methods **8:** 80–84

Xu K, Babcock HP, Zhuang X (2012) Dual-objective STORM reveals three-dimensional filament organization in the actin cytoskeleton. Nat Methods **9:** 185–188

Zipfel WR, Williams RM, Webb WW (2003) Nonlinear magic: multiphoton microscopy in the biosciences. Nat Biotechnol **21:** 1369–1377

Chapter 4

Preparative Methods for Imaging Plasmodesmata at Super-resolution

Karen Bell and Karl Oparka

Abstract

Much of our knowledge of plasmodesmata has come from the ability to visualize them. Light microscopy is a popular tool for exploring subcellular structures but is limited in its resolving power due to the diffractive properties of light. At 50 nm in diameter plasmodesmata are below this limit and so cannot be resolved. Super-resolution microscopy operates beyond the limits of conventional light microscopy affording a more detailed view. Although lacking the ultrastructural resolving power of the electron microscope (EM), super-resolution microscopy helps to bridge the gap between conventional light microscopy and EM.

Here we present three preparative methods for studying plasmodesmata at super-resolution using 3D-structured illumination microscopy (3D-SIM).

Key words Plasmodesmata, Super-resolution microscopy, Immunofluorescence, 3D-SIM, Electron microscopy, Correlative microscopy

1 Introduction

Due to its compatibility with many molecular methods, light microscopy remains a powerful tool for the plant-cell biologist. Light microscopy has enabled the imaging of live cells, the study of dynamic processes, and the genetic labelling of multiple targets using the ever-expanding pallet of fluorescent proteins. However, conventional light microscopy is still limited by a comparative lack of resolution compared to electron microscopy. This is due to the diffraction limit of light which dictates that, in an ideal system, objects closer together than approximately 200 nm laterally (x–y) and 500 nm axially (in z) cannot be resolved but instead appear blurred (for brief discussion *see* [1] and references therein). The point scanning and optical sectioning capacity of confocal laser scanning microscopy (CSLM) has allowed researchers to work close to this limit. This has brought many cellular components in sharper focus but, at 50 nm in diameter, plasmodesmata (PD)

Manfred Heinlein (ed.), *Plasmodesmata: Methods and Protocols*, Methods in Molecular Biology, vol. 1217,
DOI 10.1007/978-1-4939-1523-1_4,

cannot be resolved. Proteomic approaches have identified new PD-associated proteins [2, 3] but their location at or within the PD pore remains speculative due to the lack of detail afforded by CSLM. Recent innovations in biological imaging have broken the diffraction limit and promise to offer new views of structures and cellular processes. One example we have used to image PD is structured illumination microscopy (SIM). SIM uses spatially patterned excitation to extend resolution. This involves introducing a defined patterned structure to the incident light which when it interacts with the sample structure, as represented by the distribution of the dye/fluorescent protein, produces emitted light that contains interference fringes. This is best explained in terms of the moiré effect [4] that dictates that if two fine patterns are superimposed multiplicatively, a moiré fringe will result in the product. This fringe may be coarser than either of the original patterns and so may be more readily observable in the microscope. As the illumination pattern is known, this can be readily accounted for within the moiré fringe, allowing additional information about the unknown sample structure to be determined. As the patterning of the incident light is directional, it is necessary to shift and rotate the phase over 360° resulting in multiple images, each taken 125 nm apart in Z [5]. The images are then processed to produce the final super-resolution image. Currently the resolution achievable with 3D-SIM is 100 nm in xy direction and 200 nm in *z* direction [6]. This increased resolution is of obvious benefit to PD researchers but equally so is the increased optical sectioning capacity (125 nm steps). The typical plant cell is 700 nm thick and 3D-SIM allows up to five images to be taken in this volume (c.f. approximately only once every 500 nm with CSLM). This allows different components of PD to be spatially resolved (Fig. 1).

3D-SIM has been commercialized by Applied Precision Inc. (Washington, USA) and released with the title Optical Microscope eXperimental (OMX). The OMX design seeks to maximize the photon budget (number of photons transmitted through the microscope) by optimizing the efficiency of light transmission, and by the suppression of stray light and noise [5]. The illumination and imaging systems are placed in an acoustically isolated, thermally controlled room. A dedicated auxiliary microscope, with transmission and epi-fluorescence illumination, is used for sample location and mapping. The high-precision motorized stage is cross-linked with that of the OMX to allow coordinate sharing. A tile scan is performed of the sample before it is mounted on the OMX stage, which is then used as a high-resolution location map for finding specific features/locations, preserving the sample from further illumination prior to imaging.

3D-SIM is compatible with standard fluorochromes and sample preparation techniques. The utility of 3D-SIM in PD and phloem research has already been established [8, 9] and detailed preparative methods for its use are described in this chapter.

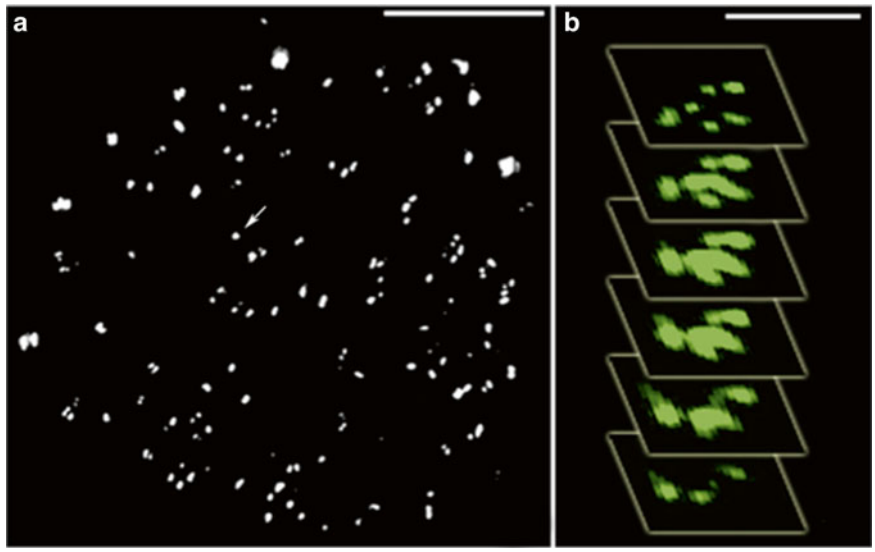

Fig. 1 3D-SIM images of branched plasmodesmata. (**a**) A volume projection showing all the branched plasmodesmata at the trichome-epidermis interface (as highlighted by TMV MP-GFP; [7]). Scale bar 5 μm. (**b**) Optical sections (125 nm apart) of a single branched PD (*arrowed* in **a**). Note that six branches can be detected at the trichome face with only three emerging in the epidermis. Pores fuse in the middle lamella region of the wall. Scale bar 1 μm. Figure (**a**) and (**b**) reproduced from Fitzgibbon, J., Bell, K., King, E., and Oparka, K. (2010) Super-resolution imaging of plasmodesmata using three-dimensional structured illumination microscopy. *Plant Physiol* 153, 1453–1463. www.plantphysiol.org Copyright American Society of Plant Biologists

Although super-resolution microscopy offers a bridge between conventional light microscopy and electron microscopy, it would be desirable to confirm that observations made using this technology are robust and that they can be readily confirmed using the transmission electron microscope (TEM). It is, however, a considerable challenge to produce material that has been adequately fixed and processed so that it can withstand the rigors of imaging with the electron microscope while still retaining fluorescence and antigenicity. London Resin (LR) is an acrylic-based resin that is compatible with light and electron microscopy. The resin is hardened by free radical chain polymerization that shows no affinity for proteins or nucleic acids in the sample. In this chapter we mention the use of LR to embed material while retaining fluorescence and antigenicity, allowing the same cells to be imaged using light and transmission electron microscopy. This approach generates complementary structural information beyond that possible using a single imaging technique [9].

Many of the new super-resolution approaches currently suffer from a comparative lack of "user friendliness" that is taken for granted with conventional imaging. Live-cell imaging, for instance, has been done at super-resolution [10–12] but is by no means routine, and has yet to be conducted in plants. Currently, super-resolution techniques

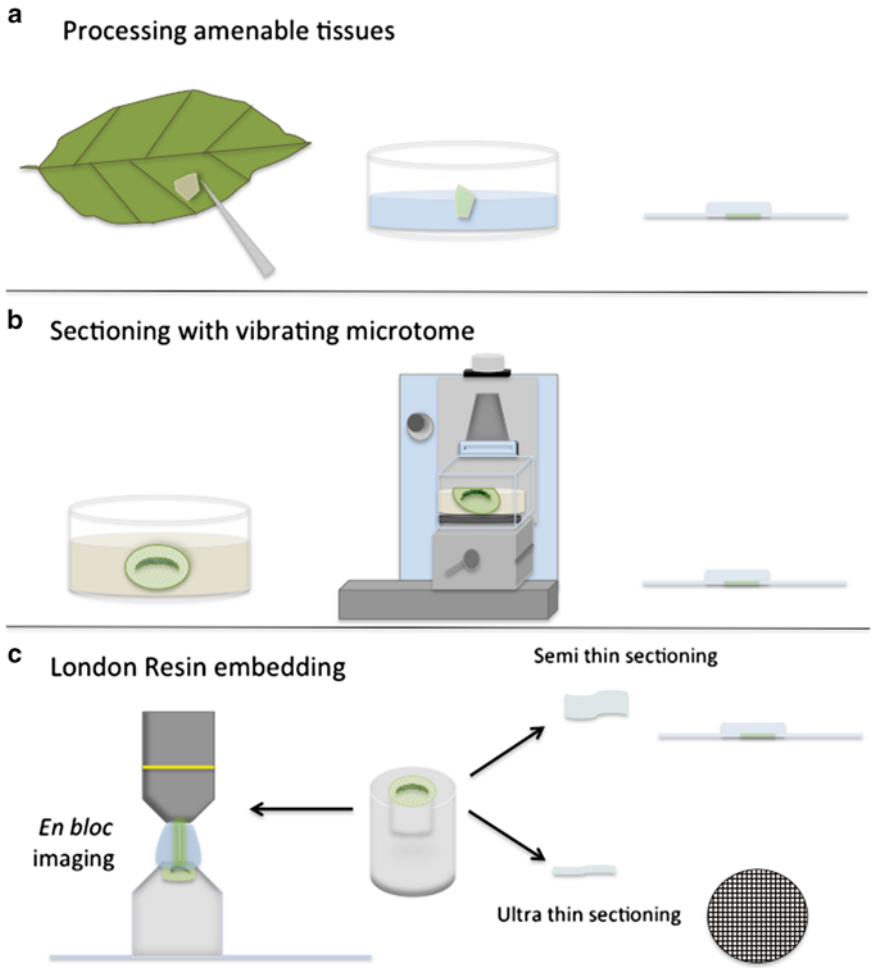

Fig. 2 Three methods for preparing materials for 3D-SIM. (**a**) Processing amenable tissues or preparing epidermal peels. Tissues and peels are processed in a petri dish and then mounted on a slide under a number 1.5 cover slip for fluorescence and SIM imaging. (**b**) Sectioning with a vibrating microtome. Samples are first fixed and then stabilized with phytoagar in a petri dish ahead of sectioning with a vibrating microtome. Sections are then processed essentially as in (**a**), ahead of mounting and imaging for fluorescence and SIM. (**c**) Embedding in London Resin. Samples are fixed and dehydrated ahead of embedding in London Resin. The sample can then be viewed *en bloc* using a confocal microscope ahead of cutting semi-thin sections for fluorescence, immunofluorescence, or SIM imaging. Ultrathin sections can also be cut for transmission electron microscopy (TEM). This method allows the same cells to be imaged using fluorescence, SIM, and TEM, allowing a direct comparison of these imaging technologies

offer the greatest, and most readily achievable, advantages when using fixed, thin, or sectioned samples. In this chapter we present three methods for preparing material for 3D-SIM (Fig. 2). The first is direct processing of amenable plant tissues, e.g., fine roots, hypocotyls, or epidermal leaf peels that can be readily mounted under a cover slip (Fig. 2a). The second is a method suitable for imaging the vasculature (Fig. 2b). Vascular tissues generally lie deep within plant organs, exceeding the working distance of conventional lenses.

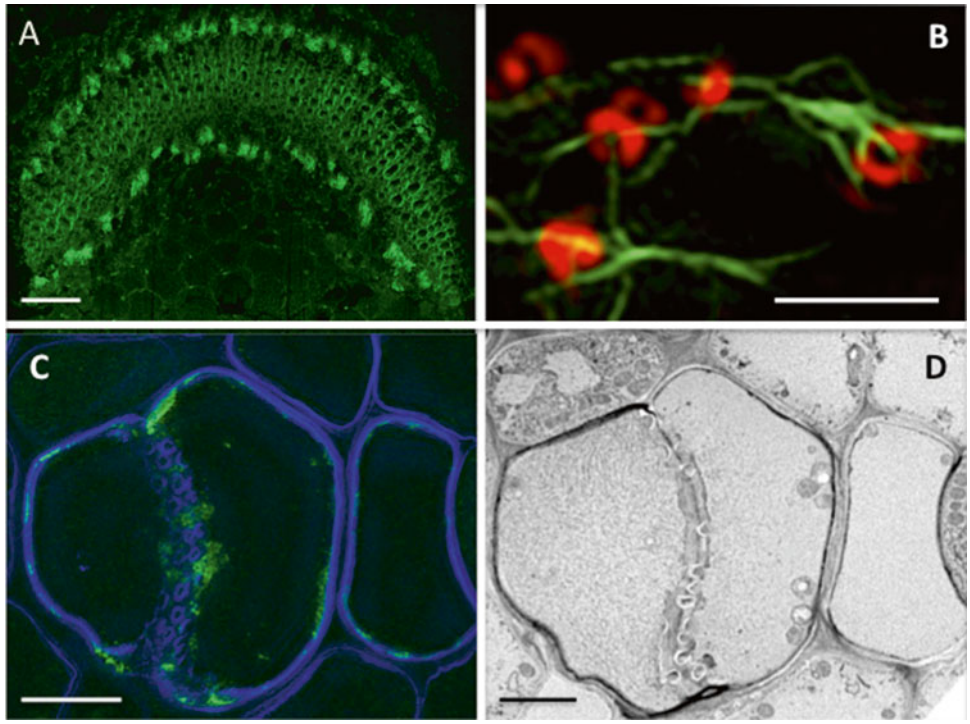

Fig. 3 Images of processed material. (**a**) *En bloc* image of a London Resin-embedded tobacco petiole expressing pSEO2.HDEL:GFP (shown in *green*; [13]), which highlights the sieve element reticulum and making the sieve elements clearly visible. Scale 600 μm. (**b**) 3D-SIM image showing tobacco mosaic virus movement protein fused to GFP (TMV MP-GFP) expressed from the CaMV 35S promoter. TMV MP-GFP is associated with the pore plasmodesma units (PPUs) at the sieve element-companion cell interface. 3D-SIM image reveals that individual strands of MP connect many PPUs. Scale 5 μm. (**c**) 3D-SIM image of phloem expressing pSEO2. HDEL:GFP and counterstained with calcofluor white to highlight the cell wall and sieve-plate callose. The image was reconstructed from 20 serial Z sections and reveals callose collars in the sieve plate as well as the intricate nature of the sieve-element reticulum. Scale 5 μm. (**d**) TEM image of the same field of view shown in (**c**). Greater ultrastructural detail is revealed than in (**c**) but the image lacks the 3D context afforded by SIM. Scale 3 μm. Figure (**a**), (**c**), and (**d**), reproduced from Bell, K,. Mitchell, S., Paultre, D., Posch, M., and Oparka, K. (2013) Correlative imaging of fluorescent proteins in resin-embedded plant material. Plant Physiology, 161: 1595–1603. www.plantphysiol.org Copyright American Society of Plant Biologists. Figure (**b**) reproduced from Fitzgibbon, J., Bell, K., King, E., and Oparka, K., (2010) Super-resolution imaging of plasmodesmata using three-dimensional structured illumination microscopy. *Plant Physiol* 153, 1453–1463. www.plantphysiol.org Copyright American Society of Plant Biologists

By stabilizing the material and sectioning with a vibrating microtome it is possible to produce 50 μm sections. The vibrations of the blade ensure that the cut is made with less pressure than with a static blade, which is desirable when cutting tissues that have not first been reinforced with resin. The final method uses London Resin to infiltrate the tissue, allowing semi-thin (0.5–2 μm) and ultrathin (60 nm) sections to be obtained from the block (Fig. 2c). All three methods preserve fluorescence and antigenicity (*see* Fig. 3 for a panel of representative images). However, the method selected will depend on the

specific question being addressed. Making epidermal peels may be sufficient to analyze cells for transient assays, while investing time in embedding tissue in London Resin has more flexibility and allows long-term storage (>1 year at 4 °C).

2 Materials

2.1 Processing Epidermal Peels for Antibody Labelling

1. Fixative: 50 mM 1,4-piperazinediethanesulfonic acid (PIPES) pH 6.9, 2 mM EGTA, 1 % (w/v) bovine serum albumin (BSA) in distilled H_2O (dH_2O). Add 4 % (v/v) formaldehyde and 0.25 % (v/v) glutaraldehyde. Prepare fresh (*see* **Note 1**).
2. Wash buffer: 2 mM EGTA, 1 % (w/v) BSA, 50 mM PIPES pH 6.9 in dH_2O.
3. PBS: Phosphate-buffered saline: 1 mM KH_2PO_4, 155 mM NaCl, and $Na_2HPO_4{\cdot}7H_2O$ in dH_2O, pH 7.4.
4. Blocking solution: 3 % (w/v) BSA and 50 mM glycine in PBS.
5. Antibody solution: Pertinent antibody diluted in PBS containing 1 % (w/v) BSA and 0.02 % (v/v) Tween-20.
6. Mount: Use a number 1.5 cover slip (0.17 mm thick) and antifade mountant, such as Citifluor AF1 (Citifluor Ltd. Leicester, UK). Seal cover slips on a slide using nail varnish.

2.2 Producing Sections Using a Vibrating Microtome

1. Stabilizer: 5 % (w/v) phytoagar in dH_2O (*see* **Note 2**).
2. Enzyme solution: 2 % (w/v) driselase (w/v) in PBS with 1 % (w/v) BSA and 5 mM EDTA (*see* **Note 3**).
3. Rinse buffer: 50 mM PIPES, 2 mM EGTA, 1 % (w/v) BSA in dH_2O with 10 % (v/v) glycerol, and 0.2 % (v/v) Triton X-100.

Otherwise the same solutions are used as in Subheading 2.1.

2.3 Embedding in London Resin for Retention of Fluorescent Proteins [9]

Green and yellow fluorescent protein fluorescence has been retained in tobacco and Arabidopsis leaves, stems, petioles, and roots using this method [9].

1. Fixative: 50 mM PIPES (pH 6.9) and 1 mM $CaCl_2$ in dH_2O. Add formaldehyde to 4 % (v/v) and glutaraldehyde to 2 % (v/v). Make fresh (*see* **Note 4**).
2. Wash buffer: 50 mM PIPES (pH 6.9) and 1 mM $CaCl_2$ in dH_2O.
3. Dehydration solutions: 50, 70, and 90 % (v/v) ethanol diluted with dH_2O and supplemented with 1 mM dithiothreitol (DTT) (*see* **Note 5**). Store at 4 °C.
4. Infiltration solutions: 90 % (v/v) ethanol with 1 mM DTT (as prepared above) and London Resin Medium Grade (LR; Agar Scientific, Essex, UK) in a 1:1, 1:2, 1:3 (90 % ethanol:LR) ratio. Store components at 4 °C and use while chilled.

5. Staining solutions: (a) 1 μg/mL propidium iodide in dH_2O; (b) 10 μg/mL calcofluor white in dH_2O.
6. Poly-l-lys-coated glass slides: Immerse slides into poly-l-lys diluted 1:10 with dH_2O and agitate for 5 min. Drain and then dry the slides at 60 °C for 60 min or at room temperature (18–26 °C) overnight.
7. Ultrathin section stains: (a) 1 % uranyl acetate in double-distilled H_2O (ddH_2O) (*see* **Note 6**); (b) lead citrate staining solution: 40 nM lead nitrate, 61 nM sodium citrate in ddH_2O: mix to a uniform milky suspension. To this add 0.2 M sodium hydroxide, and mix by inversion until suspension clears completely (*see* **Note 7**).

   Otherwise the same solutions are used as in Subheading 2.1.

3 Methods

3.1 Processing Epidermal Peels for Imaging PD

This method is compatible with fluorescence microscopy immunofluorescence labelling and 3D-SIM.

1. Make an abaxial leaf peel and float it immediately on the fixative at room temperature for 45 min (*see* **Note 8**).

From now on all processing should occur at room temperature with gentle agitation unless stated otherwise.

2. Replace the fixative with wash buffer and incubate for 10 min. Make a further two changes of wash buffer, changing the solution every 10 min as before.

Samples can now be mounted (*see* Subheading 3.1, **step 7**) *or processing can continue for antibody labelling*:

3. Replace with the blocking solution and incubate as above for 20 min.
4. Replace with the antibody solution with primary antibody diluted as appropriate. Incubate for 16 h at 37 °C without agitation (*see* **Note 9**).
5. Rinse by replacing the primary antibody solution with the blocking solution. Change the solution three times, once every 10 min.
6. Replace with the antibody solution, with secondary antibody diluted as appropriate, and incubate for 3 h at 37 °C without agitation.
7. Rinse with PBS twice for 5 min each before mounting directly upon a number 1.5 cover slip. Add a drop of Citifluor AF1 antifade medium (Citifluor Ltd., Leicester, UK) to the slide and then press gently to spread the mountant (*see* **Note 10**).

3.2 Producing Sections Using a Vibrating Microtome

This method is compatible with fluorescence microscopy, immunofluorescence labelling, and 3D-SIM, and is best accomplished using a vibrating microtome.

1. Vascular tissues can be fixed effectively by allowing the fixative to transpire in the xylem from where it moves laterally to other tissues, including the phloem. This method allows delivery of fixative to delicate cells (e.g., sieve elements), avoiding the need for cutting live tissues. To achieve this, immediately submerge the cut petiole or stem in the fixative solution and then trim the bottom 5 mm from the submerged tissue to eliminate any potential airlocks. Leave to transpire in an illuminated fume hood for 60 min.
2. Pour cooled (40 °C) molten stabilizer into a petri dish and add trimmed tissue on top. Push down gently with a blunt implement to submerge. Take care to remove any surrounding air bubbles and orientate the sample to reflect the direction of sectioning desired, e.g., lying flat at 180° to the surface to produce longitudinal sections or at 90° to the surface to cut transversely. Once set, trim any extra stabilizer from the surface and section with the vibrating microtome (we use a Vibroslice HA752 from Campden Instruments, Leicestershire, UK) at a medium-fast setting to produce 100 μm sections.

All further processing occurs at room temperature with gentle agitation unless stated otherwise.

3. Transfer sections to a 5 mL petri dish filled with wash buffer. Replace every 10 min three times.

Samples can now be counterstained (Subheading 3.2, **step 9**) *and mounted* (Subheading 3.2, **step 10**) *for imaging or processed further for immunofluorescence*:

4. Optional driselase digestion: Replace wash buffer with enzyme solution and incubate for 15 min at 37 °C without agitation. Using rinse buffer wash three times replacing every 10 min. Then wash with PBS three times, changing every 5 min.
5. Replace with the blocking solution and incubate for 20 min.
6. Remove the blocking solution and replace with the antibody solution, with the primary antibody diluted as appropriate. Incubate for 16 h at 37 °C without agitation.
7. Rinse the sections using the blocking solution. Change the solution three times, once every 10 min.
8. Dilute the secondary antibody in the antibody solution and incubate the sections in this solution for 3 h at 37 °C without agitation.
9. *Optional counterstaining*: Rinse the sections with PBS, twice for 5 min each time. Stain briefly for 1 min by replacing the

PBS with stain (e.g., Calcofluor White at 10 μg/mL to highlight cellulose in cell walls) prior to rinsing with dH_2O.

10. Rinse with PBS, twice for 5 min each time (*unless following* Subheading 3.2, **step 9**, *above*), and then mount sections directly on a number 1.5 cover slip. Add a drop of Citifluor AF1 antifade medium (Citifluor Ltd. Leicester, UK) to the slide and then press gently to spread the mountant. Seal with nail varnish to facilitate long-term storage.

3.3 Correlative Imaging of Fluorescent Proteins in Material Embedded in London Resin

3.3.1 Tissue Processing

This method is compatible with en bloc imaging, fluorescence microscopy, immunofluorescence, 3D-SIM, and TEM.

1. Fix the sample using the fixative described in Subheading 2.3 and in the manner described in Subheading 3.1, **step 1**, if using peels or seedlings, or as in Subheading 3.2, **step 1**, if fixing vasculature tissues. Following the initial 60-min fixation, peels and seedlings are fixed further by incubating on a rolling-bed platform in the dark at 8 °C for 16 h. To ensure that the dense vasculature is well fixed after the 60-min xylem irrigation of fixative, the petiole or stem is trimmed into approximately 2 mm segments using a double-sided razor blade and fixed for a further 16 h on a rolling-bed platform in the dark at 8 °C.

From now on processing is done at 8°C in the dark, with constant gentle agitation using a rolling-bed platform unless otherwise stated.

2. Remove the fixative and rinse the tissues three times in wash buffer, changing every 10 min.
3. Dehydrate the tissue using a series of dehydration solutions (each for 15 min) that contain increasing concentrations of ethanol. Use the 90 % ethanol-containing solution twice.
4. Infiltrate the tissue sections with infiltration solutions (containing increasing concentrations of the LR resin) for 45 min each followed by two 60-min changes in 100 % LR, the final one of which is incubated at room temperature.
5. Transfer the samples to gelatine capsules and fill to overflowing with 100 % resin at room temperature. Close the lid tightly (*see* **Note 11**). Polymerize the resin for 24 h at 50 °C (*see* **Note 12**).
6. Remove the gelatine capsule with a razor blade. Trim the block top carefully to a trapezoid with the section area being as small as possible to include the part(s) of the specimen of interest.

The specimen may now be viewed directly en bloc, or sections can be taken using an ultramicrotome for fluorescence microscopy, antibody labelling, or ultrastructural observation in the transmission electron microscope.

3.3.2 ***En Bloc*** *Imaging and Staining*

This is a simple way to check the quality and orientation of the specimen ahead of further sectioning.

1. Stick the base of the polymerized block to a slide with adhesive tack and then carefully lower the objective lens in place (*see* **Note 13**). The optical sectioning properties of a confocal microscope should allow imaging up to 40 μm into the block where, if present, the fluorescent protein should still be visible [9] which is useful for identifying structures of interest and to allow targeted sectioning.
2. The cell-wall stains propidium iodide or calcofluor white penetrate the resin block well and provide a useful reference point for imaging cell walls. Add a drop of either staining solution to the trimmed block face and allow the stain to penetrate into the tissue for 20 min at room temperature. The remaining dye can then be rinsed from the block face by immersing it in distilled water for 2 min and gently agitating the block using a rolling-bed platform.
3. Stained or unstained, the blocks may be stored for up to 1 year in the dark at 4 °C (*see* **Note 14**).

3.3.3 *Dye Staining of Semi-thin Sections for Fluorescence Microscopy*

1. Cut semi-thin sections (1–2 μm) using a glass knife and, if not already stained *en bloc*, stain these briefly as in Subheading 3.2, **step 9**, prior to rinsing in dH_2O and mounting with Citifluor antifade agent under a number 1.5 cover slip. Seal the cover slip to the slide with nail varnish.

3.3.4 *Labeling Semi-thin Sections with Antibodies for Fluorescence Microscopy*

1. Affix semi-thin sections to poly-l-lys-coated slides by heating briefly (1–2 min) on a slide warmer.
2. Incubate the sections in blocking solution for 10 min and rinse three times for 1 min with PBS.
3. Dilute primary antibody as appropriate in the antibody solution and incubate the sections for 90 min at 37 °C in this solution.
4. Rinse sections three times for 1 min with blocking solution.
5. Dilute the secondary antibody in the antibody solution and incubate the sections in this solution at 37 °C for 60 min.
6. Mount and counterstain, if desired, as in Subheading 3.2, **steps 9** and **10**.

3.3.5 *Preparing Sections for TEM*

1. Cut ultrathin (60 nm) sections using a glass or diamond knife and mount on an EM grid. To do this, have sections floating on water and touch the dull side of the grid to the center of the section briefly taking care not to break the surface tension of the water. If the grids are clean the sections should readily transfer from the water to the grid.

2. To stain, first quickly wet the grids in ddH_2O (*see* **Note 15**) and then float section side down, on a drop (*see* **Note 16**) of uranyl acetate for 45 min. Using forceps grasp the grid by its edge and wash by dipping it rapidly in ddH_2O for 1 min and then repeat for a further 1 min in a fresh pool of ddH_2O. Counterstain with lead citrate by inverting the grid section side down onto a drop and leaving for 10 min. Wash again, as above, and then allow to air-dry prior to imaging with the TEM.

4 Notes

1. While it is advisable to prepare the fixative solution on the day of use, the stocks (PIPES, EGTA, BSA) may be prepared ahead of time and autoclaved to facilitate long-term storage. Use fixatives supplied in single-use glass ampules. Use EM-grade glutaraldehyde and a methanol-free preparation of formaldehyde. Decant into screw-cap glass bottle (store glutaraldehyde at 4 °C and formaldehyde at RT) and use within 1 month.
2. It is necessary to support the tissue during sectioning. Phytoagar is a plant tissue culture agar with a high gel strength and can be used at a minimal concentration of 5.0 g/L to obtain a solid gel. This concentration matches the mechanical properties of a young petiole well and so adequately supports sectioning. However, it will be necessary to vary the concentration of phytoagar when handling other tissues (e.g., leaves) so that the agar does not buckle or break away from the tissue.
3. Driselase is useful when processing vasculature as it allows the sectioned material to separate slightly, affording a better view of phloem strands.
4. In order to preserve fine structure at the TEM level it is necessary to increase the concentration of glutaraldehyde. We found 2 % to be sufficient to preserve ultrastructure while retaining fluorescence and antigenicity, at least for callose labelling [9].
5. When dehydrating before London Resin embedding it is necessary to use ethanol because acetone can act as a free radical scavenger that interferes with the polymerization of the resin. To limit aldehyde-induced autofluorescence, DTT is included during dehydration and infiltration. When used in combination with low-temperature processing, DTT reduces background autofluorescence [14], preserves antigenicity during chemical fixation [15, 16], and may prevent quenching of fluorescent proteins [17].
6. 1 % uranyl acetate takes between 1 and 2 h to dissolve in ddH_2O on a rotary mixer. Filter through a syringe-driven 33 mm gage filter unit prior to use.

7. It is necessary to shake the constituents of the lead citrate stain vigorously intermittently for up to 30 min to ensure adequate mixing to a uniform milky suspension. This should clear following addition of 0.2 M sodium hydroxide and mixing by inversion. The solution can be stored at 4 °C in a tightly capped bottle for up to 1 month.
8. Peeling the lower rather than the upper leaf surface is advantageous as in some species it avoids trichomes that can be autofluorescent. Use ultrafine forceps to peel tissue. Thickness will vary along the length of the peel but trim any extraneous tissue prior to mounting.
9. It is necessary to empirically determine the concentration and duration of incubation necessary for each primary antibody.
10. Add the tissue directly to the cover slip to ensure that it is as close as possible to the lens. A thick layer of mountant can be difficult to image through and for 3D-SIM best results are achieved when material is within 16 μm of the cover slip.
11. Although it is reported that LR will not polymerize in the presence of oxygen [18], we have found that blocks will polymerize well if a small air bubble remains after capping.
12. If the blocks still seem soft, yield when squeezed, or are tacky when handled, they can be hardened up by incubating them at 50 °C for a further 8 h. Further incubation may also aid in the cutting of ultrathin sections for TEM.
13. This method is suitable for water-dipping lenses that have a working distance of up to 0.5 cm. Low-magnification (5×, 10×) dry lenses also image the block well. Take care when imaging the blocks and ensure that there are no hanging or rough edges to that might catch and damage the lenses.
14. 14 months is currently the longest time we have stored blocks. There has been no obvious deterioration in fluorescence or structure in this time.
15. Wetting the grids briefly prior to staining prevents extensive air-stain contact, thereby reducing contamination [19].
16. It is necessary to spot stain onto a plastic rather than glass petri dish to achieve a drop with the desired size and shape. Cover the petri dish during staining to protect from dust, evaporation, and CO_2 from expelled air. Protection from CO_2 is particularly pertinent when staining with lead citrate.

Acknowledgements

We would like to thank Steve Mitchell for help when developing the LR method and Dr. Alison Roberts for advice in using the vibrating microtome.

References

1. Bell K, Oparka K (2010) Imaging plasmodesmata. Protoplasma 248:9–25
2. Thomas CL, Bayer EM, Ritzenthaler C et al (2008) Specific targeting of a plasmodesmal protein affecting cell-to-cell communication. PLoS Biol 6:180–190
3. Simpson C, Thomas C, Findlay K et al (2009) An Arabidopsis GPI-anchor plasmodesmal neck protein with callose binding activity and potential to regulate cell-to-cell trafficking. Plant Cell 21:581–594
4. Gustafsson MGL (2000) Surpassing the lateral resolution limit by a factor of two using structured illumination microscopy. J Microsc 198: 82–87
5. Dobbie IM, King E, Parton RM et al (2011) OMX: a new platform for multimodal, multichannel wide-field imaging. Cold Spring Harb Protoc 8:899–909
6. Schermelleh L, Carlton PM, Haase S et al (2008) Subdiffraction multicolor imaging of the nuclear periphery with 3D structured illumination microscopy. Science 320:1332–1336
7. Roberts IM, Boevink P, Roberts AG et al (2001) Dynamic changes in the frequency and architecture of plasmodesmata during the sink-source transition in tobacco leaves. Protoplasma 218:31–44
8. Fitzgibbon J, Bell K, King E et al (2010) Super-resolution imaging of plasmodesmata using three-dimensional structured illumination microscopy. Plant Physiol 153:1453–1463
9. Bell K, Mitchell S, Paultre D et al (2013) Correlative imaging of fluorescent proteins in resin-embedded plant material. Plant Physiol 161:1595–1603
10. Kner P, Chhun BB, Griffis ER et al (2009) Super-resolution video microscopy of live cells by structured illumination. Nat Methods 6: 339–342
11. Wombacher R, Heidbreder M, van de Linde S et al (2010) Live-cell super-resolution imaging with trimethoprim conjugates. Nat Methods 7:717–719
12. Balint S, Verdeny Vilanova I, Sandoval Alvarez A et al (2013) Correlative live-cell and super-resolution microscopy reveals cargo transport dynamics at microtubule intersections. Proc Natl Acad Sci U S A 110:3375–3380
13. Knoblauch M, Peters WS (2010) Münch, morphology, microfluidics: our structural problem with the phloem. Plant Cell Environ 33: 1439–1452
14. Brown R, Lemmon B, Mullinax J (1992) Immunofluorescent staining of microtubules in plant tissues: improved embedding and sectioning techniques using polyethylene glycol (PEG) and Steedman's wax. Bot Acta 102: 54–61
15. Baskin TI, Busby CH, Fowke LC et al (1992) Improvements in immunostaining samples embedded in methacrylate: localisation of microtubules and other antigens throughout developing organs in plants. Planta 187: 405–413
16. Baskin TI, Miller DD, Vos JW et al (1996) Cryofixing single cells and multicellular specimens enhances structure and immunocytochemistry for light microscopy. J Microsc 182: 149–161
17. Thompson MV, Wolniak SM (2008) A plasma membrane-anchored fluorescent protein fusion illuminates sieve element plasma membranes in Arabidopsis and Tobacco. Plant Physiol 146:1599–1610
18. Keene DR, Tufa SF, Lunstrum GP et al (2008) Confocal/TEM overlay microscopy: a simple method for correlating confocal and electron microscopy of cells expressing GFP/YFP fusion proteins. Microsc Microanal 14: 342–348
19. Hayat MA (1968) The principles and techniques of electron microscopy, vol 1. Van Nosttand Reinhold Company, New York, NY

Super-resolution Imaging of Live BY2 Cells Using 3D-structured Illumination Microscopy

Karen Bell, Karl Oparka and Kirsten Knox*

Institute of Molecular Plant Sciences, School of Biological Sciences, University of Edinburgh, Edinburgh, UK

*For correspondence: kirsten.knox@ed.ac.uk

[Abstract] Light microscopy is the standard tool for studying sub-cellular structures however, owing to the diffractive properties of light, resolution is limited to 200 nm. Super-resolution microscopy methods circumvent this limit, offering greater resolution, particularly when studying fluorescently labeled sub-cellular structures. Super-resolution methods such as 3D-SIM (Structured Illumination Microscopy) fill a useful niche between confocal and electron microscopy. We have previously had success using fixed plant tissue samples with 3D-SIM (Bell and Oparka, 2014). However, sensitive structures can be altered by fixation and embedding procedures, so we developed a method for imaging live cells. In this protocol we used 3D-SIM to image the ER and Hechtian Strands in live, plasmolysed BY2 cells.

Materials and Reagents

1. Microscope slides (Thermo Fisher Scientific)
2. #1.5 coverslips (0.17 mm thick) (Thermo Fisher Scientific)
3. BY2 cells expressing fluorescent marker
4. 250 ml Erlenmeyer flasks (Thermo Fisher Scientific)
5. Murashige and Skoog (MS) basal salt media (Sigma-Aldrich, catalog number: M5519)
6. Sucrose (Thermo Fisher Scientific)
7. (2, 4-Dichlorophenoxy) acetic acid sodium salt monohydrate (Sigma-Aldrich, catalog number: D6679)
8. Calcofluor white/Fluorescent Brightener 28 (Sigma-Aldrich, catalog number: F3543)
9. 1 M D-Mannitol pure (Scientific Laboratory Supplies, catalog number: CHE1796)
10. Nail varnish
11. BY2 growth media (see Recipes)
12. Calcofluor White Stock solution (see Recipes)

Equipment

1. Controlled temperature (28 °C) incubator or room
2. Orbital shaker

3. PersonalDV Deltavision Epi-fluorescence Inverted Microscope (GE Healthcare, Dharmacon)
4. 3D-SIM microscope [DeltaVision OMX Blaze (GE Healthcare, Dharmacon) fitted with an Olympus PlanApo N 100x 1.42 NA oil objective]
5. Edge sCMOS camera (PCO AG)

Software

1. SoftWoRx 6.0 (GE)

Procedure

A. Sample preparation

1. Culture 40 ml of BY2 cell lines stably expressing a fluorescent reporter in 250 ml Erlenmeyer flasks with sterile Murashige and Skoog Basal Salts media supplemented with 3% sucrose and 2 µg ml^{-1} 2,4-Dichlorophenoxyacetic acid. Grow cultures at 28 °C, in the dark, on an orbital shaker at 140 rpm. Aseptically sub-culture cells to fresh media weekly using a dilution of 1 ml of cells to 40 ml of media. Healthy cultures are pale yellow to light beige in colour and there should be sufficient growth that the cell suspension is more viscous than the media (Figure 1).
2. At 4 days post-subculture, pipette 1 ml of cells into an Eppendorf tube and then stain cell walls (if required) with a final concentration of 3.5 µg ml^{-1} Calcofluor white for 5 min at room temperature. Excess stain is removed by allowing the cells to settle to the bottom of the tube and exchanging the media for fresh, twice.
3. Plasmolyse cells by removing 450 µl of media and replacing it with 450 µl of 1 M Mannitol.
   Note: Plasmolysis is not required, but enabled us to observe plasmodesmata more accurately.
4. Incubate at room temperature for 10 min, gently inverting the tube every 2 min to keep cells in suspension and then pipette 40 µl of cells onto a microscope slide. Lay a rectangular coverslip gently on top. Remove excess media by gentle pressure using a folded flat piece of absorbent tissue paper.
   Note: It is important not to damage the cells, so the pressure must be light.
5. Seal all edges of the coverslip with nail varnish and begin imaging as soon as the varnish has dried.
6. Locate candidate cells for imaging using a PersonalDV DeltaVision live-cell imaging system, which has stage coordinates mapped to the OMX. Use low level bright field illumination and mark the position on the slide using point visiting tool.
7. Expose all marked cells to the appropriate wavelength of fluorescent light to check the calcofluor stain ($_{abs}$350 nm/$_{em}$455 nm) has worked well and that the cells are

expressing a good level of fluorescent reporter (Figure 2). It is vital to keep this exposure as brief as possible in order to minimize bleaching prior to 3D-SIM imaging. The point visiting function allows the marked cells to be found swiftly on the OMX, thus avoiding unnecessary exposure to light.

B. 3D-SIM Imaging

1. We acquire 3D-SIM images using a DeltaVision OMX Blaze fitted with an Olympus PlanApo N 100x 1.42 NA oil objective. The 3D-SIM imaging protocol is based on that described in Schermelleh *et al.* (2010). Place the slide on the OMX and apply immersion oil. To minimise spherical aberration and optimize illumination modulation contrast, adjust the type of immersion oil to match the Refractive Index (RI) of the sample and imaging depth. Ideally, BY2 cells would be mounted in glycerol or similar to maintain the RI of the oil immersion objective but to keep the ER in good condition the cells must be mounted in media. Cells also need to be as close to the coverslip as possible.
2. Find the selected cells using the Point List and then the Spiral Mosaic function to center the cell in the image. Determine top and bottom limits of z-stack quickly and efficiently, continuing to minimize the cell's exposure to light.
3. In the OMX 3D-SIM system, light from solid state lasers (405, 488 and 564 nm), shuttered by high speed tilt mirrors and coupled into a broadband single mode optical fiber is split into three beams. 3D-interference patterns in the sample plane are generated by focusing the beams onto the back focal plane of the objective lens. Striped illumination patterns are shifted by five phase steps and rotated by 3 angles (-60°, 0° and +60°), providing a set of 15 images per unprocessed z-section. Interference patterns are phase shifted by directing the outer two beams through a separate pair of windows with individual tilt control. Phase of the interference pattern at the sample plane is shifted due to the change in the path length for the respective outer beam, while lateral refractive beam translation is canceled by tilting a given window pair in complementary directions. Angles of pattern orientation are shifted by a tilt mirror, directing the three beams pattern to one of three mirror clusters; the beam pattern from each of the three rotation paths is redirected back to a common exit path by reflecting a second time from the tilt mirror. For descriptive diagrams see http://microscopy.lifesci.dundee.ac.uk/omx/omx.html.
4. Select the lowest possible laser power and exposure times for each channel to minimize photo bleaching. Adjust exposure times similarly, typically between 100 and 200 ms, and also adjust the power of each laser to achieve optimal intensities of between 1,000 and 3,000 counts in a raw image acquired by a 15-bit dynamic range Edge sCMOS camera. Acquire image stack.
5. Unprocessed image stacks are composed of 15 images per z-section (five phase-shifted images per each of three interference pattern angles). The microscope

must be routinely calibrated by measuring channel specific optical transfer functions (OTFs) to optimize both lateral and axial image resolution.

6. Adjust images from the different color channels, recorded on separate cameras, with the SoftWorx 6.0 alignment tool, based on alignment parameters obtained from calibration measurements with 100 nm-diameter TetraSpeck beads. Reconstruct super-resolution 3D image stacks with SoftWoRx 6.0 using channel specific OTFs and Wiener filter setting of 0.002.

Representative data

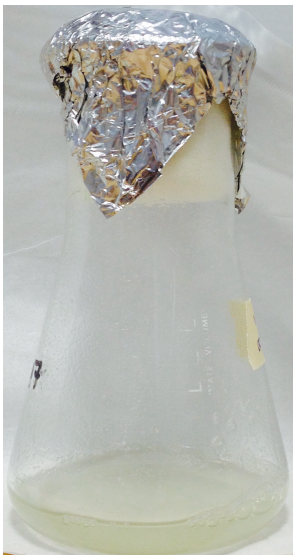

Figure 1. Healthy 4-day old BY2 cell culture

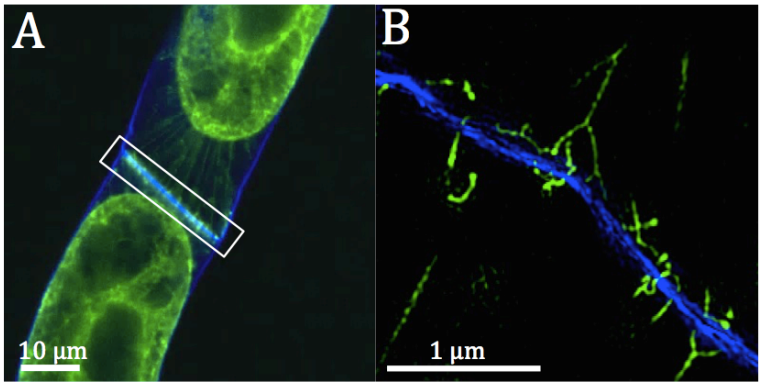

Figure 2. Representative image showing the resolution obtainable with 3D-SIM using plasmolysed live BY2 cells. A. Standard confocal image of BY2 cells expressing RTN6:GFP (green) and the cell wall stained with Calcofluor White (blue). B. Pseudo-coloured 3D-SIM image of the boxed region in A showing high resolution of the Hechtian strands at high magnification.

Notes

A 3D-SIM microscope takes considerable expertise to operate, with different manufacturers using bespoke software specifically designed for their hardware. Therefore, the 3D-SIM imaging part of this protocol is provided as a guide only. Each experiment will take considerable optimization of all 3D-SIM parameters as outlined in the protocol.

Recipes

1. BY2 growth media
   0.43% MS Basal Salts media
   3% sucrose
   2 µg ml^{-1} 2, 4-Dichlorophenoxyacetic acid
   ddH_2O
   Sterilize the media by autoclaving
2. Calcofluor White Stock solution
   170 µg ml^{-1} Calcofluor white
   Dissolve in ethanol
   Stored in the dark at -20 °C

Acknowledgments

Use of the Deltavision OMX Blaze microscope at Dundee University was supported by an MRC Next Generation Optical Microscopy Award (Ref: MR/K015869/1). Development of this protocol was part of a project funded by grant BB/J004987/1 from the British Biotechnology and Biological Sciences Research Council (BBSRC) to Karl Oparka. We are grateful for the expert assistance of Dr. Markus Posch. Elements of this protocol have been adapted from those previously described in Bell and Oparka (2015) and Knox *et al.* (2015).

References

1. Bell, K. and Oparka, K. (2015). Preparative methods for imaging plasmodesmata at super-resolution. *Methods Mol Biol* 1217: 67-79.
2. Knox, K., Wang, P., Kriechbaumer, V., Tilsner, J., Frigerio, L., Sparkes, I., Hawes, C. and Oparka, K. (2015). Putting the squeeze on Plasmodesmata: A role for reticulons in primary plasmodesmata formation. *Plant Physiol* 168(4): 1563-1572.
3. Schermelleh, L., Heintzmann, R. and Leonhardt, H. (2010). A guide to super-resolution fluorescence microscopy. *J Cell Biol* 190(2): 165-175.

Available online at www.sciencedirect.com

ScienceDirect

Current Opinion in Plant Biology

Sieve-element differentiation and phloem sap contamination

Michael Knoblauch[1], Winfried S Peters[1], Karen Bell[2], Timothy J Ross-Elliott[1,3] and Karl J Oparka[2]

Sieve elements (SEs) degrade selected organelles and cytoplasmic structures when they differentiate. According to classical investigations, only smooth ER, mitochondria, sieve element plastids, and, in most cases, P-proteins remain in mature SEs. More recent proteomics and immunohistochemical studies, however, suggested that additional components including a protein-synthesizing machinery and a fully developed actin cytoskeleton operate in mature SEs. These interpretations are at odds with conventional imaging studies. Here we discuss potential causes for these discrepancies, concluding that differentiating SEs may play a role by 'contaminating' phloem exudates.

Addresses
[1] School of Biological Sciences, Washington State University, Pullman, WA 99163, USA
[2] Institute of Molecular Plant Sciences, University of Edinburgh, Mayfield Road, Edinburgh EH9 3JR, UK
[3] Department of Biology, University of North Carolina at Chapel Hill, Chapel Hill, NC 27599, USA

Corresponding author: Knoblauch, Michael (knoblauch@wsu.edu)

Current Opinion in Plant Biology 2018, **43**:43–49

This review comes from a themed issue on **Physiology and metabolism**

Edited by **N. Michelle Holbrook** and **Michael Knoblauch**

For a complete overview see the Issue and the Editorial

Available online 5th January 2018

https://doi.org/10.1016/j.pbi.2017.12.008

Introduction

In agreement with the function of sieve elements (SEs) in long-distance transport which favors an unobstructed tube with minimal flow resistance, differentiating SEs undergo partial autolysis [1]. It may take only minutes for a young SE to lose its nucleus, vacuole, and Golgi apparatus, as it connects to the existing sieve-tube system [1,2•]. Historically, extensive electron microscopy studies of mature SEs detected mitochondria, smooth ER, SE-plastids, and phloem-specific proteins (P-proteins), but no cytoskeleton. Except for forisomes, P-protein bodies involved in reversible sieve tube occlusion in legumes [3], the functions of P-proteins [4] and SE plastids are unknown. Application of correlative microscopy and super-resolution imaging [5–7] showed that, unlike P-proteins, membrane-bound organelles are restricted to a thin parietal layer in functional SEs. Gentle preparation and flash-freezing methods enabled the identification of protein clamps linking some of the SE organelles to each other and to the cell membrane [8,9]. Despite the wealth of evidence speaking against the presence of ribosomes and a cytoskeleton in sieve tubes (reviewed in [10]), a functional actin filament network [11,12] and protein synthesis machinery [13] were postulated to exist in mature SEs. Such uncertainties concerning SE structure are partially due to methodological challenges that derive from, first, the high turgor pressure in sieve tubes usually in the range of 1–2.5 MPa, second, the embedding of SEs in parenchyma and companion cells (CCs), hindering isolation of 'pure' sieve tubes, and third, the systemic nature of the sieve tube system in which local artefacts may be transmitted over long distances [7]. Here we discuss the contamination of sieve tubes with material from differentiating SEs as an additional factor potentially responsible for the contradictory findings.

Do mature SEs have an actin cytoskeleton?

Monomeric actin and various actin-binding proteins are found routinely in phloem exudates [13–17]. The debate about their significance in SEs was stimulated greatly by Hafke *et al.* [11], who were cited as having 'unequivocably shown that SEs contain a fully developed actin network' [18]. Unsurprisingly, this fostered new hypotheses on the actin cytoskeleton in relation to phloem function and plant-pathogen interactions [12,19,20]. Hafke *et al.* [11] provided two lines of evidence for an actin network in mature SEs. First, microinjection of fluorescent phalloidin into sieve tubes resulted in labeling of an extensive meshwork in the periphery of the SEs. Unfortunately, tagged phalloidin fluoresces independently of any association with actin and may bind to unrelated targets including forisomes, as noticed in [11]. Thus, phalloidin labeling lacks actin-specificity in sieve tubes. Moreover, the structure of the putative, phalloidin-labeled actin cytoskeleton looked remarkably similar to the sieve-tube ER and P-protein meshworks described by other authors (compare Figure 1 in [11] with our Figure 1b, Figure 2 in [9], or Figure 2 in [21]). Second, immunocytochemical TEM images showed labeling in the periphery of SEs (Figure 2 in [11]). However, the putative actin filaments lack the constant diameters and distinct fibrillar structure that

Figure 1

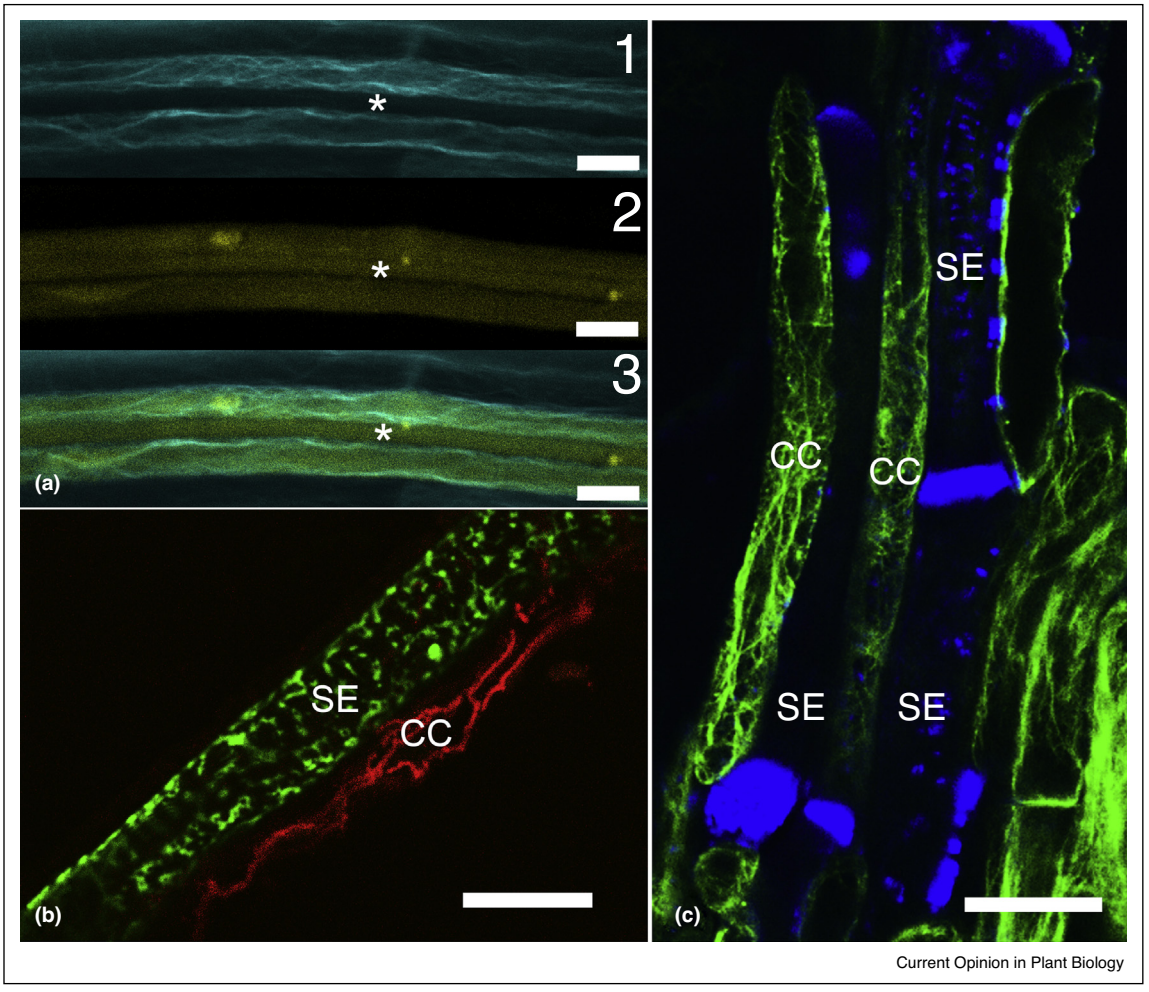

Lack of actin cytoskeleton in mature sieve elements (SEs). **(a)** *In situ* imaging of a transgenic *Arabidopsis* root expressing the actin-binding-domain-protein tagged with cyan fluorescent protein (blue; panel 1). Carboxyfluorescein (yellow; panel 2) loaded into the sieve tube system marks an SE (asterisk) from where it has moved into neighboring companion cells (CCs). Typical actin filaments are visible in CCs but not in the SE (combined image; panel 3). **(b)** Confocal micrograph of transgenic *Nicotiana tabacum* expressing GFP tagged to the ER under the control of the SE-specific SEOR promoter (green). The section was immunolabelled with the anti-actin antibody C4 (red). Actin filaments and tagged ER are seen in the CC and SE, respectively; there is no overlap of the signals. **(c)** Confocal micrograph of a transgenic *N. tabacum* line expressing GFP fused to the actin-binding protein fimbrin (green). Aniline blue stains callose in SEs (blue). Well-developed actin filaments are visible in parenchyma and CCs but not in SEs. Scale bars: *A* = 10 μm; *B* = 20 μm; *C* = 20 μm.

usually characterize actin filaments. The labeled, inhomogeneous structures [11] resembled the parietal ER meshwork reported by others (e.g. Plate 3 in [22]). Therefore, rather than indicating the presence of a functional actin cytoskeleton, the immuno-labeling probably identifies monomeric actin that was translocated in the sieve tubes at the time of fixation. Our interpretation is influenced by our complete failure to detect actin filaments in mature SEs using two fluorescent actin probes, actin-binding-domain-CFP (Figure 1a) and fimbrin-GFP (Figure 1c), both of which labeled actin filaments clearly in CCs. Similarly, we detected actin in CCs but not in SEs by immuno-fluorescence using the same antibody as Hafke *et al.* [11] (Figure 1b). Our data support the conventional wisdom that differentiating SEs dissolve their cytoskeleton. Breakdown products such as monomeric actin may then enter the translocation stream (as suggested in [15]), potentially causing confusion when detected in mature SEs.

Do immature SEs 'contaminate' exudates collected from mature SEs?

Sieve tube exudates can be collected by a variety of methods and are the primary source for analyses of SE contents [23]. The collected sap is subjected to proteomics, metabolomics or RNA analysis. Long-distance signaling by sap

Figure 2

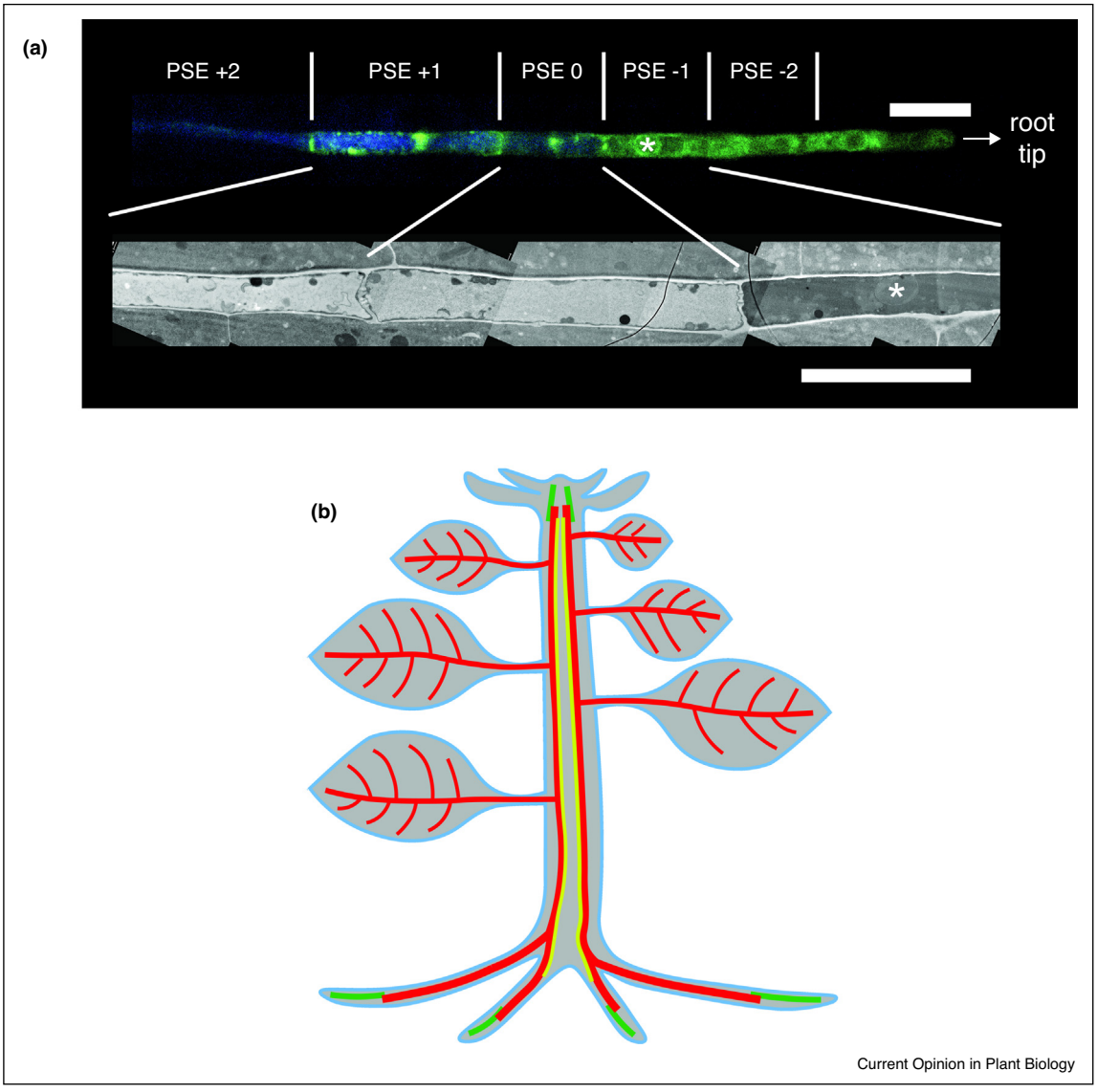

Locations of sieve elements (SEs) potentially contaminating phloem exudates. **(a)** Confocal micrograph (top) showing a terminal file of protophloem sieve elements (PSEs) in the root of a transformed *Arabidopsis*, in which the ER in SEs is tagged with GFP (green). Esculin translocating towards the root apex (i.e. from left to right) appears blue. The most apical SE active in translocation, as indicated by the esculin signal, is PSE 0. Its proximal neighbor, PSE +1, is evidently transporting. Its distal neighbor, PSE −1, still has a nucleus (asterisk) and is not yet connected to the transporting sieve tube. In the electron micrograph (bottom), the cytoplasm appears much denser in PSE −1 than in PSE 0; the degradation of cytoplasmic structures is not completed yet in PSE −1. The degradation products will become part of the sieve tube sap when the sieve pores between PSE 0 and PSE −1 open. At that time, PSE −1 will become the new PSE 0. **(b)** Model showing the location of different SEs and the fate of their cytoplasm following their connection to sieve tubes. With the exception of protophloem SEs (green) whose content will be unloaded directly into the nearest sink, all metaphloem SEs (red) and secondary SEs derived from the cambium (yellow) release their contents into translocating sieve tubes. Scale bars = 10 μm.

components including peptides and RNAs, an important yet controversial topic [24,25•,26•], will be discussed in separate contributions to this issue, but parts of the following discussion may apply to these putative signals.

Up to several thousand proteins have been found in phloem exudates from various species [27], including proteins involved in metabolism, oxidative stress, signaling, protein turnover, as well as structural components of the cytoskeleton, ribosomes, and proteasomes. SEs are connected to neighboring CCs by unique pore-plasmodesmata, and symplasmic import through these channels is thought to explain the presence of the various proteins in exudates. However, the size exclusion limit of the

Figure 3

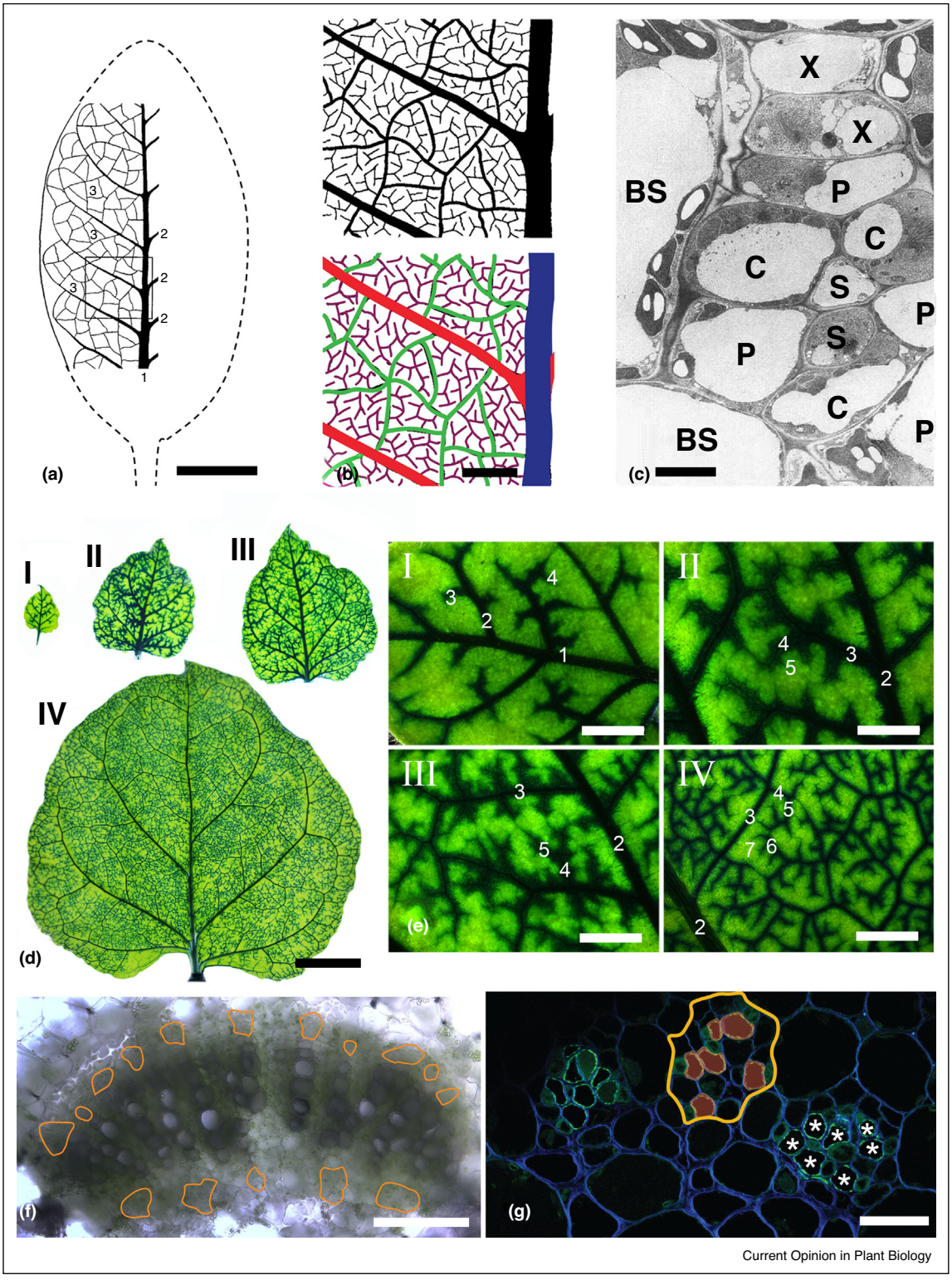

Anatomical basis for estimating the contribution of differentiating sieve elements (SEs) to the phloem flow exiting a leaf. **(a, b)** Vein system in a *Nicotiana benthamiana* leaf during the source/sink transition. Vein classes defined by branching hierarchy are blue, class 1; red, class 2; green, class 3; purple, class 4 and 5 minor veins (adapted from [31]). **(c)** Electron micrograph of a cross-section of a class 5 vein; S = young SEs, C = companion cells, P = phloem parenchyma cell, BS = bundle sheath cell, x = xylem (a–c slightly modified from [31], Copyright of American Society of Plant Biologists). **(d)** *N. benthamiana* leaves at four stages of development (I–IV), stained with methylene blue to highlight the vein

plasmodesmata between SEs and CCs (70 kDa [26•]) prevents the passage of particles as large as the ribosome and proteasome fragments identified in exudates [28••]. If loading through plasmodesmata from neighboring cells into SEs is impossible, these structures can only originate from within the sieve-tube system itself. This conclusion seems to conflict with the fact that the functional ribosomes required for translation have not been observed in mature SEs yet.

Differentiating SEs could be an alternative source for the macromolecules found routinely in phloem exudates. SE precursor cells contain the standard set of organelles, but at the final stage of differentiation selected cellular structures disintegrate. The degradation products remain within a dense cytoplasmic 'soup' until the sieve pores open (Figure 2a); their subsequent fate depends on the location and nature of the SE (Figure 2b). Protophloem SEs derived from apical meristems are part of the unloading zone of sinks. Their degradation products will not move as they are released at endpoints of phloem transport routes, and ultimately will be driven out of the sieve tube into neighboring cells such as the phloem-pole pericycle [2•]. However, not all new SEs form in sinks (although this sometimes is assumed, e.g. [25•]). Degradation products from secondary phloem SEs in the axial cambium or SEs in source organs such as young leaves [29] will enter the translocation stream. In *Populus tremula* × *alba* leaves, the total SE cross-sectional area increases exponentially from the major veins in the petioles to the minor veins in the blade [30•]. Therefore the proportion of degradation products in the phloem sap exported from a leaf may be significant. Detailed studies on young, still importing *Nicotiana benthamiana* leaves showed that prior to the sink/source transition, minor vein SEs are present but remain immature until the leaf becomes a source [31]. During this transition, the minor vein SEs mature, connect to translocating sieve tubes, and become active in loading [31]. Their intracellular degradation products thus will be found in the phloem sap that exits the leaf.

We evaluated the contribution of young SEs to volume flow based on the data from *N. benthamiana* leaves undergoing the sink/source transition [31]. At that stage, leaves are typically 2.5 cm long and contain five vein classes. The main vein is defined as class 1, and veins branching from it represent class 2. Veins branching from class 2 veins form class 3, and so on. Minor vein sieve elements (class 4 and 5) are present but rest in an immature state until the leaf transitions into a source when the cells mature and become active in loading [31]. The total length of class 4 and 5 minor veins in leaves of this stage is about 1 m (Figure 3a and b). On average, the minor vein SEs shown in [31] have a cross-sectional area of 8.1 μm^2. Since there are two sieve tubes in each minor vein (Figure 3c), a volume of approximately 1.6×10^7 μm^3, or 16 nL, will be released when the young SEs mature. During leaf expansion, new minor veins are added and class 6 and 7 minor veins appear (Figure 3d, e). After 5 days of leaf expansion, the total length of minor veins has increased to roughly 16 m. Thus a total of 256 nL of minor-vein SE contents enter the translocation stream over the 5 days after the leaf has started to export.

How does this quarter microliter of cytoplasmic material compare to the total volume flow of phloem sap from the leaf? All export from the leaf passes through the petiole, which has a main vein with a phloem cross-sectional area of some 32 000 μm^2 (Figure 3f; lateral bundles combined contribute below 10% of the total phloem area and are disregarded here). Since about 25% of this area are covered by SEs (Figure 3g), the estimated conducting area is 8000 μm^2. Flow velocities in petioles of different species vary from 3 to 150 $\mu m/s$ [32]. Lacking data for *Nicotiana*, we assume a velocity of 100 $\mu m/s$, and arrive at an export rate of just below 3 $\mu L/h$. We are considering a leaf over 5 days from the initiation of the sink/source transition, a stage of leaf growth often used for exudate collection. At the beginning of this period, phloem export velocity is zero, increasing over time as the exporting leaf grows. Thus, in our example, significantly less than 360 μL phloem sap is exported within 5 days, of which some 0.25 μL are derived from differentiating SEs. In other words, the cytoplasm of differentiating SEs represents significantly more than 0.07% of the phloem sap passing through the petiole during this period. This proportion, and the corresponding dilution factor of about 1400, refers to fluid volume *per se*. The proportion of young SE-derived material in a given class of molecules in the phloem sap might be different, depending on any active loading or degradation that may occur. Measurements of the proportion of RNA in sieve tube sap range from 0.003% of the fresh weight in a recent study [33] down to <0.0002% in a classical investigation [34]. Conventional text-book wisdom suggests that RNA represents over 1% of the fresh-weight of eukaryotic cells [35]. Assuming these figures hold in our example, and applying

(Figure 3 Legend Continued) system. All pictures are taken at the same magnification. It is apparent that the number of vein orders increases with increasing area of the lamina. **(e)** Higher magnification of the same leaves as in (d); 1–7 indicate vein classes. **(f)** Cross-section of the central vein in the petiole of leaf IV in (d). Orange outlines mark the area of internal and external phloem in the bicollateral bundles interrupted by rays for parenchyma cells. **(g)** Confocal micrograph of a petiole cross-section in a transgenic *N. tabacum* line carrying GFP tagged to the ER in sieve tubes (asterisks). In one bundle, the phloem is outlined in orange and SEs are marked red. About 25% of the phloem area are covered by sieve elements. Individual phloem areas are interrupted by large parenchyma cells. Scale bars: *A* = 5 mm; *B* = 1 mm; *C* = 4 μm; *D* = 2 cm; *E* = 2 mm; *F* = 200 μm; *G* = 30 μm.

the volumetric dilution factor calculated above, we find that RNA released from young SEs could account for anywhere between one quarter and the three-fold of the RNA in the phloem stream that exits the leaf. Similar arguments can be made for SEs differentiating in the axial cambium (Figure 3), which release the remnants of their cytoplasm into the translocation stream when they connect to it. Obviously, our arguments call for experimental verification. However, we suggest that the cellular components of immature SEs might contribute significantly to the composition of phloem exudates.

Waste not, want not

The release of degradation products from differentiating SEs into the phloem sap, instead of recycling them in source tissues, might be beneficial. As recently shown for growing *Arabidopsis* root tips, large molecules are unloaded from protophloem SEs into the phloem pole pericycle cells through specific funnel plasmodesmata with large size exclusion limits [2•]. Delivery of the degradation products to sinks such as root growth zones could provide carbon and nitrogen skeletons for growth and development.

Conclusions

The mere presence of a molecule in phloem sap is insufficient evidence for a specific function of that molecule within SEs, or indeed the sink to which it is delivered [36]; additional functional evidence is imperative. For example, blue native electrophoresis applied to phloem exudates indicated the presence of ribosomal and proteasomal protein complexes [28••]. However, essential functional components of ribosomes were missing; translation in mature SEs therefore seems unlikely. In contrast, functional tests demonstrated proteasome activity [28••], providing strong support for the hypothesis that proteasomes in sieve tubes function in pathogen defense [37]. It will be interesting to see whether these proteasomes originate from differentiating SEs.

Volume flow in the phloem of a young exporting leaf will increase with the expansion of photosynthetic area. The release of cytoplasmic materials from differentiating SE, on the other hand, will slow as the leaf approaches full expansion. Thus, using fully expanded leaves for exudate studies would minimize contamination from immature SEs. However, secondary growth in axial cambia will continue to release cytoplasmic SE contents into the system. Due attention to these developmental and structural aspects will improve the rigor of exudate analyses.

Acknowledgements

We thank Elison B. Blancaflor for providing seeds of transgenic *Arabidopsis* lines with the actin binding domain-CFP reporter. This work was supported by the National Science Foundation [NSF-IOS 1656769, 1456682] (MK) and the Biotechnology and Biological Sciences Research Council [BB/M025160/1] (KJO).

References and recommended reading

Papers of particular interest, published within the period of review, have been highlighted as:

- • of special interest
- •• of outstanding interest

1. Heo J-O, Blob B, Helariutta Y: **Differentiation of conductive cells: a matter of life and death**. *Curr Opin Plant Biol* 2017, **35**:23-29.

2. • Ross-Elliott TJ, Jensen KH, Haaning KS, Wagner BM, Knoblauch J, Howell AH, Mullendore DL, Monteith AG, Paultre D, Yan DW *et al.*: **Phloem unloading in *Arabidopsis* roots is convective and regulated by the phloem pole pericycle**. *eLife* 2017, **6**:e24125.

This paper shows how unloading takes place in the protophloem of *Arabidopsis* roots. A new type of plasmodesmata of high conductivity that enable a combination of bulk flow and diffusion is described.

3. Knoblauch M, Stubenrauch M, Van Bel AJE, Peters WS: **Forisome performance in artificial sieve tubes**. *Plant Cell Environ* 2012, **35**:1419-1427.

4. Knoblauch M, Froelich DR, Pickard WF, Peters WS: **SEORious business: structural proteins in sieve tubes and their involvement in sieve element occlusion**. *J Exp Bot* 2014, **65**:1879-1893.

5. Mullendore DL, Windt CW, Van As H, Knoblauch M: **Sieve tube geometry in relation to phloem flow**. *Plant Cell* 2010, **22**:579-593.

6. Fitzgibbon J, Bell K, King E, Oparka K: **Super-resolution imaging of plasmodesmata using three-dimensional structured illumination microscopy**. *Plant Physiol* 2010, **153**:1453-1463.

7. Knoblauch M, Oparka K: **The structure of the phloem — still more questions than answers**. *Plant J* 2012, **70**:147-156.

8. Ehlers K, Knoblauch M, van Bel AJE: **Ultrastructural features of well-preserved and injured sieve elements: minute clamps keep the phloem transport conduits free for mass flow**. *Protoplasma* 2000, **214**:80-92.

9. Froelich DR, Mullendore DL, Jensen KH, Ross-Elliott TJ, Anstead JA, Thompson GA, Pelissier HC, Knoblauch M: **Phloem ultrastructure and pressure flow: Sieve-Element-Occlusion-Related agglomerations do not affect translocation**. *Plant Cell* 2011, **23**:4428-4445.

10. Behnke HD, Sjolund RD: *Sieve Elements — Comparative Structure, Induction and Development*. Springer; 1990.

11. Hafke JB, Ehlers K, Foller J, Holl SR, Becker S, van Bel AJE: **Involvement of the sieve element cytoskeleton in electrical responses to cold shocks**. *Plant Physiol* 2013, **162**:707-719.

12. van Bel AJE, Furch ACU, Will T, Buxa SV, Musetti R, Hafke JB: **Spread the news: systemic dissemination and local impact of Ca^{2+} signals along the phloem pathway**. *J Exp Bot* 2014, **65**:1761-1787.

13. Lin MK, Lee YJ, Lough TJ, Phinney BS, Lucas WJ: **Analysis of the pumpkin phloem proteome provides insights into Angiosperm sieve tube function**. *Mol Cell Proteomics* 2009, **8**:343-356.

14. Schobert C, Baker L, Szederkényi J, Großmann P, Komor E, Hayashi H, Chino M, Lucas WJ: **Identification of immunologically related proteins in sieve-tube exudate collected from monocotyledonous and dicotyledonous plants**. *Planta* 1998, **206**:245-252.

15. Giavalisco P, Kapitza K, Kolasa A, Buhtz A, Kehr J: **Towards the proteome of *Brassica napus* phloem sap**. *Proteomics* 2006, **6**:896-909.

16. Fröhlich A, Gaupels F, Sarioglu H, Holzmeister C, Spannagl M, Durner J, Lindermayr C: **Looking deep inside: detection of low-abundance proteins in leaf extracts of *Arabidopsis* and phloem exudates of pumpkin**. *Plant Physiol* 2012, **159**:902-914.

17. Batailler B, Lemaitre T, Vilaine F, Sanchez C, Renard D, Cayla T, Beneteau J, Dinant S: **Soluble and filamentous proteins in**

***Arabidopsis* sieve elements**. *Plant Cell Environ* 2012, **35**:1258-1273.

18. Anstead JA, Hartson SD, Thompson GA: **The broccoli (*Brassica oleracea*) phloem tissue proteome**. *BMC Genomics* 2013, **14**:764.

19. Buxa SV, Degola F, Polizzotto R, De Marco F, Loschi A, Kogel K-H, di Toppi LS, van Bel AJE, Musetti R: **Phytoplasma infection in tomato is associated with re-organization of plasma membrane, ER stacks, and actin filaments in sieve elements**. *Front Plant Sci* 2015, **6**:650.

20. Furch ACU, Buxa SV, van Bel AJE: **Similar intracellular location and stimulus reactivity, but differential mobility of tailless (*Vicia faba*) and tailed forisomes (*Phaseolus vulgaris*) in intact sieve tubes**. *PLOS ONE* 2015, **10**:0143920.

21. Anstead JA, Froelich DR, Knoblauch M, Thompson GA: ***Arabidopsis* P-protein filament formation requires both AtSEOR1 and AtSEOR2**. *Plant Cell Physiol* 2012, **53**:1033-1042.

22. Esau K: **Developmental features of the primary phloem in *Phaseolus vulgaris* L.**. *Ann Bot* 1978, **42**:1-13.

23. Dinant S, Kehr J: **Sampling and analysis of phloem sap**. In *Plant Mineral Nutrients: Methods and Protocols.* Edited by Maathuis FJM. Humana Press; 2013:185-194.

24. Ham B-K, Lucas WJ: **Phloem-mobile RNAs as systemic signaling agents**. *Annu Rev Plant Biol* 2017, **68**:173-195.

25. • Thieme CJ, Rojas-Triana M, Stecyk E, Schudoma C, Zhang WN, Yang L, Minambres M, Walther D, Schulze WX, Praz-Ares J *et al.*: **Endogenous Arabidopsis messenger RNAs transported to distant tissues**. *Nat Plants* 2015, **1**:15025.

Studying grafts of genetically different *Arabidopsis* ecotypes, the authors demonstrate the unexpected phenomenon of bidirectional RNA transport.

26. • Paultre DSG, Gustin MP, Molnar A, Oparka KJ: **Lost in transit: long-distance trafficking and phloem unloading of protein signals in Arabidopsis homografts**. *Plant Cell* 2016, **28**:2016-2025.

Using a combination of imaging and bioinformatics, this work shows that for proteins synthesised in companion cells, the size exclusion limit for symplastic transfer into the sieve element is about 70 kDa.

27. Turnbull CGN, Lopez-Cobollo RM: **Heavy traffic in the fast lane: long-distance signalling by macromolecules**. *New Phytol* 2013, **198**:33-51.

28. •• Ostendorp A, Pahlow S, Krüßel L, Hanhart P, Garbe MY, Deke J, Giavalisco P, Kehr J: **Functional analysis of Brassica napus phloem protein and ribonucleoprotein complexes**. *New Phytol* 2017, **214**:1188-1197.

This study analyzes native protein complexes in the phloem sap of *Brassica napus.* Most importantly, the authors evaluate the activity of the complexes in mature sieve tubes.

29. Turgeon R: **Phloem loading: how leaves gain their independence**. *BioScience* 2006, **56**:15-24.

30. • Carvalho MR, Turgeon R, Owens T, Niklas KJ: **The scaling of the hydraulic architecture in poplar leaves**. *New Phytol* 2017, **214**:145-157.

An important step towards a fully quantitative understanding of vascular structure on the organ level.

31. Roberts AG, Cruz SS, Roberts IM, Prior D, Turgeon R, Oparka KJ: **Phloem unloading in sink leaves of *Nicotiana benthamiana*: comparison of a fluorescent solute with a fluorescent virus**. *Plant Cell* 1997, **9**:1381-1396.

32. Jensen KH, Lee J, Bohr T, Bruus H, Holbrook NM, Zwieniecki MA: **Optimality of the Münch mechanism for translocation of sugars in plants**. *J Roy Soc Interface* 2011, **8**:1155-1165.

33. Buhtz A, Springer F, Chappell L, Baulcombe DC, Kehr J: **Identification and characterization of small RNAs from the phloem of *Brassica napus***. *Plant J* 2008, **53**:739-749.

34. Ziegler H, Kluge M: **Die Nucleinsäuren und ihre Bausteine im Siebröhrensaft von *Robinia pseudacacia***. *Planta* 1975, **58**:144-153.

35. Alberts B, Johnson A, Lewis J, Raff M, Roberts K, Walter P: *Molecular Biology of the Cell*. edn 4. Garland Science; 2002.

36. Oparka KJ, Santa Cruz S: **The great escape: phloem transport and unloading of macromolecules**. *Annu Rev Plant Physiol Plant Mol Biol* 2000, **51**:323-347.

37. Hipper C, Brault V, Ziegler-Graff V, Revers F: **Viral and cellular factors involved in phloem transport of plant viruses**. *Front Plant Sci* 2013, **4**:154.

Chapter 4

Preparation and Imaging of Specialized ER Using Super-Resolution and TEM Techniques

Karen Bell, Karl Oparka, and Kirsten Knox

Abstract

The plant endoplasmic reticulum (ER) forms several specialized structures. These include the sieve element reticulum (SER) and the desmotubule formed as the ER passes through plasmodesmata. Imaging both of these structures has been inhibited by the resolution limits of light microscopy and their relatively inaccessible locations, combined with the fragile nature of the ER. Here we describe methods to view desmotubules in live cells under 3D-structured illumination microscopy (3D-SIM) and methods to fix and prepare phloem tissue for both 3D-SIM and transmission electron microscopy (TEM) which preserve the fragile structure and allow the detailed imaging of the SER.

Key words 3D-SIM, BY2, Endoplasmic reticulum, Desmotubule, Sieve element reticulum, Imaging, OMX, ZIO

1 Introduction

The limit of lateral resolution in light microscopy was determined more than 100 years ago [1]. The diffraction limit of light means that objects closer together than 200 nm cannot be fully resolved, instead appearing blurred. This limit remained largely unchallenged, despite the development of confocal laser scanning microscopy (CLSM). Theoretically, CLSM can produce images below the diffraction limit, but this is not generally seen with biological samples, principally as the pinhole needs to be smaller than the Airy pattern [2]. This results in most of the superfluous out-of-focus light being discarded, but also has the unwanted consequence of losing a significant portion of the in-focus emission. With biological specimens the fluorescence is often too weak, or labile, to sustain a detectable signal when emission light is discarded. Therefore, in practice, the pinhole is used at an aperture larger than the Airy pattern, and as such any chance of significantly increased lateral resolution is lost.

Chris Hawes and Verena Kriechbaumer (eds.), *The Plant Endoplasmic Reticulum: Methods and Protocols*, Methods in Molecular Biology, vol. 1691, DOI 10.1007/978-1-4939-7389-7_4,

Structured Illumination Microscopy (SIM) offers an alternative method to gain greater resolution while avoiding discarding the desired emitted light [3]. Optimally conducted, SIM can increase the lateral resolution to 100 nm and the axial resolution to 200 nm [4]. The technique relies on using spatially patterned excitation light. By introducing structure to the excitation light, and subtracting that known value from the emitted light pattern, it is possible to gain new information about the unknown sample. Exciting a fluorescently labeled sample with such structured light results in a Moiré interference fringe, created by the two different fine patterns being superimposed. As the illumination pattern is predetermined, the Moiré Fringe will describe the unknown structure of the sample, thus accessing super-resolution data otherwise unobtainable [3].

Due to the directionality of the light, and to gain a complete image, it is necessary to shift the phase of the light through five patterns, and then the orientation angle, which is usually shifted three times by at least 60° [5]. Post-imaging processing then produces the final image from 15 raw images from each *z*-plane.

The 3D-SIM imaging system was developed commercially by Applied Precision Inc. (Washington, USA) and the platform was named Optical Microscope eXperimental (OMX). The OMX is designed to maximize physical stability and photon budget with the aim of producing a platform suited to both rapid live-cell imaging and super-resolution of fixed material [5–7]. The basic components of the OMX system are described in [5] and the current Deltavision OMX Blaze model specification is available on the GE Healthcare website (http://www.gelifesciences.com).

In this chapter, we present protocols that describe methods of preparing fixed and live plant cells in order to visualize specialized ER components. Each protocol presents its own challenges concerning image optimization. Elements of these protocols have been described elsewhere [8–10] but here we describe methods optimized for the imaging of specialized ER structures.

Acquiring high-resolution 3D-SIM images from fixed tissue requires that the samples are labeled with a probe that is specific, highly photostable and with a high quantum yield. The tissue must be carefully fixed in order to preserve as much of the fine morphological structure as possible.

Imaging live cells requires a highly stable fluorophore for labeling structures that will not move during the timescale required to capture an image. During live-cell imaging, speed is of the essence in order to avoid any blur caused by components streaming within the cells. In this regard, the OMX system offers several advantages; simultaneous recording of up to four separate channels, or in cases where there may be some emission overlap between fluorophores, sequential imaging combined with rapid shuttering and fast, stable focusing resulting in delays of less than 1–2 ms. This means that together with its fully integrated electronic control, fast and precise

3D high-resolution image capture is possible [5, 6]. Despite this, many live cells will suffer bleaching during the image capture so it is important to optimize the setup to minimize bleaching, although this may come at the cost of losing some of the resolution.

The sieve element reticulum (SER) is a specialized ER system in the phloem of higher plants [11] and has long posed difficulties when imaging, as the sieve elements are located deep within tissues, beyond the working distance of most objectives. Fixation and sectioning is therefore a good way to visualize this structure (Fig. 1e and f). However, extreme care must be taken that the fixation method chosen does not disrupt the delicate structure.

In addition, tobacco-derived BY2 cell lines make good model systems as they are readily transformable, both transiently and stably with fluorescent reporters and often divide in long chains along one plane, allowing single cell layers to be imaged [12]. Close to the cell wall the ER is tightly appressed as it passes through the plasmodesmata, forming a desmotubule [13]. At just 15 nm wide this structure is well beyond the resolution limit of a standard confocal, but 3D-SIM allows greater resolution [14] (Fig. 1b and c).

Although super-resolution imaging can resolve structures beyond the diffraction limit, it cannot compete with transmission

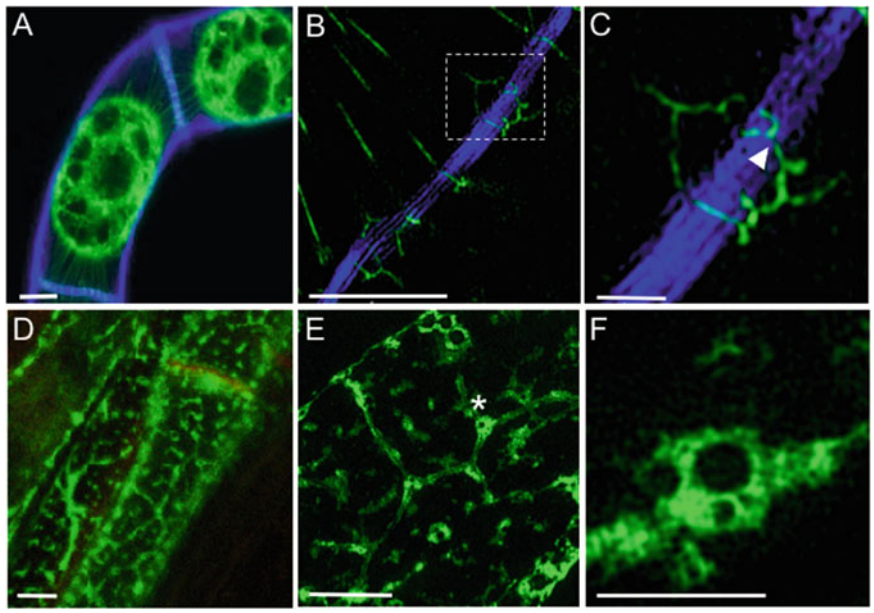

Fig. 1 (**a**) Confocal image of plasmolyzed BY2 cells, showing ER labeled by RTN6-GFP (*green*) and the cell wall labeled with Calcofluor White (*blue*); scale 10 μm. (**b**) 3D-SIM image of the cross wall between two BY2 cells; scale 5 μm. (**c**) Detailed view of the *boxed area* in (**b**), showing the narrowing of the ER as it forms the desmotubule (*arrow*, scale 1 μm). (**d**) Confocal image of sieve elements showing the SER labeled by pSEO2: GFP-HDEL; scale 5 μm. (**e**) 3D-SIM image showing structural details of the reticulum not resolved by the confocal scale 5 μm. (**f**) Detailed view of a region of SER similar to the region marked (*asterisk*) in (**e**); scale 2 μm

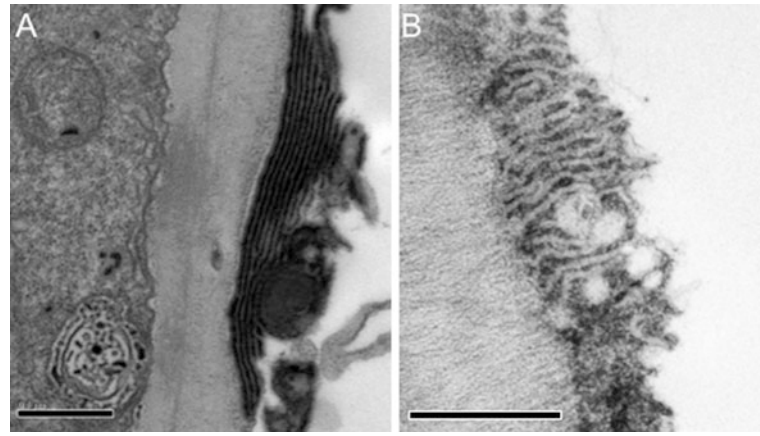

Fig. 2 TEM images taken at the sieve element and companion cell walls of tobacco petioles, stained with ZIO. (**a**) The SER adjacent to the cell wall has strongly labeled showing detailed structure of the SER cisternae. (**b**) An alternate angle section of the SER, with ZIO clearly enhancing the contrast between the lumen and the membranes. Scale 0.5 μm

electron microscopy (TEM) for the magnification of fine structures. To observe such fine structures requires contrast enhancement and this is usually achieved by using specific electron dense heavy-metal based stains. In this chapter, we describe a protocol for zinc-iodide osmium tetroxide (ZIO) staining of the SER (*see* Fig. 2 for representative images). The impregnation of tissue with ZIO was initially used to stain autonomic nerve fibers for visualization using light microscopy and subsequently TEM [15]. Notable for forming electron dense accumulations between double-membraned structures, it was soon adopted for the study of the ER in general [16], and by our group for imaging the SER.

2 Materials

2.1 Preparation of Phloem Tissue for 3D-SIM

1. Fixative: 50 mM 1,4-piperazinediethanesulfonic acid (PIPES) pH 6.9, 2 mM EGTA, 1% (w/v) bovine serum albumin (BSA) in dH_2O. Add 4% (v/v) formaldehyde and 0.25% glutaraldehyde (*see* **Note 1**).
2. Stabilizing solution: 5% (w/v) Phytoagar in ddH_2O (*see* **Note 2**).
3. Wash Buffer: 2 mM EGTA, 1% BSA, 50 mM PIPES, pH 6.9 in ddH_2O.
4. PBS: Phosphate buffered saline, 1 mM KH_2PO_4, 155 mM NaCl and 10 mM Na_2HPO_4 in ddH_2O, pH 7.4.
5. Calcofluor White solution: 10 μg/ml in dH_2O.

2.2 Growth and Preparation of BY2 Cells for Live Imaging

1. BY2 growth media: 0.43% MS Basal Salts media, 3% sucrose, 2 μg/ml 2,4-Dichlorophenoxyacetic acid in ddH_2O. Sterilize by autoclaving.
2. 1 M Mannitol: dissolved in dH_2O.
3. 170 μg/ml Calcofluor White Stock Solution: dissolved in ethanol. Stored in the dark at −20 °C.
4. 100 mM $DiOC_6$ (3,3′-dihexyloxacarbocyanine iodide) stock solution: dissolved in DMSO. Stored in the dark at −20 °C.

2.3 ZIO Staining

1. Fixative: 3% (v/v) glutaraldehyde in 0.1 M sodium cacodylate (*see* **Note 3**).
2. 0.2 M sodium cacodylate: In a fume cupboard, add 21.4 g sodium cacodylate to 400 ml dH_2O. Mix well and add dH_2O to a final volume of 500 ml. Add 0.1 M HCl dropwise until the solution reaches pH 7.3. For wash buffer dilute 1:1 with dH_2O.
3. 1% Osmium tetroxide in 0.1 M sodium cacodylate: Add a 0.25 g glass vial of osmium tetroxide to a glass duran bottle and screw lid on. Shake to break vial and then add 12.5 ml dH_2O, mix gently on a rocking platform. Mix equal volumes of osmium tetroxide and sodium cacodylate buffer
4. Zinc iodide: 3 g zinc powder and 1 g resublimed iodine to 20 ml dH_2O, stir for 5 min and then filter. Leave to mature in flow hood for 4 h (*see* **Note 4**).
5. ZIO: Combine equal volumes of zinc iodide with 2% osmium tetroxide in a small aliquot, mix and use immediately.
6. Epon812.
7. 1:1 ratio of Epon812:propylene oxide.
8. 2:1 ratio of Epon812:propylene oxide.

3 Methods

3.1 Preparation of Phloem Tissue

1. Cut the stem or petiole of a 35–55-day-old tobacco plant expressing the desired fluorescent reporter (in this case pSEO2.GFP-HDEL [17]) and transfer immediately to a glass beaker containing the fixative solution and submerge the cut end. Trim approximately 5 mm from the end of the stem to avoid air blocks. Allow to transpire in an illuminated fume hood for 1 h (*see* **Note 5**).
2. Trim the tissue and add to molten stabilizer cooled to 40 °C. Submerge sample fully by gently pressing with a blunt instrument. Remove any air bubbles and carefully orient the tissue to allow for the desired angle of sectioning, e.g., positioned at 90° to the surface for transverse sections or at 180° for longitudinal sections.

3. When set, trim around the sample to form a block and then section using a vibrating microtome on a medium-fast setting to obtain sections of 100 μm.
4. Place sections into wash buffer contained in a 5 ml petri dish. Wash by replacing the buffer three times, 10 min for each wash.
5. Rinse with PBS and stain with Calcofluor White (at 10 μg/ml) for 1 min at room temperature. Rinse sections well with dH_2O.
6. Mount sections directly on a number 1.5 coverslip with a drop of Citifluor AF1 antifade medium. Apply gentle pressure to spread the mountant and remove air bubbles before sealing with nail varnish.

3.2 Preparing BY2 Cells for Live 3D-SIM Imaging

1. In advance, culture BY2 cell lines in 50 ml Erlenmeyer flasks with sterile Murashige and Skoog Basal Salts media supplemented with 3% (w/v) sucrose and 2μg/ml 2,4-Dichlorophenoxyacetic acid (*see* **Note 6**).
2. Aliquot 1 ml of cell suspension to an Eppendorf tube and stain cell walls with Calcofluor White at a final concentration of 3.5 μg/ml. Stain for 5 min at room temperature before rinsing cells twice with fresh media. Optional: if imaging wild-type cells, use $DiOC_6$ to stain the ER at a final concentration of 50 μM (*see* **Note 7**). Incubate for 10 min and then rinse twice with fresh media.
3. Induce plasmolysis by pipetting off 450 μl of media and adding 450 μl 1 M mannitol. Incubate for 10 min at room temperature before gently inverting the tube to resuspend the cells (*see* **Note 8**).
4. Pipette 40 μl of cells onto a very clean microscope slide before carefully placing the coverslip. Using a folded paper towel apply gentle, even pressure to remove excess media from the slide (*see* **Note 9**). Carefully wipe all edges, making sure the coverslip does not become smudged. Seal with nail varnish.

3.3 3D-SIM Imaging with an OMX Deltavision Blaze

1. Locate ideal cells on the auxiliary microscope (PersonalDV Deltavision) which has stage coordinates synchronized with the OMX. Use the lowest level brightfield possible to view candidate cells and mark their position on the slide using the point visiting tool. Expose all candidate cells briefly to check that both the Calcofluor White stain and the GFP reporter (or $DIOC_6$) are sufficiently bright (*see* **Note 10**).
2. Transfer the slide to the OMX and apply immersion oil (*see* **Note 11**). Using the Point List, find the marked cells and then center the cell in the image using the Spiral Mosaic function.
3. Empirically determine the lowest laser power required to achieve optimal intensities of between 1000 and 3000 counts in a raw image acquired by a 15-bit dynamic range Edge sCMOS camera.

Also optimize the shortest exposure times for each channel, typically between 100 and 200 ms (*see* **Note 12**).

4. Following optimization, acquire image stacks of appropriate cells. Set the start and end positions for a minimal z-stack quickly to avoid excess light exposure.
5. Using the SoftWorx 6.0 alignment tool, adjust the images from the separate channels and then reconstruct 3D super-resolution image stacks using SoftWorx 6.0 with channel specific OTFs and Wiener filter settings of 0.002 (*see* **Note 13**).

3.4 ZIO Staining of the SER

1. Cut the stem or petiole of a 35–55-day-old tobacco plant expressing the desired fluorescent marker (in this case pSEO2.GFP-HDEL [17]) and transfer immediately to the fixative solution and submerge the cut end. Trim approximately 5 mm from the end of the stem to avoid air blocks. Allow to transpire in an illuminated fume hood for 1 h (*see* **Note 5**).
2. Remove the leaf and chop the petiole into 5 mm by 5 mm sections.
3. Wash twice in 0.1 M Sodium Cacodylate for 10 min each wash.
4. Wash twice in dH_2O for 10 min each wash.
5. Incubate in ZIO solution at room temperature for 4 h in a sealed vial with gentle agitation on a rotating wheel.
6. Wash twice in dH_2O for 10 min each wash.
7. Dehydrate tissue in an ethanol series: submerge for 15 min per solution in 50%, 70%, and 95% ethanol before two 15 min incubations in 100% ethanol.
8. Infiltrate dehydrated tissue with a 1:1 ratio of Epon812 and propylene oxide at room temperature for 2 h.
9. Continue infiltration overnight in a 2:1 ratio of Epon812: propylene oxide at 58 °C.
10. Incubate in 100% Epon812 at room temperature for 1 h. Replace the Epon812 and incubate for one further hour.
11. Embed in flat bed molds, for 48 h at 58 °C.
12. Check orientation and quality of the tissue by cutting semi-thin sections (0.5–1 μm) using a glass knife. Stain sections briefly with Toluidine blue for accurate visualization on a bright field microscope.
13. Following identification of an appropriate area of a block, cut ultrathin sections (60 nm) with a diamond knife and float onto dH_2O. Mount sections on an EM grid by touching the dull face of the grid to the middle of a section without breaking the surface tension of the water. The sections will readily adhere to a clean grid.

14. Stain sections with uranyl acetate and lead citrate by first wetting the grids in dH_2O (*see* **Note 14**) and then float section side down for 45 min on a drop of uranyl acetate (*see* **Note 15**). Wash by dipping in dH_2O, manipulating the grid by its edge using fine forceps for 1 min and repeat the wash in fresh dH_2O. Invert the grid onto a drop of lead citrate for counter staining, for 10 min. Wash again in dH_2O for 1 min and then repeat for a further 1 min in fresh dH_2O.
15. Air dry before imaging with the TEM.

4 Notes

1. The fixative solution should be prepared freshly on the day of use. However, the PIPES, EGTA, and BSA stock solutions may be prepared in advance and stored on the bench following autoclave sterilization. Glutaraldehyde should be EM-grade and formaldehyde from a methanol free solution. Fixatives provided in single-use glass ampules provide the best source and any unused can be decanted into a glass bottle and sorted for up to 1 month, glutaraldehyde at 4 °C and formaldehyde at room temperature.
2. Phytoagar is a specialist agar used for plant tissue culture. With a high gel strength at a 5% solution this matches the mechanical properties of petiole tissue and thus supports the tissue well during sectioning. The concentration may require optimization when used as a stabilizer for other tissues types to avoid the agar pulling away from the tissue or disintegrating.
3. To preserve the fine ultrastructure of the cell in ultrathin TEM sections, it is necessary to increase the glutaraldehyde content of the fixative to 3%.
4. The solution should turn a light straw color during the maturation process.
5. Due to transpiration the fixative is drawn up into the xylem, from where it moves laterally to the phloem and other tissues, providing a gentle delivery system which avoids mechanical damage of the phloem cells.
6. Incubate liquid BY2 cell cultures at 28 °C, in the dark, shaking at 140 rpm. Sub-culture cells weekly using a 1:40 dilution. If the cells are stably transformed with a fluorescent marker for the ER such as RTN6-GFP, ensure that the signal is strong and relatively homogenous in the line of choice. Best results are usually obtained with cells which were subbed 3–4 days prior to imaging.
7. $DiOC_6$ will stain the ER, mitochondria, and vesicle membranes. It is, however, extremely phototoxic so the cells must

be kept in the dark once stained and illumination minimized to reduce ER damage.

8. Plasmolysis allows clearer imaging of the desmotubules as the membrane is retracted away from the cell wall, and the Hechtian strands can be clearly labeled either by RTN6-GFP or $DiOC_6$.
9. To achieve optimal imaging, the cells need to be as close to the coverslip as possible.
10. It is vital to keep all light exposure as brief as possible prior to the SIM imaging so as to minimize any pre-imaging photobleaching or phototoxicity from $DiOC_6$.
11. The type of immersion oil should be matched as closely as possible to the refractive index of the sample to minimize spherical aberrations. To achieve the best combination, in theory the cells should be mounted in a high concentration of glycerol/antifade mountant, but this was found to affect the ER structure, so cells were mounted in media.
12. It is advisable to carry out the optimization on a sacrificial cell—by the time the process is complete, the GFP is likely to have bleached sufficiently to prohibit good image capture during the 3D-SIM process.
13. The microscope must be routinely calibrated by measuring channel specific optical transfer functions (OTFs) to optimize both lateral and axial image resolution. Alignment tools should also be regularly calibrated based on alignment parameters obtained from calibration measurements with 100 nm-diameter TetraSpeck beads.
14. Pre-wetting the EM grids minimizes potential artifacts by reducing air–stain contact [18].
15. Spot stain on to a plastic petri dish and keep covered to reduce contamination or artifacts from dust, evaporation, and CO_2 (particularly important for lead citrate).

References

1. Abbe E (1873) Beiträge zur Theorie des Mikroskops und der mikroskopischen Wahrnehmung. Arkiv Mikroskop Anat 9:413–468
2. Wilson T (1995) The role of the pinhole in confocal imaging system. In: Pawley JB (ed) Biological confocal microscopy. Plenum Press, New York, pp 167–182
3. Gustafson MGL (2000) Surpassing the lateral resolution limit by a factor of two using structured illumination microscopy. J Microsc 198:82–87
4. Schermelleh L, Carlton PM, Haase S et al (2008) Subdiffraction multicolour imaging of the nuclear peripheray with 3D structured illumination microscopy. Science 320:1332–1336
5. Dobbie I, King E, Partion RM et al (2011) OMX: a new platform for multimodal, multichannel wide-field imaging. Cold Spring Harb Protoc 8:899–909
6. Kner P, Chhun BB, Griffis ER et al (2009) Super-resolution video microscopy of live cells by structured illumination. Nat Methods 6:339–342
7. Fitzgibbon J, Bell K, King E, Oparka K (2010) Super-resolution imaging of plasmodesmata

using 3-dimensional structured illumination microscopy. Plant Physiol 153:1453–1463

8. Bell K, Mitchell S, Paultre D, Posch M, Oparka K (2013) Correlative imaging of fluorescent proteins in resin-embedded plant material. Plant Physiol 161:1595–1603
9. Bell K, Oparka K (2015) Preparative methods for imaging plasmodesmata at super-resolution. Methods Mol Biol 1217:67–79
10. Bell K, Oparka K, Knox K (2016) Super-resolution imaging of live BY2 cells using 3D-structured illumination microscopy. Bio-protocol 6(1):e1697
11. Evert RF (1990) Dicotyledons. In: Behnke H-D, Sjolund RD (eds) Sieve elements: comparative structure, induction and development. Springer-Verlag, Berlin, pp 103–137
12. Nagata T, Nemoto Y, Hasezawa S (1992) Tobacco BY-2 cell line as the "HeLa" cell in the cell biology of higher plants. Int Rev Cytol 132:1–30
13. Overall RL, Blackman LM (1996) A model of the macro-molecular structure of plasmodesmata. Trends Plant Sci 1:307–331
14. Knox K, Wang P, Kriechbaumer V, Tilsner J, Frigerio L, Sparkes I, Hawes C, Oparka K (2015) Putting the squeeze on plasmodesmata: a role for reticulons in primary plasmodesmata formation. Plant Physiol 168:1563–1572
15. Maillet M (1968) Etude critique des fixations au tétraoxyde d'osmium-iodure. Bull Assoc Anat 79:233–394
16. Barlow PW, Hawes C, Horne JC (1984) Structure of amyloplasts and endoplasmic reticulum in the root caps of *Lepidium sativum* and *Zea mays* observed after selective membrane staining and by high-voltage electron microscopy. Planta 160:363–371
17. Knoblauch M, Peters WS (2010) Münch, morphology, microfluidics: our structural problem with the phloem. Plant Cell Environ 33:1439–1452
18. Hayat MA (1968) The principles and techniques of electron microscopy, vol 1. Van Nostt and Reinold Company, New York, NY

3D-structured illumination microscopy (3D-SIM) and photoactivation localisation microscopy (PALM): new tools in the study of plasmodesmal structure

Karen Bell [1], Jessica Fitzgibbon [1] , Emma King [2], Cristina Flors [3], Jens Tilsner [4] and Karl Oparka [1]

[1] Institute of Molecular Plant Sciences, School of Biological Sciences, University of Edinburgh, Daniel Rutherford Building, The King's Buildings, Mayfield Road, Edinburgh, EH9 3JR.
[2] Light Microscopy Facility, College of Life Sciences, University of Dundee, Dow Street, Dundee, DD1 5EH.
[3] School of Chemistry and Collaborative Optical Spectroscopy Micromanipulation and Imaging Centre (COSMIC), University of Edinburgh, Joseph Black Building, The King's Buildings, West Mains Road,Edinburgh, EH9 3JJ.
[4] Plant Pathology, Scottish Crop Research Institute, Invergowrie, Dundee, DD2 5DA.

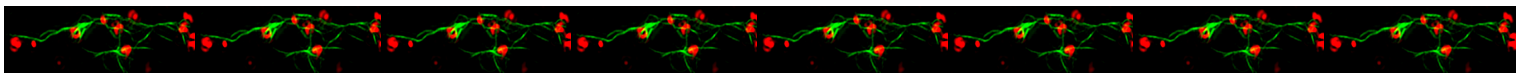

Introduction

Much of our knowledge of biological structures and processes has come from the ability to visualise them. Due to its compatibility with facile detection methods, light microscopy has become an essential tool in the elucidation of biological structures and interactions. However, the main limitation of light microscopy is spatial resolution. In an ideal system, objects closer than ~200nm , roughly half the λ of incident light, cannot be distinguished.
Gradual improvements in sample preparation and microscope design (e.g. confocal laser scanning microscopy; CSLM) have made this theoretical limit an almost daily obstacle in cell biology.
Recent developments in microscopy have overcome the limit set by the diffraction of emitted light and promise potentially unlimited resolution. These so-called 'super-resolution' techniques broadly fall into two groups that achieve improved spatial resolution either through single molecule detection or via spatially patterned excitation.
At approximately 50nm in diameter, plasmodesmata (PD) are below the theoretical diffraction limit. Therefore, the study of PD is likely to benefit significantly from the arrival of these new technologies.

3D-SIM (structured illumination microscopy)

*** A sub-diffraction imaging system that is compatible with conventional fluorochromes and sample preparation methods.**

*** Achieves double the spatial resolution possible with conventional lens-based methods (e.g. CLSM) and achieves 100nm x-y (lateral) and 200nm in z (axial) resolution**

*** Achieves 125nm Z-steps when optical sectioning**

Schematic of 3D-SIM imaging system

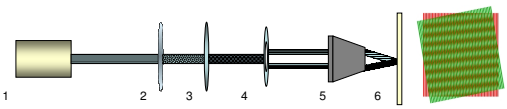

1.Laser 2.Diffuser 3.Polariser 4.Diffraction Grating

5.Objective 6.Sample

Moiré fringe

Combining the two beams of light upon the sample produces a high frequency sinusoidal illumination pattern.

High frequency excitation light and high frequency features in the sample combine to produce a Moiré pattern of much lower spatial frequency that is within the detection range of the microscope.

As the pattern of the excitation light is known, the Moiré fringe thus contains information about the unknown sample structure.

Illumination patterns are still limited by diffraction. However, recently described SSIM (saturated structured illumination microscopy) is truly 'super resolution' and has achieved 50nm resolution x-y [(2)]

3D-SIM study of *Nicotiana tabacum* TMVMP:GFP 35s

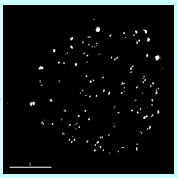

Widefield image of trichome basal cell in face view.

* Resolve individual pores in pitfield

*125nm optical sections through complex PD at trichome-epidermis interface

* 6 pores fuse in middle lamella with 3 orifices emerging in the underlying epidermis

* Complex architecture imaged non-destructively

3D-SIM optical sectioning through highlighted pitfield

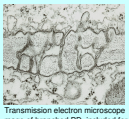

Transmission electron microscope image of branched PD included for comparison (courtesy of Rainer Kollmann).

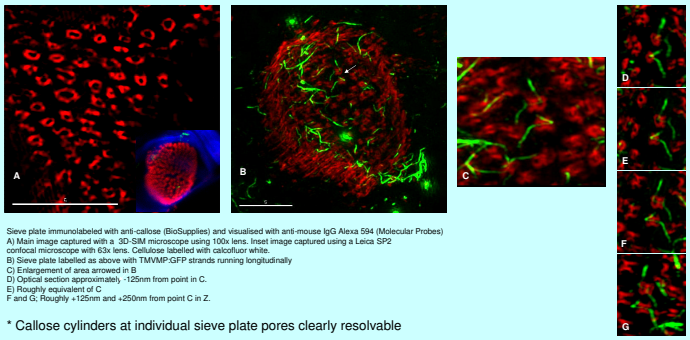

Sieve plate immunolabeled with anti-callose (BioSupplies) and visualised with anti-mouse IgG Alexa 594 (Molecular Probes)
A) Main image captured with a 3D-SIM microscope using 100x lens. Inset image captured using a Leica SP2 confocal microscope with 63x lens. Cellulose labelled with calcofluor white.
B) Sieve plate labelled as above with TMVMP:GFP strands running longitudinally
C) Enlargement of area arrowed in B
D) Optical section approximately -125nm from point in C.
E) Roughly equivalent of C
F and G; Roughly +125nm and +250nm from point C in Z.

* Callose cylinders at individual sieve plate pores clearly resolvable

* Average diameter of pore approximately 276nm, callose collar extends this to 568nm

* Optical sections through sieve plate reveals intimate arrangement of TMVMP:GFP decorated strands with callose lined sieve plate pores

* Follow strands running longitudinally through pores

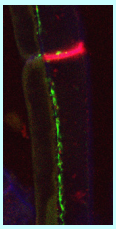

* TMVMP:GFP filaments extend from pore-PD that connect sieve element with associated companion cell

* distribution along sieve element parietal layer, no equivalent strands in companion cell

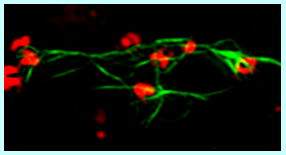

* Up to 4 strands 89nm (average diameter) from single pore PD this is the limit of 3D-SIM resolution

PALM (photoactivation localisation microscopy)

PALM can be truly described as a super resolution imaging technique as the resolution potential is not limited by the diffraction of light but by the number of photons that can be collected from each fluoroscent molecule.
A lateral resolution of 20nm has been reported [(1)]

An image is fitted by collecting multiple photons from a fluorochrome and then precisely mapping the position of each one

To achieve high precision mapping, fluorochromes with specific photophysical properties are required.

The ability to switch between a fluorescent "on" and a "dark" state allows temporal separation [(4)]

Only a proportion of the molecules are ever "on" at any one time, allowing their position to be mapped precisely.

By continually activating further subsets of the fluorochrome population, a high resolution image can be reconstructed.

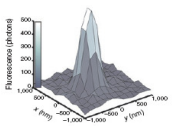

Point spread function is effectively narrowed following successive photon collection and fitting cycles

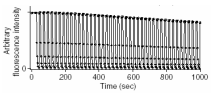

To have desired characteristics for PALM, probe must be capable of switching frequently whilst retaining a high photon output thus allowing position to be precisely mapped.

Preliminary PALM data

* LifeAct [(5)] fused to Dronpa to visualise F-actin .

* Tissue fixed, peeled and then imaged with TIRF:PALM system

* 58nm cross-section average

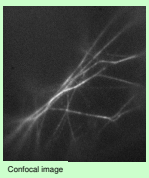

Confocal image

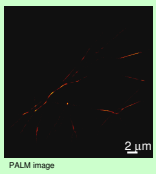

PALM image

Cross-section actin fibre (average)

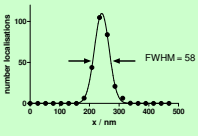

Future Directions

Optimise conditions for imaging plant cells with TIRF PALM

Generate a suite of putative and known plasmodesmal proteins compatible with super resolution imaging

Dissect viral replication complexes

Work with our collaborators to exploit future developments in super resolution imaging (e.g. live cell 3D-SIM, multicolour PALM) for plant cell study.

References

[1]Huang, B., Bates, M. and Zhuang, X. (2009). Super-Resolution Fluorescence Microscopy. Annu. Rev. Biochem. 78: 993-1016.

[2] Gustafsson, M.G.L. (2005). Nonlinear structured-illumination microscopy:wide-field fluorescent imaging with theoretically unlimited resolution. Proc.Natl.Acad.Sci. 102:13081-86.

[3] Schermelleh, L., Carlton, P.M., Haase, S., Shao, L., Winoto, L., Kner, P., Burke, B., Cardoso, M. C., Agard, D.A., Gustafsson, M.G.L., Leonhardt, H. and Sedat, J. W. (2008) Subdiffraction multicolour imaging of the nuclear periphery with 3D structured illumination microscopy. Science. 320:1332-1336

[4] Betzig, E., Patterson, G.H., Sougrat, R., Lindwasser, O. W., Olenych, S., Bonifacino, J. S., Davidson, M. W., Lippincott-Schwartz, J. and Hess, H. F. (2006). Imaging intracellular fluorescent proteins at nanometer resolution. Science. 313:1642-1645.

[5] Reidl, J., Crevenna, A.H., Kessenbrock, K., Hoachen, J.,Neukirchen, D., Bista, M., Bradke, F., Jenne, D., Holak, T.A., Werb, Z., Sixt, M. and Wedlich-Soldner, R. (2008). Lifeact: a versitile marker to visualise F-actin. Nature Methods 5: 605-607

Acknowledgements

A University of Edinburgh Staff Scholarship supports my studies